UNIVERSIDAD
DE GRANADA

DOCTORAL THESIS

High-resolution lithospheric structure in the Gibraltar arc using P and S receiver functions

---

Author:
Antonio MOLINA AGUILERA

Supervisor:
Dr. Flor de Lis MANCILLA
Dr. Jose MORALES SOTO

Programa de Doctorado Ciencias de la Tierra

Editor: Universidad de Granada. Tesis Doctorales
Autor: Antonio Manuel Molina Aguilera
ISBN: 978-84-1306-249-5
URI: http://hdl.handle.net/10481/56455

in the

Instituto Andaluz de Geofísica
Departamento de Física Teórica y del Cosmos

February 19, 2019

Declaration of Authorship

El doctorando / The doctoral candidate **Molina Aguilera, Antonio Manuel** y los directores de la tesis / and the thesis supervisor/s: **Mancilla Pérez, Flor de Lis** y **Morales Soto, José** Garantizamos, al firmar esta tesis doctoral, que el trabajo ha sido realizado por el doctorando bajo la dirección de los directores de la tesis y hasta donde nuestro conocimiento alcanza, en la realización del trabajo, se han respetado los derechos de otros autores a ser citados, cuando se han utilizado sus resultados o publicaciones. / Guarantee, by signing this doctoral thesis, that the work has been done by the doctoral candidate under the direction of the thesis supervisor/s and, as far as our knowledge reaches, in the performance of the work, the rights of other authors to be cited (when their results or publications have been used) have been respected.

Lugar y Fecha / Place and Date:

Firma / Signed (Doctorando / Doctoral Candidate): Antonio Molina Aguilera

Firma / Signed (Director / Thesis supervisor): Flor de Lis Mancilla

Firma / Signed (Director / Thesis supervisor): Jose Morales Soto

"¿Y qué es el hombre que busca sino, por definición, un ser errático?"
"And what is a man in search of something if not, by definition, an erratic being?"

Alejandro Jodorowsky

UNIVERSITY OF GRANADA

Abstract

Facultad de Ciencias
Departamento de Física Teórica y del Cosmos

Ciencias de la Tierra

High-resolution lithospheric structure in the Gibraltar arc using P and S receiver functions

by Antonio MOLINA AGUILERA

Plate margin between Africa and Eurasia in westernmost Mediterranean is distributed as an irregular boundary that configures a tight orogenic belt, the Gibraltar arc. The region exhibits tectonic processes which may involve both oceanic and continental subduction and delamination. Thought the geodynamics of the zone has mainly been interpreted in terms of east dipping subduction rollback, the relationship between slab dynamics and surface tectonics is still under considerable debate. In this thesis we shed some light on the complex geodynamics of the Ibero-Maghrebian region by imaging precisely the crustal and upper mantle structure using the S and P receiver function approaches. The seismic imaging with S receiver functions all along the Gibraltar arc reveals the connection through an oceanic corridor between the Alboran slab under the Alboran Sea and the Atlantic oceanic crust. Previous P receiver function interpretations showed significant lateral heterogeneities in the lithosphere and suggest processes of underthrusting and continental delamination occurring mainly in Southeastern Spain. We analyze two high-resolution passive seismic profiles to probe the crustal structure in the central and eastern Betic orogen, implementing different and complementary receiver function interpretation techniques: (1) the conventional Common Conversion Point stacking method based on the simplifying flat-layered assumption that enhances the main crustal structure along the profiles; (2) the reverse time migration technique, which exploits the whole complexity of the wavefield, produces clearer images of the Moho topography; (3) backazimuth harmonic decompositions of receiver functions to constrain the geometry and strength of lateral heterogeneities that also allows to obtain an only sensitive to the flat-layered structure receiver function to be (4) jointly inverted with surface wave dispersion curves and therefore obtain the average 1D S-wave velocity depth profile.

All these methods give coherent and complementary results. A sharp and prominent crustal step ($\sim$15-17 km) is observed in both profiles, coinciding with the boundary between the Iberian and Alboran domains and interpreted as a near-vertical STEP fault that propagates to the surface as a positive flower fault structure. This STEP fault accommodated the differences in the subduction rollback velocity along the strike, at the northern edge of the Western Mediterranean system, when the thinned Iberian continental lithosphere started subducting under the Alboran domain. The changes in the topography of the Moho discontinuity, and the geometry of the STEP fault in Central Betics is driven by inherited weaknesses in the Iberian paleomargin. No crustal roots are observed under the highest altitudes of both profiles suggesting that its high topography is due to a combination of the uplift produced by the positive flower structure and the push up of the asthenosphere after the lithospheric removal of the underthrusting Iberia along the STEP fault. Using the harmonic decomposition of radial and transverse receiver functions we obtain a continuous representation of the lateral heterogeneity with depth along the crust and the uppermost mantle, determining the orientation of anisotropy and dipping interfaces. This analysis distinguishes several zones along the region: (1) the Alboran domain located in the SE section nearby the coastline and mainly characterized by a dipping NNW Moho discontinuity and a regional anisotropy governs by stress-induced shear anisotropy and structural anisotropy nearby the main faults of the Eastern Betics shear zone, (2) the transition zone between the Alboran domain and the Iberian Massif coinciding with the STEP fault and marked by the presence of significant dipping and/or anisotropy at crustal and subcrustal depths and (3) a stable region without considerable lateral heterogeneity.

Resumen

El límite de las placas eurasiática y africana en la zona más occidental del Mediterráneo se distribuye de forma irregular y configura un arco orogénico, el arco de Gibraltar. La región exhibe procesos tectónicos que incluyen subducción oceánica y continental así como delaminación continental. Aunque la geodinámica de la zona está ampliamente interpretada de acuerdo a una subducción en retroceso hacia el este, la relación entre la dinámica de la laja que subduce y la tectónica más superficial es aún controvertida. En esta tesis aportamos luz sobre la compleja geodinámica de la región Íbero-Magrebí mediante la obtención de imágenes de alta resolución de la estructura cortical y del manto superior usando la técnica de funciones receptoras de onda P y S. Las imágenes sísmicas obtenidas con las funciones receptoras S a lo largo del arco de Gibraltar muestran la conexión mediante un corredor oceánico entre la laja de Alborán situada bajo el mar de Alborán y la corteza oceánica Atlántica. Interpretaciones de funciones receptoras previas revelaron la presencia de heterogeneidades laterales significativas en la litosfera sugiriendo procesos de cabalgamiento y delaminación continental en el sudeste de España. Analizamos dos perfiles sísmicos pasivos de alta resolución para dibujar la estructura cortical en la zona central y oriental del orógeno Bético, implementando una variedad de métodos de funciones receptoras que son complementarios: (1) la migración convencional de punto de conversión común (*Common Conversion Point stacking*, basada en la hipótesis simplificadora de

modelo de capas plano-paralelas, que ha permitido iluminar la estructura cortical más importante a lo largo de los perfiles; (2) la migración de tiempo invertido (*Reverse Time Migration*), que emplea toda la complejidad de la forma de onda, que ha generado imágenes más claras de la topografía de la discontinuidad entre la corteza y el manto (Moho); (3) la descomposicion en armónicos de las funciones receptoras de onda P según el back-azimuth que ha ayudado a constreñir la geometría e intensidad de las heterogeneidades laterales así como la obtención de una función receptora solo sensible a la estructura plano-paralela del subsuelo que puede (4) ser invertida conjuntamente con curvas de dispersión de ondas superficiales y así obtener un perfil promedio 1D de velocidad en profundidad.

Todos estos métodos arrojan resultados coherentes y complementarios. Uno de los resultados mas importantes de este trabajo es la presencia de un salto cortical brusco y prominente (15-17 km) observado en ambos perfiles de alta densidad, que coincide con el límite entre los dominios de Alborán y el domino Ibérico, y es interpretado como una falla de desgarro vertical (o STEP) cuya propagación hasta la superficie a lo largo de la placa que cabalga (dominio de Alboran) se produce en forma de estructura de flor positiva. Esta falla de desgarro acomodó las diferencias en la velocidad de la subducción en retroceso (*roll-back*) a lo largo de la dirección de subducción, en el flanco norte del sistema Mediterráneo occidental, cuando la litosfera continental Ibérica comenzó a subducir bajo el dominio de Alborán. Los cambios en la topografía de la discontinuidad Moho, y la geometría de la falla de desgarro en la parte central de las Béticas ha venido propiciados por debilidades en el paleomargen de Iberia. No se aprecian raíces corticales bajo las mayores altitudes en ambos perfiles sugiriendo que la topografía más elevada se debe a la combinación del levantamiento producida por la estructura en flor positiva y el empuje de la astenosfera producido por el desgarro de la litosfera subducida de Iberia a lo largo de la falla de desgarro. Usando la descomposición en armónicos de las funciones receptoras de componente radial y transversal se ha obtenido una representación continua de la heterogeneidad lateral en profundidad a lo largo de la corteza y el manto superior, determinando la orientación de la anisotropía y el buzamiento de las discontinuidades principalmente corticales. Este análisis distingue varias zonas con características propias a lo largo de la región: (1) el dominio de Alborán localizado en el sudeste de Iberia, cerca de la linea de costa, se distingue principalmente por una Moho que buza en dirección NNO y una anisotropía regional gobernada por el esfuerzo regional (*stress-induced shear*) y anisotropía estructural en la zona cercana a las fallas principales de la zona de cizalla de las Béticas orientales (*Eastern Betics shear zone*), (2) la zona de transición entre el dominio de Alborán y el macizo Ibérico que coincide con la falla desgarro está caracterizada por la presencia significativa de buzamiento y/o anisotropía a profundidad cortical y subcortical y (3) la región estable sin presencia importante de heterogeneidad lateral asociada al macizo Ibérico.

Acknowledgements

Un folclorista tejano decía que una tesis promedio no es más que un tránsito de huesos de un cementerio a otro. Espero que esta tesis diste de ser promedio y pueda movilizar algo más que material inerte. Si se ha conseguido, no se debe sin duda alguna únicamente a mi esfuerzo. Tengo que agradecer a mis dos directores de tesis, Flor de Lis Mancilla y José Morales, primero por haberme dado la oportunidad de embarcarme en este viaje, que no sé si me ha hecho más conocedor de la sismología pero desde luego que sí una persona más paciente. Agradezco también su supervisión atenta, bien guiada y alentadora. De Flor destaco que se haya bajado a la arena para trabajar codo con codo conmigo cada vez que ha hecho falta. Su esfuerzo ha permitido que esta tesis acabe fructificando. Gracias también a Pepe, por su entusiasmo continuo que ha disparado mis ganas de seguir peleándome con datos y códigos.

Tengo que agradecer también a todos aquellos doctores que me han supervisado durante las estancias que he realizado en centros de investigación extranjeros. Del GFZ en Berlín, agradezco a Xiaohui Yuan por su ayuda alegre en todo momento, a Felix Schneider por supervisar de cerca y prestar desinteresadamente sus códigos y a Benjamin Heit por sus consejos siempre acertados y mostrarme más de un sitio donde cenar en Berlín. Agradezco al Dr. Jordi Julià facilitarme sobremanera mi estancia en Natal, abriéndome las puertas de su casa. También al Dr. Marteen V. der Hoop que tutorizó entusiasmadamente mi estancia en Houston.

Gracias a mis compañeros del Instituto Andaluz de Geofísica, que han hecho más liviana la carga a fuerza de cafés y gratas conversaciones al sol. Gracias a mi árbol genealógico más inmediato por su sacrificio desde siempre en garantizar mi formación.

Y gracias a M, que me acompañó estos cinco años y dio una consistencia real y humana a tanto aparataje teórico.

Contents

List of Figures

List of Abbreviations

AMF	**A**lhama de **M**urcia **F**ault
BFT	**B**etic **F**rontal **T**hrust
CCP	**C**ommon **C**onversion **P**oint
CF	**C**revillente **F**ault
EZP	**E**xternal **Z**ones **P**rebetics
EZS	**E**xternal **Z**ones **S**ubbetics
GB	**G**uadix **B**asin
HD	**H**armonic **D**ecomposition
HSC	**H**alf **S**pace **C**ooling model
IM	**I**berian **M**assif
IZAL	**I**nternal **Z**ones **AL**pujarride
IZNV	**I**nternal **Z**ones **N**evado-**F**ilabride
JOL	**J**urassic **O**ceanic **L**ithosphere
LAB	**L**ithosphere **A**sthenosphere **B**oundary
MCCC	**M**ulti-**C**omponent **C**ross **C**orrelation
MCD	**M**id-**C**rustal **D**ecollment
PCA	**P**rincipal **C**omponent **A**nalysis
PRFs	**P** **R**eceiver **F**unctions
PM	**P**late **M**odel
RF	**R**eceiver **F**unction
SRFs	**S** **R**eceiver **F**unctions
RTM	**R**everse **T**ime **M**igration
SMD	**S**ubbetic **M**id-crustal **D**ecollment
STEP	**S**ubduction **T**ransform **E**dge **P**ropagator fault
TASZ	The **T**rans- **A**lboran **S**hear **Z**one

Chapter 1

Introduction

Plate margin between Africa and Eurasia in westernmost Mediterranean is distributed as a diffuse and irregular convergence boundary that configures a tight orogenic belt, the Gibraltar arc. Tomographic studies in the region display an arcuate strongly-dipping mantle fast body located in the inner arc (e.g., Bezada et al., 2013; Palomeras et al., 2014; Levander et al., 2014). Based mainly on this geophysical evidence together with slab-evolution modelling (Vergés and Fernàndez, 2012; Van Hinsbergen, Vissers, and Spakman, 2014; Chertova et al., 2014), the geodynamics of the region is interpreted primarily in terms of east dipping subduction rollback. However, the relationship between the slab dynamics and the surface tectonics is still an ongoing debate. The region exhibits a wide range of plate-tectonic processes which involve both oceanic and continental subduction. Furthermore, the existence of an extensional basin formed at a site of colliding continents have driven to alternative tectonic models.

The complexity of the Iberia-Maghreb plate boundary zone has been represented with ever-increasing detail as more and more observational data from different disciplines were becoming available. Geophysical studies more focused on the crustal and upper-mantle structure have revealed the presence of significant lateral heterogeneities in the lithosphere and suggest processes of underthrusting, continental delamination and slab tearing (e.g., Thurner et al., 2014; Mancilla et al., 2015b; Palomeras et al., 2017). Among these techniques, the receiver function (RF) method (Vinnik, 1977, Langston, 1979) based on teleseismic converted waves produced at interfaces separating materials with different physical parameters proves to be a very appropriate approach to determine the depth and velocity contrast of lithospheric discontinuities. By employing P-to-S conversions, PRF method, we map the crust-mantle or Moho discontinuity. The Lithosphere-Asthenosphere Boundary (LAB) can be imaged using S-to-P converted waves (SRF method).

Geophysical studies have not clarified so far how the high-velocity body, possibly corresponding to oceanic lithosphere, is connected with the surface and thus to the continental lithosphere of North Africa and Iberia. Lithospheric thickness knowledge might shed light on this but LAB studies are scarce in the region, based on LAB modelling (Fullea et al., 2007; Fullea et al., 2010) and SRF methods (Dündar et al., 2011; Miller et al., 2015) they do not lead to identical results. In the first part of this thesis we apply the SRF technique to the large-scale seismic network extended along the Gibraltar arc during the last decade to map the LAB discontinuity using an unprecedented amount of data and provide new hints about the slab and the upper-mantle structure.

Recent PRF studies have reported significant topographic variations of the Moho discontinuity from the western to the eastern sides of the Gibraltar arc confirming that continental delamination processes are involved (Mancilla et al., 2013; Mancilla et al., 2015b; Thurner et al., 2014). Motivated by these important Moho gradients we perform a high-resolution passive seismic experiment in Southeastern Spain to image in detail the lithospheric structure along the region. The high density seismic array, with an averaged inter-station spacing of 4-5 km, permits not only employ conventional RF applications based on simplifying assumptions but also call for emerging RF imaging techniques (Reverse Time Migration) (Shang, Hoop, and Hilst, 2017) that exploit the full complexity of recorded wavefields. In addition, the region is distinguished by the presence of appreciable lateral heterogeneities that cause characteristic variations on RFs. Using these variations we develop refined applications (harmonic decomposition analysis) that separate in the RFs the signal regarded to the dipping and/or anisotropic layers from the one associated to the flat-layered isotropic structure. In this way we can constrain the geometry and strength of the lateral heterogeneity and invert the S-wave velocity-depth profile.

This thesis is ordered as follows: In the second chapter we introduce the tectonic setting and current day knowledge of the Gibraltar arc region. The chapter 3 focuses on the data and method employed in this thesis; the instrumentation involves both (1) the virtual seismic network deployed during the last decade within the Ibero-Maghrebian region and (2) the high-resolution seismic experiment performed in Southeastern Spain. We describe as well in this chapter the basis of the receiver function (RF) method and the several applications that we will use in the thesis. Chapters 4 and 5 present and discuss S-RF and P-RF cross-sections, respectively, using a Common Conversion Point stacking migration scheme. This conventional approach is based only on the radial component of RFs and assume that the medium is isotropic and flat-layered. Next chapters pursue to take into account the more complex information contained in RFs following different strategies. In chapter 6 we apply the Reverse Time Migration procedure adapted to teleseismic dataset to the high-dense seismograph. Since the method solves the wave equation, it exploits the whole complexity of the waveform being able to include complex wave propagation phenomena such as scattering and diffraction. In chapter 7, based on a harmonic decomposition analysis, we use the known behaviour that RFs have in presence of lateral heterogeneity to estimate the strength and geometry of dipping and/or anisotropic structures. Chapter 8 makes use of the harmonic decomposition analysis to employ the joint inversion of RFs and surface wave dispersion curves in regions with considerable presence of lateral heterogeneity.

Chapter 2

The Gibraltar arc tectonic setting

Continental convergence zones around the world are commonly highly sinuous and include orogenic arcs of variable curvature, ranging from very open, broad arcs, such as the Himalayan mountain chain, to very tight, small scale arcs, such as the Gibraltar or Betic-Rif arc (Fig. 2.1a). Many of these mountain chains follow plate boundaries though, neither the local trend nor the degree of curvature is predictable from the magnitude or orientation of relative plate motions. Similar to the characteristic coupled intraoceanic subduction zones and marginal basins of the western Pacific, the orogenic arc systems present a hinterland region that shows evidence for crustal thinning and, in some cases, rifting and the formation of a new oceanic lithosphere (Faccenna et al., 2001; Platt, 2007; Jolivet et al., 2008). In contrast, continental orogenic arcs give evidence for significant shortening and thickening of continental crust, and in some cases subduction of subcontinental mantle and perhaps also lower crust. These systems therefore represent large areas of tectonism that involve tectonic processes we still do not fully understand.

The Gibraltar arc straddles the westernmost section of the Africa-Eurasia plate boundary in Europe. It is marked by slow oblique convergence and diffuse seismicity distributed in a wide zone of deformation (Fig. 2.1b). Considerable focus was obtained by seismic tomographies (Spakman, Wortel, and Wortel, 2004; Bezada and Humphreys, 2012; Gutscher et al., 2012; Villaseñor et al., 2015) which have imaged the mantle structure beneath the Gibraltar Arc.

These studies revealed a high velocity anomaly extended in depth continuously from ∼60 km to the bottom of the transition zone which has been interpreted as an eastward dipping oceanic slab (Blanco and Spakman, 1993; Zeck, 1996; Calvert and Alguacil, 2000; Gutscher, 2002; Bezada et al., 2013; Palomeras et al., 2014). Tectonic reconstruction (Vergés and Fernàndez, 2012; Van Hinsbergen, Vissers, and Spakman, 2014) and three-dimensional (3D) slab-evolution modelling (Chertova et al., 2014) demonstrated that westward subduction rollback was a prime driver of tectonic evolution during the Neogene in the region.

The Alboran slab is a key element for understanding regional geodynamics. Together with the Calabrian slab, these structures represent the present configuration of the Western Mediterranean subduction system, involving the cold oceanic lithosphere of the Alpine Tethys (e.g. Lonergan and White, 1997; Van Hinsbergen, Vissers, and Spakman, 2014). While the Calabrian subduction remains clearly active today, with associated seismicity, active volcanism and an active accretionary wedge (e.g. Gutscher et al., 2017; Scarfì et al., 2018), there is a lack of evidence for ongoing subduction of the Alboran slab. Deep and intermediate earthquakes do not depict a continuous Wadati-Benioff zone (e.g. Buforn, Udías, and Madariaga, 1991; Heit et al., 2017). Earthquake focal mechanisms, stress field and geodetic deformation (e.g. Stich et al., 2006) reflect Nubia-Eurasia plate motion rather than subduction dynamics. Furthermore, it seems that the absolute motions leads the current slab dynamics (Spakman et al., 2018).

The region is characterized by complex tectonics, widespread deformation, and the interaction between continental and oceanic domains. The specific role of the slab in determining regional tectonics is still equivocal, being no yet integral explanation for important first-order tectonic features that characterize the Gibraltar arc region. Some of these puzzling features comprise; the seemingly contradictory observation of an extensional basin formed at a site of colliding continents, the geodynamic origin of a regionally prominent fault system (the seismically active West Trans Alboran Shear Zone and the Eastern Betics Shear Zone), the WSW–ENE extension of the central–eastern Betics and the contrasting main tectonic shortening directions of the Rif and Betic orogens.

These geophysical and geologic evidences have led to competing geodynamic models (Platt et al., 2013). The region has the potential to enlighten us about a range of plate-tectonic and post-plate-tectonic processes. The aim of this chapter is to highlight what we know about the Gibraltar arc system and what we need to know to elucidate the controversy.

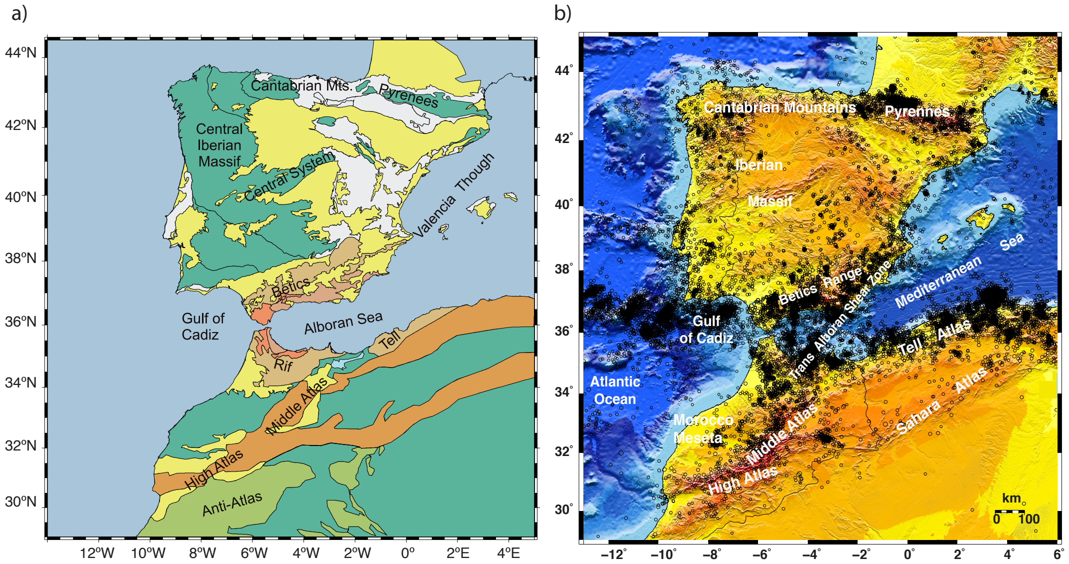

FIGURE 2.1: a) Main geological, tectonic and geographic domains in the Iberia-Maghreb region, covering the Iberian Peninsula, NW-Africa, and nearby offshore regions (modified from Mancilla, Diaz, and Team, 2015); b) map with the seismicity (magnitude > 3) in the Iberia-Maghreb region from ISC on-line bulletin (International Seismological Centre, www.isc.ac.uk).

2.1 Plate tectonic setting

The Iberian-Maghreb region occupies the central side of the Eurasia-Nubia plate boundary, including the Iberian Peninsula, North Africa and nearby offshore areas in the Gulf of Cadiz and the western Mediterranean Sea (Fig. 2.1). The main geological feature of the region is the Gibraltar arc system; an alpine orogenic belt which comprises the Betics-Rif Cordilleras accompanied by a frontal sedimentary wedge in the Gulf of Cadiz and the Alboran forearc extensional basin in the inner part. At the center of the region, the Gibraltar strait separates the Atlantic Ocean (Gulf of Cadiz) from the Mediterranean (Alboran Sea), and at the same time connects the Alpine Mountain ranges in Iberia (Betics) and Africa (Rif) (fig. 2.1a). The present-day configuration, with the characteristic, tightly curved orogenic arc, results mainly from the interplay between slow, NW-SE convergence between Eurasia and Nubia and fast westward slab retreat since the Miocene (e.g. Lonergan and White, 1997; Spakman, Wortel, and Wortel, 2004; Faccenna et al., 2004; Chertova et al., 2014).

The boundary between Eurasia and Nubia plates is clearly delineated by the seismicity in its western region changing from an extensional tectonic framework in the West, close to the Mid-Atlantic Ridge, to strike-slip tectonic behaviour along the Azores-Gloria transform fault system. Further to the east, from cape San Vicente to the Strait of Gibraltar, a slight obliquity between the relative plate motion and the boundary generates an increasing component of convergent motion (Stich, Mancilla, and Morales, 2005, Stich et al., 2007). The boundary then passes into a zone of diffuse deformation with several hundreds kilometers wide, mainly associated, but not exclusively, with shallow seismicity (h<30km) (Buforn et al., 2004), which extends eastward from the Gulf of Cadiz along both flanks of the Gibraltar arc and the Alboran sea (fig. 2.1b).

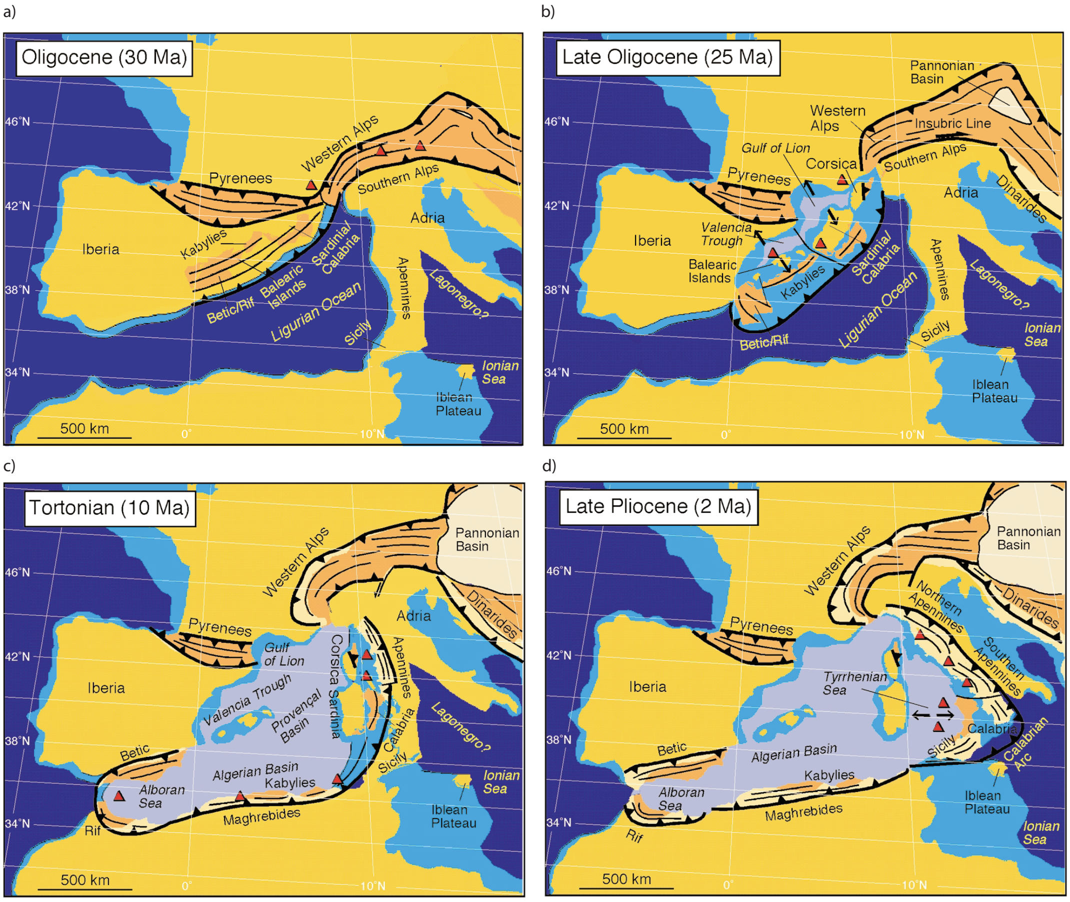

FIGURE 2.2: Reconstruction of the Western Mediterranean tectonics since the Oligocene made by Rosenbaum, Lister, and Duboz, 2002.

2.2 Tectonic evolution of the western Mediterranean

Since Royden, 1993 and Lonergan and White, 1997, the westward subduction migration of the Gibraltar trench as due to a rollback mechanism has been confirmed as the main driver of the tectonic evolution not only to understand the Alboran domain evolution but also the complete western Mediterranean region during the Neogene. In the last years, there exist a large consensus about its spatial-temporal evolution mainly established by tectonic reconstruction (Rosenbaum, Lister, and Duboz, 2002; Faccenna et al., 2004; Vergés and Fernàndez, 2012; Van Hinsbergen, Vissers, and Spakman, 2014) and three-dimensional (3D) slab-evolution modelling (Chertova et al., 2014; Spakman et al., 2018). Since the Oligocene, the geodynamic evolution has been characterized by the slow convergence of Africa towards Eurasia. This was accompanied by extension and formation of back-arc basins due to rapid rollback of subducting oceanic lithosphere (Rehault, Boillot, and Mauffret, 1984; Faccenna et al., 2004; Jolivet et al., 2008).

Subduction rollback began at 32-30 Ma probably controlled by the gravitational instability (Platt et al., 2013) produced during subduction of cold, dense and relatively old (Jurassic, >110 Ma) of the Alpine-Thetys oceanic lithosphere (Fig. 2.2a). The rapid rollback of the subduction hinge was accompanied by a relatively slow convergence between Africa and Europe since 30 Ma, and particularly since 25-20 Ma (Jolivet and Faccenna, 2000; Rosenbaum, Lister, and Duboz, 2002). Back arc extension likely occurs when the velocity of the slab retreat overcomes the absolute motion of the overriding plate (Molnar and Atwater, 1978; Royden, 1993; Lonergan and White, 1997). Therefore, the convergence could not support the rate of subduction rollback, and extension occurred on the overriding plate.

During back-arc extension, marine basins progressively formed from north to south, floored either by thinned continental crust or new oceanic crust (Fig. 2.2b). The earliest basins began to form in Late Oligocene in the Gulf of Lion, the Ligurian Sea and Valencia Trough. In Early Miocene, back-arc extension propagated to Provençal, Algerian and Alboran basins, and in the Upper Miocene, extension in the Tyrrhenian Sea commenced (Fig. 2.2). Rifting led to breakup of continental terranes, which drifted and rotated as long as the subduction zone continued to rollback. Among these terranes, located now hundreds of kilometres away from its original location, are the Internal zones of the Betic-Rif Cordillera, the Kabylies, Corsica, Sardinia, and Calabria (Lonergan and White, 1997) (Fig. 2.2a). All these terranes in its Oligocene position formed a continuous orogenic belt which was part of the overriding continental slab above the northwest dipping subduction zone. The extensional regime to which they were subjected imprinted in them the signature of metamorphic core complexes and exhumation of high-pressure metamorphic rocks (Platt et al., 1983; Azañón, Crespo-Blanco, and Garcia-Dueñas, 1997).

Rollback continued only in areas where the existence of oceanic lithosphere still permitted oceanward retreat of the subducting lithosphere. The subduction zone has therefore progressively retreated from its Oligocene position near the southern margin of Europe to its final configuration in the Calabrian arc, North Africa and the Gibraltar arc (Fig. 2.2d). Slab rupture and tearing under the resulting orogenic wedge at the Algerian margin during the early Miocene probably triggered the development of the two branches of the western Mediterranean; the Calabrian arc that migrated towards the east and the Gibraltar arc that advanced towards the west (e.g., Lonergan and White, 1997; Faccenna et al., 2004; Booth-Rea et al., 2007; Van Hinsbergen, Vissers, and Spakman, 2014). Subduction rollback temporally or permanently ceased when continental crust arrived at the subduction zone, impeding subduction processes. The continental terranes have then been accreted to the continents and considerable crustal shortening occurred.

The formation of the Alboran Sea basin occurred in this context during the westward migration of the subduction hinge. Rapid rollback was compensated by wholesale extension in the overriding Alboran continental crust, which was accurately thinned between 23-10 Ma (Lonergan and White, 1997). Contemporaneously, the orogenic wedge collided laterally with the Maghrebian and South-Iberian paleomargins (e.g., Booth-Rea et al., 2007; Van Hinsbergen, Vissers, and Spakman, 2014), fragments of continental crust were thrust onto the passive margin of Africa and Iberia forming the External Zones. Continental shortening was produced and the westward advance of the Alboran domain was coeval to continued extension in the hinterland during the early to late Miocene (e.g., García-Dueñas, Balanyá, and Martínez-Martínez, 1992; Martínez-Martínez and Azañón, 1997; Martínez-Martínez, Soto, and Balanyá, 2002; Booth-Rea et al., 2003; Platt et al., 2013). This process consumed the Flysch Trough oceanic basin under the central area of the advancing arc, between the two paleomargins (e.g., Gutscher et al., 2012, as well as the current existence of the Jurassic old oceanic crust and its connection with the Alboran slab. Sallarès et al., 2011 suggest that this ancient oceanic crust still can be found at the Gulf of Cádiz under the Gibraltar accretionary wedge.

2.3 Geology

The Gibraltar Arc System comprises the distinct features of a slab roll-back setting. A strongly arcuate and thickened **orogenic belt** integrating the Betics and Rif cordilleras, the Betic–Rif arc. This arc is traditionally divided into External and Internal zones and the Flysch Domain (e.g. Platt et al., 2013 and references therein). The External Zone constitutes the **foreland thrust belt** and consist primarily of folded Mesozoic and Cenozoic sedimentary rocks from the former Iberian and African paleomargins, while the Internal Zone is composed of a stack of pre-Mesozoic and Mesozoic metamorphic rocks. The **Alboran Sea Basin**, is thick in sediments and floored by thinned continental crust in the inner part (Booth-Rea et al., 2007; Do Couto et al., 2016). The Internal Zones, jointly with the Alboran Sea crust, are termed the Alboran Domain, an allochthonous unit which was separated from the eastern Iberian margin and drifted to its current position during Cenozoic subduction rollback (e.g., Rosenbaum, Lister, and Duboz, 2002). The **frontal sedimentary wedge** is represented by the Gulf of Cadiz (Fig. 2.1a).

2.3.1 External Zone or foreland thrust belt

The defining characteristic of the Betic-Rif arc is the external thrust belt. Trends of folds and thrust traces are continuous around the arc. The arc as a whole is distinguished from the Alboran Domain by its thin-skinned character, the lack of significant metamorphism, and the fact that contractional deformation is restricted to the Miocene (e.g., Flinch, Bally, and Wu, 1996). This zone, in Iberia known as the External Betics and in Africa as the External Rif, is interpreted as being the passive continental paleomargins of Iberia and North Africa (e.g., García-Hernández et al., 1980) and is commonly subdivided into different domains according to their regional geographic position, sedimentary facies and paleogeographical characteristics (fig. 2.3).

The higher rank division of the Betic External Zones is into Prebetic and

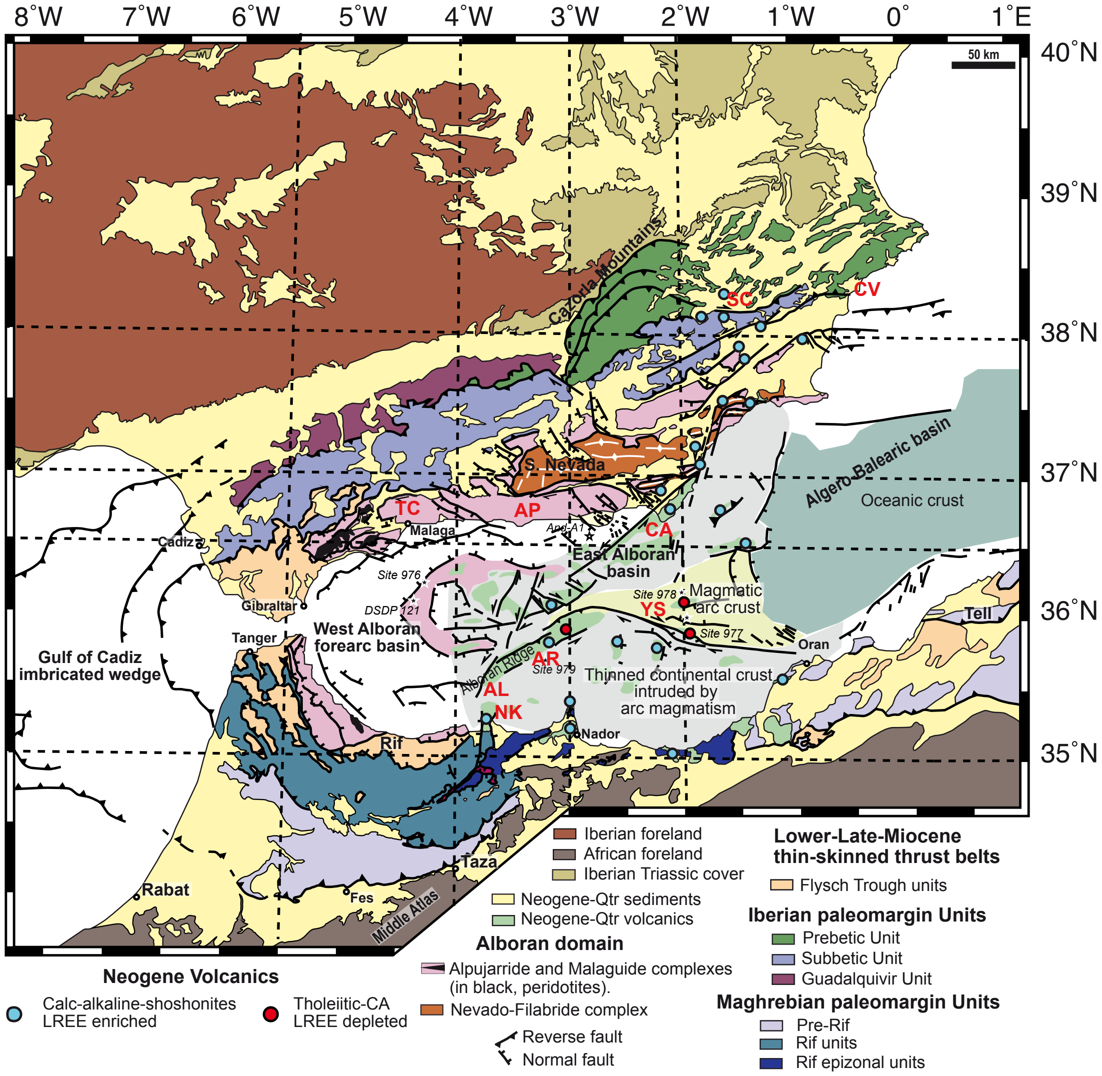

FIGURE 2.3: Geological map of the Gibraltar arc that shows the different tectonic domains and the location of the main faults and volcanism (modified from Booth-Rea et al., 2007). In red capital letters, we mark the faults named in the text (AL: Al-Idrissi fault; AP: Alpujarras fault; AR: Alboran Ridge; CA: Carboneras fault, CV: Crevillente fault; NK: Nekor fault; SC: Socovos fault; TC: Torcal fault; YS: Yusuf fault).

Subbetic. From a stratigraphic and palaeogeographic point of view, the Prebetic, located to the north, mainly contains shallow marine facies, with important continental episodes. In contrast, in the Subbetic the pelagic facies indicate basinal realms (e.g., García-Hernández et al., 1980). Further in the North of the External Zones we find the Iberian massif which forms a major part of the Iberian Peninsula and represents one of the best exposed fragments of the European Variscan orogen.

The External Rif units include Jurassic carbonates and Cretaceous to Tertiary sediments and metasediments deposited at the North Maghrebian passive margin in a deep marine environment on oceanic crust and exhumed mantle domains (e.g., Benzaggagh et al., 2014). The Maghrebian cover is divided into the Prerif, Mesorif and Intrarif from the outer to the inner part of the arc and sedimentary facies indicate a progressive increase of paleobathymetry from the Prerif to the Intrarif.

Between the Gulf of Cadiz and the west Alboran basin in the Gibraltar strait we find the Flysch units, allochthonous sedimentary covers deposited in a deep sea trough. They are turbiditic series that have been tectonically deformed during the Middle-Late Miocene into a thick nappes stack (several kilometres). They are the last remnant of the deformed frontal wedge associated to the oceanic subduction (Booth-Rea et al., 2007).

2.3.2 Internal Zone or Alboran domain

The Alboran Domain is largely made up of rocks that represent paleogeographic realms distinct from those that make up the external thrust belt. It acted as the hinterland during the Neogene creation of the external thrust belt, and its westward motion seems to have been responsible for the formation of the arcuate system. It is composed mainly of Paleozoic and Mesozoic metasedimentary rocks with varying metamorphic grade, and Neogene basin deposits (e.g. Lonergan and White, 1997).

The contact between the Internal and External zones is marked by a series of linked structures with different characteristics, and in places, it has been cut or reactivated by later structures. In the eastern and central Betics, its surface expression is a gently north-dipping backthrust. Parts of this External-Internal boundary zone in the Betics have been cut by strike-slip shear zones, including the dextral Socovos fault, the reverse-sinistral Crevillente fault (Balanyá et al., 2007).

The Internal Zone is constituted by several main tectono-metamorphic complexes that are tectonically stacked. These complexes are distinguished by their stratigraphy, degree of metamorphism, and structural position (Fig. 2.3). In the Betics these complexes have traditionally been grouped in the Nevado-Filabride, Alpujarride and Malaguide complexes, from bottom to top (Balanya and Garcia-Duenas, 1987). In the Rif, showing very similar characteristics (Michard et al., 2002), the Alpujarride and Malaguide complexes are named Sebtide and Ghomaride, respectively (Michard et al., 1983; Chalouan and Michard, 1990).

The structurally highest is the Malaguide-Ghomaride Complex which comprises a series of thrust sheets of largely unmetamorphosed Paleozoic to Paleogene rocks. This complex includes the most complete and tectonically least disturbed stratigraphic sections in the Alboran Domain providing crucial information on the nature and timing of tectonic events (Platt et al., 2013). The

Malaguide/Ghomaride complex overlies the Alpujarride Complex (in the Betics) and the equivalent Sebtide Complex in the Rif, which are made up of Paleozoic and Triassic sediments, strongly deformed and metamorphosed in the Eocene to early Miocene.

The Alpujarride/Sebtide Complex makes up the bulk of the Alboran Domain, including part of the floor of the Alboran Sea (Comas et al., 1999). It is most clearly characterized by its complex metamorphic history, involving early high-pressure–low-temperature (HP-LT) metamorphism associated with subduction and accretion, followed by an evolution to low pressures and locally very high temperatures.

In the central and eastern Betics, the Alpujarride Complex overlies the Nevado-Filabride Complex, comprising Paleozoic and Mesozoic sediments and igneous assemblages with a history of high-pressure metamorphism and deformation that continued into the middle Miocene. The Nevado-Filabride Complex is the structurally deepest and most recently exhumed tectonic complex in the Alboran Domain. it is exposed only in the central and eastern Betic Cordillera, where it forms broad east-west-trending antiformal mountain ranges with Nevado-Filabride rocks in the cores. The Nevado-Filabride Complex shows evidence of a complex metamorphic history involving early HP-LT metamorphism followed by decompression, but PT conditions vary through the sequence.

In addition to these three complexes, a stack of thrust sheets of largely unmetamorphosed Mesozoic carbonate rocks known as the Dorsale Calcaire delineates the margin of the Alboran Domain from the southern Rif around the arc into the western Betics.

2.3.3 Alboran basin

The Alboran basin, occupying the inner side of the Betic–Rif system, is an extensional basin formed as a direct result of the dramatic extension and thinning of the Alboran Domain in the early Miocene (e.g., Platt and Vissers, 1989; Comas et al., 1999; García-Dueñas, Balanyá, and Martínez-Martínez, 1992).

In the west, the basin has up to 8 km of Neogene sediment fill (Torne and Fernhndez, 2000) and is underlain by continental basement that largely corresponds to metamorphic rocks that share a common origin, history and timing with the exposed Alpujarride units in the Betics. (Comas et al., 1999).

The Alboran Sea exhibits moderately high heat flow (Torne and Fernhndez, 2000). Much of the central and eastern Alboran Sea is underlain by Neogene volcanics lying on an unknown basement, and parts of it may be entirely volcanic in origin (Booth-Rea et al., 2007). Further east, the Alboran Sea passes into the Neogene oceanic crust of the Balearic Basin. The bulk of the volcanics, which range in age from 8 to 17 Ma, are generally regarded as being subduction related (Duggen et al., 2004), but the predominantly intermediate to silicic character of the volcanics onshore suggests assimilation of the continental crust (Turner et al., 1999). A transition to more alkaline magmatism in the onshore Betics and Rif occurred at around 10 Mya.

2.3.4 Gulf of Cadiz

The Gulf of Cadiz lies offshore south-west of Iberia at the eastern end of the Azores–Gibraltar fracture zone. It forms a thick imbricate wedge (>11 km in its internal and eastern part) and a tongue-shape tectonic unit that occupies a large area of the Atlantic margin in both NW Africa and SW Iberia (e.g., Gutscher, 2002; Iribarren et al., 2007a).

The possible presence of an oceanic basin of Jurassic age in this area is a largely debated question that has profound implications in the geodynamic evolution of the Western Mediterranean, and specifically the Gibraltar arc system (e.g., Lonergan and White, 1997; Faccenna et al., 2014; Gutscher, 2004). Gutscher, 2002 defined the Gibraltar accretionary wedge as active above a narrow east-dipping subducting oceanic slab but the nature of the crust in the deep oceanic domains offshore SW Iberia is still under debate. The seafloor is covered by a thick layer of Mesozoic to recent sediments, thus basement samples are difficult to obtain.

Because of the lack of basement samples, current knowledge of the crustal domains in the Gulf of Cadiz is based almost exclusively on geophysical data. Available multi-channel seismic data (e.g., Docherty and Banda, 1995; Sartori et al., 1994), as well as refraction and wide-angle reflection data (e.g., Gutscher, 2002) and models based on potential field data (e.g.; Fullea et al., 2010; Gràcia et al., 2003), globally highlight the eastward increase in sediment thickness, depth to basement, and depth to Moho (Iribarren et al., 2007b), but do not provide information on the crustal nature across the different tectonic boundaries.

2.3.5 Intramountain basins

Apart of the Alboran basin, there are many intramountain sedimentary basins within the Betic-Rif-Alboran system formed during Miocene coeval with the formation of the external thrust belt. The large Guadalquivir and Rharb flexural foreland basins resulted from the emplacement of the external thrust wedge and the periphery of the Alboran Domain onto the Iberian and African continental margins (Galdeano and Vera, 1992; Garcia-Castellanos, 2002).

Numerous basins in the eastern and central Betics formed in the middle to late Miocene as a response to the extensional exhumation of the Nevado Filabride Complex. The present day topography configures a basin-and-range morphology dominated by an alternation of basins and main east to west ranges of the Betic Cordillera. These basins formed in response to southwest-directed extension, with conjugate sets of northwest-trending normal faults (Meijninger and Vissers, 2006; Morales et al., 1990. They also show a distinctive pattern of broad normal-fault-bounded basins linked by narrow corridors defined by dextral transtensional faults. The Granada Basin is the deepest and largest of these basins (Martínez-Martínez et al., 2006).

2.4 Seismicity and active tectonics

The seismicity in the region (Fig. 2.4a) do not delineate a linear Eurasian-African plate boundary clearly occurring from shallow to intermediate depth in a diffuse band which mainly extends to both sides of the Strait of Gibraltar (Buforn et al., 2004). The geographical distribution of earthquakes, their focal mechanism and source depths show complex patterns across the region. The main concentration of seismicity occurs along a wide zone from the Gorringe Bank in the Atlantic Ocean into southern Spain and to the Tell Atlas in North Algeria, as well as along an orthogonal fault zone from Southeastern Iberia to North Morocco crossing the Alboran Sea (The Trans-Alboran shear zone-TASZ) (Buforn, Sanz de Galdeano, and Udías, 1995; Stich, C.J., and J., 2003, Stich et al., 2006, Stich, Martín, and Morales, 2010).

Most earthquakes over the region show small magnitude at shallow (crustal) source depths (0–40 km). Larger shallow earthquakes indicate ongoing activity on a set of sinistrally transpressive faults in the eastern Betics ((Lorca earthquake) Vissers and Meijninger, 2011) and on dextral and reverse faults along the north African margin (Morel and Meghraoui, 1996). However, sub-crustal earthquakes are documented in two different zones; (1) at the Southwest Iberian Atlantic margin (eastern end of the Azores Fracture Zone) (Stich, Mancilla, and Morales, 2005), being this a source of powerful earthquakes such as the 1969 Ms 7.9 earthquake on the Horseshoe fault (Fukao, 1973), and tsunamigenic 1755 Lisbon earthquake and tsunami (e.g., Bartolome et al., 2012; Stich et al., 2007) and (2) along a narrow, north-south elongated zone beneath the Alboran Sea at around 4.5° W (Calvert and Alguacil, 2000; Buforn et al., 2004). Seismic activity stops at 150 km depth and reappears with a small number of earthquakes in a small area south of Granada at about 630-660 km depth (Buforn et al., 2011).

The faulting style over the Iberian-Maghreb region ranges from pure reverse to pure normal focal mechanisms (e.g., Stich, C.J., and J., 2003), showing a pronounced geographical variability as well as local heterogeneity of faulting in several areas (e.g., Stich, Martín, and Morales, 2010). Recent moment tensor solutions (Martín et al., 2015) of earthquakes at lower crustal or subcrustal depths in Betic-Rif-Alboran region suggest heterogeneous faulting styles from normal to reverse mechanisms, including opposite kinematics in some cases. This heterogeneity appears to indicate the superposition of different geodynamic processes, in particular extensional processes coeval to oblique plate convergence compression (Martín et al., 2015). Extension may be driven by delamination as inferred from recent studies of PRFs (Mancilla et al., 2013, Mancilla et al., 2015b).

At present, the patterns of active deformation determined from GPS measurements, seismicity and morphotectonics show a strong dichotomy between the East and the West of the Betics and Rif. The east of the Betics and Rif are mostly deformed in response to NNW-SSE convergence between Africa and Iberia, whilst the western areas of the Betics and Rif show westwards to south-westward displacements respect to fixed Iberia and active extension (Stich, C.J., and J., 2003, Stich et al., 2006; Koulali et al., 2011; Mancilla et al., 2013; Echeverria et al., 2013). Morphotectonic studies in the regions with westward and south-westward displacement prove the existence of active extensional faulting in the central Betics and active normal-sinistral faulting along the Nekor fault and its continuation offshore along the Al-Idrissi fault (Azañón et al., 2004; Pérez-Peña et al., 2010; Martínez-García et al., 2013; Poujol et al., 2014).

2.5 Current models and present-day lithospheric structure

Although the geology and shallow structure of the region have been intensively studied (see recent reviews by Gutscher et al., 2012; Platt et al., 2013) the debate over the kinematics and dynamics of its formation is still intense. There are still many uncertainties regarding what caused the westward motion of the Alboran domain and its overthrust above the Iberia and northwestern Africa paleomargins and the onset of the Alboran extension.

The P-wave velocity anomaly in the upper mantle, interpreted as a body of cold and dense lithosphere, that early tomography studies revealed in the area, initially triggered several different scenarios to explain the evolution of the western Mediterranean (see Platt et al., 2013 for a review). Two main different geodynamic models can be summarized according to the driving forces processes involved to explain the evolution of the Gibraltar arc:

1. **Mantle lithospheric instability**: The tectonic evolution of the region was caused by removal of gravitationally unstable lithosphere form beneath the Alboran basin and Gibraltar arc by either convective processes or delamination not being subduction essential in this type of models (Seber et al., 1996; Houseman and Molnar, 1997; Calvert and Alguacil, 2000; Duggen et al., 2005; Platt et al., 2013).

   The dense lithospheric body is therefore interpreted to be a body of delaminated over-thickened orogenic continental lithosphere. The P-T-t paths observations are explained by the cause of a rapid uplift and subsequent exhumation of overlying crustal rocks (Platt and Vissers, 1989; Vissers, Platt, and Wal, 1995. Acutely thin crust and lithosphere and high-heat flow in the Alboran Sea in addition to the negative P-wave velocity anomaly in the upper-mantle, indicative of a hot asthenosphere at shallow upper mantle depths, were also interpreted as supporting this geodynamic evolution (Calvert and Alguacil, 2000; Torne and Fernhndez, 2000).

An appropriate way to discern between delamination or convective removal might require to determine the symmetric/asymmetric character of the extension that occurred in the Alboran basin. Delamination is an asymmetric process that makes the extension caused in the overlying crust migrate in one direction. In contrast, convective removal is supported by the simultaneous and symmetric extension throughout the region (Platt and Vissers, 1989; Houseman and Molnar, 1997; Platt and Houseman, 2003). The geodynamical models implying asthenospheric upwelling seem hardly compatible with recent SKS splitting measurements, because the Fast Polarization Direction exhibits along the Gibraltar arc a tangential (Buontempo et al., 2008; Diaz et al., 2010) arc parallel distribution instead of an approximately expected radial pattern (Walker et al., 2005).

2. **Subduction and slab rollback with or without slab break off**: Among the models proposed to explain the kinematic evolution of the westernmost Mediterranean, the one receiving a wider consensus is the already detailed in section 2.2, envisaged by Rosenbaum, Lister, and Duboz, 2002 and also supported by many other authors (e.g., Blanco and Spakman, 1993; Lonergan and White, 1997; Zeck, 1996; Gutscher, 2002; Spakman, Wortel, and Wortel, 2004; Duggen et al., 2004; Booth-Rea et al., 2007, Bezada et al., 2013; Chertova et al., 2014; Van Hinsbergen, Vissers, and Spakman, 2014; Palomeras et al., 2014; Do Couto et al., 2016; Spakman et al., 2018). This group of models involves east-dipping subduction of a narrow corridor of Alpine Tethyan oceanic lithosphere whose deeper prolongation is given by the Alboran slab. SKS splitting (Diaz et al., 2010) and dispersion of body waves measurements (Bokelmann et al., 2011) support the subduction rollback model.

One important question that bears on these evolutionary models of the Gibraltar Arc orogeny is whether or not the slab currently forms part of an active subduction zone. Body wave tomography does not have resolution at depths shallower than 150–200 km therefore it cannot resolve whether the slab is attached or not (Calvert and Alguacil, 2000). Slab detachment was used to explain the uplift of the Betic lithosphere as well as magmatism and anatexis within the Betic Mountains (Blanco and Spakman, 1993; Duggen et al., 2005). However, The evidence for complete slab break-off appears weak, recent tomographic images extend the high velocity anomaly almost continuously from the transition zone up to very shallow depths (50 km) (Bezada et al., 2013, Palomeras et al., 2014).

The presence of an accretionary wedge west of Gibraltar imaged by multichannel seismic profiles has led to Gutscher, 2002 to suggest that the east-dipping subduction zone is still active (with a slow convergence speed ($\leq$1 cm/yr)). Despite the absence of a Wadati-Benioff style subduction geometry, they argued that the fault plane could be locked. This suggestion is attractive because it provides a possible explanation for the powerful earthquake and tsunami thought to have been somewhere in the area of the Gulf of Cadiz in 1755 and known as the Great Lisbon earthquake (e.g., Gutscher, 2004). However, the existence of an oceanic corridor under the Gibraltar strait does not favor by itself the argument of the active subduction proposed by Gutscher et al., 2012. Furthermore, active oceanic subduction is contradicted as a working hypothesis by a number of observations; GPS observations do not support a significant differential movement of the presumed overriding arc (Stich et al., 2006), the intermediate-depth earthquakes are located within a region that shows low velocity and density in comparison with surrounding mantle and the proposed accretionary wedge appears to be presently inactive, as it is covered by post-Miocene sediment and cut by younger dextral faults.

Recent geophysical models based on seismic data, tomography and potential fields show a strong asymmetry in the crustal and lithospheric mantle structures along the Gibraltar arc region. Tomography models (e.g., Bijwaard and Spakman, 2000; Spakman, Wortel, and Wortel, 2004; Garcia-Castellanos and Villaseñor, 2011) and SKS anisotropy analysis (Diaz et al., 2010) image an arcuate mantle slab located below the Betic–Rif orogen, with an east dipping direction in the Gibraltar Strait and turning to the SE and S beneath the Betics. The slab ends abruptly beneath the eastern Betics and detaches vertically along a tear zone beneath the central-eastern Betics. Furthermore, strong asymmetry in the crustal structure of the south-Iberia and north-Morocco margins is shown by integrated modeling of the crustal and lithospheric structures (e.g., Torne and Fernhndez, 2000; Fullea et al., 2007). The southeastern Iberian margin, at the eastern Betics, is characterized by a sharp crustal thinning toward the Alboran basin whereas the northern Moroccan margin presents a much smoother thinning. Recent seismic analyses based on the RF method also show a sharp decrease of the crustal thickness from the central Rif with values of 35–44 km to 22–30 km near the Morocco–Algeria border (e.g., Mancilla et al., 2012; Thurner et al., 2014; Mancilla et al., 2015b).

The most recent proposed models then support combined geodynamic mechanisms to explain the tectonic of the region. Subduction rollback under the Alboran and Algerian basins, together with continental slab tearing or detachment producing edge delamination under the Betics and Rif.

Duggen et al., 2005, Gutscher et al., 2012,Mancilla et al., 2013, Thurner et al., 2014 and Palomeras et al., 2014 suggest that slab rollback has initiated delamination of the continental mantle lithosphere beneath the Gibraltar Arc. According to them the descending slab is still attached to the crust beneath the Rif and the central Betics beneath the Granada basin and removing the lithospheric mantle of the continental margins beneath both Iberia and Morocco. This lithospheric removal appears to control the development of topography along both continental margins, as seen in the recent rapid uplift of the Sierra

Nevada as well as the active extension in the Granada Basin.

Using PRF methods with high-dense seismic arrays Mancilla et al., 2015b support this kind of models with the main difference that no crustal detached window exists in the western Betics (fig. 2.5). The most important feature that support this scenario is the drastic gradient of crustal thickness observed in the Betics and Rif from west to east (fig. 2.4b)). By mapping the geometry of the Iberian and Maghrebian Moho and the edge of the Iberian slab beneath the Betics, they define the locus of tearing or slab detachment and the region to the south of the ruptured slab where edge delamination has occurred (stars in Fig. 2.4). The over-thickened crust beneath the external thrust belt probably represents an area where the Iberian and Maghrebian underthrust the Alboran domain. The Iberian and Maghrebian slabs are still attached to the oceanic slab imaged under the Alboran basin at the western Betics (further to the west of Malaga (MA) and the Nekor fault in fig. 2.5). The Iberian Moho at this region shows a strong inflection, deepening fast towards the east along a N-S hinge that coincides with the region of important intra-slab intermediate depth seismicity (Morales et al., 1997)(fig. 2.4a). Great parts of the Betics and the easternmost Rif lack an orogenic root and probably represents regions where delamination has already occurred. To the NE of the Betics no slab is attached to the Iberian crust, indicating that tearing and delamination of the Iberian slab took place to the east southeast of this Cazorla mountain. A stronger lithospheric thickness gradient appears from west to the east at the Nekor sinistral strike-slip fault where slab tearing still occurs.

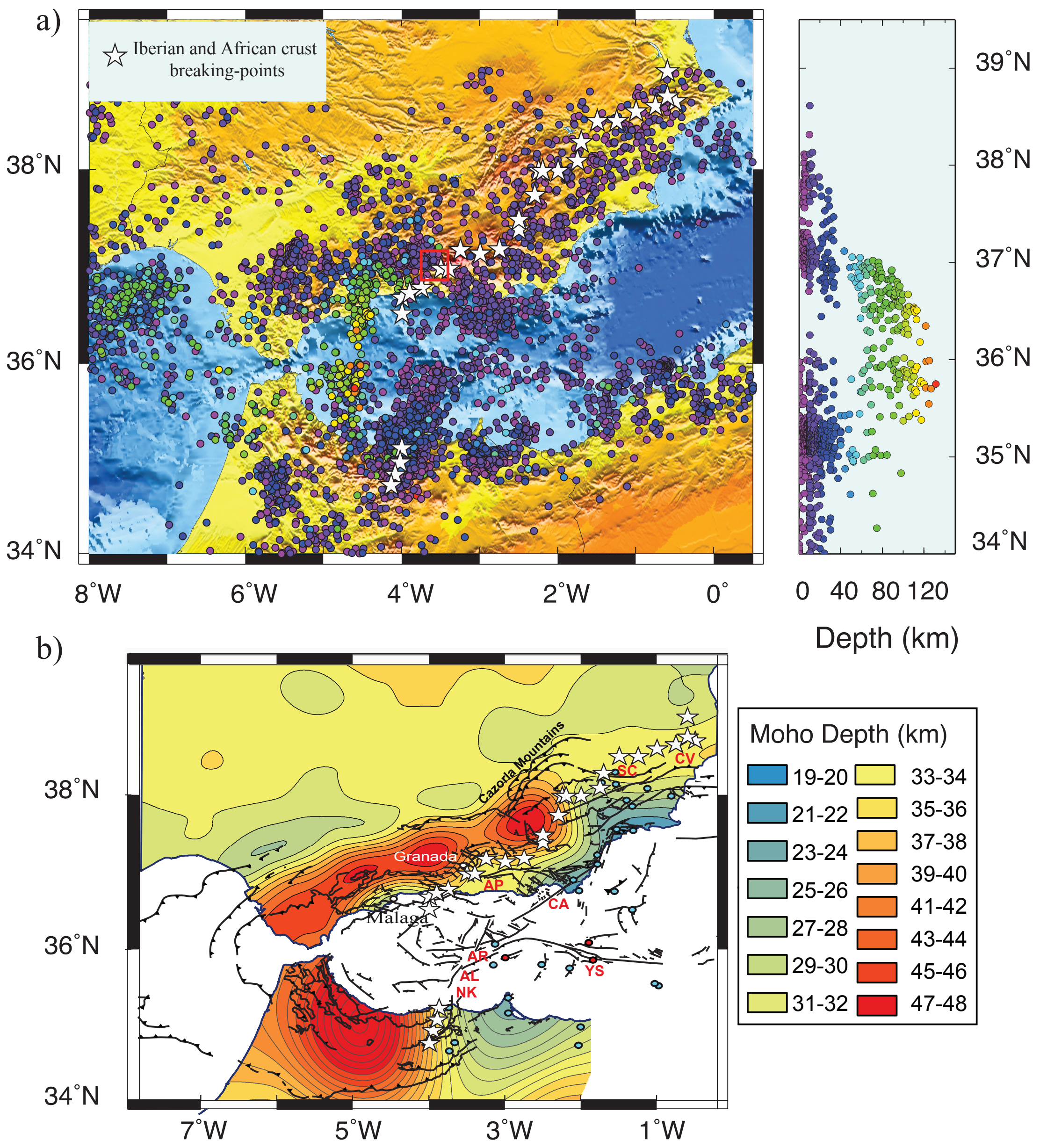

FIGURE 2.4: Seismicity and crustal thickness. a) Right panel: Topographic map. The coloured circles are the locations of the shallow and intermediate seismicity and the red square marks the location of the deep seismicity; Left panel: Projection on a NS profile of the earthquakes situated between 4°W and 5 °W; b) Crustal thickness map from Mancilla et al., 2015b. Stars in both figures indicate the locations where the Iberian and Maghrebian subducted crust ends beneath the Betics and Rif. The faults and volcanism from Fig. 2.3 are included.

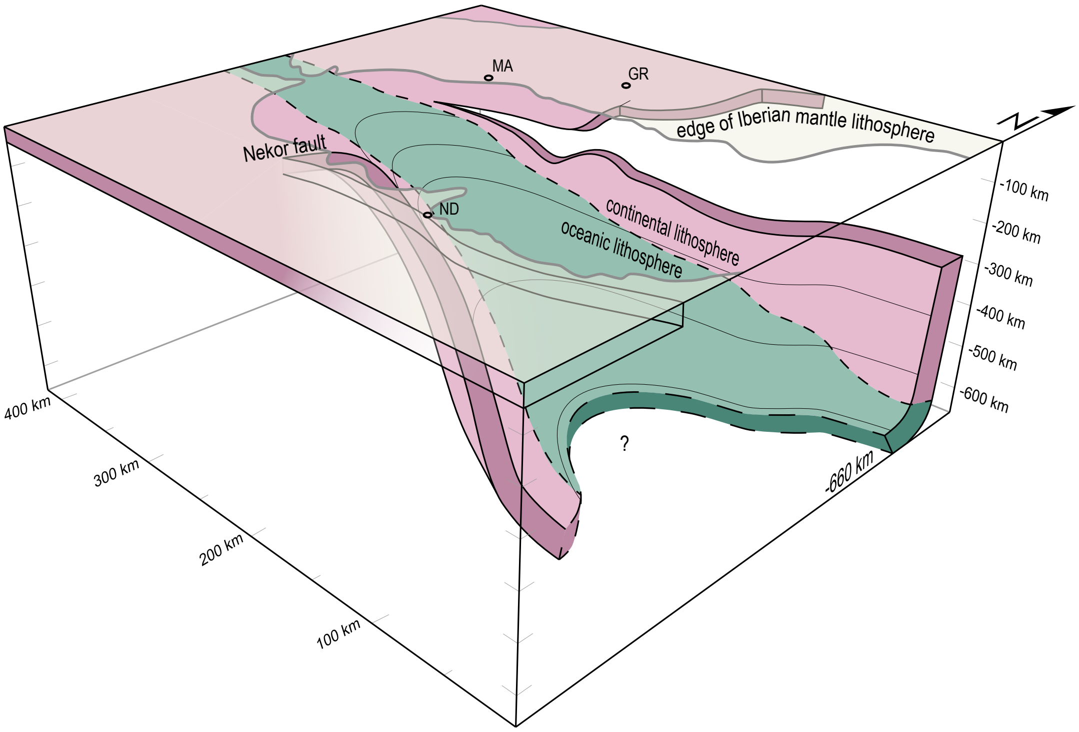

FIGURE 2.5: Sketch of the proposed geometry of the underthrusted Iberian and Maghrebian lithospheres extracted from Mancilla et al., 2015b, stripped from their overlying crust, and their relation with the subducted oceanic slab observed by tomographic studies (Spakman, Wortel, and Wortel, 2004; Garcia-Castellanos and Villaseñor, 2011; Bezada et al., 2013. [MA: Malaga; GR: Granada; ND: Nador]. The boundary between continental and oceanic mantle lithosphere in the foundered slab is drawn tentatively taking into consideration surface geological data above the slab like the geochemistry of the volcanic rocks, the area where continental HP rocks crop out, the position of the oceanic-continental boundary further west in the Gulf of Cádiz. The thickened continental crust found in the Betics and Rif and the Betics-Rif Moho have not been represented in this figure and would occur above the represented image.

Chapter 3

Data and Method

In this chapter, we depict the data (section 3.1) sets used in the different analysis done and the methodology (section 3.2) applied to them.

3.1 Data

Thanks to a concerted effort by various national and international programs, in the past decade several important research initiatives have succeeded in collecting a large amount of high quality geophysical data in the Iberia-Maghreb region. The IberArray seismic network was part of the large scale "TopoIberia" research project, funded by the Spanish Ministry of Science and Education under the "CONSOLIDER-INGENIO 2010" programme of excellence.

The pioneer tomographic images that displayed the upper-mantle structure in the western Mediterranean (e.g.; Blanco and Spakman, 1993; Piromallo and Morelli, 2003) were made mainly with the disperse permanent seismic stations located in Spain, Morocco and north Algeria. But the interesting observed features leaded to general idea between seismologists that it was necessary to improve the spatial resolution of the seismic studies in the area. To better resolve the complex structures in the region, several affiliated projects were started between 2007 and 2014, including researchers from a variety of institutions in the Spain, U.S., Morocco, Ireland, and Germany. These extensive deployments of temporary land seismic arrays, both on the Iberian Peninsula and North Africa, comprise the Spanish IberArray broadband seismic array

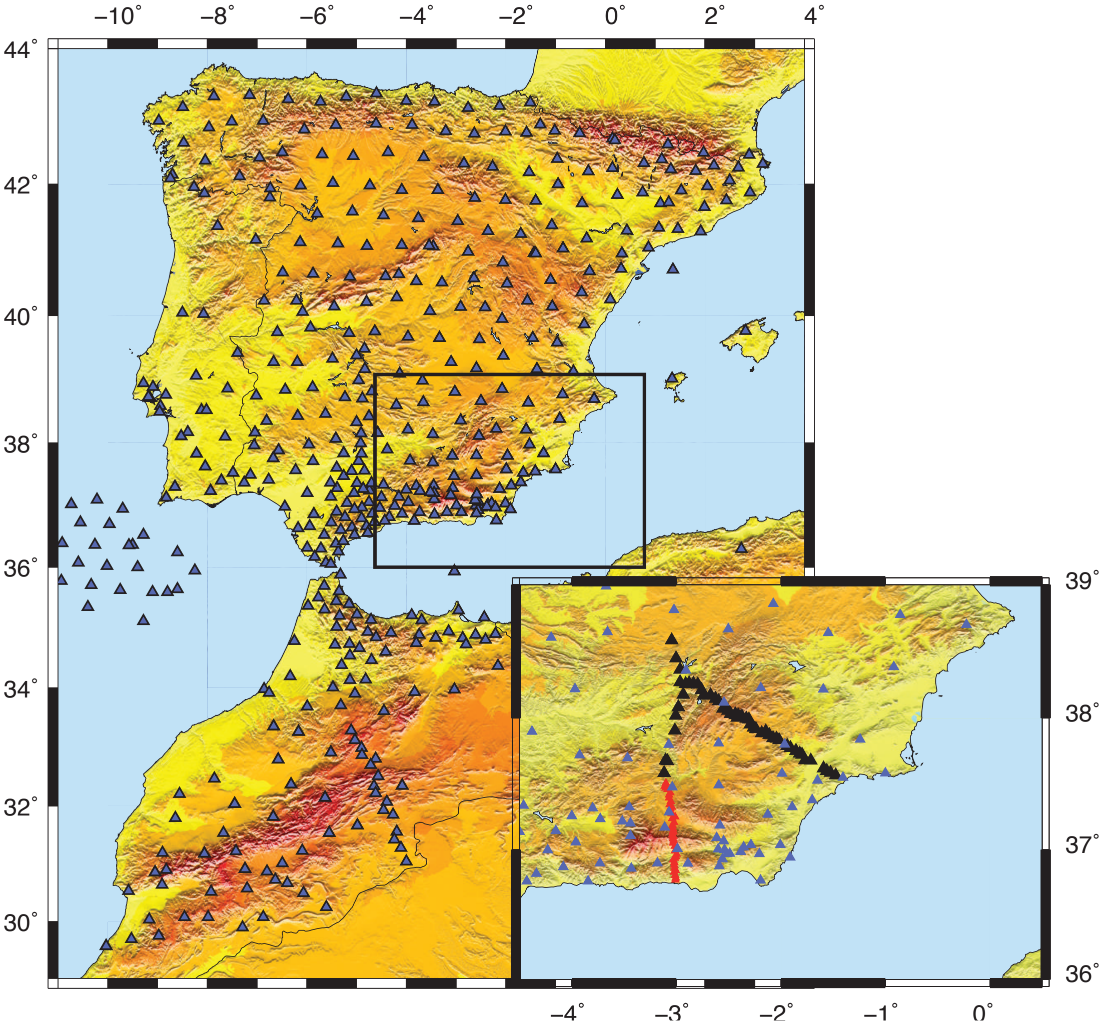

FIGURE 3.1: Permanent and temporary seismic stations deployed in the Ibero-Maghreb region during the last decade. Zoom-in the Central and Eastern Betics region where the high-resolution seismic experiment has been performed.

(Díaz and Gallart, 2009, Iberarray), and the PICASSO (Program to Investigate Convective Alboran Sea System Overturn) project. Small scale temporary deployment (INDALO, NEAREST, Hire and Transcorbe) in southern Spain contributed to generate, in addition to permanent recording networks operated by various institutions (IGN, IAG-UGR, ROA), the largest seismic network ever deploy in the region with more than 500 broadband stations (Fig. 3.1).

One of main goals of these seismic networks was to image the crustal and upper-mantle structures under the region serving to shed some light about their geodynamic evolution and present framework. Recent crustal studies using mostly RF methods (Mancilla et al., 2013; Thurner et al., 2014; Mancilla et al., 2015b; Mancilla et al., 2015a) tried to explain the controversial relationship between the dynamics of the Alboran slab and the surface tectonics. These works have permitted roughly to delineate the boundary between different domains reporting strong lateral variations of the Moho discontinuity in Southern Spain. A slab-like feature of Iberian lithosphere nature has been proposed at the western Betics while the same Iberian slab exhibits tearing in the central and eastern Betics regions.

To confirm this hypothesis we need to know in detail the lithospheric structure of the region. With this intention were performed two large scale seismic passive field experiment (Heit, B., Yuan, X., Mancilla, 2010 and transcorbe network) crossing the central and eastern Betics in Southeast Spain: The Hire (High Resolution) and Transcorbe (Seismic Transect along the Betic Cordillera) experiments. The array geometries of both experiments were designed mainly for RF processing/interpretation and intended to probe with unprecedented detail the contact between the two main geologic domains of Southern Iberian involved in the Nubia-Eurasia collision: the Betics orogeny and the Iberian Massif as well as their lithosphere architecture.

In this thesis we use first, the virtual seismic network called as Gibraltar

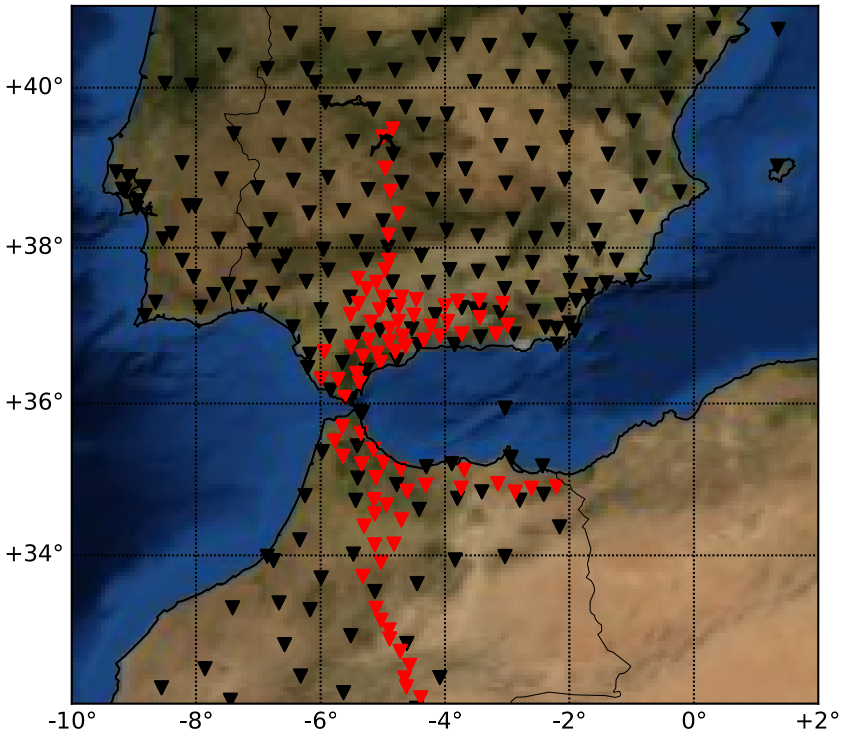

FIGURE 3.2: Location of seismic stations configuring the Gibraltar arc virtual seismic network used in the LAB study.

seismic network to image the LAB discontinuity all along the region (Fig. 3.2) and second, two high-density seismic arrays to study the crustal structure in the central and eastern Betics (Fig. 3.3b).

3.1.1 Gibraltar arc virtual seismic network

We defined the Gibraltar arc virtual seismic network as the set of broad band seismic stations deployed in the Iberian peninsula and northwestern of Africa between latitude 32^{o}N to 41^{o}N and between longitude 10^{o}W to 1^{o}E (black and red triangles in fig. 3.2). The total number of stations used are 300. These stations belong to permanent and temporal networks with different recording times from one year to 5 years.

The TopoIberia project provided the main skeleton of these virtual network (the Iberarray seismic network Iberarray); a dense array with average inter-station distant of 60 km. The temporal seismic stations were equipped with Nanometrics Taurus 24-bits dataloggers and Trillium 120s seismometers. The temporal part of the Iberarray network, composed of 80 stations, covered Iberia and North Morocco in three successive footprints, each lasting for about 24 months. The deployments started in the south in 2007 and ended in the north in 2013. Some of the nodes in the network were covered by permanent stations of the national broadband network (Instituto Geográfico Nacional, IGN) and other permanent networks operating in the region: Instituto Andaluz de geofísica (IAG-UGR), Western Mediterranean network(WM(ROA-UCM)), and Portuguese National Seismic Network (PM). In the analysis we used the two first legs of the TopoIberia experiment with recording times from 2007 to 2010. The raw data from these stations is available through the European Integrated Data Archive (EIDA).

In addition to the stations provided by the TopoIberia consortium two temporal networks were used in the analysis: PICASSO (Picasso network) and INDALO (IAG-UGR). From 2010 to 2013, the temporal experiment PICASSO (Picasso Project) deployed 85 broadband seismic stations in southern Spain and northern Morocco distributed along the Gibraltar arc in a roughly north-south line from the Iberian Massif in central Spain, across the Betics, the Gibraltar Strait, the Rif Mountains, the Middle Atlas, and the High Atlas and ending on the Sahara Platform (red triangles in Fig. 3.2). The broadband seismic instrumentation consisted of Streckeisen STS-2, GURALP CMG3T and CM3ESP sensors using Q330 dataloggers (Pascal instrument center, IRIS). Part of the PICASSO stations were deployed in around the Alboran Sea in the Betic and Rif Mountains to increase the density of the more regionally distributed IberArray network (see Fig. 3.2). Other projects complemented the Picasso network deployment in Morocco: the Morocco-Münster project (MM network) with 15 broadband seismic stations located in the Western High Atlas and operated by the University of Münster; and the CoMITAC project (Morocco-Bristol Nekwork (MB)) operated by Bristol university. These two temporal networks

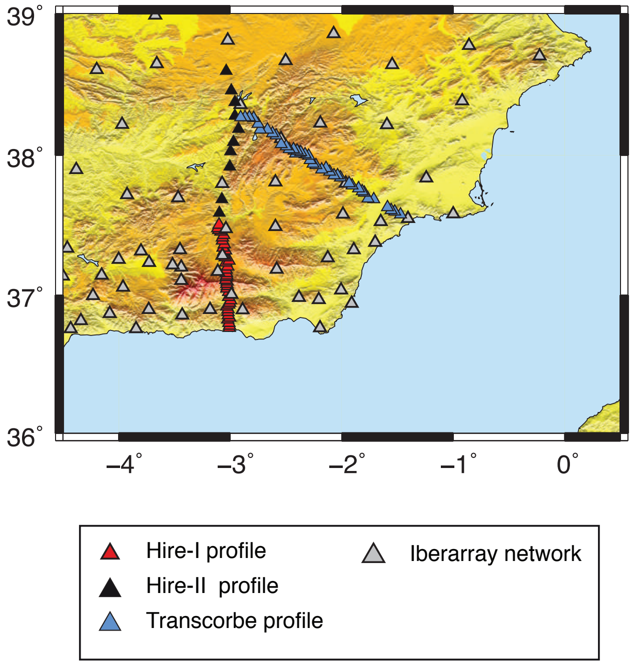

FIGURE 3.3: Location of the stations of the high-density experiments used in the Central and Eastern Betics studies (see fig. 3.1 for relative position respect to the Iberian Peninsula). Red, black and blue triangles mark the Hire-I, Hire-II and Transcorbe stations, respectively. Grey triangles denote the permanent and temporary stations in the area.

recorded during two years since the end of 2010 until 2013. The raw data from Picasso , MM and MB networks are available through the Incorporated Research Institutions for Seismology data center (IRIS).

3.1.2 High-resolution passive seismic profiles: Hire and Transcorbe experiments

The high resolution seismic networks consisted of 2 densely spaced broadband seismic arrays (Hire array: HR-I and HR-II, and Transcorbe array: TR) whose 87 of their stations were borrowed from the GFZ-Potsdam Seismic pool (GFZ-Pool). The arrays are formed by broadband seismic sensors (GURALP CMG 3ESPC with periods of 60 s and 120 s) and short period instruments (MARK L4C). The installation and maintenance of the stations have been made by a

FIGURE 3.4: Sequence of photos depicting the installation process of a seismic station.

joint effort of GFZ Potsdam (GFZ) and the Instituto Andaluz de Geofísica, University of Granada (IAG-UGR). The data of this two network are stored in the GFZ-Postdam institute through the GEOFON data center (GEOFON)

The Hire seismic profile, with a total length of ∼230 km, is composed by 50 seismic stations. This profile was deployed in two legs operating in different periods of time: the first leg (Hire-I) consists of 40 stations spaced ∼2 km apart (red triangles in Fig. 3.3, HIRE project, Heit, B., Yuan, X., Mancilla, 2010) and the second one, Hire-II consists in 10 stations with an average inter-station distance of ∼10 km. The first leg, Hire-I, recorded for 14 months from 09/2010 until 11/2011. The second leg, Hire-II, recorded for 22 months since July 2013 and includes 10 seismic stations. Some permanent stations located nearby the profile and operating by the IAG, as EBER and GORA stations, were used to complement the profile.

The Hire array probes the crustal structure of different geological units; from the metamorphic rocks of the Alboran domain in the south, through the External Zones with sedimentary rocks to the Variscan terrains of the Iberian Massif in the North. The Hire I crosses transversely the Sierra Nevada mountain range and was designed to save the topographic obstacle for low altitudes

(2000 m). Hire II turns slightly in a NE direction in order to follow the Cazorla mountain range and avoid the proximity of the Guadalquivir sedimentary basin.

The Transcorbe array was formed by 40 receivers with an average interstation distance of ∼3.5 km. It operated since July 2013 during 22 months. We used one permanent station, SESP, and two temporal, VALD and MAZA (belonging to the INDALO network) to complement the profile. This array defines a 170 km long transect following a NNW-SSE direction across the Eastern Betic Cordillera, from Mazarron village, in the South extreme, through the arched Cazorla Mountains, and ending in the Iberian Massif (blue triangles in Fig. 3.3).

Compared to earlier seismic deployments made in the region with a station spacing ∼50 km, these seismic profiles constitutes a considerable increase in the instrumental spatial resolution.

3.2 Receiver Function Method

We use receiver function (RF) methods to investigate the crustal and upper mantle seismic structure in the Gibraltar Arc (see Kind, Yuan, and Kumar, 2012 for a revision of the technique). Strong teleseismic phases (P, S, PP or SKS) convert to other modes when impinging from below on a seismic discontinuity. After encountering the seismic interface the transmitted and converted waves travel with different wave velocities up to the receiver. The RF method employees these converted phases recorded on the three-component seismograms to get information on the seismic discontinuities.

Depending on the incoming seismic energy, P or S wave types, the conversions that take place will be P-to-S (P-RFs) or S-to-P (S-RFs), respectively (Fig. 3.5). Though the SKS phase is also sometimes used in RF studies we do not employ it in this thesis. The epicentral distance range for P- and S-RFs is 30^o-95^o and 55^o-85^o, respectively. The lowest value is constrained by the far-field assumption of plane waves and the guarantee that the conversion at the discontinuity has occurred (i.e., vertical incidence angles are too large that no converted Ps and Sp phases will be produced). The limitation for large distances avoids the waveform contamination from conversions generated at the core mantle boundary. P-RFs and S-RFs are used differently to map the Moho and LAB discontinuities, respectively

Compared to other seismic methods, the RF technique brings some advantages, especially to image the crust. Teleseismic body waves are nearly ubiquitous, in contrast to body waves from local seismicity. The depth penetration of the short period ambient noise seismic waves are limited and lose horizontal resolution at longer wavelengths, teleseismic body waves suffer less of a depth versus lateral resolution trade-off. Because of the steep incidence angles of the teleseismic body waves, converted waves provide good illumination of subhorizontal to steeply dipping interfaces.

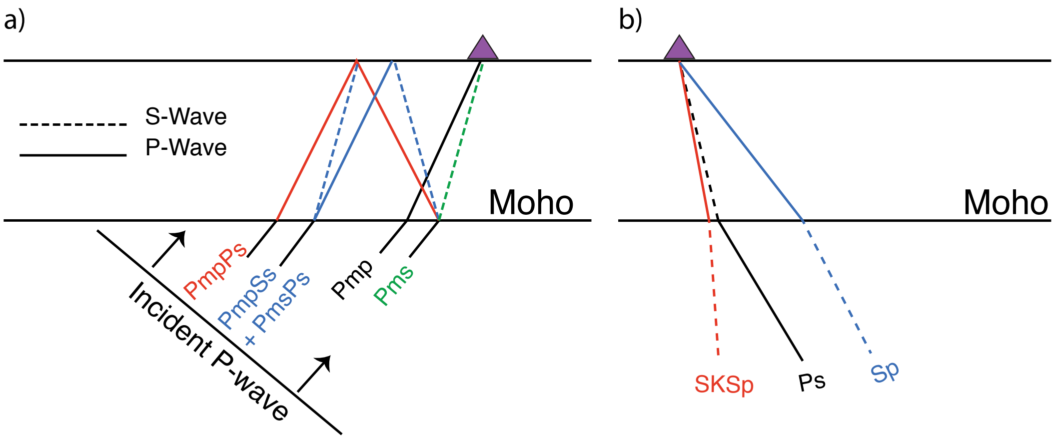

FIGURE 3.5: Sketch of the ray paths for a) P- and b) S- receiver functions.

Early RFs investigations were focused mainly on crustal structures and mostly performed analysis using individual permanent stations (Vinnik, 1977, Langston, 1979). Assuming conditions of low lateral heterogeneity, first inversion methods inverted for a single-station stacked RFs from different backazimuth to obtain a velocity model (Ammon and Zandt, 1993). As other fields in geophysics, RFs have been inverted jointly with other independent and complementary measurements to bridge resolution gaps associated to each data type. The joint inversion of RFs and surface wave dispersion curves started to be applied two decades ago (e.g., Last et al., 1997, Özalaybey et al., 1997), being linearized joint inversions particularly popular (e.g., Du and Foulger, 1999, Julià et al., 2000, Julià, Ammon, and Herrmann, 2003, Pasyanos et al., 2007). The H-k stacking technique also use RFs obtained by a single station, transforming the time-domain RFs into the depth-V_p/V_s domain using a grid search method (Zhu and Kanamori, 2000).

In the last decades, the research has been successfully directed towards studying the lateral variability of major velocity boundaries in the crust and upper mantle by dense array RFs datasets (e.g., Dueker and Sheehan, 1997, Kosarev, 1999), Revenaugh, 1995, Yuan et al., 1997, Gilbert et al., 2003, Frassetto et al., 2010). Due to uneven distribution of stations and events in earthquake seismology simplified migration approaches are often used which employs back projection of converted phases along the incoming ray path in a 1-D model. This scheme, known as Common Conversion Point (CCP) stacking, sum the amplitude of RFs from several station-event pairs sampling the same subvolume and generating a 2-D cross-section (Dueker and Sheehan, 1997, Yuan et al., 1997, Gilbert et al., 2003). CCP stacking relies on the assumption of a 1-D Earth where discontinuities are horizontal. If significant lateral heterogeneities are present, structures cannot be correctly imaged by the CCP stacking of RFs due to the diffraction or scattering effects produced by dipping and laterally discontinuity interfaces. More complex migration techniques rely on fewer assumptions about the Earth's structures and can provide finer resolution images with less artifacts, as the Reverse Time Migration approach recently implemented for RFs high-resolution seismographs.

A receiver function is a time series obtained from the original seismic traces through two main processing steps; rotation and deconvolution. In this chapter we will present in detail the RF method, starting with the physics of the problem (3.2.1). Techniques for generating Ps and Sp RFs (e.g., Vinnik, 1977; Langston, 1979; Ammon, 1991; Bostock, 1998; Farra and Vinnik, 2000) have become relatively standard (e.g., Oreshin et al., 2002; (Vinnik, Farra, and Kind, 2004; Vinnik, Kurnik, and Farra, 2005); (Kumar et al., 2005a; Kumar et al., 2005b; Kumar et al., 2006); (Rychert, Fischer, and Rondenay, 2005; Rychert, Rondenay, and Fischer, 2007); (Yuan et al., 2006); Li, Yuan, and Kind, 2007; Rychert and Shearer, 2009). Due to the large number of waveforms employed in this thesis we have developed a semi-automated waveform analysis procedure. We provide details on several key steps of our methodology (rotation, deconvolution and move-out correction) in order to minimize ambiguity and to allow for our work to be more easily replicated. Finally, we will describe briefly the different RFs interpretation methods employed in this thesis and which will be applied in the next chapters; CCP stacking, Reverse Time Migration, Harmonic Decomposition analysis and joint inversion.

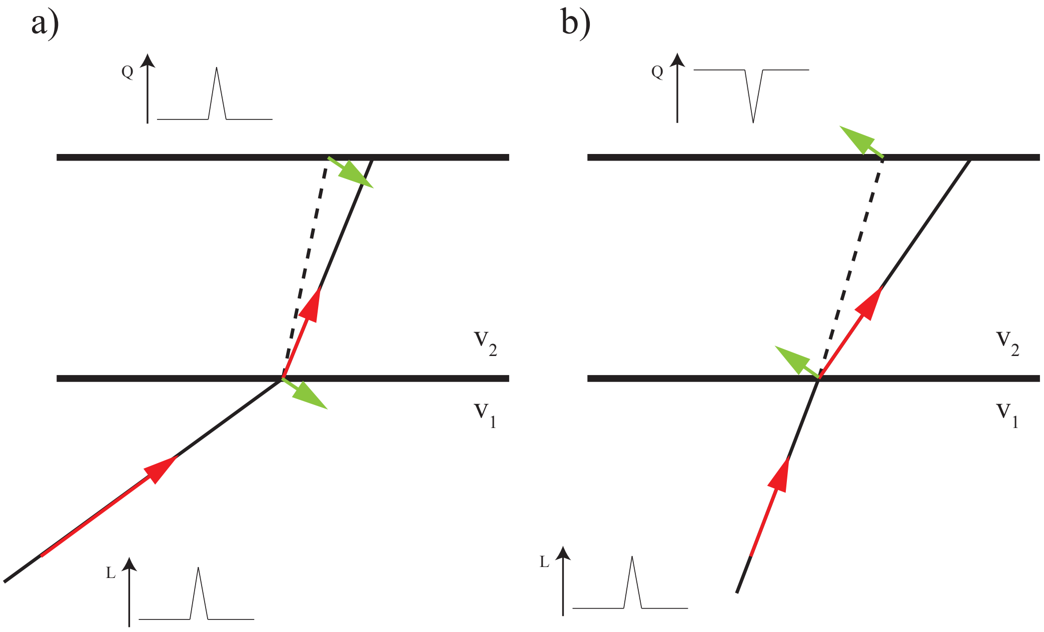

FIGURE 3.6: Simplified model perception for P-to-S conversion at a positive velocity contrast (Moho-like, i.e. v1 > v2) resulting in a positive peak on the Q-component (a) and for negative velocity contrast (v1 < v2) (b). Red Arrows denote particle motion of the P-wave, whereas green arrows denote the particle motion of the S-wave.

3.2.1 Methodology

Conversion: Physics of the problem

When seismic waves impinge with non-normal incidence on a boundary between two materials with different acoustic impedances, not only refracted and reflected waves are generated, but also converted waves. This is a consequence of the two wave-type nature, longitudinal (P) and transversal (S), of seismic waves. The boundary conditions that the physics of the medium imposes on the solution at the junction causes part of the incoming seismic wave energy gets converted into the complementary body wave type, i.e., P-to-S (Ps) and S-to-P (Sp) conversions (Fig. 3.5).

Zoeppritz equations determine the amplitudes of reflected, refracted and converted waves in the discontinuity as a function of the angle of incidence.

These equations reveal that for both direct P-to-S and S-to-P conversions, the shear velocity contrast has by far the largest effect on conversion amplitude in terms of material parameters. Therefore P- and S-RFs methods can be used to study the S-velocity structure below a seismic receiver. Fig. 3.6 illustrates the process of conversion, displaying Ps conversions at a) positive and b) negative velocity contrasts.

We say that a velocity contrast is positive if the velocity above is slower compared to the velocity below such as the crust mantle boundary (Moho discontinuity). Analogously, the velocity contrast is negative for a fast-over-slow contrast such as the lithosphere asthenosphere boundary (LAB). When the conversion takes place at a horizontal, isotropic interface, the energy is confined to the P-SV plane. Original P- and S- waves will generate SV- and P- types pure conversions making the longitudinal L and Q components the depositories of the incoming and converted waves.

In the next sections we will explain in detail the standard procedure of processing RFs (Vinnik, 1977, Langston, 1979). First, in an attempt to separate the P, SV and SH energy, the seismograms are rotated from the vertical/horizontal to the LQT coordinate system (Yuan et al., 1997). This step is followed by a deconvolution to remove the effect of different source time functions and far-receiver earth structure effects. We then apply a moveout correction to remove the kinematic effect of different earthquake distances before stacking individual RFs.

Rotation

Since the original and converted phases are different wave types, they are recorded in different components of the ground motion. As already mentioned, planar, isotropic interfaces confine the energy in the P-SV plane. The usual vertical, north-south and east-west (ZNE) components of the seismic ground motion should be rotated into a local coordinate system, where each wave type (P, SV and SH) is on its own component. This rotation is done in two steps using backazimuth and incidence angles. First, the ZNE coordinate system is rotated around the Z axis, into the ZRT system using the backazimuth angle. Note that the steep incident angle of teleseismic waves makes the along-ray P particle motion be predominantly recorded on the vertical component and the converted ray-perpendicular S particle motion on the radial component. Many RF studies employ these two components and avoid the incidence angle rotation which can be quite sensitive to the shallow velocity structure. This will be our strategy for the joint inversion application in chapter 8. In order to achieve a complete isolation of the P- and SV- waves we rotate the Z and R components into the L and Q components using the incidence angle. The SH, which should be in the T component, is free of converted waves in the case of a laterally homogeneous and isotropic Earth. We will treat in detail how the heterogeneity affect radial and transverse RFs in chapter 7.

The back azimuth and incidence angles can be calculated theoretically from the event and receiver locations using a global earth model, such as IASP91 (Kennett, 1991). This is achieved using the method of Buland and Chapman, 1983 as implemented in the TauP toolkit (Crotwell, Owens, and Ritsema, 1999. Alternatively, the angles can be computed also directly from the data by diagonalizing the covariance matrix (Kanasewich, 1983). Optimized rotation of the components of ground motion is very important for identifying and enhancing the weak converted phases such as the LAB conversion in the case of S-RFs. In this case, we use a theoretical backazimuth angle to perform the first rotation since the theoretical angle do not differ importantly with the real angle. In contrast, in the second rotation we employ a calculated incidence angle by minimizing the SV-wave energy on the Q component at the S-onset. The advantage of this approach has been pointed out and demonstrated by Kumar et al., 2006.

Deconvolution

The seismogram recorded at a station is a composite of source and propagation effects and instrument response. RFs studies intend to remove the effects of the

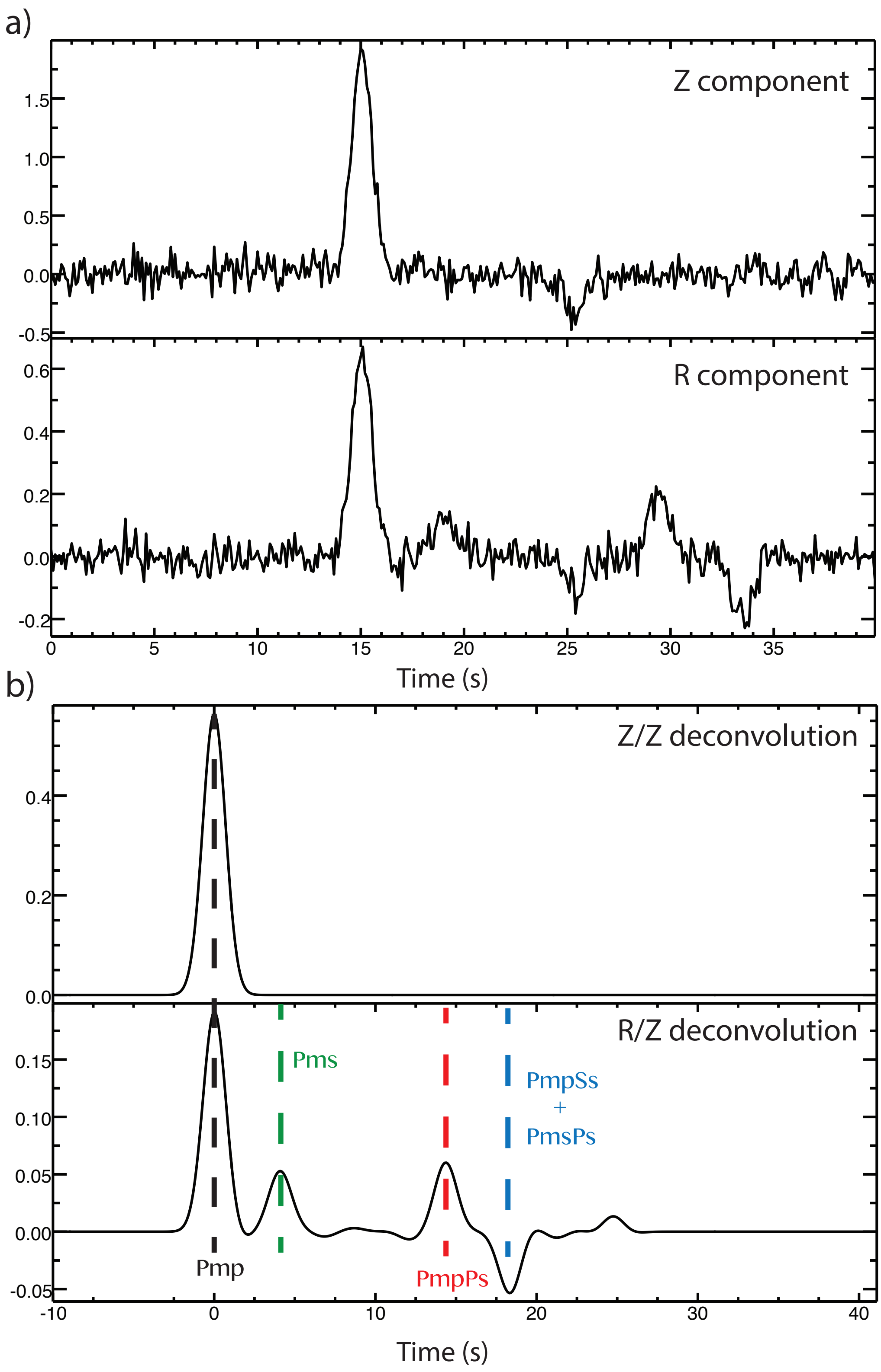

FIGURE 3.7: Illustration for deconvolution method. In a) noise added synthetic Z and R seismograms are displayed (a Gaussian pulse is used as the source). Figure b) shows the result of deconvolution of the Z and R components. Converted phases as shown in fig. 3.5 have been marked.

source, the far propagation path, and the instrument response, retaining only the information on receiver-side wave conversions caused by the local structure (Vinnik, 1977, Langston, 1979). Since the converted wave is excited by the original wave, the waveforms of the converted and original waves resemble each other, only scaled in amplitude. Therefore, the source and near-source information that we want to remove is at the same time contained in the direct and converted waves. The availability of three-component observations allows us to use this redundancy on the components to isolate the receiver structure effects on the waveforms.

With respect to P-RFs, by deconvolving the L component from the Q component we isolate the P-to-S converted wave energy on the Q-component. The process can be thought as finding matches to the L component waveform in the Q component with a delay time between both signals. In RFs studies, we know as the "response component" that one recording predominately the converted phases and the "source component" that one containing mostly the original incoming waveform. As pointed out in the previous section, P-RFs studies can employ indifferently as source the Z and L components and as response the R and Q components, respectively.

The sketch of Fig. 3.7 illustrates the process of deconvolution using synthetic seismograms. We use a quite simple model consisted in an 35 km depth interface and a Gaussian pulse with 1s width as the source. The source time function of the Z component is deconvolved from itself and the R component. This maps the waveform recorded on the L component to a spike located at 0 s delay time. The P-to-S converted energy from the interface recorded on the Q component has the same waveform as the P wave of the L component but with smaller amplitude and shifted in time, depending on the converter depth. The amplitude of the converted arrival carries information on the strength of the shear velocity contrast.

The deconvolution process is in general an ill-posed problem because of the existence of random noise, limited frequency bandwidth and inaccurate source signature estimation. Therefore, the process has to be regularized. Different deconvolution methods are known such as iterative deconvolution, spectral division or multichannel Wiener deconvolution. We use in this study the iterative time deconvolution method developed by Ligorria and Ammon, 1999 (for details visit Charles Ammon's webpage). The deconvolution method is free of complex relationships between water-level values, time-domain smoothing and damping parameters characteristic of other methods with a modest increase in computation costs. It is based on a least-squares minimization of the difference between the observed response seismogram and a predicted signal generated by the convolution of a iteratively updated spike train with the source-component seismogram. A low-pass Gaussian filter is used to clean up high-frequency noise in the receiver function. The frequency content/pulse width of the receiver function is controlled by the Gaussian filter-width parameter a. For P-RF studies, mostly employed to probe the crustal structure, values of $a = 2.5$ with pulse width of 1 s are commonly used. S-RFs works try to image the LAB discontinuity located at larger depth and employing S-waves as the incoming source. This delimits the frequency content at higher ranges using generally pulse-widths of 6 s.

Single-station RF stacking and moveout correction

As a first approach to the interpretation of RFs we can sum many single event RF traces and therefore enhance the signal to noise ratio of converted Ps phases. The moveout must be corrected before summation of RFs since both delay times and amplitudes are dependent on the slowness. Only the time moveout correction is generally applied in CCP stacking methods eluding to correct for the amplitude because some applications do not need to preserve strictly the amplitudes of RFs. Harmonic decomposition analyses investigate the backazimuth amplitude variation that inclined and/or anisotropic structures generate on RFs. In this case, we must correct the amplitude dependence that the ray parameter produces on RFs in order not to interfere with the backazimuth dependence.

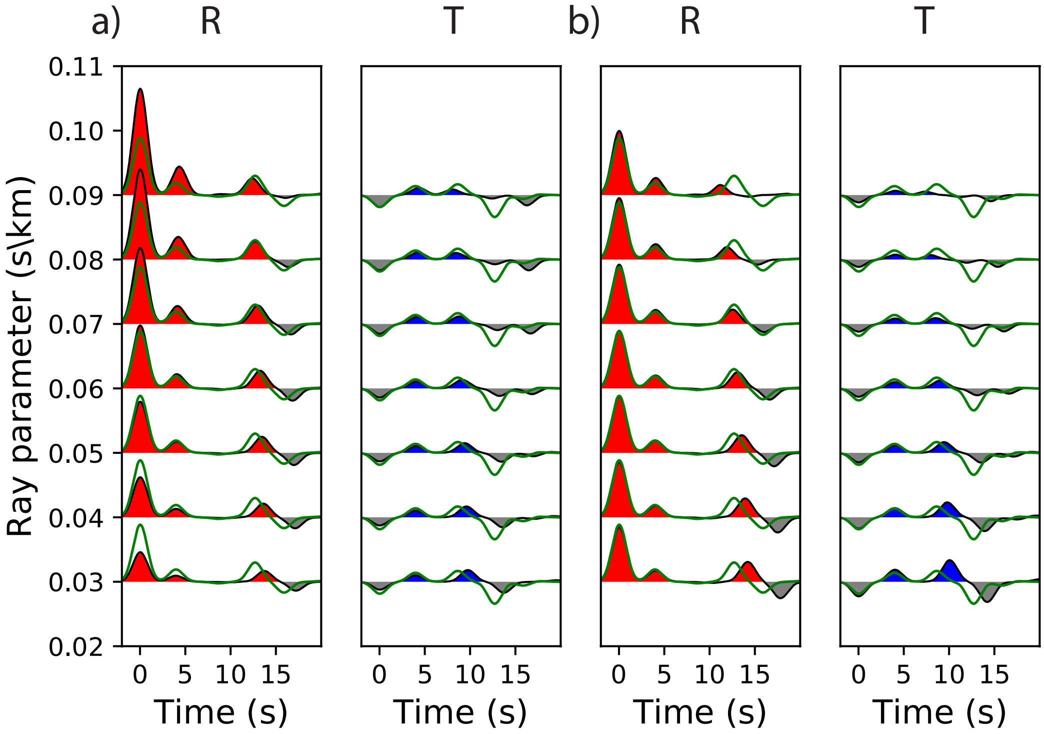

FIGURE 3.8: Synthetic radial (filled red traces) and transverse (filled blue traces) RFs with a constant 0° back-azimuth and variable ray parameter considering a model with a 15° dipping interface and 0° of strike direction. a) Without and b) with amplitude and time move-out correction. Green line depicts the receiver function with the ray parameter value that we have used to apply the correction (0.055 s/km).

Time moveout correction consists simply in stretching or compressing the traces depending if the event slowness is smaller or larger than a reference slowness previously chosen. To carry out the moveout correction a reference velocity-depth model is needed. Once corrected, the single-station RFs can be stacked to enhance the conversion. The moveout correction in amplitude consists in a multiplicative factor I_{Ref}/I, being I_{Ref} and I the reference and the trace incidence angles, respectively. The reference incidence angle is obtained from the reference slowness according to the expression $u = \sin(I)/v_{s_0}$, where v_{s_0} is the S-wave velocity at the surface. Figure 3.8 illustrates the goodness of this correction ((a) without and (b) with correction) for radial (filled red lines) and transverse (blue red lines) RFs in a scenario with a dipping discontinuity. The green trace depicts the receiver function with the ray parameter value used in the move-out correction. As we can see in fig. 3.8a the transverse component exhibits less variation of the amplitude with respect to the slowness. The move-out correction works properly in the whole ray parameter range used in RFs analysis, between $0.03 - 0.08$ s/km.

3.2.2 Interpretation Methods

Phase-weighted Common Conversion Point stacking migration

Simplified migration methods are frequently used in earthquakes seismology due to uneven distribution of stations and events. When many receivers are arranged in a linear profile this migration approach is based on the back projection in a 1D model of transmitted and converted phases along the incoming ray path. It transforms the arrival time difference between transmitted and converted phases as measured at a single station down to the depth where the conversion occurs. Ray tracing is done for P and S waves using known back-azimuth and slowness values into a 1D model. RFs obtained from different earthquakes are binned and the signal-to-noise ratio is enhanced by stacking over data with common conversion point. The result is a 2D distribution of seismic energy which enables mapping the seismic discontinuities of the crust and upper mantle.

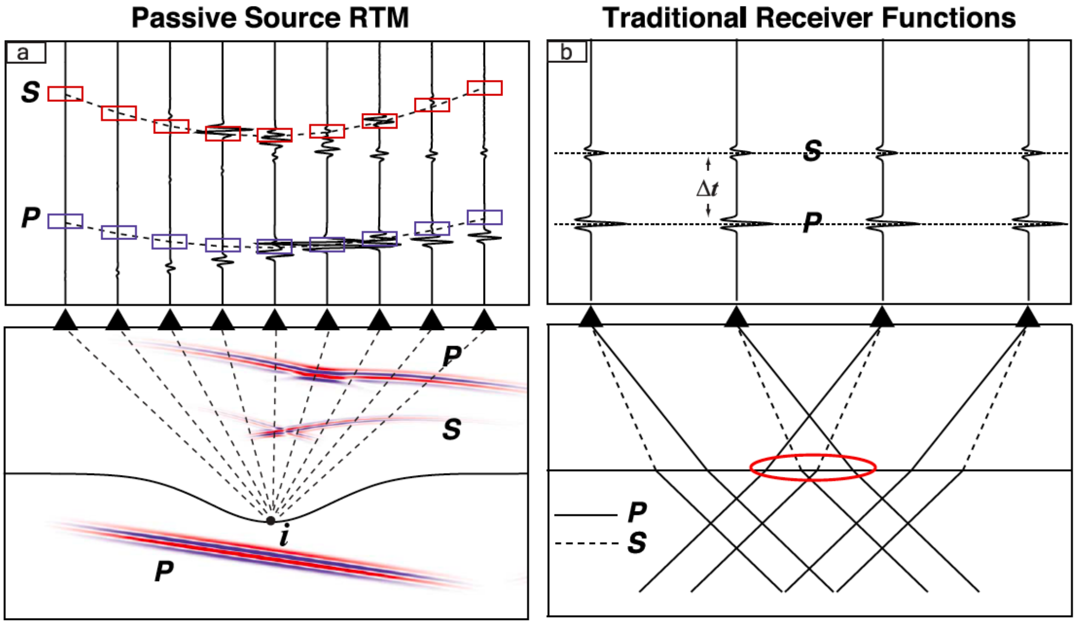

FIGURE 3.9: Schematic illustration of (a) passive-source reverse time migration and (b) common conversion point (CCP) stacking of traditional RFs. (a) (bottom) P waves impinging on a contrast produces direct P and converted S waves, which can be recorded at an array of seismograph stations at the surface (black triangles). (top) P and S energy due to scattering at, say, point i arrives at different times (blue and red boxes, respectively). In inverse sense, the location point i can be reconstructed by optimization of the correlation between the back-projected P and S wavefields. (b) (bottom) In traditional receiver functions, the P-SV conversion is assumed to occur at an interface that is (locally) horizontal. (top) The travel time difference Δt between transmitted P and converted S is a measure of interface depth, and data redundancy is obtained by stacking over common conversion points (CCP), shown as a red oval.

In order to apply the binning of RFs the 2D plane must be divided into a grid in the lateral (along the section) and depth directions. The size of the grid depends on the maximum frequency we want to resolve in the migration.

The CCP stacking method used in this study is released in the FORTRAN code of Yuan et al., 2000 (see Schneider, 2014 for detailed discussion). An improvement of this CCP scheme is the inclusion of scattering waves by back projecting along the range of a Fresnel Zone. According to the Huygens' principle each part of a wavefront is the source of a new wave. A refraction that we think of as coming to the surface from a point of an interface is actually being scattered from an area with the dimension of the First Fresnel Zone. Having multiple registrations in the array the constructive interference permits to enhance the signal at the location of the real structure. The radius of the Fresnel Zone depends on the depth h and wavelength λ according to:

$$r_{FZ} = \sqrt{\frac{1}{2}\lambda h + \frac{1}{16}\lambda^2} \tag{3.1}$$

where the wavelength depends on the S-velocity and the dominant T period of the signal.

In CCP stacking methods noisy RFs may produce spurious secondary arrivals that obscure the main conversions at large contrasts in seismic discontinuities. A possible approach to minimize the constructive stacking of erroneous signal is to include phase-weighting in the CCP stacking (Frassetto et al., 2010). Now, the mean, linearly stacked RF for each bin is multiplied by the sum of its correspondingly stacked instantaneous phase. Arrivals that come from the same scatter might be coherence in phase producing high values of the phase-weight. Amplitudes associated with incoherent arrivals possess low phase-weights. Therefore, for each bin amplitudes are summed, averaged using the standard CCP procedure and then multiplied by the phase-weight term $c(z)$.

$$g(z) = \left(\frac{1}{N} \sum_{j=1}^{N} s_j(z) \right) c(z)^{\nu} \tag{3.2}$$

where N is the number of RFs, and $c(z)$ represents the weighting factor which varies from 0 to 1 and can be applied directly, or modified by an exponential term ν to adjust the sharpness of the filter (a ν value of 0 corresponds to linear stacking). The weighting factor $c(z)$ is calculated as the mean-weight for a particular depth, z, obtained from the averaged absolute value of the sum of the instantaneous phases.

$$c(z) = \frac{1}{N} \left| \sum_{j=1}^{N} e^{i\phi_j(z)} \right| \tag{3.3}$$

We obtain the instantaneous phase for each trace by expressing the RF in its analytic signal form (Schimmel and Paulssen, 1997).

$$S(z) = s(z) + iH(s(z)) = A(z)e^{i\phi(z)} \tag{3.4}$$

The terms $s(z)$ and $H(s(z))$ define the real and imaginary components of that signal, where H is its Hilbert transform. The second formulation in eq. 3.4 represents $A(z)$ as the amplitude and $\phi(z)$ as the instantaneous phase.

We will employ the CCP stacking migration without and with phase-weight in chapters 5 (S-RFs in the Gibraltar arc region) and 6 (P-RFs in high-resolution profiles), respectively.

Overall, CCP stacking presents three well-known issues; (1) Poor results in the presence of lateral volumetric velocity variations. (2) If significant lateral heterogeneities are present, structures cannot be correctly imaged due to diffraction or scattering artifacts produced by dipping and laterally discontinuous interfaces. (3) Final images are strongly polluted by the signal of multiply reverberated waves. In the next sections we will describe applications that can face these issues.

Reverse Time Migration

The CCP stacking method is based on simplifying assumptions such as the locally flat interface. If significant lateral heterogeneities are present (no smoothly varying discontinuities) structures cannot be correctly imaged by the CCP stacking of RFs due to diffraction or scattering artifacts. The Reverse Time Migration (RTM) technique accounts for single scattering processes and eludes these simplifying assumptions by direct back propagating elastic waves (Brytik, De Hoop, and Hilst, 2012). Shang, De Hoop, and Van Der Hilst, 2012 have designed a RTM scheme practical to be applied to high resolution seismographs with receiver function datasets. The relevant parts of the transmitted (direct P) and converted Ps waves recorded at a seismograph array are once back propagated until they correlate at the time and space point of mode conversion. The back-propagation is done for each earthquake, each illuminating the target region from different directions. The final seismic image is obtained by stacking all of the partial images from individual events. This enhances the signal-to-noise ratio and guarantees the illumination of all the structures. These methods require uniform sampling of data in both time and space because undersampled or irregular acquisition geometries may form strong artifacts. Seismic data needs then to be interpolated and regularization methods must be used in a pre-processing step to build regularly and densely sampled data. Even with modern array deployments the sampling requirement is typically not met for teleseismic data. In chapter 6 we prove that Hire profile is a sufficiently high dense seismograph to use the RTM with P-RF dataset and therefore exploit the total complexity of the waveforms.

Harmonic Decomposition Analysis

Conventional RFs interpretations are not just based on the flat-layered media assumption but also on the absence of anisotropic structures. These heterogeneities produce on radial and transverse RFs components backazimuth amplitude and time variations on direct, converted and multiple reverberating phases. This behavior has sparked the development of harmonic analyses that allow to separate these effects into different harmonic orders. These techniques permit to separate in RFs the different effects that on the signal are caused by the flat-layered isotropic structure, the dipping interfaces and the anisotropic layers. The content concerning the flat-layered isotropic structure is useful to inversion techniques based on this assumption. The information related to dipping and/or anisotropic boundaries allow evaluate the strength of the heterogeneity and define the geometry of the structures. In chapter 7 we design a harmonic decomposition analysis based on previous studies which uses both radial and transverse component.

Joint Inversion

Other handicap of the CCP stacking method is the 1D approximation, especially in presence of significant volumetric velocity variations. The inversion of RFs solves this issue when obtaining for each receiver dataset the S-wave velocity of the subsurface structure. However, inversion techniques present considerable non-uniqueness problems. The joint inversion of P-RFs and surface wave dispersion curves makes use of the complementary sensitivity to different parameters of the model that both datasets have. RFs are primarily sensitive to the velocity contrast of the discontinuities and surface wave dispersion measurements probe mainly the averaged velocity of the media. As occurs with most methods in seismology, the inversion techniques assume as well low strength of heterogeneity in the form of dipping and/or anisotropic layers. In chapter 8 we incorporate the harmonic decomposition analysis to the joint inversion to infer the plane-layered isotropic shear-wave velocity structure of the media.

Chapter 4

S-RFs migration in the Gibraltar arc system

Establishing the boundary between lithosphere and asthenosphere is fundamental for understanding plate motions and tectonics. While the asthenosphere has been classically defined as a viscous mechanically weak layer in the upper mantle that hosts convection, the lithosphere in principle represents the rigid layer where the heat transfer is mainly conductive. The thickness of the lithosphere should vary with temperature, stress, strain rate, age, and mineralogy (Anderson, 1995). The depth of the Lithosphere-Asthenosphere Boundary (LAB) has been estimated using different properties (Jaupart and Mareschal, 1999; Gung, Panning, and Romanowicz, 2003; Conrad and Lithgow-Bertelloni, 2006; Pasyanos, 2010; Artemieva, 2011), given the variety of mechanisms that determine the transition between these two layers. Seismically, the LAB has been associated with a low-velocity zone in the upper mantle. Despite the fact that the LAB is probably the most important boundary for the description of the drifting plates, its depth and structure remain highly unknown. Hence, diverse approaches (elastic, thermal, electrical, petrologic, and seismic) have resulted in different depth values of the LAB (Artemieva, 2011).

Seismic ambient noise and wave tomography studies are insensitive to discontinuities. RF techniques are suitable to map in depth abrupt velocity contrasts. Only S-to-P conversions of teleseismic waves can be used to image the LAB discontinuity by remaining these lower lithosphere conversions free from

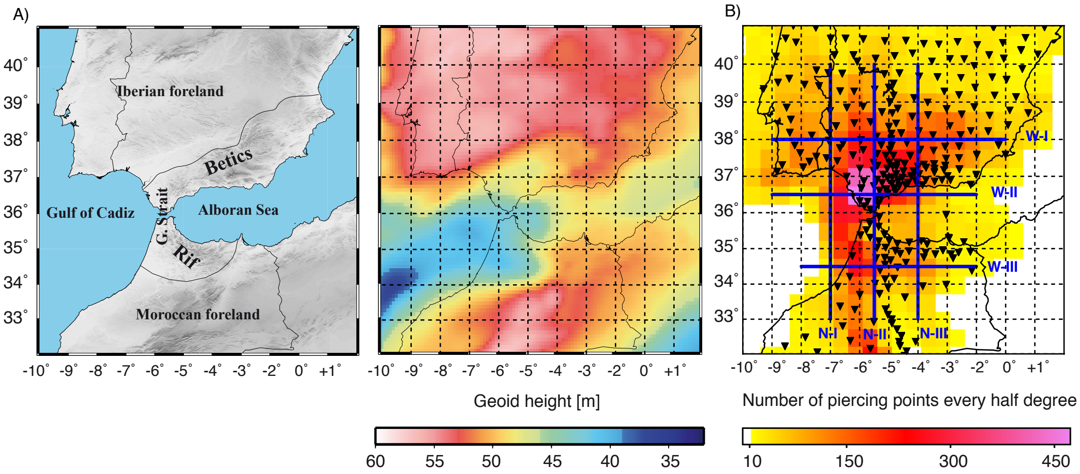

FIGURE 4.1: A) Topographic (left panel) and geoid map (right panel). B) Distribution of seismic stations and piercing points at 100 km depth. The blue lines mark the CCP profiles shown in Fig. 4.4.

crustal multiples. Many works have used this technique in different regions around the world to approximate the LAB depth (e.g., Kumar et al., 2005a; Heit et al., 2007; Abt et al., 2010; Dündar et al., 2011; Kumar et al., 2012; Rychert, Harmon, and Ebinger, 2014); they have shown how the LAB depth varies depending on the type plate; oceanic or continental, and the tectonic setting such as subduction and spreading zones. Recently, several studies have compiled previous works on LAB depth estimates using RFs (Rychert and Shearer, 2009; Kind, Yuan, and Kumar, 2012). In general, they agree in that for oceanic islands, Phanerozoic continental regions, and tectonically altered areas, the velocity contrast revealed by the RFs coincide with the LAB depth, whereas for cratons this contrast should represent a shallower discontinuity within the mantle lithosphere.

S-RF studies have been scarce in the Gibraltar arc region and have not provided conclusive results on the lithosphere thickness (Dündar et al., 2011; Miller et al., 2015) due probably to the small scale of the imaged features compared to the resolution used. In this study, we will map the depth of the LAB in the region to shed more light on the structure of the subduction system and its interaction with the surrounding lithospheres. We investigate for this purpose the conversions of teleseismic S-to-P waves at the seismic LAB using S receiver functions (SRFs). The analysis builds upon several seismic deployments during the last decade (Fig. 4.1B), which allows for broad coverage of the LAB over the region, and favors the use of stacking techniques to enhance the LAB signals.

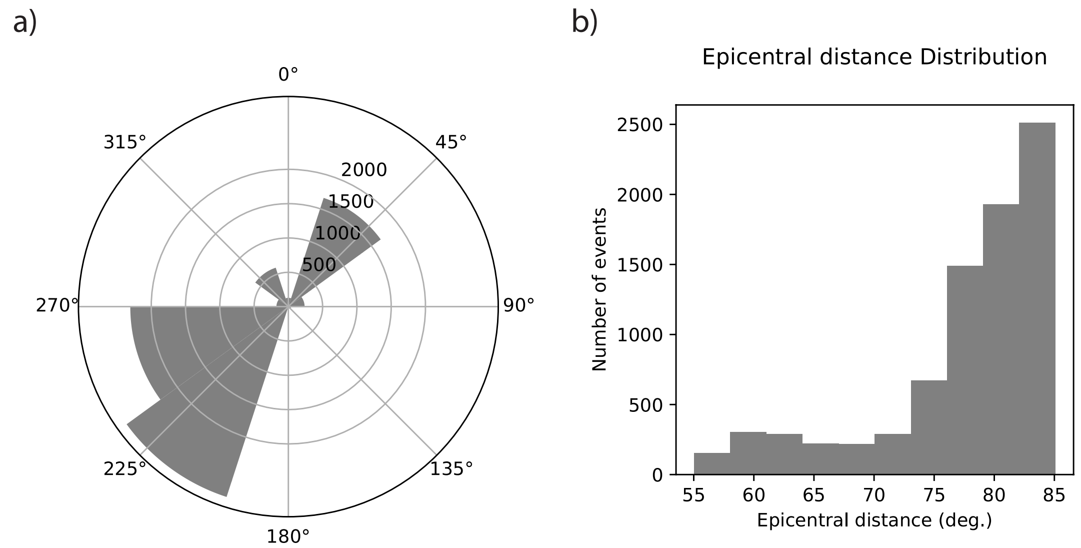

FIGURE 4.2: a) Backazimuth and b) epicentral distance distribution of the SRFs used in this study.

4.1 Data and Method

We analyze S-to-P conversions of teleseismic earthquakes recorded at a dense network of 300 permanent and temporary seismic stations in Iberia and Morocco (see Fig. 4.1B for the density of piercing points and Fig. 4.2 for the backazimuth and epicentral distribution of the SRFs). This corresponds to an average inter-station distance of 60 km over most of the area and 30 km locally. S-RF is a particularly suitable approach to study deep lithospheric structures. S-to-P conversions arrive before the direct onset, thus avoiding the interference of LAB converted signals with crustal reverberations, common in P-to-S receiver functions (PRFs) (e.g. Yuan et al., 2006). Furthermore, S-RF permits sampling larger areas compared to P-RF, due to the larger incidence angle of S waves. This allows for better coverage in offshore areas because the piercing points of SRFs are located farther away from the stations (Fig. 4.1B).

We use teleseismic events with magnitude larger than 5.8 mb, within the epicentral distance range of 55°-85° (Fig.4.2b). The available earthquakes within this epicentral distance range constrains the backazimuth mainly to the SW

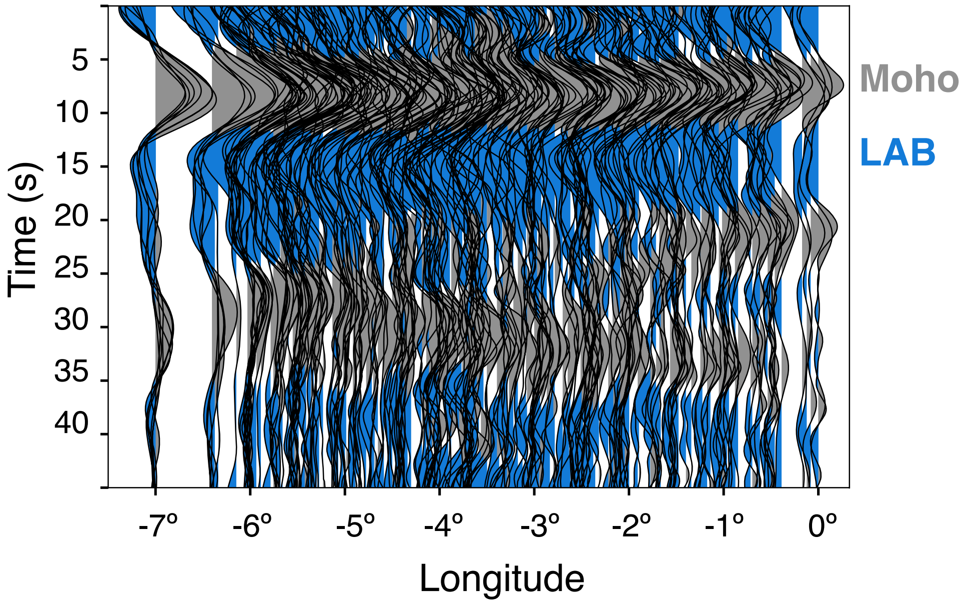

FIGURE 4.3: All S-RFs stacked along a WE profile.

and NE directions (Fig. 4.2a). We include in the analysis all the available seismograms with signal-to-noise ratio above 2.5, and rotate the three-component records into the ZRT coordinate system using theoretical back-azimuth angles. Following, a rotation into ray-based QLT coordinates is done minimizing the SV-wave energy on the Q component at the theoretical S-onset. We time-reverse the traces about the S-wave onset in order to analyze the SRFs in the precursor time window, only affected by the primary S-to-P conversions.

Prior to deconvolution, we used a band-pass filter from 1 to 30 s. We applied a time-domain deconvolution method of the SV (Q component) from the vertical component (L component) using the iterative deconvolution method developed by Ligorria and Ammon, 1999 with a 2 s wide Gaussian basis function. A 6 s low-pass filter is applied after deconvolution to enhance the LAB conversion. We obtain more than 10,000 individual SRFs. Fig. 4.3 display them stacked along a WE profile. The LAB can be identified with the prominent negative signal (blue color) after the Moho conversion, at 15-20 s travel time.

Piercing points at 100 km depth show a dense distribution, including offshore areas in Alboran Sea and Gulf of Cádiz (Fig. 4.1B). This enables us to build cross sections by stacking SRFs amplitudes applying a CCP approach (e.g. Mancilla et al., 2015a). We consider single scattering, taking into account the first Fresnel zone, for back projection of SRFs in the IASP91 velocity model. We built North-South and West-East cross-sections by stacking all RF amplitudes with piercing points within 1° distance at both sides of the profile (Fig. 4.4). We apply a binning of 5x5 km; bins with less than 10 samples are not taken into account.

4.2 Results

Migrated profiles show clear and coherent signals. Two principle signals can be recognized in all cross-sections. The shallower signal corresponds to a positive conversion (increasing velocity with depth) within the first 60 km, attributed to the Moho discontinuity. Although SRFs have lower resolution than PRFs, we point out that the lateral variations of the Moho topography in this study agrees with previous PRFs observations (e.g. Mancilla, Diaz, and Team, 2015). The deeper signal corresponds to a negative velocity contrast at depths among 50 to 180 km. This signal is interpreted as the seismic LAB discontinuity.

CCP sections across the Iberian Massif show a relatively flat LAB located at 80-90 km depth (IBL, Fig. 4.4, W-I profile). Similar lithospheric thickness has already been reported by previous tomographic (e.g. Palomeras et al., 2017), PRFs (Mancilla et al., 2015a), and SRFs (Miller et al., 2015) studies. This shallow LAB discontinuity has been attributed to a large-scale delamination of thickened continental lithosphere of the Variscan belts in Europe at Middle Permian age (e.g. Gutierrez-Alonso et al., 2011).

In Northern Morocco, a West-East profile shows relatively large topographic variations in the LAB (Fig. 4.4, W-III). An offset of about 40 km occurs near 4ºW of longitude from 100 km depth under the Rif Mountains to 60-50 km east to the Nekor fault. This observation agrees with previous studies that reported strong crustal and lithospheric thickness contrasts in the area, coincident with the intersection between the Trans Alborán Shear Zone and the Moroccan margin (e.g. Mancilla et al., 2015a; Miller et al., 2015).

The largest variations in the topography of the LAB discontinuity are observed beneath the Strait of Gibraltar and Gulf of Cádiz. The CCP profiles reveals two different negative converters (Fig. 4.4, W-II, N-I and N-II). The shallower one has depths of 80-90 km and represents the Iberian LAB (IBL,

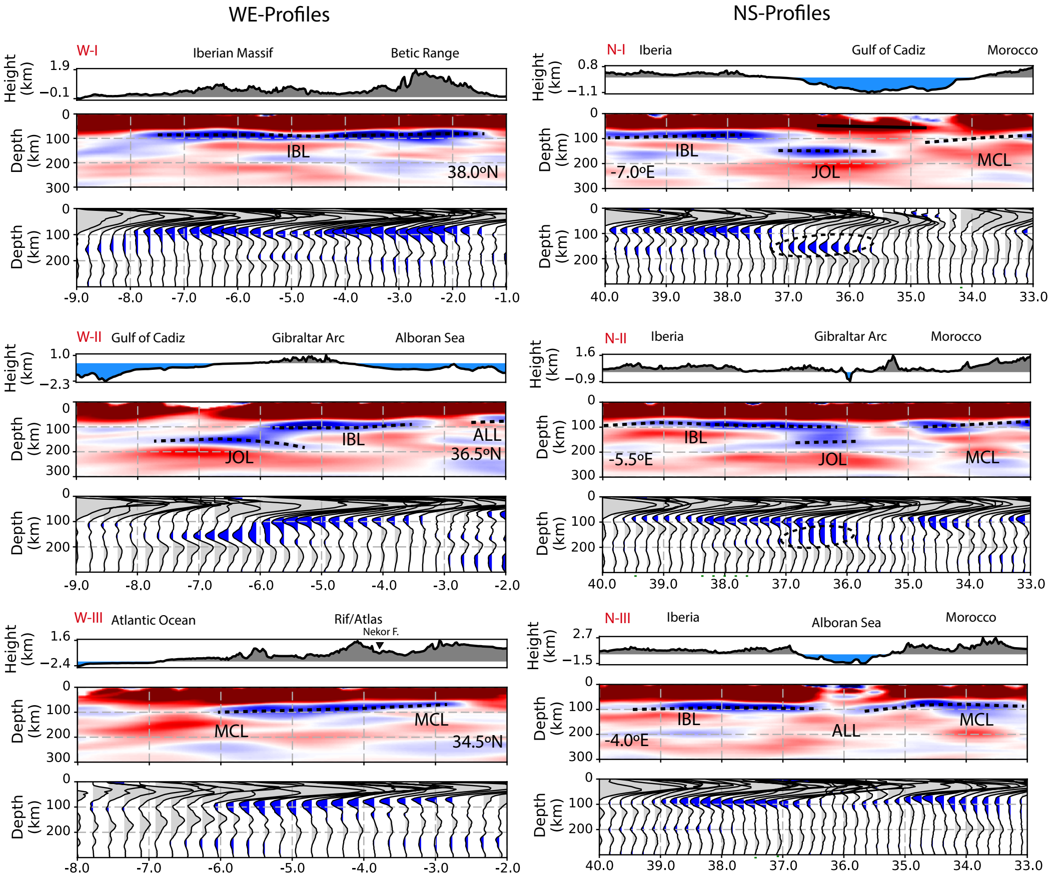

FIGURE 4.4: CCP profiles in E-W (left) and N-S (right) direction (compare Fig. 4.1), red and blue for positive and negative amplitudes, respectively. For reference, we show the topography along the profiles. For consistency among different cross-sections, we use the same normalization for all profiles. The lower panels show the stacked traces derived directly from the migrated images. The dashed black lines delineate the LAB discontinuity along the different domains: Alboran (ALL), Moroccan (MCL); Iberian (IBL), and the Jurassic Oceanic corridor (JOL) lithospheres.

Fig. 4.4). The deeper signal is emerging at 8°W at 150 km depth (Fig. 4.4, W-II), starts deepening eastward under the Gibraltar strait (6.5°W), reaching 180 km depth at 5°W beneath the Alborán Sea (JOL, Fig. 4.4, W-II). At 4°W, the oceanic LAB (JOL) has disappeared completely and a shallow LAB at 50 km depth emerges eastern side of the profile W-II (Fig. 4.4), corresponding to the thinned continental Alborán lithosphere already imaged in previous studies (ALL, Fig. 4.4, N-III e.g Mancilla et al., 2015a; Heit et al., 2017). The western termination of the oceanic LAB signal (JOL) can be attributed to the lack of the data coverage beyond 8°W (Fig. 4.1).

We associate this deeper negative velocity contrast (JOL, Fig. 4.4, W-II), under the Alborán Sea, to the LAB discontinuity of the Alborán slab observed in tomography studies (e.g. Spakman, Wortel, and Wortel, 2004; Bezada et al., 2013, Palomeras et al., 2017). The eastern termination of the LAB signal (5°W, Fig. 4.4, W-II) agrees with the location where the Alborán slab starts subducting vertically, impeding detection by S-to-P conversions. Our results show the continuity of the LAB discontinuity from Alborán slab oceanic lithosphere across the Gibraltar strait to the Gulf of Cadiz (JOL, Fig. 4.4, W-II). This allows for connecting the Alborán slab with the oceanic crust detected in the Gulf of Cadiz (Sallarès et al., 2011), providing direct evidence for the presence of a corridor of oceanic lithosphere beneath the Gibraltar strait. This corridor has been predicted by paleogeographic reconstructions as Jurassic age oceanic materials connecting the Alpine-Tethys with the central Atlantic Ocean (Frizon de Lamotte et al., 2011; Stampfli and Borel, 2002). The extent of the oceanic LAB along the N-I cross-section shows a good match with the geoid low under the Gibraltar strait (Fig. 4.1).

The apparent width of the oceanic corridor can be estimated as 200 km in NS profiles (Fig. 4.4, N-I). To the north, the flat oceanic LAB is limited by an offset of 70 km with respect to the Iberian continental LAB at 37°N. This lithospheric offset may be related to a prior transform fault in agreement with the sharp transition between continental and oceanic crust observed by

Sallarès et al., 2011, and with the location and focal mechanism of subcrustal earthquakes (Stich, Mancilla, and Morales, 2005) possibly associated with this structure. This observation is supported, too, by CCP images of PRFs along a similar NS-profile (Mancilla et al., 2015a). The PRFs profiles image a Moho offset of roughly 6 to 9 km, representing an increase in crustal thickness under the Gibraltar strait that agrees with an average thickness of oceanic crust (Fig. S3 in SOM). The apparent overlap of the Iberian-continental and oceanic LAB in profile N-II (Fig. 4.4) is likely an artifact due to the projection of independent structures within 1 degree at both sides of the profile. To the south the transition to the African foreland LAB is imaged less abruptly at 35°N. This mayor change in lithospheric structure may define the present day Nubia-Eurasia plate boundary, in prolongation of the SWIM-lineaments in the Atlantic (Zitellini et al., 2009).

The observed LAB depth of the oceanic corridor is unusually large in a global comparison (e.g. Rychert and Harmon, 2018). The thickness of oceanic lithosphere depends on age and is currently explained by two competing models: half space cooling (HSC, Stein and Stein, 1992) and plate model (PM, Grose and Afonso, 2013). They differ for ages larger than 70 My. The oceanic lithosphere in the Gulf of Cadiz is from middle-to-late Jurassic (>145 My, e.g. Stampfli and Borel, 2002), one of the oldest not been yet consumed by subduction. For these ages, PM predicts a lithospheric thickness of slightly less than a 100 km and HSC predicts values of about 110-130 km (Rychert and Harmon, 2018). The observed LAB of the oceanic corridor supports the HSC model. The remaining difference can be attributed to the presence of 35 km thick continental crust of the Gibraltar strait on top of the oceanic lithosphere.

4.3 Conclusions

The analysis of a large amount of SRFs (> 11.000) has revealed the topography of the seismic LAB discontinuity beneath the complex plate boundary zone between Iberia and northern Africa. Four different domains can be clearly distinguished, some of them limited by sharp vertical offsets. We confirm the previous LAB depth estimates for the Iberian and Moroccan forelands. Under the Alboran domain, we find a thin lithosphere of 50-60 km thickness. The largest LAB depths are observed under the Gibraltar strait outlining 200 km wide corridor of Middle-to-Late Jurassic age lithosphere with about 120 km thickness, being one of the thickest oceanic lithospheres ever detected. The main conclusion that emerged from the CCP image is the clear spatial connection between the Alboran slab under the Alboran Sea and the Atlantic oceanic crust through this oceanic corridor below the Gulf of Cadiz.

Chapter 5

P-RF migration in high-dense profiles: Hire and Transcorbe

At edges of a subduction system, STEP faults (Subduction-Transform-Edge-Propagator, also called tear fault) occur and enable the continuation of subduction (Govers and Wortel, 2005). These faults are strike-slip transfer faults that produce tearing in the subducted plate lithosphere and propagate, approximately, perpendicular to the subduction strike (Nijholt and Govers, 2015). The slab tearing may result in sharp changes in lithospheric and crustal thickness across the STEP fault, strike-slip motion in the upper plate and vertical motion between the two blocks of the STEP fault (Govers and Wortel, 2005; Baes, Govers, and Wortel, 2011). In addition, the juxtaposition of overriding plate and the continental part of the subducting plate causes an increase of the crustal thickness that contributes to the relatively sharp contrast in the Moho depth.

Observations of faults produced by slab tearing (STEP fault) have been found in subduction system worldwide (e.g. North Fiji Basin, Eastern Caribbean plate, Sulawesi Indonesia, see e.g. Govers and Wortel, 2005) and in the Mediterranean region in particular: e.g. in Northern Apennines (e.g. Piana Agostinetti, 2015), in the southern Tyrrhenian subduction system (e.g. Bianchi et al., 2016) and in the Hellenic arc (e.g. Pearce et al., 2012). While STEP faults at the subducting slab have been studied largely in last years, deformation produced at the top of them in the overridden plate is still poorly understood. Some observations correlate the location of the STEP faults in the subducting plate with a wide shear zone in the overriding plate formed by strike-slip faults (e.g. Özbakır et al., 2013; Piana Agostinetti, 2015). Özbakır et al., 2013 following observations at the surface above the STEP fault suggested that the shear zone at depth is not sharp in its early stage of formation. However, there is no clear observation of how the deformation is distributed from the tear fault in the subducted slab to the entire crust in the overriding plate.

At the northern edge of the westernmost Mediterranean subduction system where continental crust started to be involved at Miocene ages, slab tearing along STEP fault has been suggested to occur (e.g. Faccenna et al., 2004; Duggen et al., 2004; Govers and Wortel, 2005; Garcia-Castellanos and Villaseñor, 2011; Mancilla et al., 2015b). Using RF migration techniques Mancilla et al., 2015b marks with a Moho step the approximate position of the tear fault (or STEP fault) along the northern edge of the subduction system under eastern and central Betics (see white stars in fig. 2.4). The large inter-station distance (∼50 km) used in these studies, however, prevents an accurate estimation of the sharpness and size of the jump and the geometry of the contact between the subducting and the overriding plates.

In this study we use the data from Hire and Transcorbe high-density seismic profiles and other stations in the close vicinity to perform an analysis of P-wave RF in order to image with high resolution the crustal and the lithospheric mantle structures. By making use of the RF CCP stacking migration technique we delineate the Moho and lithosphere–asthenosphere boundary (LAB) and other intracrustal discontinuity across the different geological units.

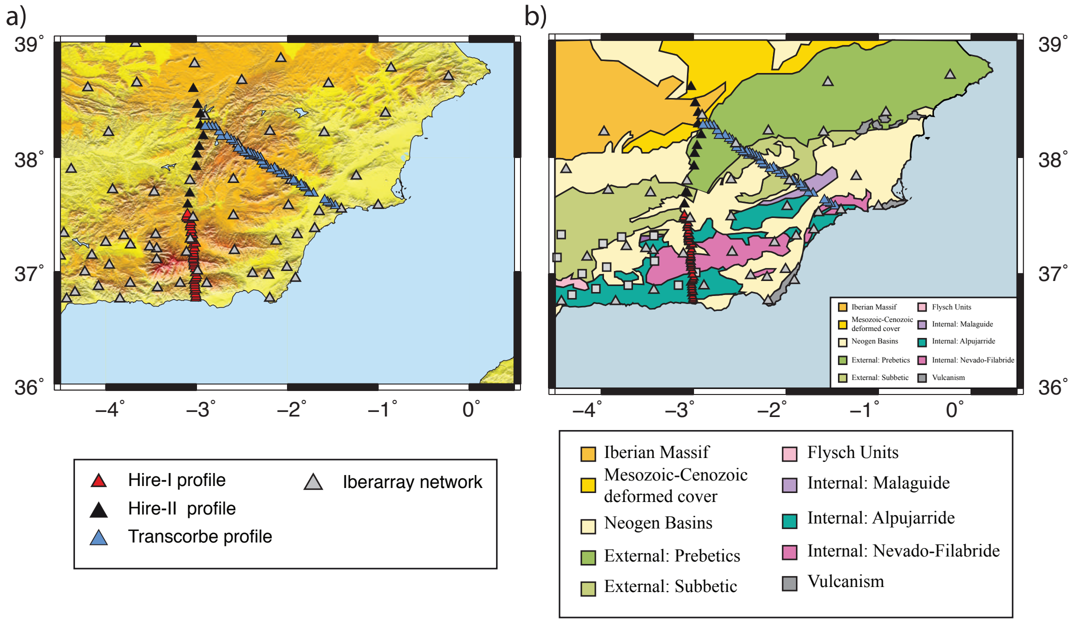

FIGURE 5.1: Topographic (a) and geologic (b) maps. Red triangles mark the Hire-I stations, black triangles the Hire-II stations and blue triangles the Transcorbe stations. Grey triangles denote the permanent and other previous temporary stations in the area.

5.1 Data and Method

We calculate PRFs from teleseismic seismograms recorded by the two high-resolution seismic profiles, Hire and Transcorbe. In addition, we use data from permanent and other temporary seismic stations located close to the profiles (gray triangles in Fig. 5.1) that were analyzed by Mancilla et al., 2015a. See chapter 3 for a detail explanation of the instrumentation.

For the RF analysis, we consider earthquakes with magnitude larger than 5.5 in the distance range between 30° and 90°. The number of obtained RFs for the temporal stations ranges from 8 to 56 and from 5 to 68 for the Hire and Transcorbe profiles, respectively. The difference in the number of RFs between stations is mainly due to technical problems for some stations during the experiment. In the case of the permanent stations, we use from 4 to 6 years of data (i.e., 159 RFs for SESP and 129 for VALD). After following the standard P-RF processing workflow described in the chapter 3, we display in Fig. 5.2 the Q component and in Fig. 5.3 the Q and T components of the RFs for some representative stations located in different geologic domains along the Hire and Transcorbe profiles, respectively. Even though, the transverse components contain significant energy and we observe features that can be explained by dipping layers or anisotropy, in this chapter we only focus on the Q component. We show the T component for the Transcorbe profile to note the amount of energy present in the tangential component, aspect that will be studied in detail in chapter 7.

To follow the Moho discontinuity along the profiles, in Fig. 5.4 and 5.5, we plot the Q-component summation traces at each stations for Hire and Transcorbe profiles, respectively. RFs show in general clear conversion phases at the Moho discontinuity (Pms) beneath most of the stations. We observe a great variability in the form of RFs between stations along the profiles increasing their complexity in the contact area between the Iberian Massif crust and the Alboran domain (stations HR25-HR41 and TR13-TR22 in Hire and Transcorbe profiles, respectively).

The dense distribution of seismic stations in the profiles, allows for building migration images of the lithospheric discontinuities with high spatial resolution. Ray tracing is performed using a 1D modified IASP91 reference velocity model using crustal information from previous refraction profiles (see Díaz and Gallart, 2009, for a review). We use a 2 x 2 km grid to do the binning of RFs.

In Fig. 5.6, the PRFs from the high density seismic array (Hire-I, $\sim$2km inter-station distance) are back-projected along the incident ray path and then stacked using different swaths (10, 20 and 35 km). The horizontal and vertical sizes of the bins are 1 and 2 km, respectively. A swath of 20 km pays off to enhance the lithospheric discontinuities and its continuation along the profile in the migrated cross-sections (Fig. 5.6).

We select this 20 km value for the halfwidth and include data from neighboring stations within this swath (Fig. 5.8). In the migration images we observe the continuation of the conversion discontinuities along the profile and interpret them in Fig. 5.8B. In the crust at the depth range of <50 km, we can identify a series of conversion phases with positive amplitudes. We interpret the deepest one (at depths of 30-50 km) as the base of the crust, and other dome-shape features as intracrustal discontinuities. Contrary to other PRFs studies that basically focus on the Moho geometry, a first-order discontinuity, the high spatial resolution of our profiles allows to resolve Ps conversion associated to intracrustal interfaces. A discontinuity with negative amplitude (blue color) is inferred at the depths of 60-100 km, coinciding with the LAB discontinuity observed in previous studies (Palomeras et al., 2014, Mancilla et al., 2015a). We mark the location of the inferred LAB discontinuity with a magenta line.

In Fig. 5.9, we extend the profile toward the north with data form Hire-I and II stations and use all the available data in the area from the closest temporary and permanent stations (grey triangles in Fig. 5.1). In this migration we take into account the increase of the Fresnel zone with depth and include the phase-weighting factor (see Fig. 5.7 to observe how the phase-weighting factor improves the imaging of the discontinuities). We stack in the cross-sections all PRFs amplitudes with piercing points inside a band with halfwidth of 20 km at both sides of the profile (Fig. 5.1). We spatially smooth the stacking using a Gaussian filter of 3 km. In these figures, we can delineate the Moho discontinuity and other intracrustal structures from the Iberian Massif in the north to the Mediterranean coast in the south. Using the same parameters we obtain the cross-section for the Transcorbe profile (Fig. 5.10).

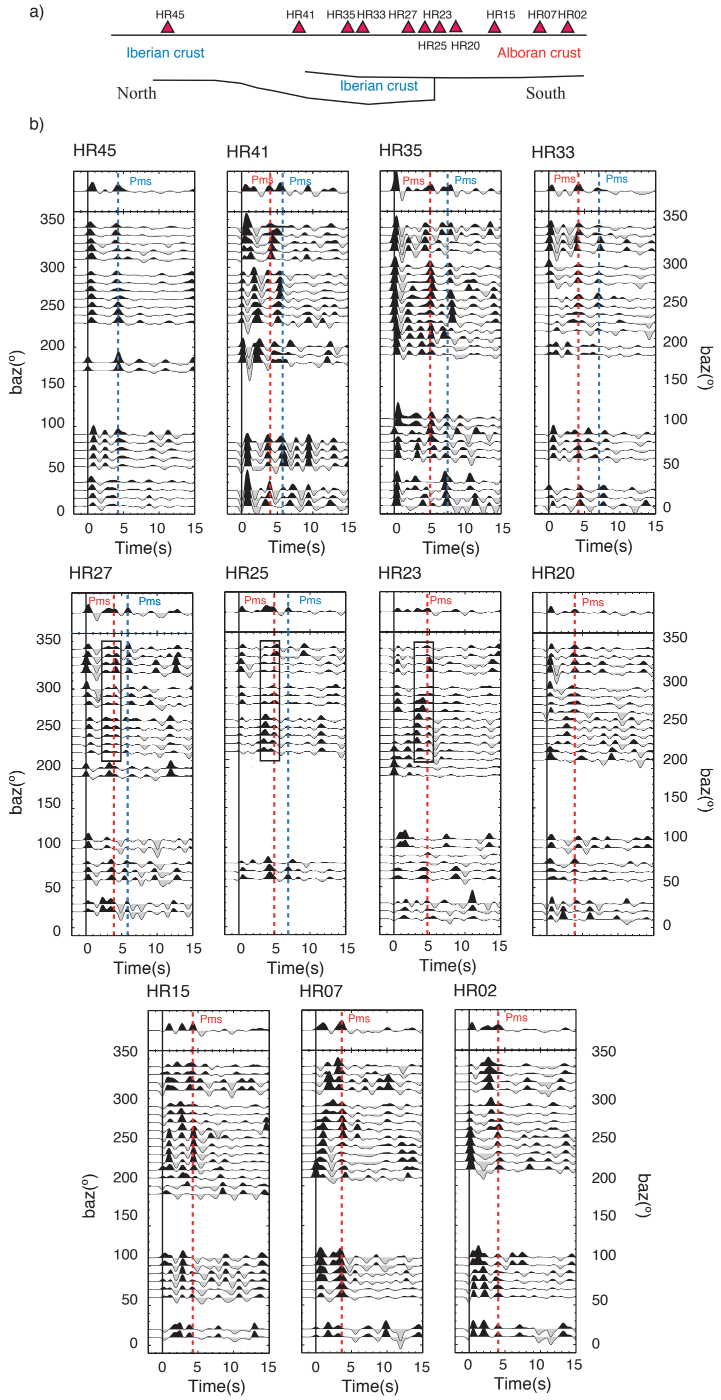

FIGURE 5.2: a) Location of the stations shown in b) along the profile with a simplified crustal structure obtained from the migration image of fig. 5.9. b) Q component RFs for some representative stations stacked by backazimuth (bins of 10° with an overlap of 5°). Q component summation trace displayed on the top. Traces are Ps moveout corrected prior stacking. Dashed red and blue lines mark the arrival times for the converted phase (Pms) at the Moho discontinuity for the Alboran and Iberian domains, respectively.

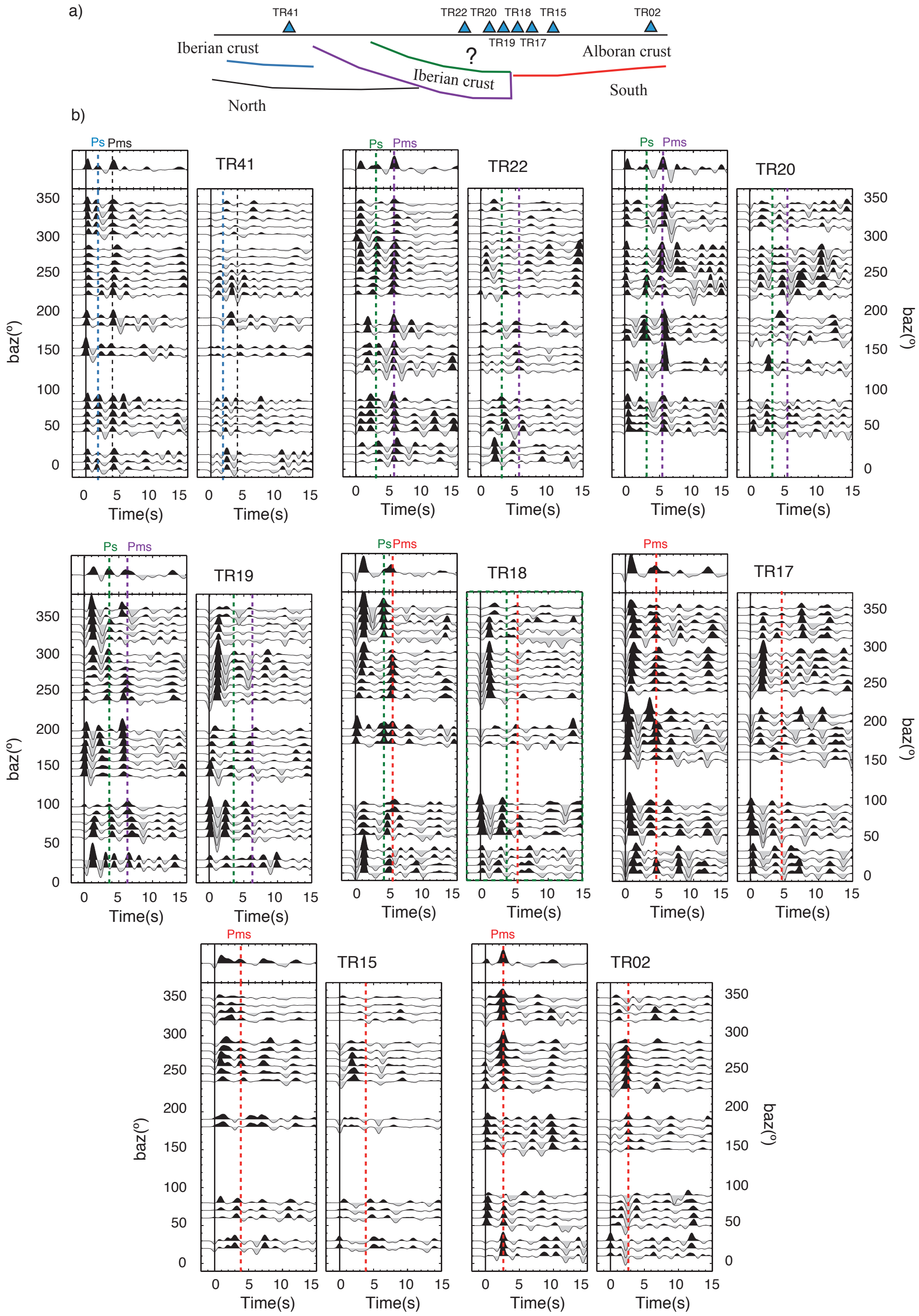

FIGURE 5.3: The same as Fig. 5.2 for the Transcorbe profile. Now the simplified crustal structure below them has been obtained from the migration image of Fig. 5.10. In this case we include the transverse component (right panels) of the PRFs.

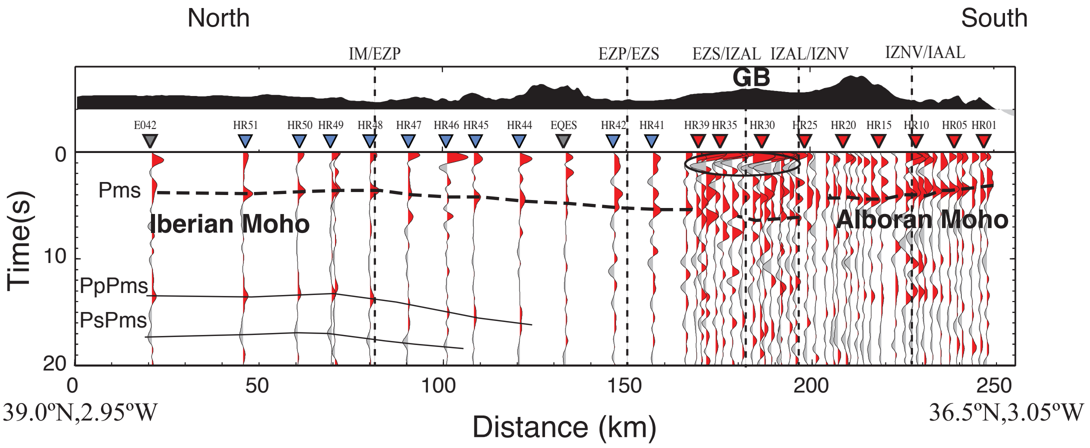

FIGURE 5.4: Summation traces of the RFs for all the stations along the Hire profile. All the traces have been corrected for Ps-moveout prior to stacking. At the top of the figure, we display the topography along the profile. The horizontal dashed black lines mark the converted phase at the Moho discontinuity (Pms) and the continuous black lines the arrival time of the multiples phases from the Moho. The vertical dashed lines mark the limit between different geologic units at surface (IM: Iberian massif; EZP: External Zones Prebetics; EZS: External Zones Subbetics; IZAL: Internal Zones Alpujárride; IZNV: Internal Zones Nevado-Filábride). The black circle labeled with GB at the top of the topography encloses the multiples related with the sedimentary cover of the Guadix Basin. The inset map shows the locations of the earthquakes used in the RFs analysis. The red stars are the ones recorded by the Hire-I stations and blue stars by the Hire-II stations.

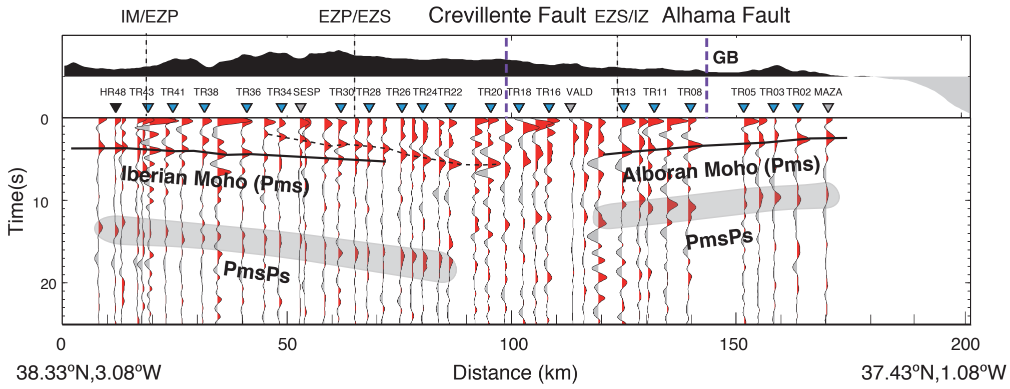

FIGURE 5.5: The same as Fig. 5.4 for the Transcorbe profile. The black lines mark the converted phase at the Moho discontinuity (Pms), the dashed line marks an intracrustal discontinuity and the grey-shadow areas enclose the arrival time of the multiples reverberated phases from the Moho. Geologic units acronyms are explicit in Fig. 5.4. GB denotes the location of the Guadalentín Basin.

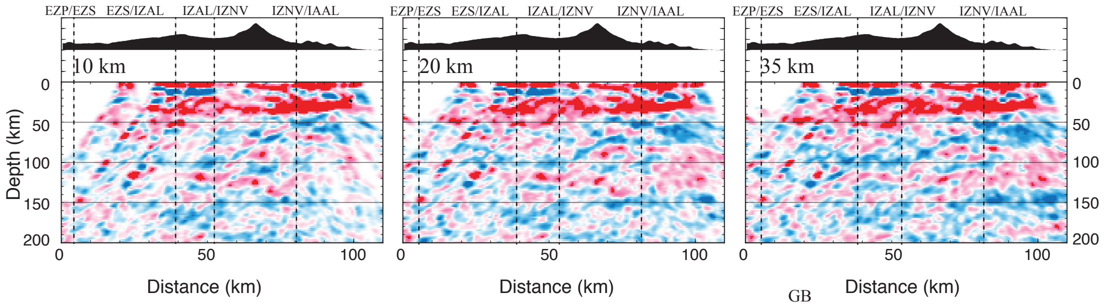

FIGURE 5.6: CCP stacking cross-sections for the Hire-I seismograph (red triangles in Fig. 5.1) using different swaths at both side of the profile (10, 20 and 35 km from left to right). At the top of the figures, we display the topography along the profile. In these images, red color (positive amplitudes) in a seismic discontinuity means a velocity increase with depth.

5.2 Results

5.2.1 Hire profile

Four stations, located in the Guadix-Baza basin (GB in Fig. 5.4), are excluded from the analysis. Strong reverberations from the sedimentary cover that these stations exhibit hide the conversion phase from the Moho discontinuity and other intracrustal structures.

The summation traces plotted in Fig. 5.4 along the Hire profile in a near NS direction, show variations in the Pms arrival time (black-dashed line in Fig. 5.4). In the southern side of the profile, RFs represent the response of the crustal structure underneath the Alboran domain near the Mediterranean coast. Stations HR01-HR03 show the earliest arrival of the Pms phase at ∼3 s, corresponding to a crustal thickness of ∼25 km. Towards the north, the arrival time of the Pms phase (and therefore, the crustal thickness) increases gently to ∼4.5 s (∼35 km) underneath stations HR17-HR18 located at the highest altitude along the profile. Farther north, the arrival time decreases to ∼3.9 s (∼30 km) and remains constant from station HR21 to HR24. Between stations HR25 and HR42, our data suggests the presence of two Moho phases, one pulse at

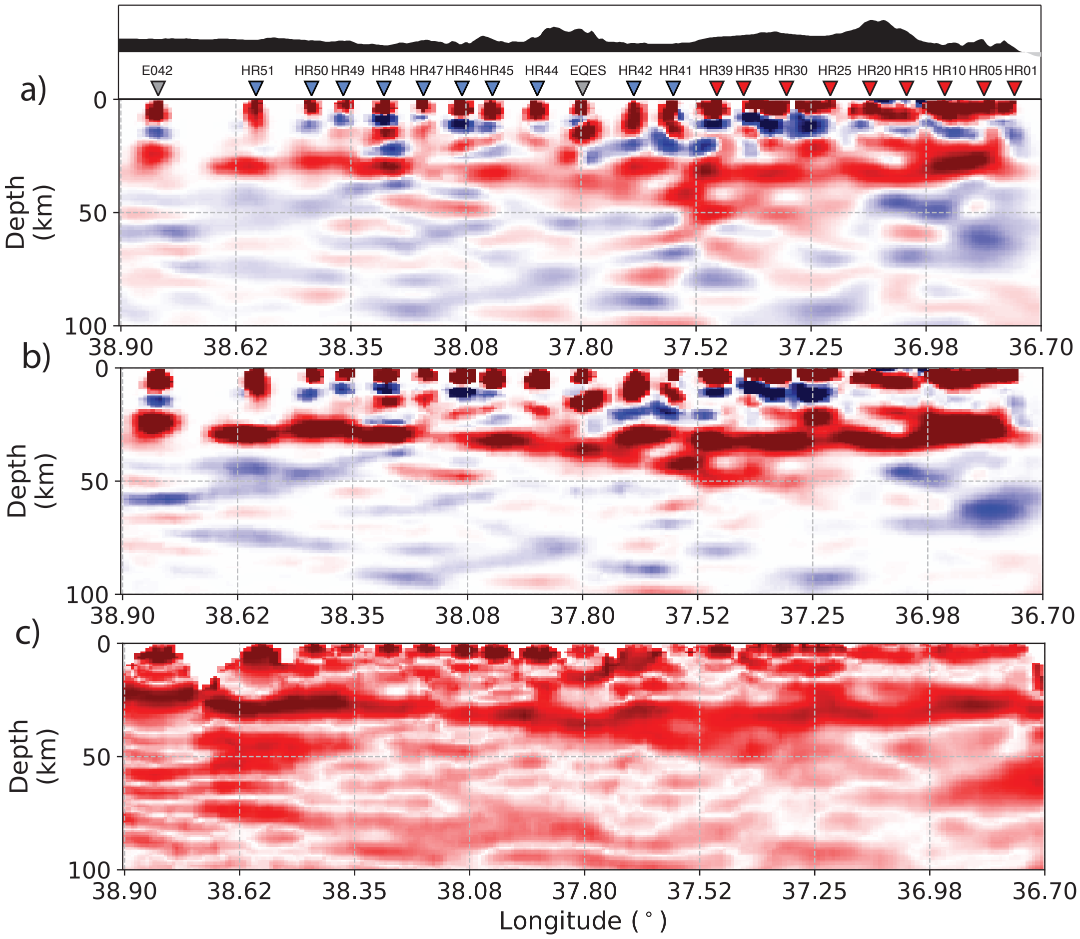

FIGURE 5.7: Comparison of migrated PRFs (a) without and (b) with phase-weighting along the Hire profile including stations located within a half-width of 20 km at both sides of the profile. c) Displays the weight-phase factor. The topography along the profile is displayed on the top.

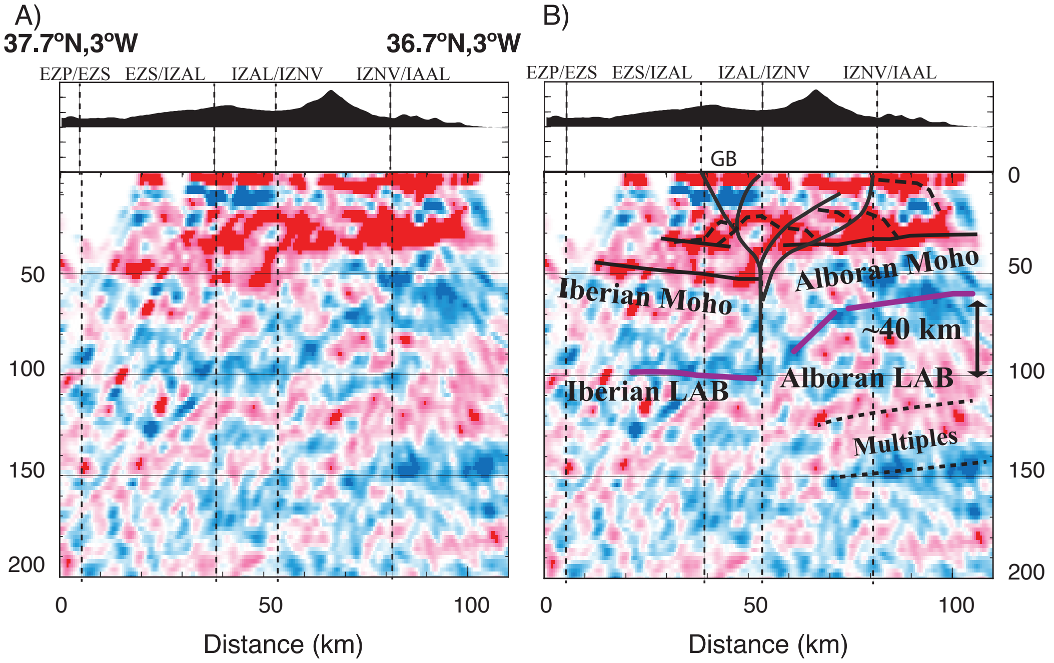

FIGURE 5.8: A) Migration images built with RFs from the Hire-I stations and neighboring stations located within a distance of 10 km from the profile at 3° W of longitude. Topography along the profile is shown at top of each panel. In these images, positive amplitudes (red color) represent seismic discontinuities with velocity increase with depth, while negative amplitudes (blue) represent velocity decrease. B) Same as (A) but including interpretations lines of tectonic character. Continuous black lines mark the Moho discontinuity and positive flower structure faults; the LAB discontinuity is marked with magenta lines, and intracrustal structures with dashed black lines. We show the inferred positive flower-fault structure that propagates the tear fault toward the surface. GB marks the location of the Guadix-Baza basin. The vertical/horizontal scale is 1 to 2.

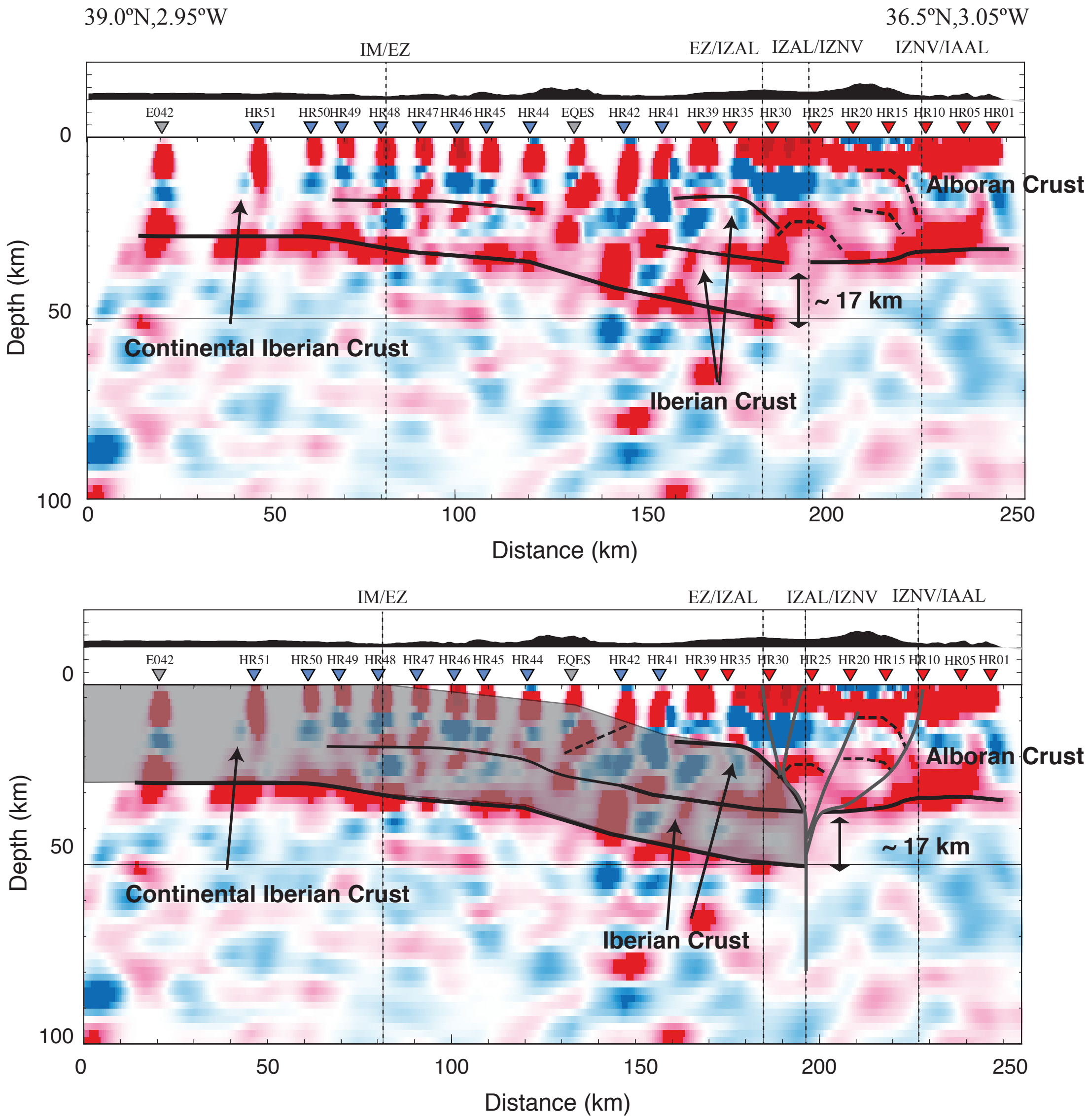

FIGURE 5.9: Migrated PRFs along the Hire profile including stations located within a half-width of 20 km at both sides of the profile. The topography along the profile is displayed on the top. In the RF images, red color (positive amplitude) denotes a seismic discontinuity with a velocity increase with depth. The dashed black lines mark the inferred conversion depth of the Ps converted phase at different intra-crustal discontinuities with dome-shape. With continuous lines, we delineate the bottom of the crust (black color, the Moho discontinuity) and other flat intracrustal discontinuities, and gray color the inferred positive flower-fault structure with the vertical STEP fault (bottom panel). The transparent-gray shade marks the Iberian Massif block.

approximately the same time of the Pms from the closest southern stations (∼3.9 s) and the other pulse arriving later at ∼5.5-7 s (implying a crustal thickness of ∼46-48 km). North of station HR42, RFs present a simple crust and resemble the ones obtained beneath stations in the Iberian massif (Mancilla et al., 2015a). At the northern edge of the profiles the arrival time of the Pms phases is ∼3.7-3.9 (∼30-32 km of crustal thickness). The arrival times and the inferred crustal thickness along the profile correlate well with results obtained by previous seismic studies and the Bouguer anomaly map (e.g. Mancilla et al., 2015a, Mancilla et al., 2015b).

The same pattern in crustal thickness is observed in the migration images (Fig. 5.8 and 5.9). The deepest positive conversion (continuous black line) represents the base of the crust (Moho discontinuity). The stations located in the Iberian massif present a similar crustal thickness of 30-32 km (Fig. 5.9). Different geophysical techniques carried out at the Iberian-Variscan crust confirm a Moho discontinuity at ∼31 km steadily detected throughout the southern Iberia foreland (e.g., Banda et al., 1983, Palomeras et al., 2009, Thurner et al., 2014, Mancilla et al., 2015b, Mancilla, Diaz, and Team, 2015). The structure of the Iberian crust remains homogeneous from the northern side of the profile until the middle of the External Zones (under station EQES, Fig. 5.9) where we clearly observe a stacking of crustal layers (Alborán at the top and Iberian crust at the bottom) producing an increase in the crustal thickness to a maximum of ∼46-48 km. We interpret the double phase as the stacking of the crust resulted from the continental collision where the Iberian crust underthrusts the Alborán crust (Fig. 5.9). The continuous increase of the crustal thickness from ∼30 km under the Iberian Massif in the north to ∼46-48 km underneath the External Zones (∼17 km of increase) occurs within a distance of ∼60 km along the profile. The crustal stacking ends very sharply below the contact at the surface between the Alpujárride and the Nevado-Filábride units (Internal zones, Figs. 5.8 and 5.9). The area with the thickest crust is below the Altiplano of the Guadix-Baza basin with an average altitude of ∼1000 m but not below the highest topography along the profile (∼2100 m, Sierra Nevada Mountain). This maximum crustal thickness coincides with a minimum in the Bouguer anomaly (∼120-150 mGal, Bureau Gravimétrique International).

Towards the south, in the area where the density of seismic station increases, the observed step in the Moho discontinuity (∼17 km) occurs in a short distance along the profile, less than 3 km (Fig. 5.8), approximately under the contact between the Nevado-Filábride and the Alpujárride units (Internal Zones). Schulte-Pelkum and Ben-Zion, 2012 show that observed velocity contrasts in the crust across large continental strike-slip faults are sufficient to produce artificial vertical Moho offsets of >5 km. From seismic refraction profile and gravity data in the area no strong velocity contrasts are found between the Iberian crust and Alborán crust (Banda et al., 1993) apart from the presence of the Guadix basin in the northern side of the STEP fault (Fig. 5.8). The thickness of the sedimentary cover in the influence area for our profile is less than 1000 m in its thickest part (Sanz de Galdeano et al., 2007). Even though this contrast could bias the size of the Moho step, the error is less than 4 km (Schulte-Pelkum and Ben-Zion, 2012).

This step at crustal level correlates with a step of ∼40 km at lithospheric level (magenta lines at the bottom panels in Fig. 5.8). In Fig. 5.8, we can observe a negative converted phase below the Moho at a depth of ∼100 km in the north (at distance of 20-50 km), which shallows to a depth of ∼60 km until the southern end of the profile (at distance of 100 km). We interpret this negative phase as the LAB. In general, the conversion phase at the LAB, for average lithospheric thickness, is difficult to detect in P-wave RFs analysis because it is often interfered by crustal multiples. In our case, the crustal multiples arrive later than the LAB phase arrival, which enables the identification of the LAB discontinuity (Fig. 5.8). Following the profile from north to south the LAB depth increases from 85-90 km to 100 km depth underneath the Moho discontinuity jump and suddenly decreases to ∼60 km in the south (Fig. 5.8). Similar values are obtained in previous studies in the area using P-wave RFs (Mancilla et al., 2015a), S RFs (Dündar et al., 2011, Heit et al., 2017) and surface wave tomography (Palomeras et al., 2014, Palomeras et al., 2017).

The anomalies in the crust and mantle lithosphere are vertically correlated (Fig. 5.8). The STEP fault is almost vertical from the LAB discontinuity (at ∼100 km depth) through the Moho discontinuity (at 48 km depth in the northern side) until reaching ∼30 km depth. The vertical aspect is inferred by the observed Moho step with a jump of ∼17 km between stations separated less than 5 km (between stations HR27 and HR25, Fig. 5.2). The spacing between stations (∼2 km) allows mapping with high accuracy the variations of the crustal structure in short distance. Therefore, the lithospheric mantle and the underthrusting Iberian crust are cut almost vertically. Above the lithospheric step, from 30 km depth to the surface, and mostly at its left side intra-crustal structures with dome shapes (marked by dashed lines in Fig. 5.8 and 5.9) that resemble positive flower structures observed in seismic reflection profiles. We draw the possible segments of the flower structure along the changes in the continuation of the discontinuities and we connect them to the geologic boundaries at the surface.

Positive flower structures are present in transpressional settings (e.g., Park, 1988, Kearey, Klepeis, and Vine, 2009) such as the central Betics region (e.g., De Galdeano, Rodriguez-Fernandez, and Lopez-Garrido, 1985). In central Betics the compression component came from the oblique collision between Iberia and Nubia in a current WNW-ESE direction (e.g., Nocquet and Calais, 2003, Stich et al., 2006, Serpelloni et al., 2007). The trasncurrent movement needed to produce the positive flower structure came from the rollback process directed toward the west (e.g., Lonergan and White, 1997).

The inferred positive flower structure seems to extend for 60 km along the profile and 30 km in the vertical direction cutting mainly the Alboran crust. The presumed fault segments of the positive flower fault structure correlate well, in its southern part, with the observed faults of the Alpujarran Corridor (De Galdeano, Rodriguez-Fernandez, and Lopez-Garrido, 1985). In the northern part, the surface expressions of the flower structure are included in a narrow deformation zone between the External (Iberian paleomargin units) and

Internal Zones (Alborán Domain) of the Betic Cordillera (e.g., De Smet, 1984, De Galdeano, Rodriguez-Fernandez, and Lopez-Garrido, 1985) (Fig. 5.8 and 5.9). This ENE-SSW zone is characterized by sub-vertical faults, with an important right-lateral component of movement, separating pluri-kilometer lense-shape domains belonging to the Iberian paleomargin units or Alpujárride units (Alborán domain). This strike-slip deformation zone, also called External Internal Shear Zone (EISZ), is the southwestern spatial continuation of the Crevillente fault (e.g., De Galdeano, Rodriguez-Fernandez, and Lopez-Garrido, 1985, Nieto and Rey, 2004), and can be mapped to the northern boundary of Sierra Harana where transpressive structures have been classically defined (e.g. De Galdeano, Rodriguez-Fernandez, and Lopez-Garrido, 1985). Thus, the outcrop of the Nevado-Filábride complex in the Sierra Nevada mountains would be the central part of this flower structure bounded by these two major right-lateral strike-slip shear bands (Alpujarran Corridor to the south and EISZ to the north). This strike-slip fault system started developing in the Middle Miocene and presents remarkable tectonic deformation and uplifting since the Late Miocene (e.g., De Galdeano, Rodriguez-Fernandez, and Lopez-Garrido, 1985, Martínez-Martínez et al., 2006). The dextral strike-slip Socovos Fault in the central Betics may represent one of the surface expressions of this process. The $^{40}Ar/^{39}Ar$ analysis of the lamproites melts channelized along the Socovos Fault shows an age of 9.3-7.1 Ma, which are compatible with a right-lateral lithosphere tearing in the Miocene (Pérez-Valera et al., 2013).

STEP faults can be expressed by shear zones in the crust and mantle lithosphere, associated to the tearing process at depth. However, it is not clear, how the strain and deformation are distributed in the overriding plate and if there is regional difference in the sharpness of the shear zone. Large shear zones at the surface of the overriding plate associated with STEP faults have been observed in other regions with average width in the order of 40-60 km: e.g. The Pliny-Strabo shear zone (Özbakır et al., 2013); and the Ionian fault system in the Messina Strait, (e.g. Bianchi et al., 2016). The width is similar to the one we observe in this study. Özbakır et al., 2013 argue that such a width is because its immaturity evolving towards a more localized strain onto a most localize single fault. However, the sharp crustal step observed here and the tectonic flower structure observed implies a more localized shear strain distribution at crustal level, that marks the termination of the underthrusting of the Iberian Massif crust beneath the Alborán crust.

In the collision between the Iberian and Alboran domains the highest deformation is found in the Alborán crust. In contrast, the Iberian crust maintains its structure unperturbed, as suggested by the continuity in its internal structure until the collisional front. The dome structures observed by field works in Sierra Nevada, Sierra de los Filabres and Sierra Alhamilla Mountains in the Internal Zones were proposed to be crustal-scale feature (e.g. Martínez-Martínez, Soto, and Balanyá, 2002). In Fig. 5.8, similar dome structures have been imaged in the Alborán crust (Internal Zones) confirming that hypothesis. The lateral extension of shallowest one is coincident with the Nevado-Filabride outcrop in that part of the Sierra Nevada Mountains (Martínez-Martínez, Soto, and Balanyá, 2002).

Our interpretation is that a lithospheric step was produced by a STEP fault that disconnects the transitional crust of the Iberian paleomargin from the oceanic slab imaged under the Alborán Sea. This fault represents the lateral removal of the underthrusted Iberian lithosphere along the northern edge of the westernmost Mediterranean subduction system. The tearing of the Iberian lithosphere along this fault presumably occurred as a consequence of the reduction in the roll-back velocity at the northern edge of the subduction system when the southern Iberian continental margin started to be subducted, compared with the roll-back velocity below the Alborán basin where oceanic lithosphere were consuming (e.g. Duggen et al., 2004, Duggen et al., 2005). The expected consequence of this change in velocity along the strike of the subduction system is the tear of the oceanic lithosphere from the continental-transitional lithosphere along sub-vertical tear faults called STEP fault (Govers and Wortel, 2005). This type of fault is present or thought to be present at the edges of many subduction systems as Calabria and Hellenic arc in the Mediterranean Sea (e.g. Govers and Wortel, 2005, Gallais, Graindorge, and Gutscher, 2014).

In general, the STEP faults develop, mainly, along continent-oceanic boundaries of the same lithospheric plate, e.g., along South the American-Caribbean plate boundary, in the Calabria arc, in western Algeria margin (Clark et al., 2008, Gallais, Graindorge, and Gutscher, 2014, Badji et al., 2015), but sometimes in purely oceanic domains, e.g., in South Sandwich trench and Tonga subduction zone (Govers and Wortel, 2005). However, we observe that in central Betics, the tearing seems to occur at the transitional lithosphere instead of at the boundary between the continental-oceanic lithosphere as expected (Govers and Wortel, 2005). The thickness of the removed underthrusted Iberian crust is ∼17-20 (Fig. 5.9). The structure of the Iberian crust remains constant from the northern side of the profile until the contact with the External Zone. This continuity and the thickness of the removed Iberian crust imply a transitional character. That could mean that tearing of this transitional lithosphere probably occurred along inherited weaknesses of the pre-rifted continental paleomargin (García-Hernández et al., 1980).

In the central Betics, the surface expression of the inferred STEP fault is marked by regional uplift, denudation of high-pressure rocks in elongated core-complex type domes (e.g., Sierra Nevada Mountains), late Miocene volcanism at Eastern Betics, and by large ENE-WSW strike-slip transfer faults (e.g. Platt et al., 2006, Platt et al., 2013).

Another important result from the migration images is the absence of correlation among the highest altitude along the profile and the biggest crustal and lithospheric thicknesses (Fig. 5.8 and 5.9). The coincidence of the highest topography with the positive flower structure suggests that at least part of this topography is produced by the compressive structure. However, this structure could not be enough to explain a mean uplift of 0.5 mm/y during last 8 Ma (Azañón et al., 2015). The lithospheric removal should promote a complementary asthenospheric push up to this area. In western Betics, Heit et al., 2017 found that the highest topography of Sierra Nevada Mountain correlates well with a possible asthenospheric influx due to ongoing delamination, at the position where they detected a jump in the depth of the LAB discontinuity.

5.2.2 Transcorbe profile

The high resolution defined by the short distances between seismic stations permits us to identify and delineate a coherent positive pulse due to Ps conversion phase at the Moho discontinuity (Pms) along most of the profile (continuous black line in Fig. 5.10). Furthermore, it is possible to define several sectors where the complexity in the RFs reflects conspicuously changes in the crustal architecture. In the NW sector of the summation trace profile (Fig. 5.5) we appreciate a positive Pms pulse at ∼4 s (Ib-Pms, corresponding of a ∼32 km Moho depth) that can be followed as a continuous and flat trend until reaching the stations TR27-TR28 where the Moho interface bumps abruptly with another positive Ps converted phase (dashed black line in Fig. 5.5). We identify the Ib-Pms phase in this sector with the crust-upper mantle discontinuity under the Iberian domain. The inferred Moho depth correlates well with the depth of the Variscan crust-mantle transition found in another Geophysical studies (Mancilla et al., 2015a). In this northwestern sector, the first multiple (Ppms) appear around ∼13-14 s (grey-shadow area in Fig. 5.5) following a similar tendency than the converted phase.

Another important observed feature is a coherent Pms pulse (De-Pms, dashed black line in Fig. 5.5) that relieves the Ib-Pms phase observed in the northwestern sector (continuous black line) showing up under TR27-28 stations. This De-Pms phase appears as an intracrustal conversion phase from the TR27-28 until TR35 station (with arrival time of 2 s). The De-Pms phase continues towards the southeast with a deepening tendency until reaching arrival times of ∼5.5-6

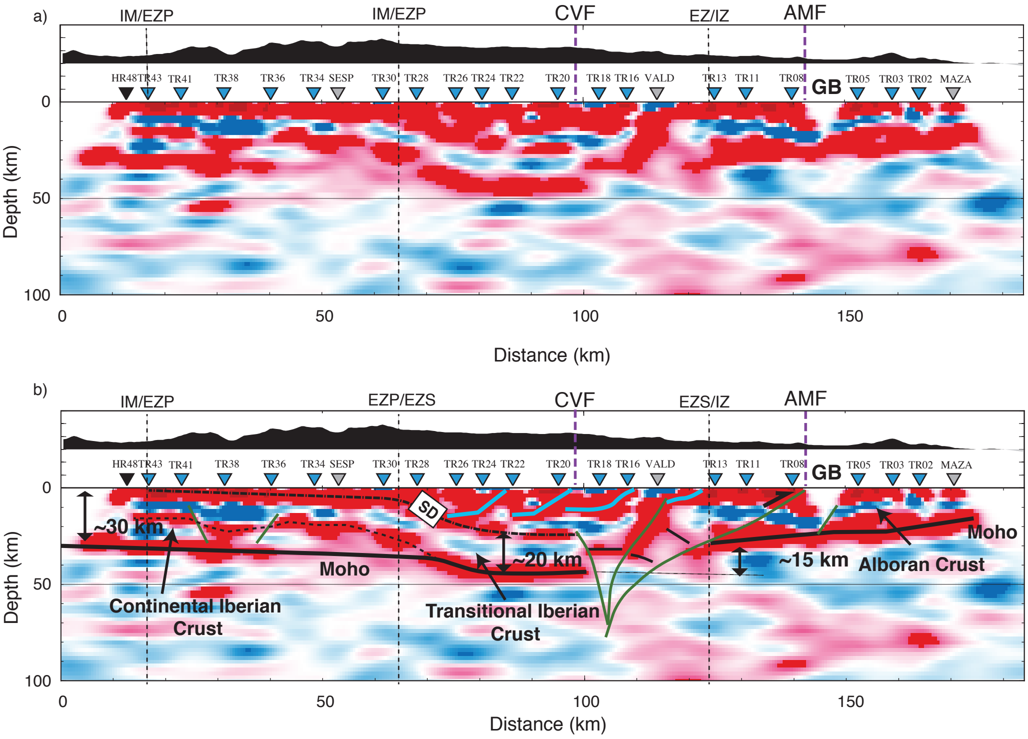

FIGURE 5.10: Migrated PRFs traces along the Transcorbe profile including stations located within a half-width of 20 km at both sides of the profile. The topography along the profile is displayed on the top. In the RF images, red color (positive amplitude) denotes a seismic discontinuity with a velocity increase with depth. The dashed black lines mark the inferred conversion depth of the Ps converted phase at different intra-crustal discontinuities. With continuous black lines, we delineate the bottom of the crust (the Moho discontinuity) and with green color the inferred faults. GB marks the location of the Guadalentin Basin. The vertical to horizontal scale is 1 to 2.

s (∼42-45 km) after the direct P below TR18 station (still Iberian domain) just before its signal is drastically cut (Fig. 5.5).

In the sector between TR18 and TR13 stations, the summation traces are more complex (Fig. 5.5) being difficult to identify a clear and continuous coherent Pms phase. This region coincides at the surface with the presence of the Crevillente fault and with the transition between the External (EZ) and Internal zones (IZ) (Banks and Warburton, 1991, Platt and Houseman, 2003, Nieto and Rey, 2004, Meijninger and Vissers, 2006, Jabaloy-Sánchez, Fernández-Fernández, and González-Lodeiro, 2007). From TR13 station towards the south of the profile we recognize a clear Pms phase around 4 s (Al-Pms, corresponding to a ∼30 km Moho depth), which we attribute to the crust-mantle discontinuity belonging to the Alboran domain. This Moho converted phase becomes shallower toward the coastline reaching the shortest arrival time of 2 s (∼20 km of Moho depth).

Fig. 5.10 displays the CCP stacking cross-section for the Transcorbe transect. We observe the lateral continuation of the discontinuities along the profile and interpret them in Fig. 5.10b. At depths <50 km, we can identify a series of positive converted phases. We interpret the deepest one, at depths ranging from 20 to 45 km, as the base of the crust. The crustal structure and tectonic features observed along the cross-section are heterogeneous. As in the case of the Hire profile, we divide them into three main sectors for the discussion (Fig. 5.10).

At the NW sector, the Moho interface reveals a sharp positive interface at a 30-32 km depth, with almost flat topography until reaching approximately the TR30 station (black line in figure 5.10b). As in the northern region of Hire, we associate this Moho, which seems not to be deformed by the collision, with the Variscan crust-upper mantle discontinuity.

In the middle sector, we observe a strong positive converted phase (De-Pms) which starting beneath the TR30 station and dipping to the southeast replaces the Iberian converted phase (Ib-Pms). Notice that the same pattern was also observed in the 2D cross-section of the summation traces (Fig. 5.5). We focus with special interest in this southeast-dipping converter interface that can be followed continuously towards NW until it reaches shallow depths below TR35-TR36 stations (Figs 5.5 and 5.10). We interpret this ramp and flat geometry as a intra-crustal discontinuity that separates Iberia upper crust from Iberia lower crust. The SE limit of this positive converter interface is interpreted as the Moho interface that reaches its maximum depth ∼42 km below TR19 station where abruptly its signal disappears. It is interesting to show that the maximum crustal thickness is not associated with topographic highs (1000 m) in this sector. Therefore can not be considered as an orogenic root in a strict sense. In this sector between the stations TR30 and TR19 we also detect at mid crustal depths another strong positive and coherent Ps converter with a similar ramp and flat geometry (marks with SD label). This shallower interface starts from the surface at TR29-TR30 stations, just where the Subbetics units thrust over the Intermediate-Prebetic units as Frontal Subbetic thrust, and reach a maximum depth of 20 km beneath TR19 station. We name this decollement as Subbetic mid-crustal decollement (SD, Fig. 5.10b). The estimated thickness for the crustal segment defined in this sector between SD and the Moho discontinuity is ∼20km. Possibly, this segment defines the southernmost thinned crust of the Iberian paleomargin. The Variscan crust in the NW sector of the profile (∼32 km thick) acts as the rigid and undeformed block in this collisional setting.

Furthermore, other relevant feature of the cross-section is that we do not observe in the Variscan crust clear evidences of Alpine deformation or regional flexure compensation associated with the high-topography of the Cazorla range (around 2 km height).

In the southern end of the Middle sector, the sharp and strong Moho interface is severed by a subvertical structure that delimits the Iberian crust approximately below TR18-19 station (Fig. 5.10). This structure also cuts the transitional crust segment and generates a crustal deformation band that extends from TR18-19 to TR13. This deep structure approximately coincides at surface with the trace of Crevillente fault (Sanz de Galdeano and Carlos, 2008). The most prominent feature of this sector is related with a conspicuous offset of the Moho Ps pulse that below TR20 reaches value ∼42 km, ∼30 km below TR17-18. Therefore, the vertical Moho offset observed is ∼15 km in 20 km of horizontal distance. Below the VALD station an intracrustal Ps pulse can be identified and interpreted as due to a main converter. The deformation pattern observed in the mentioned spatial segment is very complex and there is not enough resolution to determine clearly, at shallow and mid-crust depths, the spatial relationship between the domains involved, the Iberian crust and Alborán crust.

However, in our interpretation small pieces of the Iberian crust might be overriding the SD suggesting that the Iberia paleomargin with its sedimentary cover (External Zones) were involved in underplating tectonics. This phenomenon must be associated to the continental subduction between the thin Iberian paleomargin and the Alboran block and the subsequent break off and tearing of the Iberian margin across a STEP fault, which allowed the exhumation of the continental crust (Duretz et al., 2012; Magni et al., 2017). Therefore, the crustal thickening observed (∼42 km) could be the result of a progressive stacking of the exhumed Variscan thinned basement and its wedge sedimentary cover (Subbetics units).

We also present evidences of a sharp and abrupt termination of the Iberian thinned paleomargin as consequence of a drastically cut by a set of high dip set of faults, which we interpret as clearly associated with the crustal-scale strike slip faults of the Eastern Betic region as the Crevillente Fault (CF) (Sanz de

Galdeano and Carlos, 2008) and the Alhama de Murcia Fault AMF (Martínez-Martínez, Soto, and Balanyá, 2002; Masana et al., 2004). Therefore, we interpret the mentioned deformation pattern observed in the Transcorbe CCP cross-section as the deep and surface expression of the same STEP fault structure observed under Sierra Nevada in the Central Betic region with the Hire profile, being this its prolongation to the northeast (Mancilla et al., 2015b; Mancilla et al., 2018).

We point out the presence, close to the Transcorbe profile, of ultrapotassic magmatism (lamproitic rocks). This magmatism is associated with the Crevillente and Socovos faults (Pérez-Valera et al., 2013), mainly distributed in the contact between the Iberian paleomargin (External zones) and the Alboran domain. This recent volcanism (8-10 My) attributed to a late Miocene lithosphere extension generated after the tearing and break off of the Iberian paleomargin (Booth-Rea et al., 2007; Pérez-Valera et al., 2013), can now after these observations, be linked to the tearing and the ultrapotassic volcanism.

Finally, In the southernmost sector of the profile, the CCP image (Fig. 5.5 and 5.10) shows a progressive thinning of the Alboran crust thickness from TR13 station (∼30 km), where the AMF fault reaches crustal scale, to the shoreline at MAZA station (∼15 km). In this sector the AMF outcrop is near TR08.

Observing the Bouguer anomaly along the Transcorbe profile (Fig. 5.11) (Ayala et al., 2016) we detect the strong relationship between the gravimetric anomaly and the Moho behaviour along the transect. The minimum values of the Bouguer anomaly -73 mGal correlates with the maximum crustal depth reached by the Iberian crust (∼42 km) below TR18-19. This sector, as we mentioned before, is related with the maximum deformation zone detected in the CCP cross-section and where a set of dipping faults associated with the STEP fault completely cut the Iberian paleomargin. The Bouguer anomaly profile is very sensitive to the crustal deformation, changing dramatically its slope

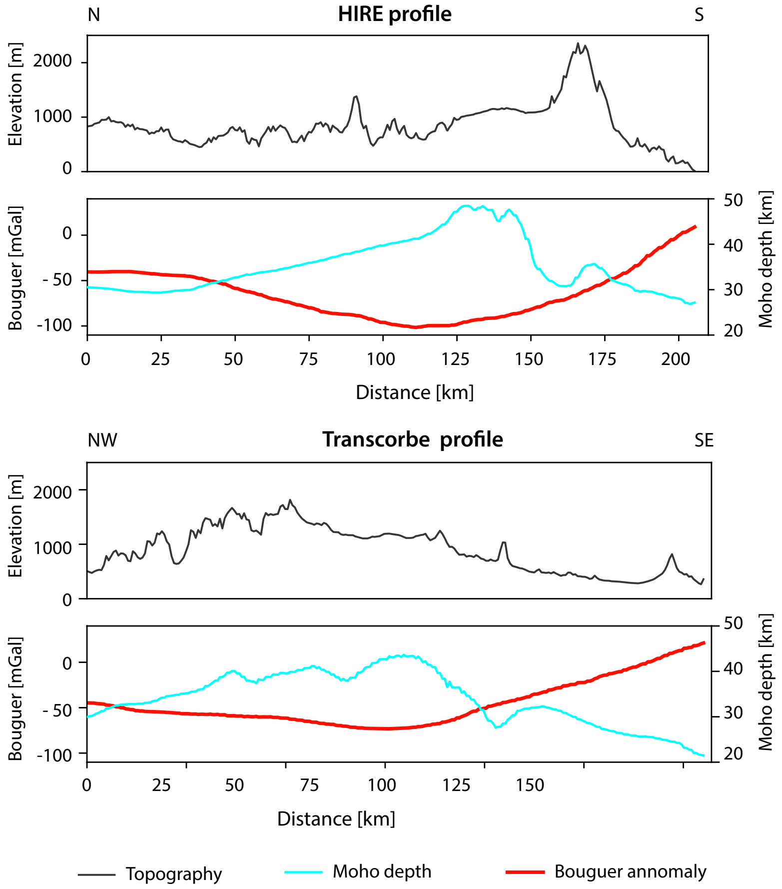

FIGURE 5.11: Comparison among the topography (black lines), Moho depth (blue lines) and Bouguer anomalies (red lines) along the Hire (top panels) and Transcorbe (bottom panels) profiles.

from TR18-20 to the south as a response to the crustal thinning. The Bouguer anomaly reaches positive values (+20 mGal) under the shoreline. In this case the change in the slope of the Bouguer anomaly is associated with the presence of the STEP fault structure. The behavior of the Bouguer anomaly is quite similar to the observed by Mancilla et al., 2018 in Central Betic along the Hire profile. In both cases (Transcorbe and Hire) the maximum depth of the Iberian paleomargin Moho agrees with the minimum values of the Bouguer anomaly and the change in the slope of the gravity anomaly profiles is associated with the presence of the STEP fault deformation zone.

However, unlike the Hire profile (Mancilla et al., 2018) where topography and Bouguer anomaly were clearly anticorrelated suggesting a non-compensation of the highest topography in Iberia (Sierra Nevada Mountain), here in the Transcorbe profile, from the crustal rupture at TR19 the Bouguer anomaly and topography correlates positively.

5.3 Conclusions

We image, by migrating the first high resolution P-RFs profiles, the crustal architecture in two sectors of the Betic orogen (central and eastern) and its transition to the Variscan terrains of the Iberian Massif in the north. We have obtained the first direct images (not inverted) of the crustal architecture in the Betic orogen. From the interpretation of the CCP images (Hire and Transcorbe) we observe as the underthrusted Iberian lithosphere terminates sharply in both profiles following at the surface the External-Internal Zone limit. In the case of the Hire profile this coincides with the contact at the surface between the Alpujarride and the Nevado-Filábride complexes. The crustal-scale strike slip faults of the eastern Betic region as the Crevillente and Alhama de Murcia faults represent the surface expression in the case of Transcorbe transect. This sharp and prominent crustal step ($\sim$15-17 km) observed in both profiles is interpreted as a near-vertical STEP fault that propagates to the surface as a positive flower fault structure. This STEP fault accommodated the differences in the subduction rollback velocity along the strike, at the northern edge of the Western Mediterranean system, when the the thinned Iberian continental lithosphere started subducting under the Alboran domain. We have not observed a crustal root under the highest altitude of both profiles. Especially under Sierra Nevada mountain at the Hire profile, this suggests that its high topography is produced by a combination of the uplift produced by the positive flower structure and the push up of the asthenosphere after the lithospheric removal of the underthrusting Iberia along the STEP fault.

Our results also present how the lithospheric tearing associated with a STEP propagation in a large scale subduction rollback framework can drive to high oblique continental collision which can be accommodated through crustal scale decollements and be a first order mechanism related with the built of fold and thrust belts of the peripheral External Betic Range.

Chapter 6

Reverse Time Migration in the Hire seismograph

Uneven and sparse distribution of stations and events in teleseismic receiver functions have promoted the use of simplified migration approaches such as the common conversion point (CCP) stacking method. This technique is routinely applied in the receiver function (RF) workflow to image crustal and upper mantle discontinuities (e.g., Dueker and Sheehan, 1997, Yuan et al., 1997, Gilbert et al., 2003, Frassetto et al., 2010). Because the CCP method relies on the simplifying assumption that (at least locally) the interface is horizontal, it produces good results for smoothly varying structures (e.g., Zhai and Levander, 2011, Kind et al., 2015). However, in the presence of significant lateral heterogeneity, such as quite inclined and laterally discontinuous interfaces, CCP stacking prevents an accurate imaging and cannot adequately suppress scattering and diffraction artifacts (Sheehan et al., 2000, Rondenay, 2009). More sophisticated seismic migration methods, relying on fewer prior assumptions about the Earth's structures, have been implemented in reflection seismology to remove such artifacts and produce significant improvements in image quality (see Chen, Wen, and Zheng, 2005 for a review of methods). Nowadays, the availability of high-dense seismographs provides the opportunity to apply these advanced migration methods to image deep structures using teleseismic data. Most of the RF migration approaches developed to date are based on ray theory (ray-based Kirchhoff migration) (Chen, Wen, and Zheng, 2005). The ray methods rely on the high frequency approximation of the wave equation and are applicable in sufficiently smooth background models. However, they face problems in the presence of caustics, multiple arrivals and chaotic rays in complex environments (Audebert et al., 1997). Wave equation based methods can avoid these difficulties. These methods exploiting the full complexity of wavefield propagation since they directly solve the wave equation.

Among the wave equation based methods, the Reverse Time Migration (RTM) technique, initially developed in reflection seismology, has been recently applied by Shang, De Hoop, and Van Der Hilst, 2012 for high resolution imaging to map crust and mantle structures using teleseismic array data. This wave equation prestack depth migration technique is based on direct back propagation of elastic waves and circumvents simplifying assumptions such as the locally flat interfaces that form the base of the CCP stacking method. RTM accounts for single scattering processes in wave propagation, including diffraction, reflection and refraction (Brytik, De Hoop, and Hilst, 2012). Subsurface imaging with time reversal techniques typically involves correlations between the adjoint wavefield and a synthetic forward wavefield (Tromp, Tape, and Liu, 2005, Hoop, Hilst, and Shen, 2006, Stich et al., 2009), which is impractical for the teleseismic short period waves that form the base of receiver functions. Instead, vertical and radial components of the waveform section are only once back-propagated into the propagation medium, either with the P-wave or the S-wave speed. Due to the difference in P and S wavespeeds, transmitted and converted wave fronts will reach the same location at the time of phase conversion. This condition yields the conversion point, the location of which is found by integrating for all time steps a cross-correlation function between P and SV wavefields (Brytik, De Hoop, and Hilst, 2012, Shang, De Hoop, and Van Der Hilst, 2012). The back-propagation step is done for each earthquake, in order to ensure the illumination of the structures along the profile and suppress noise, the final image is obtained by summation of the normalized images from individual sources (Shang, De Hoop, and Van Der Hilst, 2012).

The continuous wavefield is often sparsely and irregularly sampled in space for teleseismic observations and this acquisition footprint causes the introduction of significant artifacts in the migration images (Abma, Kelley, and Kaldy, 2007). In order to obtain dense and regular wavefields, seismic traces need to be interpolated from recorded data on sparse and irregular locations using wavefield reconstruction algorithms. Shang, Hoop, and Hilst, 2017 proves with synthetic experiments of RTM that sufficiently dense sampling wavefields are required to perform better results than CCP stacks of traditional receiver functions. This advantage is even more significant in imaging crustal discontinuities in geologically complex regions, such as steep faults and laterally discontinuous interfaces (Shang, De Hoop, and Van Der Hilst, 2012, Shang, Hoop, and Hilst, 2017). Though the RTM method exhibits promising results for synthetic experiments, it does not make a significant difference over the conventional CCP approach when Shang, Hoop, and Hilst, 2017 uses real data to image the structure of the crust beneath the Himalaya. This is probably because sampling is still too sparse for RTM and the structure is simple enough for successful CCP stacking.

To explore the capability of this technique in complex real scenarios with sufficiently high dense seismograph, we apply RTM to the Hire profile. The seismic array is located in a complex geodynamic zone, which exhibits prominent dipping and vertically offset interfaces as it has been shown in chapter 4 using the CCP stacking approach. Better resolution is needed to obtain finer details on how the deformation is distributed together with finer scale variations in the Moho topography. In this chapter, we improve the images of the crustal structure along the profile exploiting the entire wavefield complexity of teleseismic-converted phases through the application of the RTM technique (Shang, De Hoop, and Van Der Hilst, 2012).

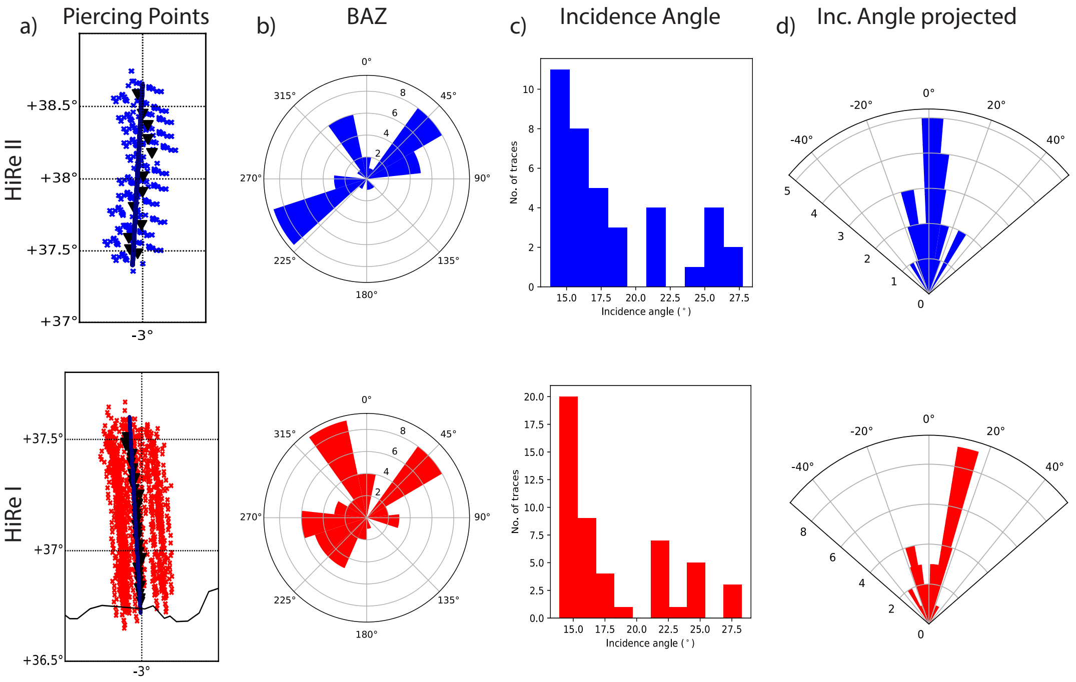

FIGURE 6.1: Dataset parameters employed in this study for each leg of the Hire profile. (a) Map showing the direction of the cross-sections (blue line) and location of stations (black triangles) and piercing points for the P phase at 30 km depth, (b) baz and (c) incidence angle distribution. (d) Ray incidence angle projected onto the profile plane

6.1 Data and Method

6.1.1 Data

We process vertical and radial components from teleseismic seismograms recorded at both profiles, Hire I and Hire II. Because the RTM method requires to backward propagate waveforms associated to each event independently and both profiles were not recording at the same time we must do the analysis separately for each leg (Fig. 6.1).

Earthquakes with magnitude larger than 5.5 in the epicentral distance range between 30º and 95º and with high Signal-to-Noise ratio (SNR > 2) are included. We do not include in our analysis events not recorded by most of the receivers in the profile (70 per cent of the stations), because they do not have high enough receiver sampling and the presence of significant gaps in the acquired data avoids to obtain a good interpolated wavefield. We retain for the last stacking step 50 and 39 events for the profiles Hire I and Hire II, respectively. Figure 6.1 shows the dataset parameters employed in the study for each leg. We have a very dense homogeneously coverage of piercing points at both sides of the profile (6.1a). The incidence ray angle and baz distribution (6.1b and c) guarantee that the wavefronts impinge the target zone from different directions providing a good illumination of the structures (Shang, De Hoop, and Van Der Hilst, 2012). This can be observed in Figure 6.1d which depicts the incidence ray angle projected onto the profile. In the case of Hire I, the incidence is coming mostly from the southern direction of the profile.

6.1.2 Method

We follow the RTM workflow described in Shang, Hoop, and Hilst, 2017: (1) Wavefield regularization: The wavefield interpolation prepares the data for crustal imaging with RTM, reconstructing a uniform sampled wavefield from real data. (2) Green's functions estimation: We need to remove the source effect from the regularized wavefield before backward propagation. This guarantees that all the earthquakes have the same weight in the final stacked image and therefore it is not dominated by large seismic sources. We obtain the Green's functions by deconvolving an estimated source signature from the interpolated radial and vertical wavefields. The common seismograph array source signature for each event is estimated from the real vertical traces by using the Principal Component Analysis (PCA). (3) Reverse Time Migration and stacking for different sources: the free of source wavefields are backward propagated using a finite difference method. The imaging condition consists in the time integral of the cross-correlation between the P and SV wavefields for each earthquake. We obtain the final image by adding the normalized images from individual events.

1. Wavefield regularization

Based on wave-equation migration methods require regular and high density sampling to make the correct constructive and destructive interference from data (Abma, Kelley, and Kaldy, 2007). This acquisition requirement is not typically satisfied for teleseismic data even in high spatial resolution modern array deployments. We have to reconstruct a high and uniform sampled wavefield from real data using interpolation algorithms. For the wavefield reconstruction we choose a signal-processing approach, exploiting the redundancy of the real wavefield this type of methods rely on transforms that compress the data in another domain and do not require information about the subsurface (Naghizadeh and Sacchi, 2010). In seismic data reconstruction, we can see the observed data d as a subset of the desired interpolated data m. It can be expressed mathematically:

$$d = Gm + n \tag{6.1}$$

where G is a sampling operator and n is additive noise (Naghizadeh and Sacchi, 2010). This motivates an inversion problem aimed at estimating m from the observations d. The principle is generally to obtain the correct coefficients in the transform domain from the irregular data and then do the data regularization through the inverse transform. The most commonly used transformations are the Fourier transform, the Radon transform and the curvelet transform (Naghizadeh and Sacchi, 2010). The curvelet transform is a very appropriate approach in seismic interpolation algorithms thanks to the curvelet properties. Curvelets are optimally sparse representations of the seismic data due to its anisotropic, dual-domain localized and oscillatory nature (e.g., Candès et al., 2006, Douma and Hoop, 2007). In our case we do the inversion in the curvelet domain. The curvelet analysis operator C decomposes the desired data m to curvelet coefficients x as $x = Cm$ (m can be recovered using the adjoint operator C^T of the curvelet transform). As in any underdetermined inversion, uneven sampling and the presence of noise introduce errors in the recovered model parameters. To avoid these errors, additional constraints have to be imposed on the problem, a process refereed to as regularization, which involves finding the single model among the infinity of permitted models that minimizes some property of the model. Therefore, to determine the curvelet coefficients x of the desired data we must minimize a cost function:

$$J = \frac{1}{2}||d - GC^T x||_2^2 + \lambda||x||_1 \tag{6.2}$$

where the positive parameter λ is the Lagrange multiplier indicating the trade-off between data misfit and model roughness. We have here a basis pursuit problem (Berg and Friedlander, 2008), aims to find a sparse solution (minimum 1-norm solution) of an underdetermined system of equations. It has been proved that there are equivalent approaches to this optimization problem (Berg and Friedlander, 2008), depending on which term is subject to constraint and which one is optimized. We use the Lasso problem approach, where there is a explicit 1-norm constraint on the curvelet coefficients. Nearly vertical curvelets are not likely true in the seismic data gather (horizontally propagated wave packets in t-x domain). A simple way to mute the vertical curvelets is to add a mask matrix in the curvelet domain (see Shang, 2014 for details), which is convenience for severely undersampled datasets reducing the number of unknowns and improving the data recovery quality. A value for the apparent velocity must be set, we use a not quite restrictive value (4 km/s) because our profiles do not present significant spatial gaps. A larger apparent value can be chosen to squeeze the model space if more prior information about the medium is known.

The interpolation distance is determined by the resolution in terms of the Rayleigh diffraction limit (e.g., $\lambda/4$ where λ is the incident wavelength) and the inter-station distance to avoid spatial aliasing (Shang, De Hoop, and Van Der Hilst, 2012). For a typical teleseismic study with frequencies about 1 Hz, the apparent horizontal wavelength is around 5 km. Considering the sampling theorem, we conclude that a station interval of 2 km should be sufficient. We take this value as a threshold, in order to obtain stable smoothed images with no artifacts there must be a balance between the time and spatial resolution used. Stable smoothed interpolated wavefields are achieved after bandpass filtering the signal between 0.8 and 20 s and using an interpolation distance of 500 m and 1000 m for the profiles Hire I and Hire II, respectively. This implies that missing traces amount to approximately 80 per cent of the total data used as previous studies (Shang, Hoop, and Hilst, 2017). Figure 6.2 depicts the interpolated vertical and radial waveforms for two events corresponding each event to each profile. As we can see there are some latitudes where oscillations traces concentrate consistent with sedimentary basin. Oscillatory behavior is predominately observed on the radial component. We use a time window (-10, 30) s around the P onset to ensure the inclusion of the Moho converted phases (Pms).

2. Green's functions: Estimation of the source signature and deconvolution

   We calculate (Fig. 6.3) the Green's functions deconvolving the common source signature from the vertical and radial interpolated wavefields. For deconvolution, we use the iterative time-domain deconvolution method (see section 3.2.1) (Ligorria and Ammon, 1999) with an approximate pulse width of 1 s ($a = 2.5$). Though the iterative time-domain deconvolution is less efficient than simpler methods such as water-level deconvolution, the estimation of the receiver function is free of complex relationships between the water-level values, time-domain smoothing and damping parameters, and the resulting receiver function (Ligorria and Ammon, 1999).

   The common source signature has been previously estimated for each event using the Principal Component Analysis (PCA) from the vertical component seismograph (Jolliffe, 2004). PCA is a statistical procedure to identify and find patterns in dataset in order to reduce the dimensions of

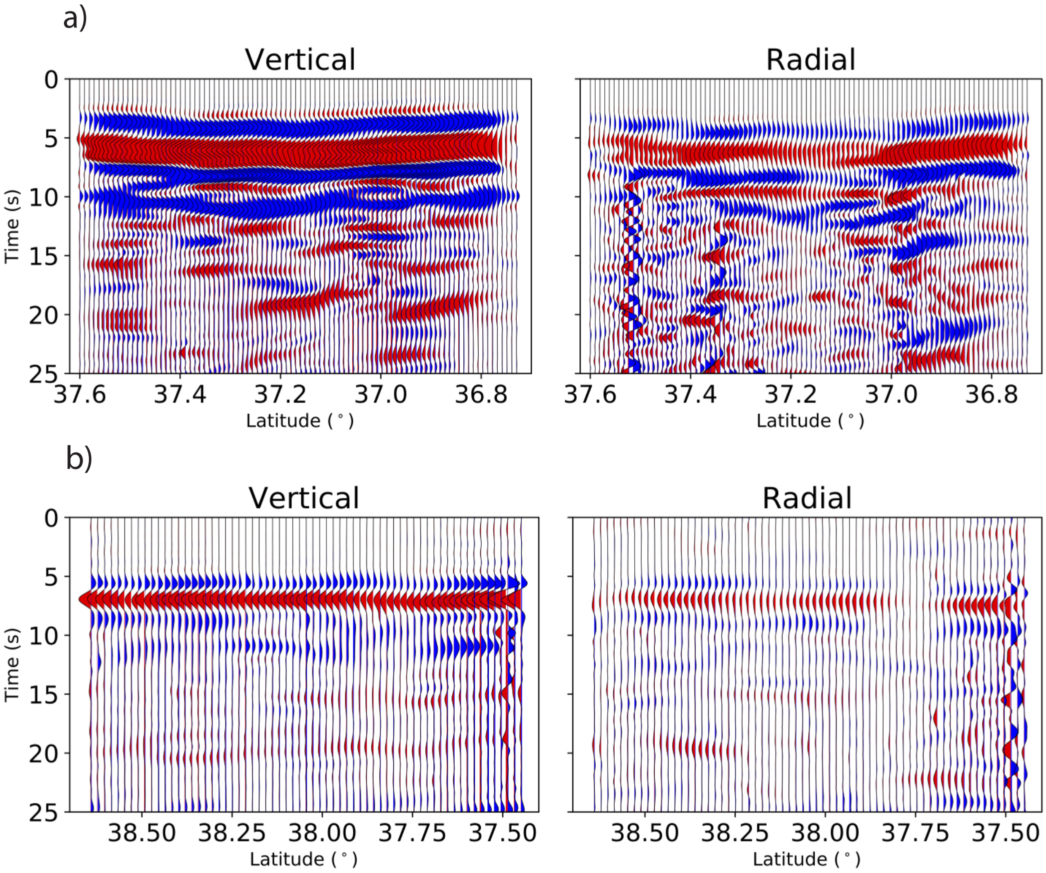

FIGURE 6.2: Examples of the interpolated vertical and radial components at a regular (a) 500 m for an earthquake recorded by the Hire I seismic array and (b) 1000 m grid for an event recorded by the Hire II seismic array

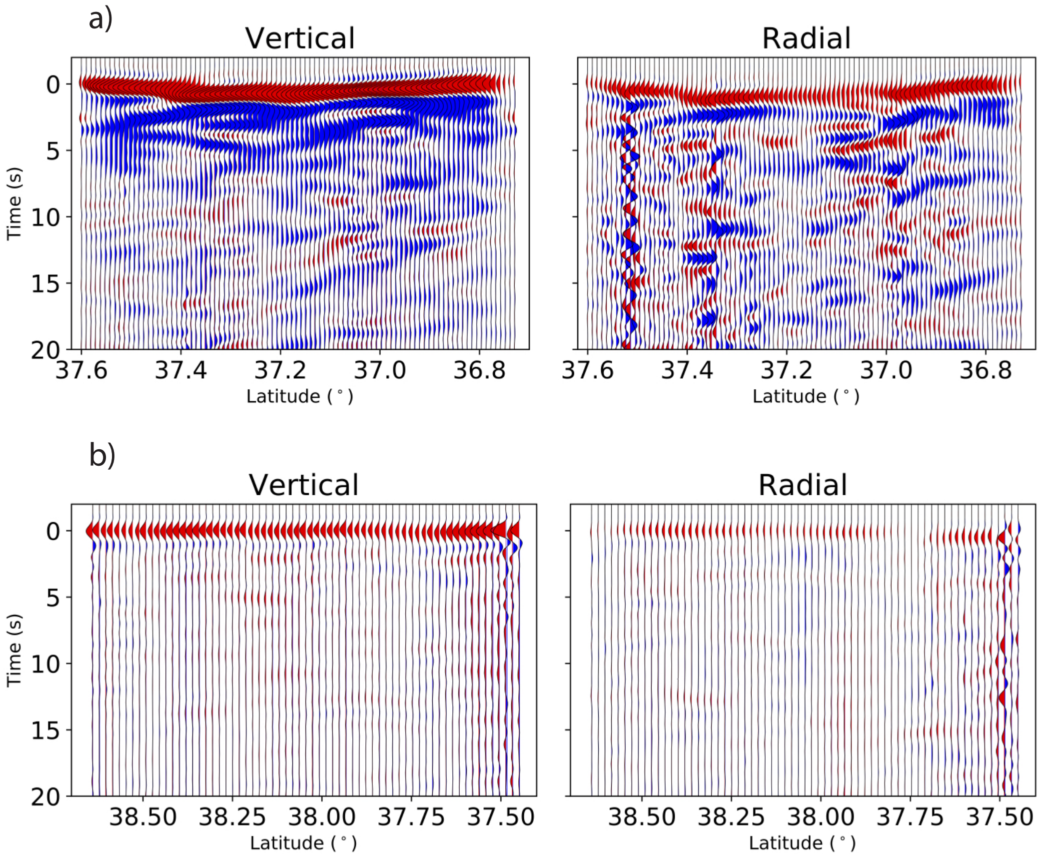

FIGURE 6.3: Interpolated vertical and radial Green's functions after deconvolution for the same events shown in figure 6.2

it with minimal loss of information. The application of PCA in estimating a common source seismic source signature takes advantage of the high degree of redundancy in the vertical component array to determine its statistical behavior and reduce it to essential features. The algorithm consists in a singular value decomposition that decomposes the seismic waveforms into orthogonal components, that is, find the axes with maximum variances where the data is most spread (Yu, Zheng, and Shang, 2017). We just use the first principal component, corresponding to the largest singular value that gives the most coherent feature contained in all the vertical seismograms. Higher-order principal components contain more detailed and stations-dependent information. In order to compute the source signature via PCA vertical traces must be previously aligned with the P onset. We use the Multi-Component Cross Correlation (MCCC) (VanDecar and Crosson, 1990) which is a semi-automated method that simultaneously align a particular seismic phase and determine relative travel times at different stations through multichannel cross-correlation. The cross-correlation may give incorrect time picks when the waveforms are not similar to each other. A data quality control of vertical and radial components is previously done of all the stations for each event in the frequency band (1, 0.03) Hz, noisy and fluctuated seismograms whose waveform differs considerably from surrounding traces are ruled out. Note that this manual selection also helps to estimate appropriately the common source signature with PCA and improve the wavefield interpolation. For MCCC we choose a correlation window of (-10, 10) s around the P onset and a maximum time lag of 10 s. Longer differences of time for the P onset between waveforms are not expected for our teleseismic data set. The PCA and MCCC tools used are included in the Matlab open-source software package Crazyseismic (Yu, Zheng, and Shang, 2017), code designed to process efficiently multichannel large-volume seismic data. Fig. 6.4 shows the vertical traces and the common source signature estimation using PCA after MCCC for the two events selected.

3. Reverse Time Migration and Stacking

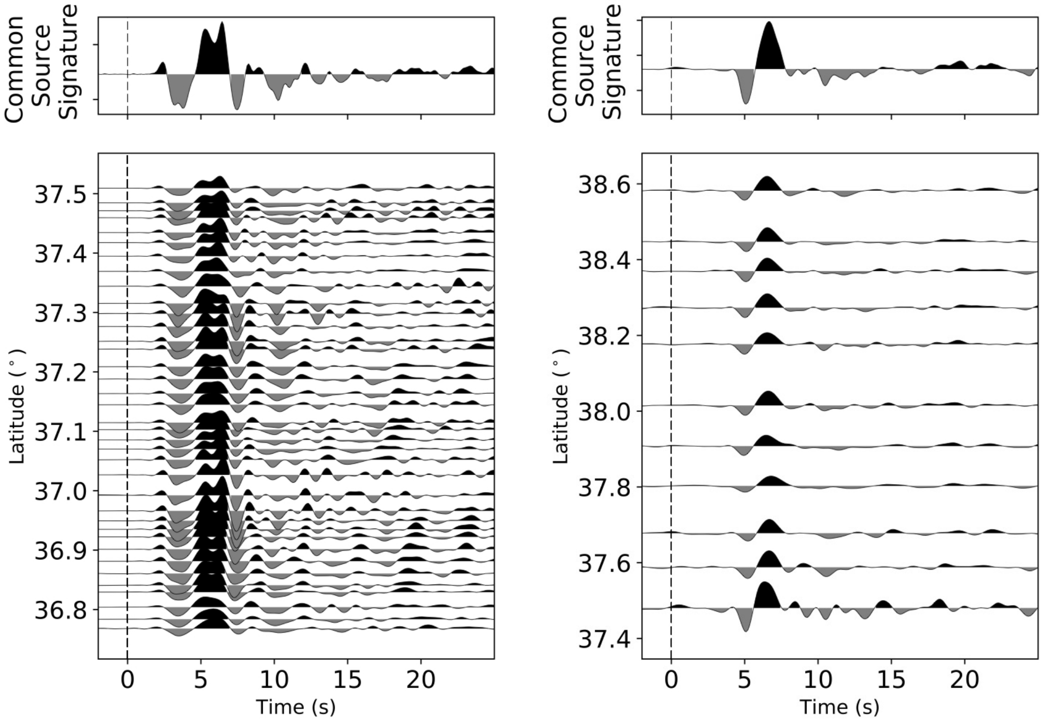

FIGURE 6.4: Common source signature estimation after MCCC using PCA for the two events selected in 6.2

We use reverse time continuation to back propagate the interpolated multicomponent waveform (free of source signature) for each earthquake. The elastic wave equation is solved in the time domain using a staggered grid finite difference propagator (Virieux, 1986). We save computational cost restricting the backward propagation within a numerical domain of 92 x 80 km (along the profile x depth) and 125 x 80 km for the Hire I and Hire II profiles, respectively. We use a propagation time of 52 s to guarantee that the P wavefront reaches the bottom boundary of the numerical domain (Fig. 6.5). We ascertain that enough grid points per wavelength are employed in the simulation in order to avoid numerical dispersion. The maximum frequency that the numerical simulation can resolved (3 Hz) is higher than the frequency content of the signal. The Earth model used to propagate the wavefield is a 1D model with gradual increase in depth of the wave velocity. It is based on an Iberian Peninsula modification of the IASP91 reference velocity model using crustal information from previous refraction profiles (Díaz and Gallart, 2009). The P and S wave velocity increases from 5.80 and 3.36 km/s at the surface up to 8.04 and 4.50 km/s at 80 km depth, respectively. The finite difference method includes computational domain boundaries that will inevitably bring the reflected energy back into the computational domain, and then contaminate the signal. To avoid artificial reflections from computational domain boundaries, the code uses the perfectly matched layer method. The idea is to add layers of absorbing material outside of the numerical domain which attenuate the entering and reflecting back energy. In Fig. 6.5 we observe no significant numerical dispersion and how the perfectly matched layer boundary condition avoid reflections coming back from the boundaries.

Due to the difference in P and S wave speed, the relevant parts of the transmitted and converted wave fronts were in the same location at the time of conversion (strictly correct only in the absence of multiple scattering). This observation is used in developing the basic imaging condition, a time integral modified cross correlation between P and SV wavefields. Polarization decomposition separates P and SV modes for each time step

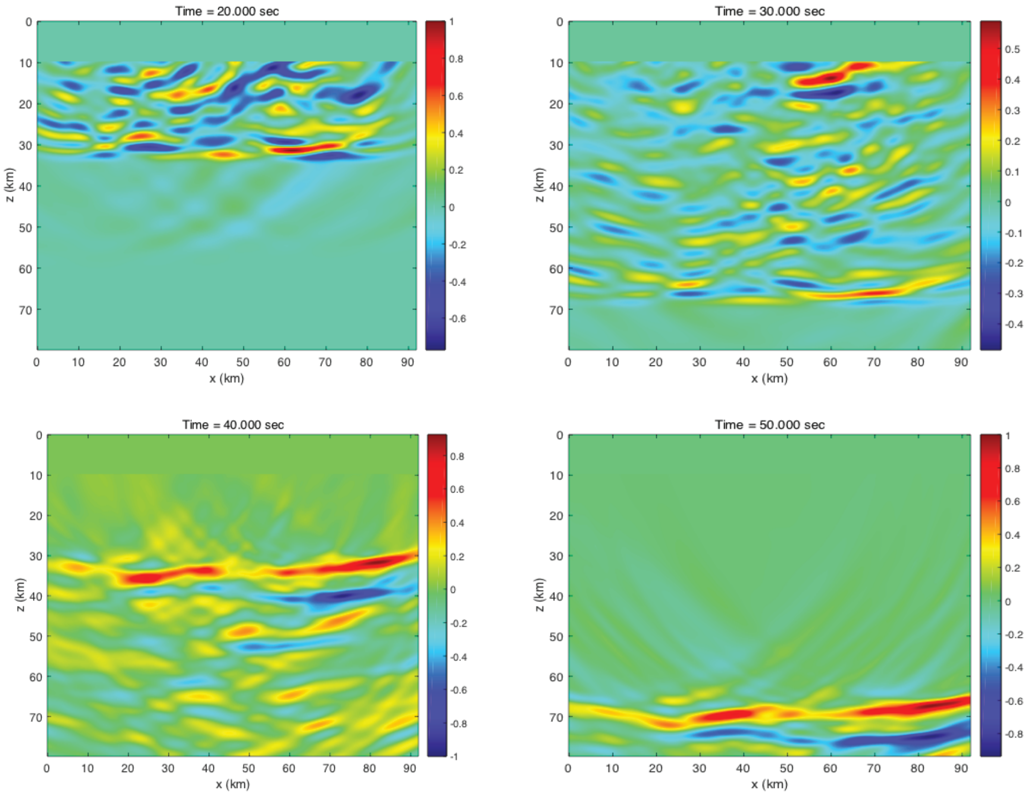

FIGURE 6.5: SV mode backward propagating wavefield at different times for the profile Hire I

(Brytik, De Hoop, and Hilst, 2012, Shang, De Hoop, and Van Der Hilst, 2012). The final image is obtained by summation of the normalized images from individual sources. This ensures the illumination of the structures along the profile and suppress noise.

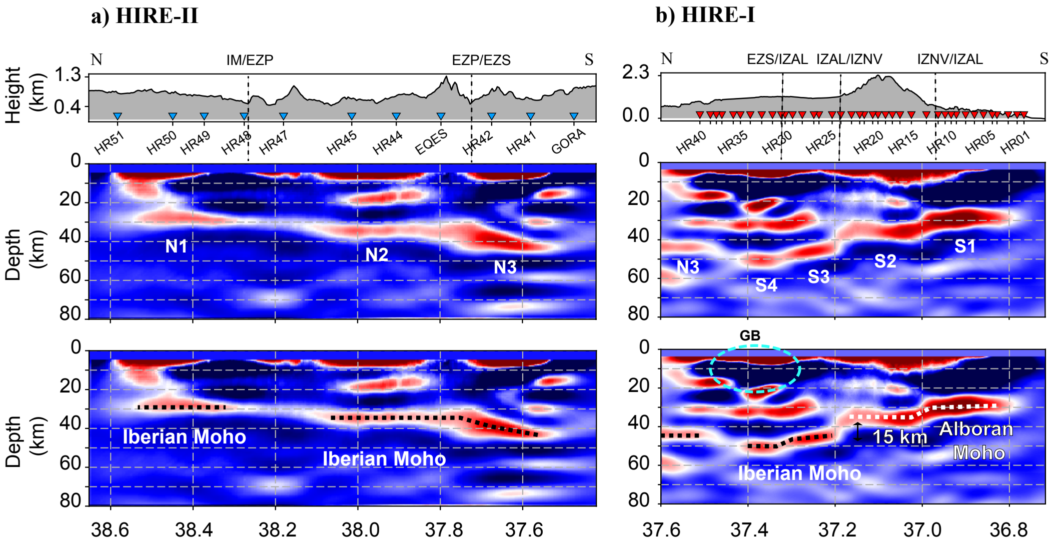

FIGURE 6.6: RTM images of Hire-I and Hire-II legs a) and b) respectively. At the top panel, we display the topography along the profile showing the location of the seismic stations and the contact at the surface of the different geological units (vertical dashed lines; IM: Iberian massif; EZP: External Zones Prebetics; EZS: External Zones Subbetics; IZAL: Internal Zones Alpujarride; IZNV: Internal Zones Nevado-Filabride). The light blue circle labeled with GB encloses the location of the Guadix Basin. At the bottom panels, the figures are the RTM images from above panels including interpretations lines of tectonic character. Dashed black (Iberian domain) and white (Alboran domain) lines mark the Moho discontinuity which its lateral variations in depth has been labeled by N1, N2, and N3 in Hire-II (a), and by S1, S2, S3 and S4 in Hire-I (b). The profiles coordinates are (37.60,-3.08)- (36.72,-3.01) for Hire-I, and (38.65, -3.00)-(37.40, -3.08) for Hire-II.

6.2 Results

We perform the above workflow independently for each profile because of different recording times. Figure 6.6 displays the final RTM images after stacking for the sources for both profiles (Hire I in the south and Hire II in the north). Different color scale has been chosen to compare easily both cross-sections.

The signal concentrates in the very first kilometers due to the injection of the wavefield from the surface; we apply a taper to the first 5 km in order to enhance the deeper structures in the images. In general with the RTM approach, the coherence of the backward propagating wavefields increases with increasing propagation time, providing better conditions for imaging deeper structures. However, coherence increases also for decreasing interstation distances. In this case the interstation distances, especially in Hire-I, are enough to illuminate adequately the intra-crustal discontinuities.

The RTM images show clearly the topography of the Moho discontinuity (dashed lines at the bottom panels, Fig. 6.6) along both profiles with the exception at the lateral edges likely due to lack of multi-fold illumination. Even with longer distances between contiguous stations of 10 km, RTM is able to enhance the first order discontinuities along the northern profile (Fig. 6.6a). Other intra-crustal discontinuities are imaged too but with far less longitudinal extension than the Moho discontinuity. The lower presence of intracrustal interfaces in Hire II compared to Hire I is due not just to coarser sampling but also to less degree of complexity in the subsurface structure.

The observed Moho discontinuity presents clear variations in its depth and in its lateral gradients along the profile including few offsets. For the sake of clarity in the discussion, we labeled each distinct segment in Fig. 6.6. The crustal thickness observed in the northern side (Fig. 6.6a), segment N1, of 30-32km is in agreement with previous studies using receiver function analysis (Mancilla et al., 2015a). The Iberian massif, in its southern part, is characterized by a homogeneous crustal structure and an almost flat Moho discontinuity (e.g., Palomeras et al., 2009, Mancilla et al., 2015b). Towards the south, the transition from N1 to N2 segments seems to be gentle to a deeper Moho (crustal thickness of 35 km). However, the lack of data from HR46, producing an interstation distance in that part of 20 km, complicate the observation of a continuous Moho discontinuity.

Following to the south, the depth and its gradient increase reaching the thickest value of crustal thickness under the Guadix Basin (45-50 km). The change in the Moho depth gradient from N2 to N3 segments occurs in a very short distance (approximately 10 km) and it is very well constraint. We interpret this section that comprised the N3, S4 and S3 segments (Fig. 6.6) as a deformed block within the Iberian Massif due to its collision with the Alboran domain. This deformed block extents 60 km along the profile until latitude 37.2°. The RTM image of the first leg in its northern flank (Fig. 6.6b) shows the continuation of the N3 segment towards the south, where the Moho discontinuity changes lightly its depth with an offset of 6 km in the transition to the S4 segment. Effects associated to lateral variation in the velocity structure along the profile, as the presence of sedimentary basins, are not considered in the wavefield propagation because a 1D model is used for the whole profile. Not introducing a correction for the propagation in sedimentary basins might cause light variations in the Moho topography displacing it to larger depths. The presence of the Guadix sedimentary basin could be one of the causes of the observed deeper Moho discontinuity in the segment S4 with respect to the adjacent segments, N3 and S3 (Fig. 6.6b). The thickness of the sedimentary cover is less than 1000 m in its thickest part and it is located in the transition from segment N3 to S4 (Sanz de Galdeano et al., 2007). This contrast could bias the size of the Moho step in less than 2 km (assuming average v_p and v_s velocities for the sediments of 3.8 km/s and 2.0 km/s, respectively). This prevents us for interpreting the small offset in the Moho discontinuity between segments S4 and S3 (3 km) as structural because it could be an artifact caused by the inaccuracy of the Earth model used for propagation. However, the Moho offset of 6 km between N3 and S4 cannot be completely due to lateral variation from the velocity model used by propagation. The occurrence of this Moho offset may imply the fragmentation of the already mentioned deformed block.

The most relevant feature of the Moho topography along the whole profile is the Moho step located at 37.2° of latitude between S2 and S3 segments with a 12 km depth offset (Fig. 6.6b). This Moho step was already imaged in previous studies utilizing CCP imaging of receiver functions in the same array seismograph (see section 5.1). Notices, however, that RTM recovers this depth offset lightly smaller than the CCP approach (17 km). The Moho offset was interpreted as produced by a STEP fault that allows the continuation along the northern edge of the easterly roll-back subduction system associated to the Gibraltar arc. This RTM study confirms the sharpness of the Moho step being constrained along 5 km. The possible appearance of continuity in this Moho step from segment S3 to S2 (Fig. 6.6b) is likely due to the trace interpolation preprocessing of 500 m.

The fragmented Iberian block (N3, S4 and S3 segments) presents the maximum crustal thickness along the profile (45-50 km), which does not coincide with the highest altitude. However, it coincides with the minimum of the Bouguer anomaly (100-120 mGal, Fig. 6.7, Bureau Gravimétrique International). Both observations point to the lack of isostatic compensation of the Sierra Nevada mountain topography associated with sudden removal along this Moho step (fault) of the Iberian lithosphere. The northern side of the fragmented Iberian Block (transition from N2 to N3 segments) is formed by continental crust of at least 35 km of crustal thickness that maybe continues to a more transitional crust near the STEP fault. This continuity and the thickness of the removed Iberian crust near the STEP fault rules out the involvement of continental-oceanic boundary. In general, the STEP faults develop along continental-oceanic or oceanic-oceanic boundaries of the same lithospheric plate [e.g., Govers and Wortel, 2005,Badji et al., 2015,Gallais, Graindorge, and Gutscher, 2014]. However, we observe that in central Betics, the tearing occurs at the continental-transitional crust meaning that the tearing process used a preexisting weakness zone associated to the rifted continental paleomargin (García-Hernández et al., 1980). This tearing, together with the other offsets and variations in depth block seems to be the result of the reactivation of previous deformation features. The current size of the weakness zone is 60-70 km.

Towards the south another Moho offset seems to occur between S1 and S2 segments inside the Alboran domain. The location of this Moho offset coincides with a high change in altitude reaching 2400 m near the center of S2

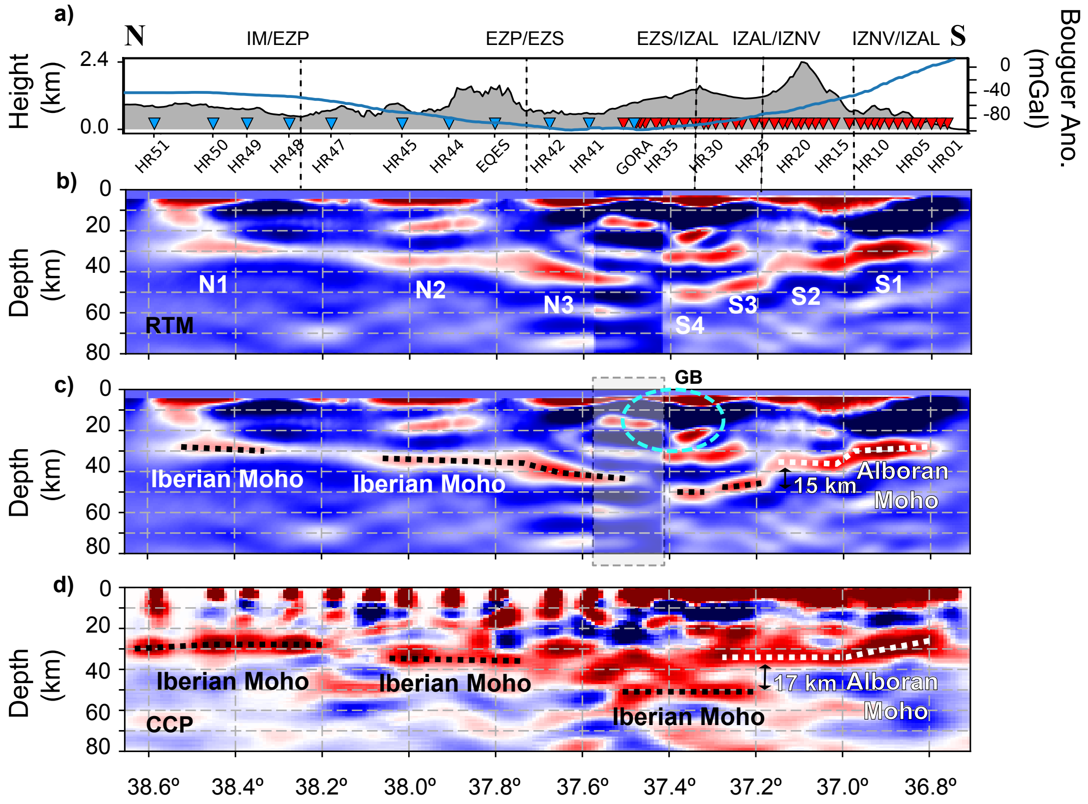

FIGURE 6.7: a) We display the topography and the Bouguer anomaly (blue line) along the combing profile showing the location of the seismic stations (red triangles, Hire-I, and blue triangles, Hire-II) and the contact at the surface of the different geological units (see 6.6 caption for details); b) combined RTM image; c) same than b) including interpretations lines of tectonic character. Dashed black (Iberian domain) and white (Alboran domain) lines mark the Moho discontinuity; c) CCP images with interpretation lines. The profile coordinates are (38.65, -3.00)-(36.72,-3.01)

segment (Sierra Nevada mountain). In our back-propagation we do not correct by topography. This would lead to travel-time and hence depth errors roughly proportional to the elevation biasing the step offset to a larger value. In this case the altitude correction would smooth this transition converting the observed step in a gentler decreasing of the Moho depth towards the Mediterranean coast (Fig. 6.6b).

Roughly, the observed crustal thickness values and its variation in the study area are in agreement with previous receiver function studies of individual stations located nearby the profile [Mancilla et al., 2015a] and the CCP images obtained in section 5.1. In figure 6.7, we compare both methodologies building images using the same seismic profile with the exception of the station HR46, not included in the RTM for not being a broadband instrument and therefore the same data set. In the CCP images, we back-projected the P-wave RFs along their incident ray path using the same 1D earth model as for the RTM images. In this back-projection, we take into account the increase of the width of the Fresnel zone with depth. We stack in the cross-section all receiver function amplitudes with piercing points inside a band with half-width of 50 km at both sides of the profile. For comparison with the CCP, we create a RTM image for the whole profile merging the independent images resulting from the analysis of both legs. The region in which both profiles intersects is emphasized by a transparent-gray square being 20 km long (Fig. 6.7). In rough outlines, the topography and depth of the first order discontinuities are traced quite similar with both RTM and CCP approaches. The largest Moho step is recovered from both methodologies, thought the depth offset is lightly smaller in the case of the RTM. The CCP stacks suggest a discontinuous Moho with an overlap between the Alboran domain and the Iberian domain (between segments S3 and S2). Comparing with the RTM image we interpret this overlap as an artifact created by the assumption in the CCP that interfaces are locally horizontal. Note that the RTM image does not show this overlap supporting a sharp separation between both domain at crustal scale. This observation suggests that the underthrusting of the Iberian lithosphere under the Alboran domain in this area is minor or negligible. The continuity of the Moho along the profile can be identified more clearly using the RTM method. This is observed especially in zones where the CCP method shows an ambiguous Moho such as the section from 37.2° to 37.6° (segments N3, S4 and S3) where the highest crustal thickness is found. Furthermore, the RTM methodology resolves finer the Moho gradient and we can identify variations in depth that are not visible in the CCP cross section where the discontinuity appears blurred (i.e. transitions from S3 to S4, and to N3). Intracrustal structures exhibit some coincidences using both approaches such as those ones located in the segments S2 and N2. However, the RTM image shows less complexity in the intracrustal depth range. As we already pointed out the coherence of the backward propagating wavefields does not emerge after some time of propagation, which means that very shallow structures could not be considerably enhanced with the RTM approach

6.3 Conclusions

We apply the RTM methodology to the teleseismic converted phases recorded in a high-density seismic profile to create a high-resolution image of the crustal structure. The profile probes the crust involved in the collision in the Central Betics, i.e. the transition between the Iberian and Alboran domains.

RTM produces clearer images of the crustal structure and better resolution of lateral changes than CCP stacking. The main observations include a sequence of abrupt Moho offsets, one of them associated with a STEP fault, and variations in Moho dip.

We propose that the principal Moho topography features conform a deformed block of 60 km length formed by continental/transitional Iberian crust which concentrates most of the deformation due to the collision. We suggest that the changes in the topography of the Moho discontinuity, and the geometry of the STEP fault in Central Betics is driven by inherited weaknesses in the Iberian paleomargin.

Chapter 7

Harmonic Decomposition Analysis in Eastern Betics

When waves propagate within an homogeneous medium the wave equation gives separated P and SV solutions. P-SV coupling occurs if waves travel through a vertical-stratified isotropic media, with no coupling between P-SV and SH waves. Translated into the recording seismograms, it means that the signal of the conversion from P to SV at a seismic discontinuities is only contained in the vertical and radial components. Therefore, the energy of the P-to-S conversion phase at a seismic discontinuity is held in the radial component of the RFs and no energy is presented in the transverse component of the RFs.

Traditionally RFs interpretations are based on the assumption of flat-layered isotropic structures and focus mostly on the amplitude and timing of the radial component to obtain the subsurface seismic structure (e.g., Vinnik, 1977, Langston, 1979). In practice the amplitudes observed in transverse RFs are only employed to validate this assumption. However, the P-SV and SH decoupling breaks down when the propagation media have non-horizontal interfaces or seismic anisotropy is present. This implies that P-to-S conversions are not restricted anymore to the P-SV plane and significant signal is transferred to the SH plane. Observed transverse energy may be attributed too to other factors as noise, scattering (e.g, Langston, 1989, Abers, 1998), fault zone guided waves or diffraction, but they do not generate characteristic back-azimuth patterns.

Though seismological investigations have largely reported and examined how anisotropy and dipping boundaries affect to seismic body phases (e.g., Keith and Crampin, 1977, Langston, 1979, Farra et al., 1991), until fairly recently, their contribution have been ignored in RFs studies. Cassidy, 1992 was the first in characterizing numerically important aspects of the RFs affected by dipping discontinuities. Levin and Park, 1997 and Savage, 1998 are among the pioneering works into exploring with synthetics RFs the effects of anisotropy and dipping interfaces. These heterogeneities cause on radial and transverse RFs components periodic azimuthal amplitude variations on direct, converted and multiple reverberating phases. The amplitude varies with the back-azimuth following different periodicity depending whether there is anisotropy or isotropic dipping boundaries. This periodic pattern has motivated the development of harmonic analysis methodologies that allow to separate these effects into different harmonic orders. Filtering out a harmonic term of the expansion may suppress the effects of lateral heterogeneity we are not interested and isolate the effect we want to model. These methodology has been used to map lateral heterogeneities as dipping isotropic interfaces (e.g., Savage, 1998, Bianchi et al., 2010) as well as anisotropy (e.g., Savage, 1998 Girardin and Farra, 1998, Levin and Park, 1997, Bianchi et al., 2010, Nagaya et al., 2008, Bianchi et al., 2010, Eckhardt and Rabbel, 2011, Bianchi, Bokelmann, and Shiomi, 2015).

In this chapter we first examine the periodic azimuthal variations of radial and transverse RFs produced by a dipping isotropic interface and a hexagonal anisotropic layer. We implement a linear harmonic decomposition analysis method similar to Olugboji et al., 2016 that exploits the azimuth symmetries of the radial and transverse components of teleseismic P-wave records. Energy due to anisotropic and/or dipping subsurface structures is separated from the isotropic signals and decomposed into harmonics that depends from the back-azimuth. Through a synthetic study we show that without making further assumptions about the earth model this methodology is adequate to extract relevant information about the geometry of the lateral heterogeneities, down-dip angle for dipping layers and trend angle for anisotropic layers. Furthermore, the geometry interpretation of the lateral heterogeneity is based on vectors associated to the different harmonic terms which helps to discriminate between the effects that isotropic dipping interfaces and anisotropic layers produce.

As a testbed for the implemented method, we apply the harmonic decomposition technique to data sampling the Eastern Betics region, a region structurally complex and deformed by large folds and a major faults system, the Eastern Betic Shear Zone (EBSZ). The motivation of using this data base is: i) Previous RFs analysis in this region report significant lateral heterogeneity associated to a dipping Moho reaching 20° of dipping (Pedrera et al., 2010; Mancilla et al., 2015a), and ii) long-standing stations provide appropriate back-azimuthal coverage for the proposed harmonic-decomposition analysis.

7.1 Methodology

7.1.1 Dependency of RFs on lateral heterogeneities

Theoretical studies have illustrated the effects of anisotropic layers and dipping interfaces on RFs (e.g., Cassidy, 1992, Levin and Park, 1997, Savage, 1998, Girardin and Farra, 1998, Piana Agostinetti, Park, and Lucente, 2008, Bianchi et al., 2010, Olugboji et al., 2016). These effects cause on radial and transverse RFs components back-azimuth periodic patterns on both arrival times and amplitudes of direct and converted phases (Fig. 7.1). Other sources of lateral heterogeneity would be expected to generate SV and SH azimuth amplitude variations but in a highly erratic way as a function of azimuth (Jones and Phinney, 1998).

To illustrate the periodic patterns produced by lateral heterogeneities, we perform synthetic examples of RFs with homogeneous backazimuth distribution and constant ray parameter in three representative scenarios:

- **A dipping interface** produces variation in amplitude by backazimuth with 2-lobed patterns affecting the direct, the converted and multiple reverberated phases. We restrict our analysis to the direct and converted phases. In Fig. 7.1 we shows a sketch in (a) depicting an interface dipping 10° to the East (0° strike relative to North) and in (b) the corresponding radial (left) and transverse (right) RFs. The tilted discontinuity bends the seismic ray outside the source-receiver plane introducing part of the direct P arrival signal into the SH component except for up- and down-dip directions (zero delay time in fig. 7.1b). The amplitude variations of the converted Ps (at $\sim$4 s of arrival time relative to the direct P) are associated with the change of the P incidence angle on the dipping interface according to the Zoeppritz equations (see section 3.2). Because of the dependence on the angle between the incident wave and the interface (larger amplitude for larger incidence angle), the radial conversion from the down-dip backazimuth (90°) has a bigger amplitude and the up-dip conversion a lower amplitude (270°) compared to a horizontal interface

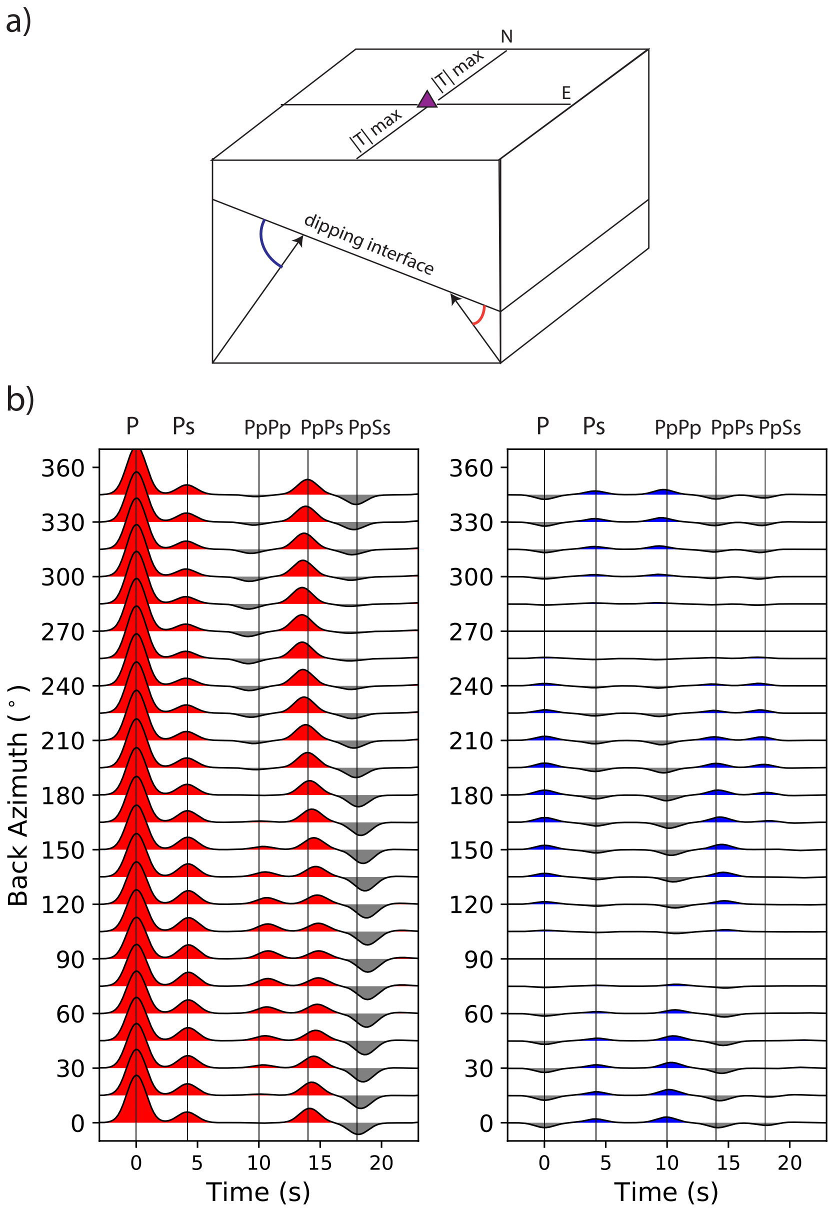

FIGURE 7.1: a) Sketch depicting a 35 km depth interface dipping 15^o with a strike angle of 0^o relative to North. (b) Synthetic receiver functions (*left* radial component, *right* tangential component) with homogeneous backazimuth distribution and constant ray parameter (0.055 s/km) generated by the dipping scenario described in a). The arrival times for the direct P, the Ps conversion and the multiple phases for the homogeneous case are marked in the figure with vertical lines in order to emphasize the variations of the delay times with backazimuth.

conversion with the same slowness. The tangential component shows no energy at the arrival time of the direct P for incidence along the up- and down-dip azimuths and maximum amplitude for conversions with incidence perpendicular to the dip, i.e. along the strike direction. The same pattern (i.e. 2π periodicity with backazimuth) is observed as well in the time delays (with respect to the first arrival) for the converted phases due to different path lengths from the interface to the receiver depending of the backazimuth. Converted arrivals are earliest for the up-dip direction and latest from the down-dip direction.

- **Hexagonal anisotropy with a horizontal symmetry axis** produces a 4-lobed back-azimuthal patterns affecting just to the converted phase at the anisotropic layer. Fig. 7.2a shows a block diagram sketching a 10-km thick anisotropic layer located at 35 km depth with 6 % of velocity variation between the fast and slow direction of P and S phases with horizontal hexagonal anisotropy and a trend oriented at 45° relative to North. No velocity contrast is considered. In this case, the direct P wave is not bent (no out-of-plane signal of the direct P arrival), so no arrival and amplitude variations are seen at the first arrival time (zero time) on the tangential and radial components. Anisotropy perturbs the orientation of particle motion and removes the decoupling between SH and P-SV waves which occurs in isotropic horizontally layered structures (Maupin and Park, 2007). The decoupling occurs at both boundaries of the anisotropic layer, hence both the top and bottom of the anisotropic layer produce a converted S wave, generating two successive P-to-S converted pulses. We observe these two converted phases around 5 s of delay time in figure 7.2a bottom. The P-SH amplitude vanishes for P waves whose baz are parallel and normal to the strike of the anisotropic symmetry axis, and has opposite polarity for impinging waves that approach from opposing sides of the symmetry axis. This azimuthal amplitude behavior on radial and tangential components applies to slow as well as fast symmetry axes, equivalent results are obtained when fast and slow axis are orthogonal to this geometry, in this case fast axis pointing at 45° and slow axis direction of 135°. The splitting of the converted S wave is generally ignored in these studies for being minimal due to the small widths of the anisotropic crustal layers. Individual RFs with observable Ps splitting between the radial and transverse components are often rare (Liu and Park, 2017). Due to no differences in path lengths, converted arrivals do no exhibit time delay variations with backazimuth.

- **When the hexagonal anisotropy presents a plunging symmetry axis** both 2-lobed and 4-lobed backazimuthal patterns appear. In Fig. 7.2b the anisotropy layer has a symmetry axis with a trend of 45° tilted 20°. The converted P-to-S wave has the largest amplitudes in the radial component for the up- and down-plunge incidence and the largest amplitudes in the tangential component along the strike directions, similar to the dipping isotropic case. As in the previous case, fast axis oriented at 45° produces equivalent results than slow axis pointing at 135°, relative to North. Since the depth to the converting interfaces is constant, there is no delay time variation.

For both dipping isotropic boundaries and anisotropic layers, radial receiver functions are symmetric, transverse receiver functions are anti-symmetric about a given back azimuth (the horizontal projection of the dip direction or the axis of symmetry), which translates into a phase shift between both components of $\pi/2$ in the case of the dipping interface and $\pi/4$ for the anisotropic case. The amplitude behavior of the converted phase as a function of backazimuth in the case of a dipping layer with aligned anisotropy is similar to the case of a horizontal layer with anisotropy with a plunging symmetry axis.

Multiple reverberated phases are affected as well in their amplitude and delay times by lateral heterogeneities as we can see in fig. 7.1b, however we do not focus on them in this study. The main reasons are: (1) different angles of incidence cause different amplitudes of the radial and transverse components even in a flat-layered isotropic media. Therefore, RFs recordings must be time and amplitude corrected to a common incident angle, (i.e. move-out

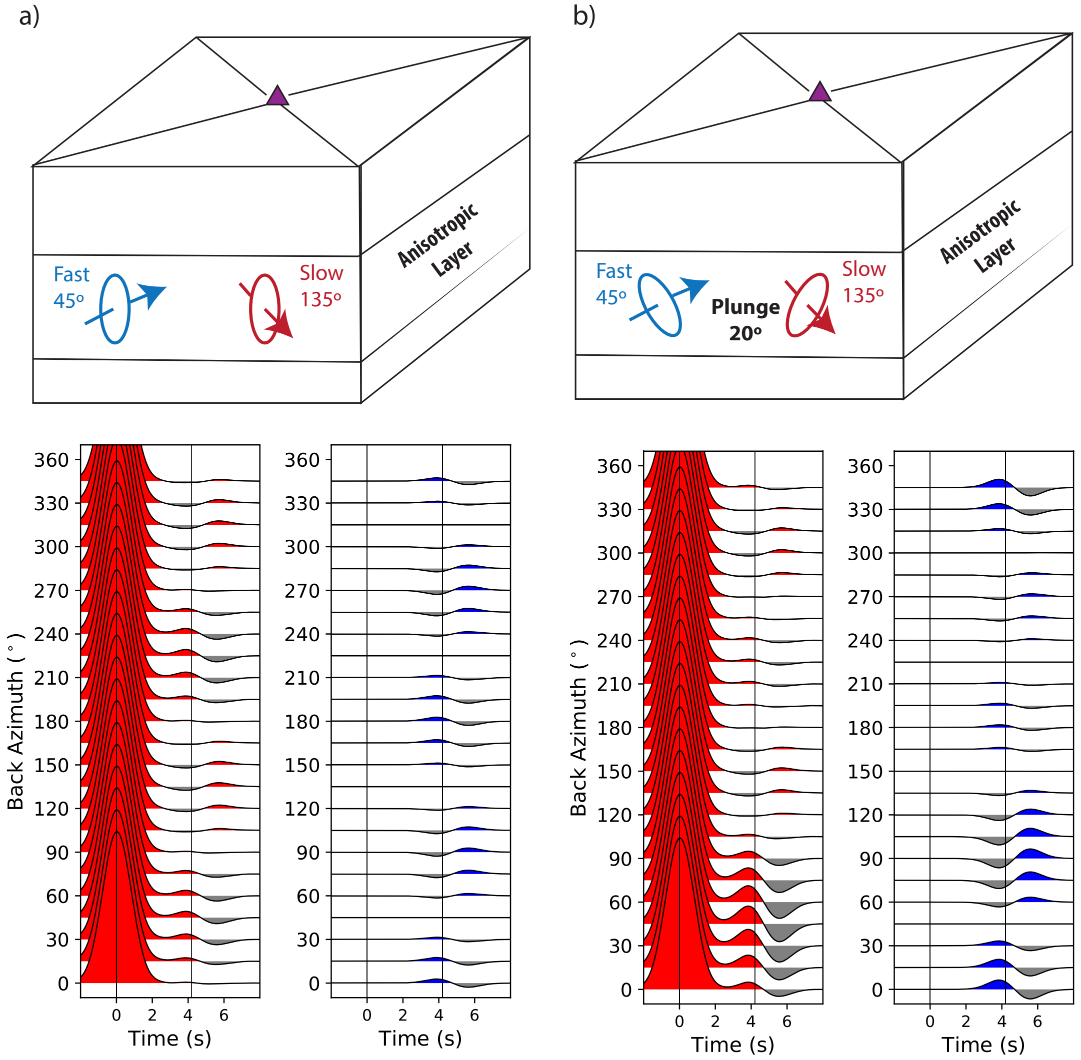

FIGURE 7.2: The same than 7.1 for a model with a 10 km thick anisotropic layer sandwiched within an isotropic crust. The anisotropic layer presents a 6 % peak-to-peak strength of P and S hexagonal anisotropy with its fast axis direction pointing at 45° relative to North (a) horizontal and (b) 20° tilted. Analogous results are obtained for a slow axis pointing at 135°. There is no isotropic velocity contrast between the anisotropic layer and the material surrounding it.

corrected). As we see in chapter 3 the move-out correction in time stretches or compresses the RFs signal for a particular phase either converted or multiples. Then, the phase need to be selected because converted and multiples can no be corrected at the same time. (2) In contrast to multiple phases, the azimuthally time delay variation that Ps converted phases experience due to dipping interfaces is small enough not to be considered in our harmonic decomposition, which takes into account only the amplitude variations in back-azimuth.

7.1.2 Harmonic Decomposition Analysis

Exploiting these symmetries of RFs with the back-azimuth, we design a linear harmonic decomposition method of the radial and transverse components that helps to separate the effects of isotropic flat-layered effective medium, dipping boundaries and anisotropic structures. We assume that at every time step the amplitude distribution by back-azimuth of radial and transverse components can be expressed as a weighted sum of harmonic functions ($sin(n\theta)$ and $cos(n\theta)$), being n the harmonic degree and θ the back-azimuth. Expressing the harmonic expansion as a matrix equation, we have an overdetermined linear equation system $D = Ax$, where D is the data, A the coefficient matrix containing the harmonic functions and x the model parameters. The solutions are the coefficients of the harmonic expansion which depict: (1) a_0 is the 0-degree term, independent of backazimuth, containing the information of the flat-layered isotropic medium, (2) (a_{1x},a_{1y}) are the orthogonal terms with the 360-periodicity associated to the presence of dipping interfaces or plunging anisotropic layers, and (3) (a_{2x},a_{2y}) are the orthogonal terms displaying the 180-periodicity characteristic of horizontal hexagonal anisotropic layers. Because the coefficient matrix specifies the harmonic behavior already mentioned in the observed data, the zero value for the first column and rows corresponding to the transverse components is due to the fact that the transverse RF component have no energy in absence of lateral heterogeneities. Since there is a half of the period shift between radial and transverse components we explicitly introduce this shift into the harmonic functions of the transverse component to consider both components in the same decomposition scheme .

$$\begin{pmatrix} R_{\theta_1} \\ . \\ R_{\theta_k} \\ T_{\theta_1} \\ . \\ T_{\theta_k} \end{pmatrix} = \begin{pmatrix} 1 & sin(\theta_1) & cos(\theta_1) & sin(2\theta_1) & cos(2\theta_1) \\ . & . & . & . & . \\ 1 & sin(\theta_k) & cos(\theta_k) & sin(2\theta_k) & cos(2\theta_k) \\ 0 & sin(\theta_1 + \frac{\pi}{2}) & cos(\theta_1 + \frac{\pi}{2}) & sin(2[\theta_1 + \frac{\pi}{4}]) & cos(2[\theta_1 + \frac{\pi}{4}]) \\ . & . & . & . & . \\ 0 & sin(\theta_k + \frac{\pi}{2}) & cos(\theta_k + \frac{\pi}{2}) & sin(2[\theta_k + \frac{\pi}{4}]) & cos(2[\theta_k + \frac{\pi}{4}]) \end{pmatrix} \begin{pmatrix} a_0 \\ a_{1x} \\ a_{1y} \\ a_{2x} \\ a_{2y} \end{pmatrix}$$

After solving the equation system for every time step the **independent of back-azimuth trace** $a_0(t)$ contains the information related to the isotropic variation of the seismic velocity with depth. Conventional RFs inversions use stacked traces from different back-azimuths to obtain a single-velocity model, which is a representative, laterally homogeneous average of the velocity structure under the station. However, this approach is only valid under conditions of low anisotropic and/or dipping boundaries. We will show in chapter 8 that this estimated back-azimuth independent trace $a_0(t)$ effectively isolate the horizontally layered isotropic effective medium in case of significant lateral heterogeneity.

As we will see in the next section the harmonic coefficients of each periodicity (a_{nx},a_{ny}) are attached to orthogonal functions (*sin* and *cos*) which allows to build a **particle motion vector** that inform us about the geometry of the lateral heterogeneity.

The **inclusion of the transverse component** in our method helps to constrain the lateral heterogeneity not just by doubling the amount of data set but also because the transverse RFs are primarily sensitive to dipping interfaces and anisotropic layers, while most of the energy contained in the radial component refers to the isotropic vertical-stratified structure.

7.1.3 Illustration of the method

We carry out a synthetic study to illuminate the capabilities of this methodology in extracting from RFs the information regarding the isotropic flat-layered, the dipping boundaries and the anisotropy effects. We use RAYSUM, a ray-based code that handles dipping interfaces and hexagonal anisotropy (Frederiksen and Bostock, 2000), to calculate synthetic seismographs. In order to illustrate the method we computed RFs with a full range of back-azimuths (0º-360º) at 15º intervals and a constant slowness in the three representative scenarios already shown in section 7.1.1: (1) a dipping interface, an hexagonal anisotropic layer with (2) horizontal axis of symmetry and (3) with axis of symmetry tilted. The flat-layered isotropic structure of the models resemble crustal and upper-mantle seismic velocities with a flat Moho discontinuity at 35 km depth.

1. Dipping scenario whose details are described in fig. 7.1. We choose this Moho dipping angle for being similar to reported values in the region of our case study (next section 7.2). Figure 7.3a depicts radial (black points) and transverse (blue points) back-azimuth RFs amplitudes for the time steps of direct (up) and converted (bottom) phases. We plot the transverse component amplitudes with a phase shift of 180º respect to the radial component. The different terms of the harmonic decomposition are shown in continuous lines; A0 (red) depicts the a_0 constant value with no back-azimuth variation, A_n showing the azimuth variation are built with the coefficients as $a_{nx} sin(n\theta) + a_{ny} cos(n\theta)$. In a dipping scenario only the 360-harmonic periodicity is expected and the 1st-order term in the expansion recovers the azimuthal amplitude variation for direct and converted phases. The harmonic expansion solution (continuous black line) made up with the superposition of the three terms fits the data. Since there is a phase shift of $\pi/2$ between radial and transverse components in the harmonic dependence, combining both components back-azimuth gaps in the data can be filled. There is no need to use regularization between radial and transverse RFs because both components have a similar variance in amplitude (Figure 7.3).

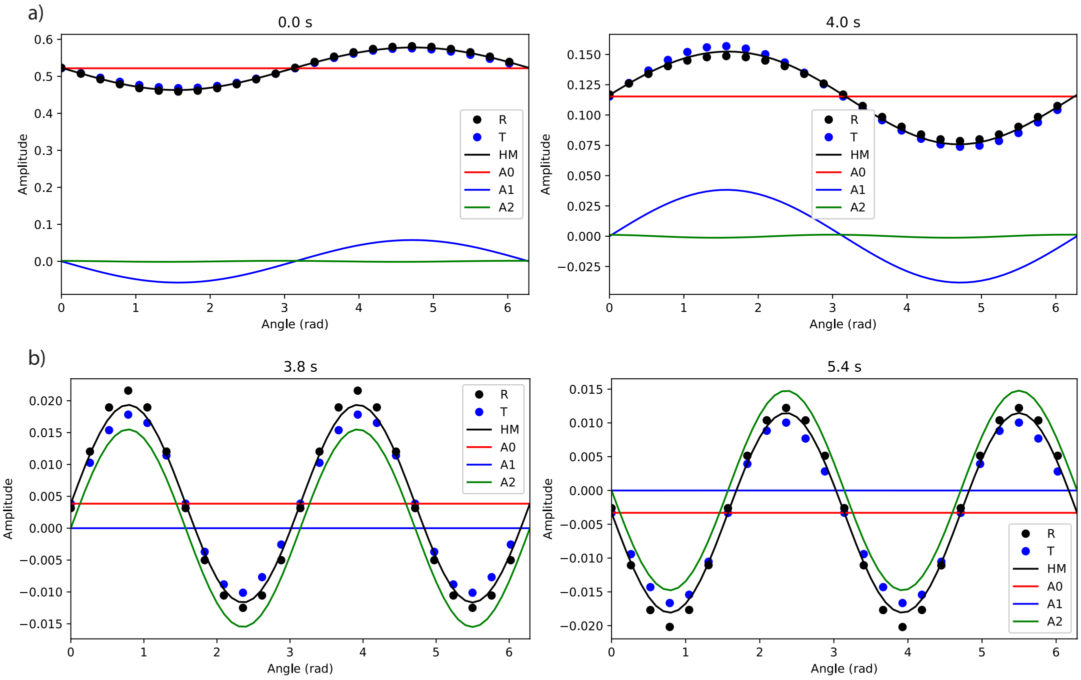

FIGURE 7.3: Radial and transverse (black and blue points, respectively) amplitudes of RFs at time of a) direct (0 s) and converted (4 s) phases for the dipping scenario and b) converted phases at the upper- (3.8 s) and lower- (5.4 s) boundary of the anisotropic layer for the anisotropy scenario. A a) 180° and b) 90° phase shift has been added into the transverse component for the dipping and anisotropy scenarios, respectively, due to the existence of phase shift in the harmonic dependence between radial and transverse components. The solution of the harmonic decomposition is shown in black continuous line. The coefficients of the expansion depict the harmonic dependencies A_0, red line, constant value with no backazimuth variations, A_1 (blue line) and A_2 (green line), displaying 360- and 180-harmonic dependencies, respectively.

To evaluate the geometry of the lateral heterogeneities, we compute the norm of the vectors $(a_{nx}(t), a_{ny}(t))$ $(n = 0, 1, 2)$ for every time step and obtain in which time window (which depth) the highest amplitudes of the harmonic terms are located. Fig. 7.4a shows the vectors and their norms along the time window for the dipping scenario. The continuous red line a_0 represents the backazimuth independent term sensitive to the isotropic flat-layered structure and accumulates most of the weight in the harmonic expansion. The length of the $(a_{1x}(t), a_{1y}(t))$ vector (blue line) reaches the highest amplitudes at the arrival times of the direct and converted phases. The vectors associated with $(a_{1x}(t), a_{1y}(t))$ at direct and converted phase delay times point at up- and down-dip directions, respectively, due to a π shift in the amplitude polarity with the back-azimuth between both phases (Fig 7.4). The norm of the second vector $||a_2||$ does not vary appreciably with time having a value of zero and therefore its associate vector a_2 does not exhibit significant lengths along the time window as expected in this scenario.

To show how this decomposition recover the original signal and related uncertainties, in Fig. 7.7 we depicts the synthetic (a) radial and (b) transverse RFs, (c) the estimated radial RFs obtained from the harmonic expansion $H(\theta, t)$, the misfit between the synthetic and harmonic expansion for the (c) radial and (d) RFs and (e-h) the estimated A_0, A_1 and A_2 components from the expansion, respectively. There is no significant misfit between the synthetic RFs and their harmonic expansion along the time window considered. The A_0 component is back-azimuth independent, the A_1 term loads most of the azimuth variation whereas the A_2 term do not contain energy. We can evaluate the relative weight of each term within the expansion (ω_n) by computing the back-azimuth averaged energy content of each harmonic component E_n normalized by the total energy content of the expansion and expressed in percentage. E_n is the Root Mean Square of the continuous-time harmonic term averaged over azimuth distribution (sum in θ) according to the equation 7.1. N_{RFs} stands for the number of RFs, the sum in t refers to the discrete time points and N to the number of samples. The value of these weights computed in a time window of 10 s are shown at the top of fig. 7.7. The weight associated to the 0-order term $\omega(A_0)$ contains the 92% of the expansion amplitude, the rest of the weight goes mostly to the 1-order harmonic component $\omega(A_1)$. We find non-zero content of energy in the 2-order harmonic component due to the influence of other phases at later times that are not move-out corrected and no taken into account in our method.

$$E_n = N_{RFs}^{-1} \sum_{\theta} \sqrt{N^{-1} \sum_{t} A_{n\theta}(t)^2} \tag{7.1}$$

2. Horizontal anisotropy scenario as described in 7.2a. We choose these parameters for being reasonable approximations for anisotropic crustal structures (e.g., Schulte-Pelkum et al., 2005). Horizontal hexagonal anisotropy causes a 180-harmonic periodicity and the 2nd-order of the expansion (a_2 coefficients) recovers the azimuthal amplitude variation of converted phases at both, upper and lower, boundaries of the anisotropic layer (fig. 7.3b). The main weights of the expansion concentrate now on the 0th- and 2nd-order harmonic (fig. 7.8) components with a characteristic two-lobes pattern in the normalized vector $||\vec{a_2}||$ (fig. 7.4b) that correspond to the conversions at the upper- and lower- boundaries of the anisotropic layer. The vector $\vec{a_2}$ for the first lobe points at a direction whose angle is the double of the trend relative to North in case of fast axis symmetry. An anisotropic layer with a slow symmetry axis orthogonal to the fast symmetry axis will produce the same result. Because we can not resolve this fast and slow symmetry axis ambiguity, we will rotate the $||\vec{a_2}||$ vectors, for both lobes, half of its angle relative to North and South in order to point them in the directions of the fast and slow symmetry axes (fig. 7.4b right). In this scenario, the vector $\vec{a_1}$ does not exhibit significant amplitudes along the time window. The weight associated to the 0-order term $\omega(A_0)$ contains the 97% of the expansion amplitude, being stored in the 2-order term $\omega(A_2)$ an approximately 3%.

3. Tilted anisotropy scenario with the same parameters than the horizontal anisotropy scenario but with the symmetry axis tilted 20º. In this case both vector norms $||\vec{a_1}||$ and $||\vec{a_2}||$ exhibit high amplitudes for the converted phases at the upper- and lower-boundary of the anisotropic layer (fig. 7.4c). The vector $\vec{a_1}$ is parallel and antiparallel to the trend direction and $\vec{a_2}$ exhibit the same behavior discussed in the horizontal anisotropy case. This intrusion of amplitude into the $\vec{a_1}$ when the symmetry axis is inclined makes difficult to distinguish anisotropy with plunge from the

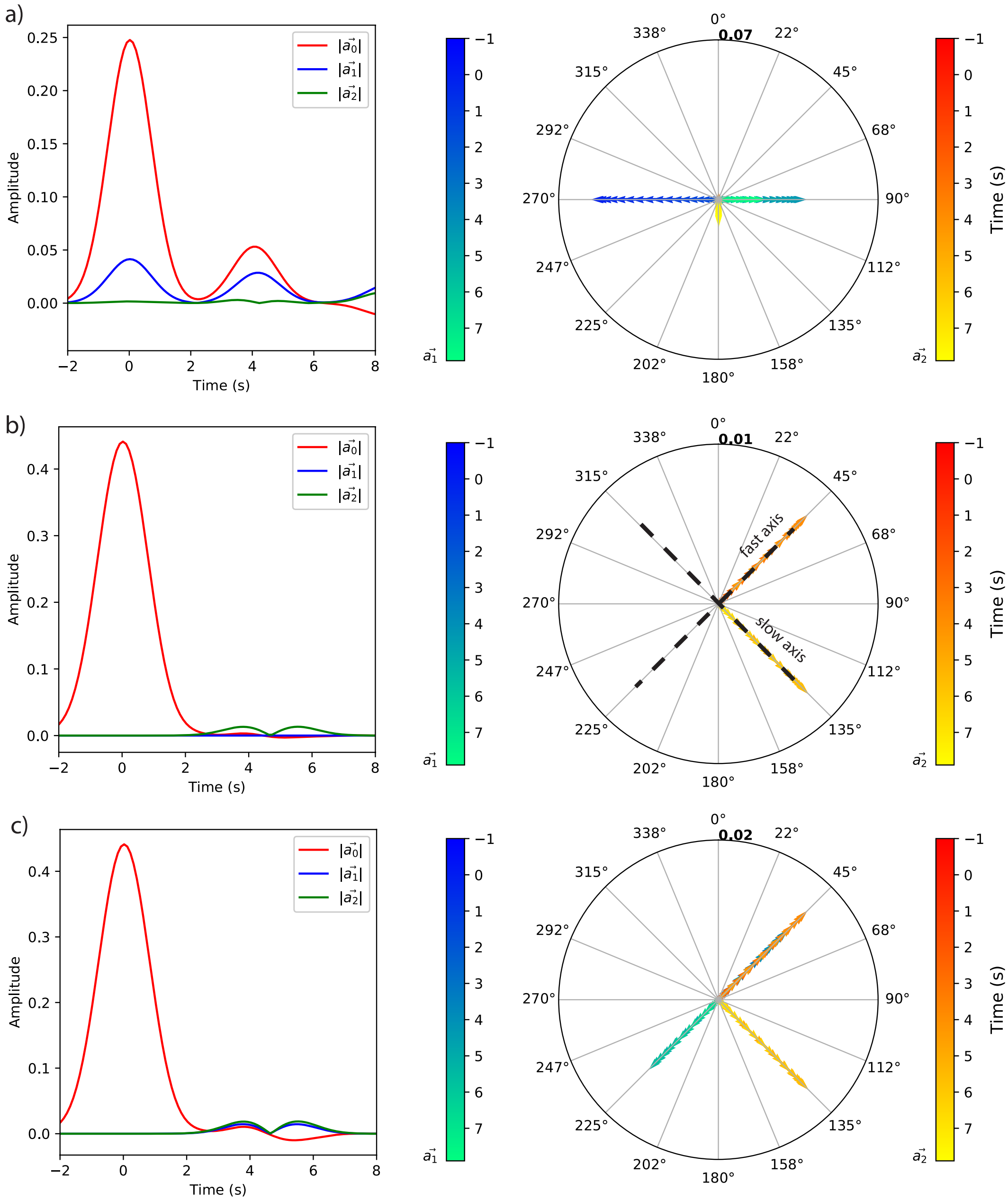

FIGURE 7.4: Norm of the coefficients $a_n(t)$, $n = 0, 1, 2$, and direction of the vectors $(a_{nx}(t), a_{ny}(t))$, $n = 1, 2$, along the time for the three scenarios: a) described in fig. 7.1, b) and c) described in fig. 7.2. The vectors at the right side of the figure are normalized.

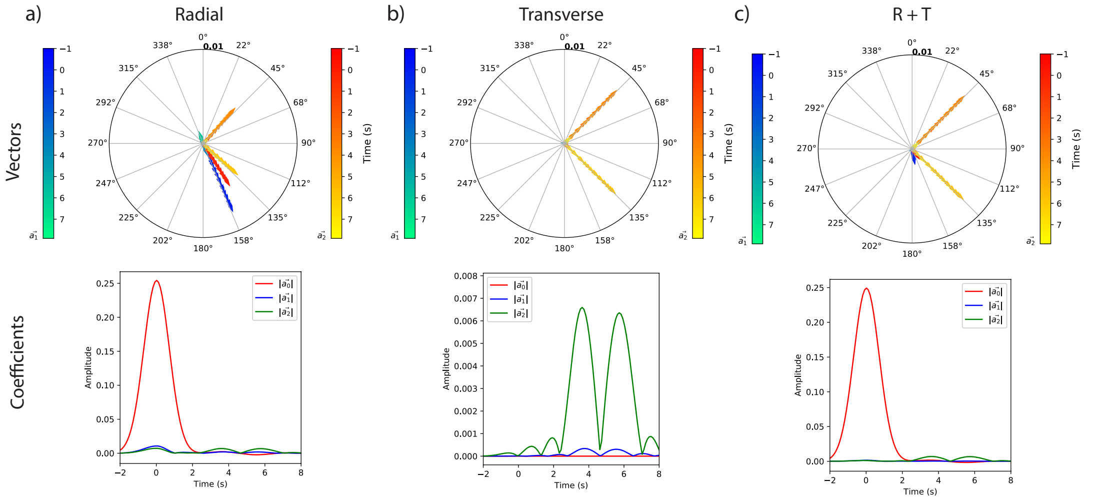

FIGURE 7.5: Directions and norm of the vectors $\vec{a_n}(t)$ for $n = 0, 1, 2$, along the time window in the anisotropic scenario. We use a realistic backazimuth and slowness distribution making necessary to applied the move-out correction.

situation in which we have horizontal anisotropy combined with dipping interfaces. However, the alignment between the vectors $\vec{a_1}$ and $\vec{a_2}$ (after this second vector is rotated as we have discussed in the previous section) can help to clarify this ambiguity.

7.1.4 Testing the inclusion of both components in the Harmonic Decomposition

In order to test, the goodness of the inclusion both components, the radial and transverse, working with the anisotropic scenario, we perform the harmonic decomposition analysis using separately the radial and the transverse components (first and second column, respectively, in fig. 7.5). We use a realistic backazimuth and slowness distribution, representative of the case study discuss later in this chapter, and apply the move-out correction. As expected, the two consecutive lobes produced by the anisotropic layer are present using both approaches (time between 3 and 6 s in fig. 7.5) and the vector $\vec{a_2}$ point at the correct directions of the fast and slow axes. However we observe that with the radial component approach a considerable amount of energy contaminates

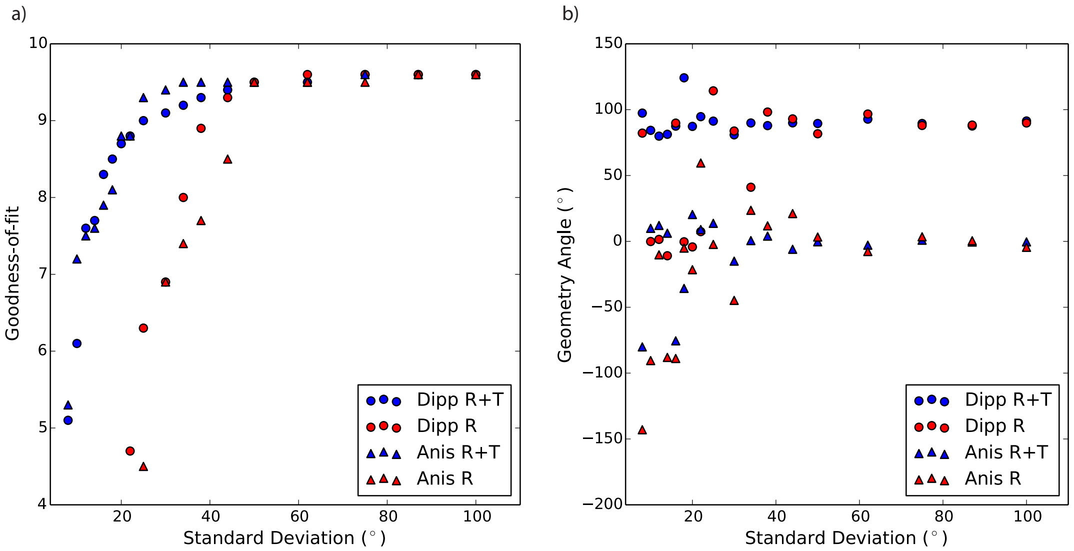

FIGURE 7.6: a) Goodness of fitness between the receiver function generated in an isotropic flat layered media and the independent of baz receiver function obtained with the harmonic decomposition method using only radial (red color) and jointly radial and transverse (blue color) components for the dipping (circles) and anisotropic (triangles) scenarios. b) Directions of the lateral heterogeneity geometry for the dipping (strike angle) and horizontal anisotropic (fast axis direction) scenarios using only radial and jointly radial and transverse components.

the vectors $\vec{a}_1$ and $\vec{a}_2$ at the direct onset (time 0 in fig. 7.5a). The contamination at 0 s delay time does not happen for the transverse component (fig. 7.5b). This phenomenon might be generated by the move-out correction which, as we have already reported (see fig. 3.8), mainly affect the radial component specially at the first arrival time. The direction at which the vector $\vec{a}_1$ points is determined by the backazimuth distribution of the data. When we combine both components in the analysis, the intrusion of energy in the vectors at 0 s delay time disappears. The combination of both components in the harmonic decomposition helps to remove these undesirable effects.

In Fig. 7.6 we investigate the convenience of using jointly the radial and transverse components in the harmonic decomposition method to properly determine the independent of backazimuth receiver function and the geometry of the lateral heterogeneity. Graphic a) shows the goodness-of-fit between the receiver function generated in the equivalent isotropic flat layered media and the independent of baz receiver function obtained with the harmonic decomposition method using only radial (red color) and jointly radial and transverse (blue color) components for the dipping (circles) and anisotropic (triangles) scenarios. Note that this baz independent trace represents the effective flat-layered isotropic medium. The harmonic decomposition has been performed for different baz distributions going from narrow to wide standard deviations. When we include both components the goodness-of-fit converges faster to high values. Once a homogeneous azimuth distribution is guaranteed both, only radial and jointly radial and transverse components approaches, give similar results. The same phenomenon can be recognized for the determination of the geometry of the others lateral heterogeneity discussed in this chapter. In Fig. 7.6b) we show the estimated strike and fast axis angles for the dipping and horizontal anisotropy scenarios, respectively. For standard deviation larger than 60^o, the backazimuth distribution is more homogeneously distributed, both approaches constrain properly the angles. Combining radial and transverse components in the harmonic decomposition for lower standard deviations (the backazimuth distribution is more concentrated in a narrow range) helps to determine more precisely the angles.

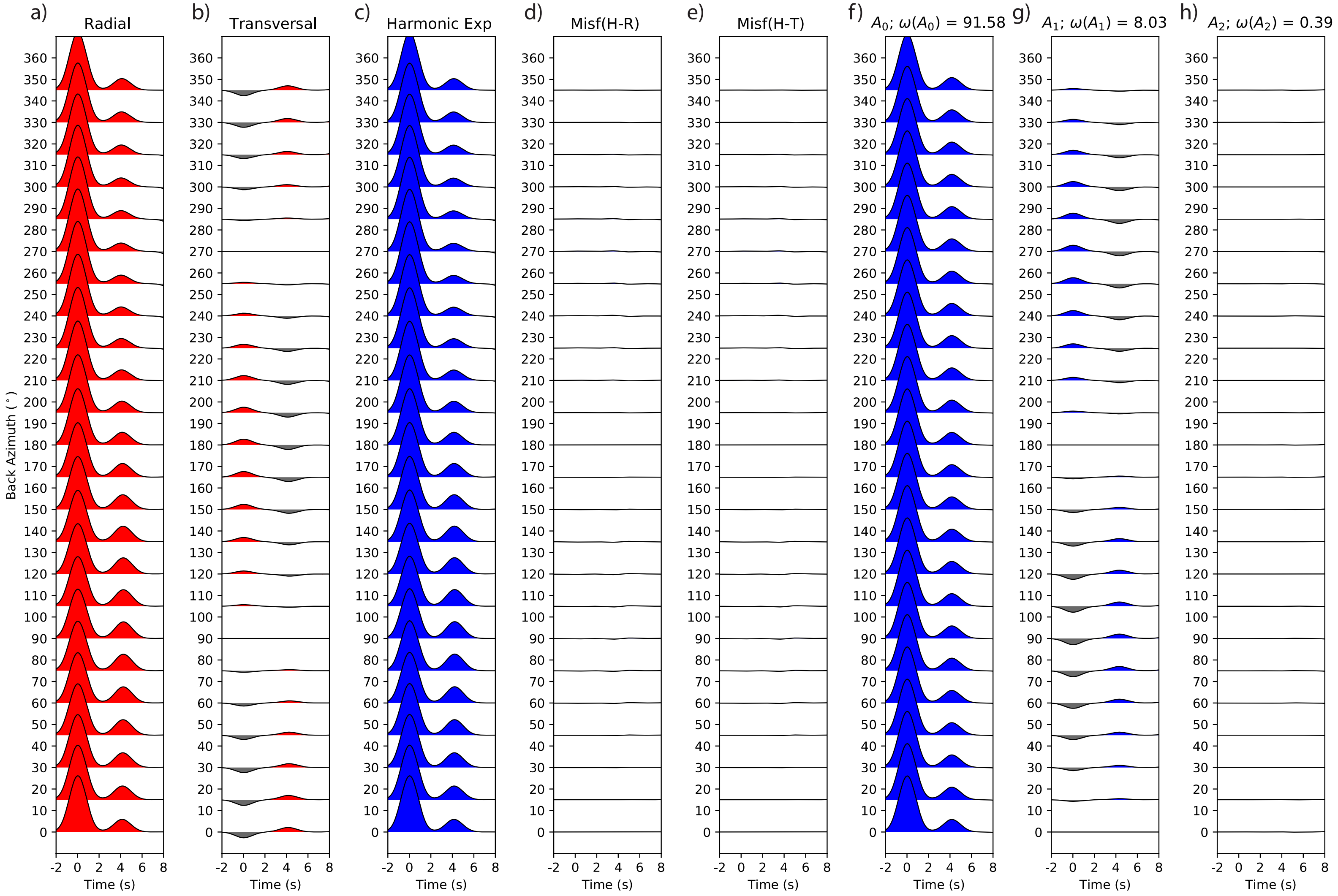

FIGURE 7.7: Synthetic RFs sorted by back-azimuth for the dipping scenario described in fig. 7.1. (a) Radial and (b) transverse components, (c) harmonic expansion for radial traces, (d) misfit between (a) and (c) traces and (e) misfit between (b) and the harmonic expansion of the transverse component, (f-h) A_n harmonic components for $n = 0, 1, 2$, respectively. Values shown on top of (f-h) panels are the relative weights ω_n of the harmonic terms within the expansion obtained according to equation 7.1.

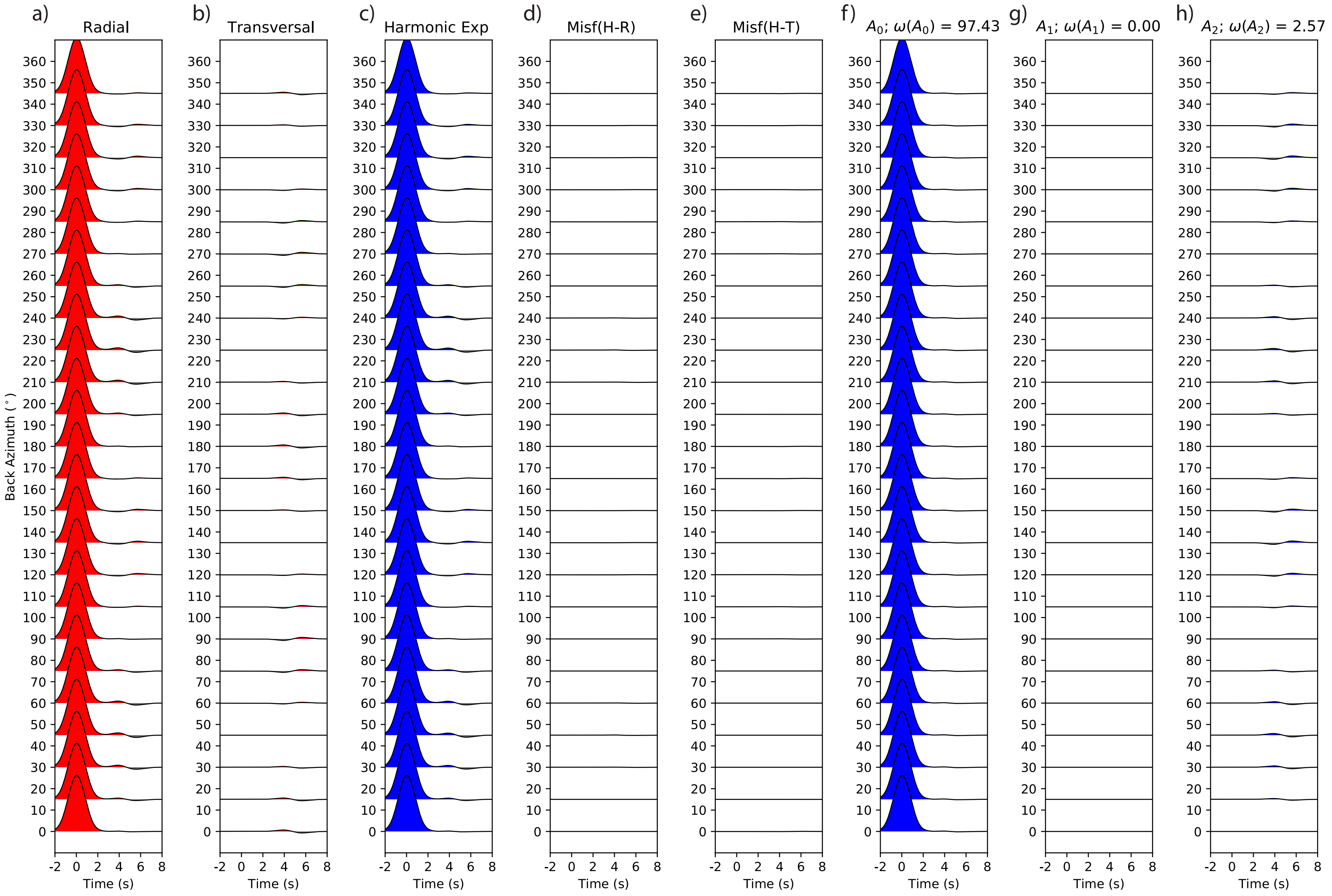

FIGURE 7.8: The same than fig. 7.7 but in the horizontal anisotropy scenario described in fig. 7.2a. Now A_2 term concentrates most of the back-azimuth harmonic energy.

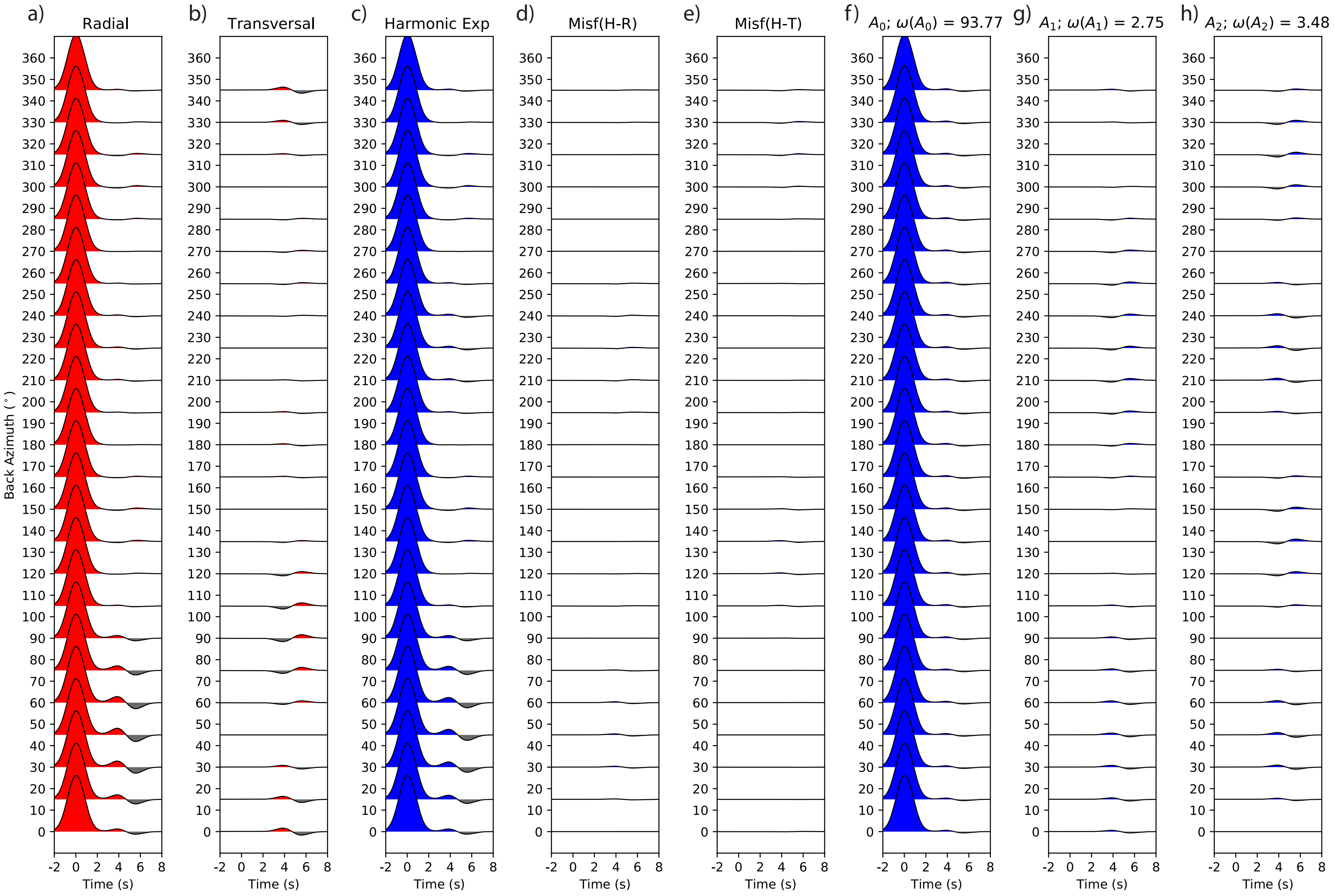

FIGURE 7.9: The same than fig. 7.8 but with the symmetry axis tilted 20°. Now the terms A_1 and A_2 contain signal.

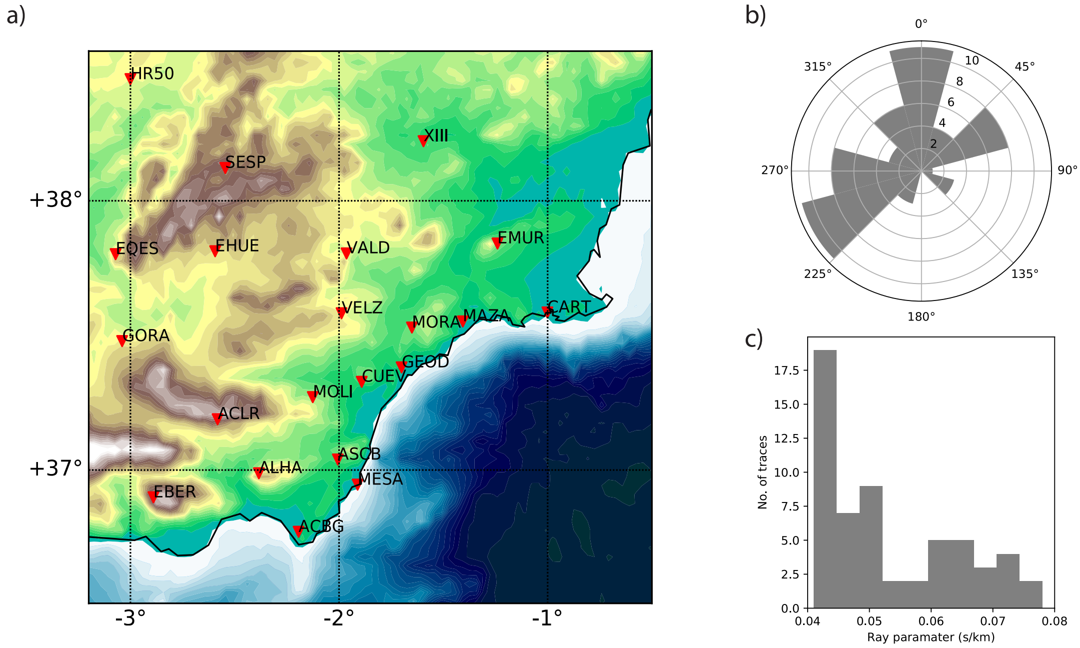

FIGURE 7.10: a) Map of the investigated area displaying the main structural features and the seismic stations (red triangles). Acronyms stand for Socovos Fault (SCF), Crevillente Fault (CVF), Alhama de Murcia Fault (AMF), Palomares Fault (PF), Carboneras Fault (CF) and Alpujarra Fault (APF). (b) Averaged back-azimuth and (c) ray parameter distribution for the stations.

7.2 Case Study

We test this method on real teleseismic data collected by 20 long-standing seismic broadband stations deployed in the Southeast of the Iberian Peninsula (Eastern Betics, fig. 7.10a). In the area previous studies of RFs have reported dipping Moho (Pedrera et al., 2010; Mancilla et al., 2015a), lateral seismic velocity heterogeneities (Docherty and Banda, 1995; Julià, 2005), and crustal and subcrustal anisotropy (Serrano et al., 2005; Buontempo and Wuestefeld, 2013). The stations are located close enough to the faults to record the passive seismic signatures that faults leave on RFs. The data were provided by the Instituto Andaluz de Geofísica (IAG), the Instituto Geográfico Nacional (IGN) and Western Mediterranean network (UCM-ROA)(section 3.1).

The study area is located in the eastern part of the Betic Cordillera and is affected by a fault system characterized by large transcurrent left[U+2010]lateral faults with approximately N35ºE trend, the East-Betic shear Zone (EBSZ, Fig. 7.11a. Relevant recent seismicity, including seismic sequences on the offshore portion and on the south-eastern Iberia, contribute to a good definition of the faulting system in the EBSZ and the stress regime (Stich et al., 2006). This structure separated the compressive tectonic regime to the east observed along the Algerian Mediterranean margin from a transtensional character of present-day deformation to the West Stich et al., 2006. The tectonic structure of the EBSZ is dominated by four major, approx. 50-150 km long, N50ºE trending, left-lateral, strike-slip faults arranged in an echelon pattern. These are, from north to south, the Crevillente fault (CVF), the Alhama de Murcia fault (AMF), the Palomares fault (PF), the Carboneras fault (CF) and the Alpujarra fault (APF) (fig. 7.11a).

Crustal geophysical data are very scarce in the study zone. Deep seismic refraction profiles have been undertaken in the Betic Cordillera and the Alborán Sean during the seventies (Banda et al., 1983, Banda et al., 1993). Interpretations of these profiles suggest that the crust east of the fault system is faster and thinner than that found to the west. P-RFs studies using local seismic networks deployed in the zone have reported significant lateral heterogeneity associated to a NNW dipping Moho reaching 20º and the presence of seismic discontinuities in the upper crust that separate detached and folded major complexes (Pedrera et al., 2010). Recent P-RFs interpretations using dense seismic network support this Moho topography and confirm strong lithospheric and crustal thickness changes between southeast side and the northwest sides of the system fault (Fig. 7.11a, Mancilla et al., 2015b, Mancilla et al., 2015a) (boundary delimited by the red line in the figure). This is also a region of widespread Neogene volcanism (Fig. 2.3) and present day heat-flow ($100 - 110 mW/m^2$, Negredo et al., 2002). This high heat-flow values have sometimes been associated with the emplacement of hot upwelling material beneath the Alborán basin (e.g., Lonergan and White, 1997), and the close spatial correlation of the volcanics with the strike of the faults has yield the image of magma upwelling

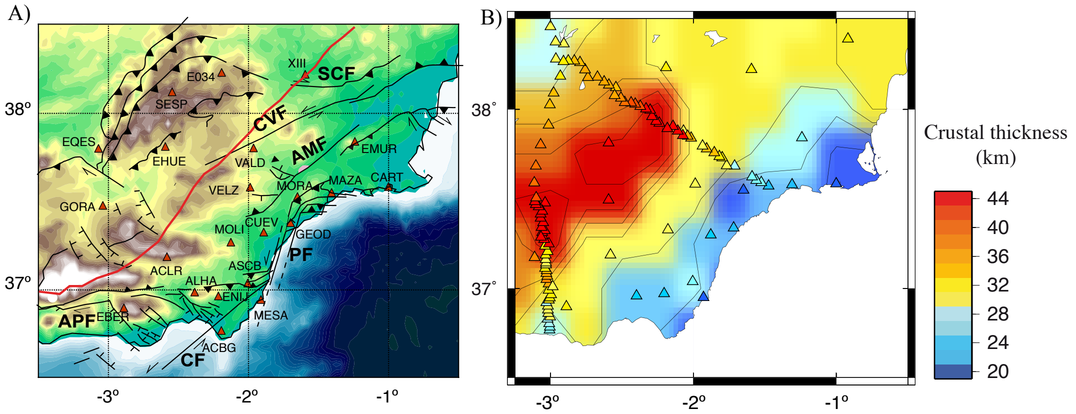

FIGURE 7.11: A) Topography map with the main faults of the Eastern Betic Shear Zone (EBSZ),the stations, B) Crustal thickness of the study area. Stations (triangles) are colour-coded according to crustal thickness

facilitated by fault zone weaknesses (De Larouzière et al., 1988).

Subject to data availability for each station, we analyze between 4 and 10 years of data. A quality control is performed in two steps, one keeping only the recordings with signal-to-noise ratio bigger than 2 and the other step is applied in the deconvolution process; we evaluate receiver function quality convolving them with the Z component of the signal and checking how well this convolution reproduces the original R and T components of the seismograms. We keep only the RFs that can reproduce 85% of the original signal. In total, we use in this study 1057 RFs, giving an average of about 52 RFs for each station (fig. 7.19f). The teleseismic distance range of interest for P-RFs analysis (from 30° to 90°) covers very active seismogenic source areas to the NE (southeastern Asia) and SW (central and South America), while northwestern and southeastern are underrepresented (fig. 7.10b). The available traces usually allow tracking the subsurface structures over a broad azimuthal range and provides acceptable backazimuthal coverage for harmonic decomposition analysis. The teleseismic distance range used makes the ray parameter distribution concentrates within an acceptable range (fig. 7.10c) to apply properly the move-out correction as we have already discussed in this section 7.1.1. The

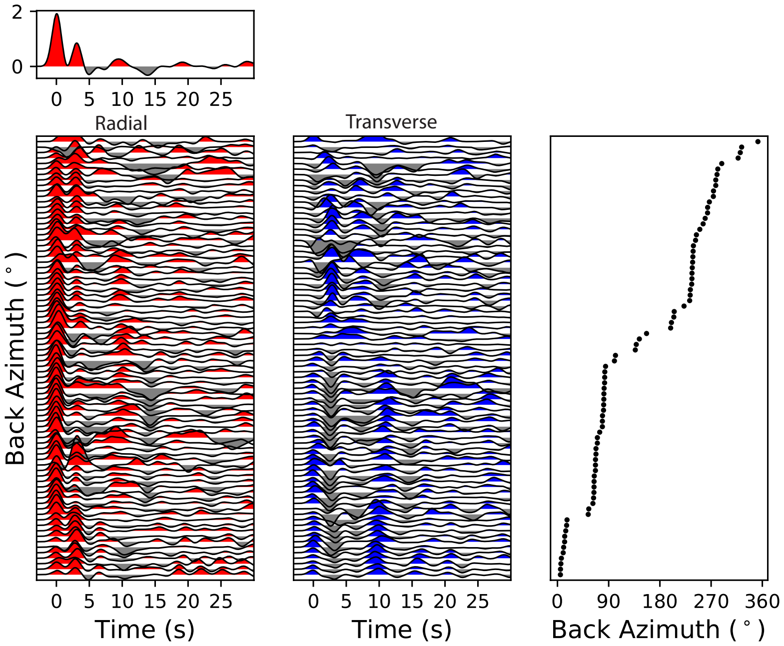

FIGURE 7.12: Radial (left) and tangential (right) RFs computed for the station ASCB sorted by backazimuth. The direct P wave arrival time is taken as origin time. At the top, we show the average radial RF. Note the presence of considerable energy in the transverse component and the backazimuth amplitude variations of RFs

slowness value used for the move-out correction is the averaged value of the slowness distribution. For the amplitude move-out correction we use a realistic surface S-wave velocity of 3.75 km/s. The observed signals are analyzed during the first 7 s after the P-wave onset to obtain information about the crust and upper-mantle structure in the vicinity of the recording station. Note that we must restrict the time domain to this range because our harmonic decomposition method can not be applied simultaneously to the converted phases and the multiples (see section 7.1.1). We use the time-iterative deconvolution technique (Ligorria and Ammon, 1999) with a Gaussian pulse width of 1.0, translating into receiver function pulses around 1.67 s wide. More stable results are obtained working in this lower frequency range, thought in most of the cases the results that we infer using higher frequencies (above 1 Hz) are consistent.

As a representative example we show the radial and transverse RFs of the ASCB station in figure 7.12. The RFs exhibit significant energy in the transverse component, being this amplitude comparable to the amplitude contained in the radial component. We can distinguish amplitude variations in both components with backazimuth in direct (0 s) and the Moho converted (3 s) phase arrivals, including changes of polarity in the transverse component. The Amplitude polarity change occurs at back azimuth $\sim 160^{\circ}$ for ASCB station. Few individual traces appear to exhibit an anomalous behavior not following the backazimuth amplitude variation trend of the surrounding traces. These traces maybe are noisy RFs not discarded by the quality control filter or signal generated by very local structures. As we use a sufficient amount of RFs, these anomalous traces do not affect the averaged structural effect that we are modeling with the harmonic decomposition method. The harmonic decomposition traces recover most of the radial and transverse backazimuth amplitude variation within the first 7 s (fig. 7.13). The misfits between real and harmonic decomposition traces of radial and transverse components exhibit aleatory fluctuations due to very local effects or the presence of significant noise (fig. 7.13d and e). Weight factors show that independent term of backazimuth, A0, holds most of the energy (60 %), followed by the A1 (26 %) and the A2 (13 %) terms.

We perform a harmonic decomposition analysis using only the radial, only the transverse and both radial and transverse components. Note that the transverse component on one hand is less sensitive to the move-out correction and on the other hand is affected mainly by the lateral heterogeneity we are modeling, dipping interfaces and anisotropic layers. Figure 7.14) shows results of the harmonic decomposition method, variation of the coefficients and vectors ($\vec{a_1}$ and $\vec{a_2}$) with time for some selected stations including ASCB station located in the Alboran Domain (or Internal zone) that present similar results and in Figure 7.15 for selected stations as representative for stations with erratic behaviour of the vectors and no clear coherence between radial and transverse components approaches. The vectors $\vec{a_1}$ and $\vec{a_2}$ are normalized by the maximum amplitude for each panel. The maximum amplitude is displayed on top of each panel. The results of all the stations, sorted out alphabetically, are

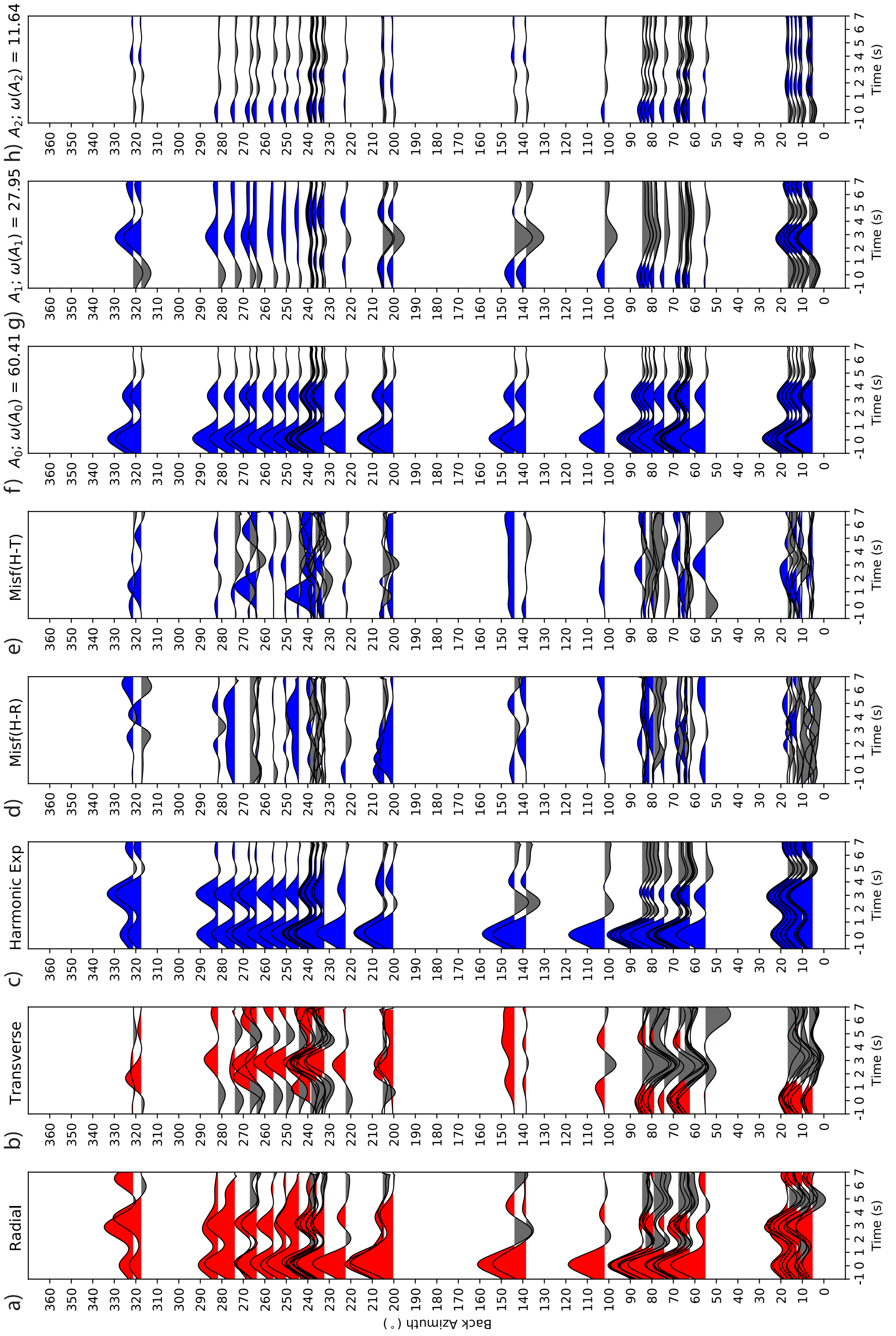

FIGURE 7.13: RFs for the station ASCB sorted by back-azimuth. (a) Radial and (b) transverse components, (c) harmonic expansion for radial traces, (d) misfit between (a) and (c) traces and (e) misfit (b) and (d), (f-h) A_n harmonic components for $n = 0, 1, 2$, respectively. Values shown on top of (f-h) panels are the relative weights ω_n of the harmonic terms within the expansion obtained according to equation 7.1.

displayed in the appendix A.

For the station located in the Alboran domain (Fig. 7.14), the largest amplitudes of the coefficients, accordingly vector norms, are found within the first 5 s, indicating that the lateral heterogeneities are mainly constrained to the crust. In the study area, the vector $\vec{a_1}$ exhibits the largest lengths for delay times corresponding to the direct and the Moho converted phases ($\sim$ 3s). This can be seen in the coefficients' panels where the peaks of the coefficient a_0 and a_1 coincide. Remember that the red curve represents coefficient independent of backazimuth. The constant backazimuth harmonic a_0 is influenced mainly by the isotropic seismic structure and informs us about the Moho depth. We find a positive pulse in all stations between 2.5s and 4 s. We associate this arrival with the positive velocity jump of the Moho discontinuity. This phase arrives progressively later from roughly SE to NW, indicating that the Moho interface dips to the NW direction (Fig. 7.11B). The vector $\vec{a_1}$ is aligned for the direct and converted delay times and point preferentially at a NNW direction in agreement with the Moho depth variations observed with the a_0 coefficient. This behaviour is characteristic of the lateral heterogeneity produced by a dipping interface.

The vector $\vec{a_2}$ present generally less length than the vector $\vec{a_1}$, its direction exhibits a more erratic pattern but mainly points at the NNW direction being aligned with the vector $\vec{a_1}$. Note that after the rotation that we apply (see fig. 7.7), the vectors associated to each lobe of the 2-lobes pattern of an anisotropic layer, have perpendicular directions. The characteristic 2 consecutive lobes (green line) appear clearly in the stations ACBG and MESA, fig. 7.14b and c, respectively, and are aligned in the coefficient panels with a_0 and a_1 coefficients. It is difficult to constrain the depth at which the anisotropic layer is located due to the low frequency range that we are using, but according to where the lobes of the vector $\vec{a_2}$ are located it seems that this anisotropy might be distributed in the whole crust. The fact that both vectors $\vec{a_1}$ and $\vec{a_2}$ have similar patterns means that either there is an anisotropic layer with its fast axis is

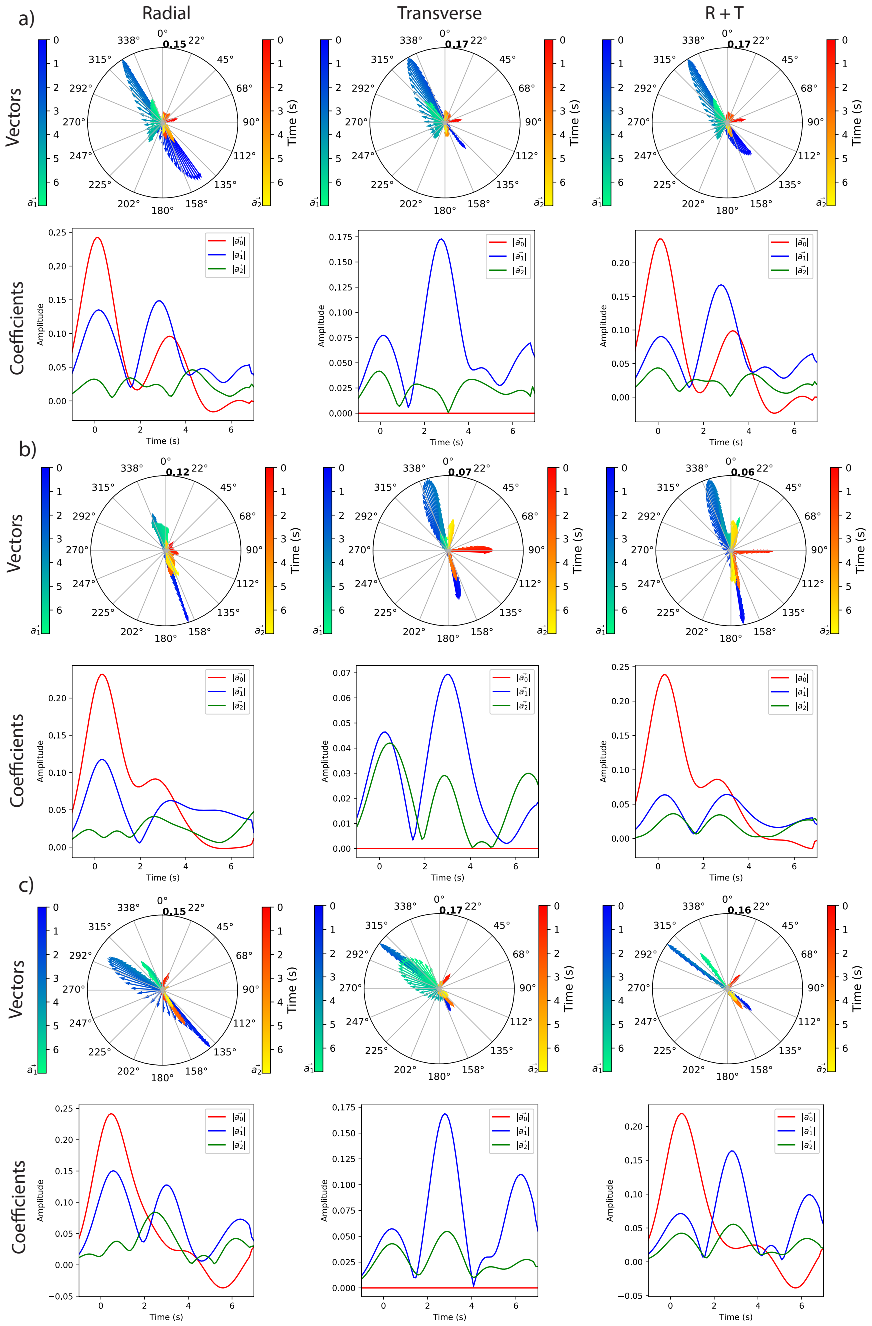

FIGURE 7.14: Direction and norm of the vectors $a_n(t)$, $n = 0, 1, 2$, along the time once applied the harmonic decomposition method using only the radial component (1st column), the transverse component (2nd column) and both components (3rd column) for the stations a) ASCB, b) ACBG and c) MESA. The vectors are normalized, the maximum amplitude is indicated on top of each vectors' image.

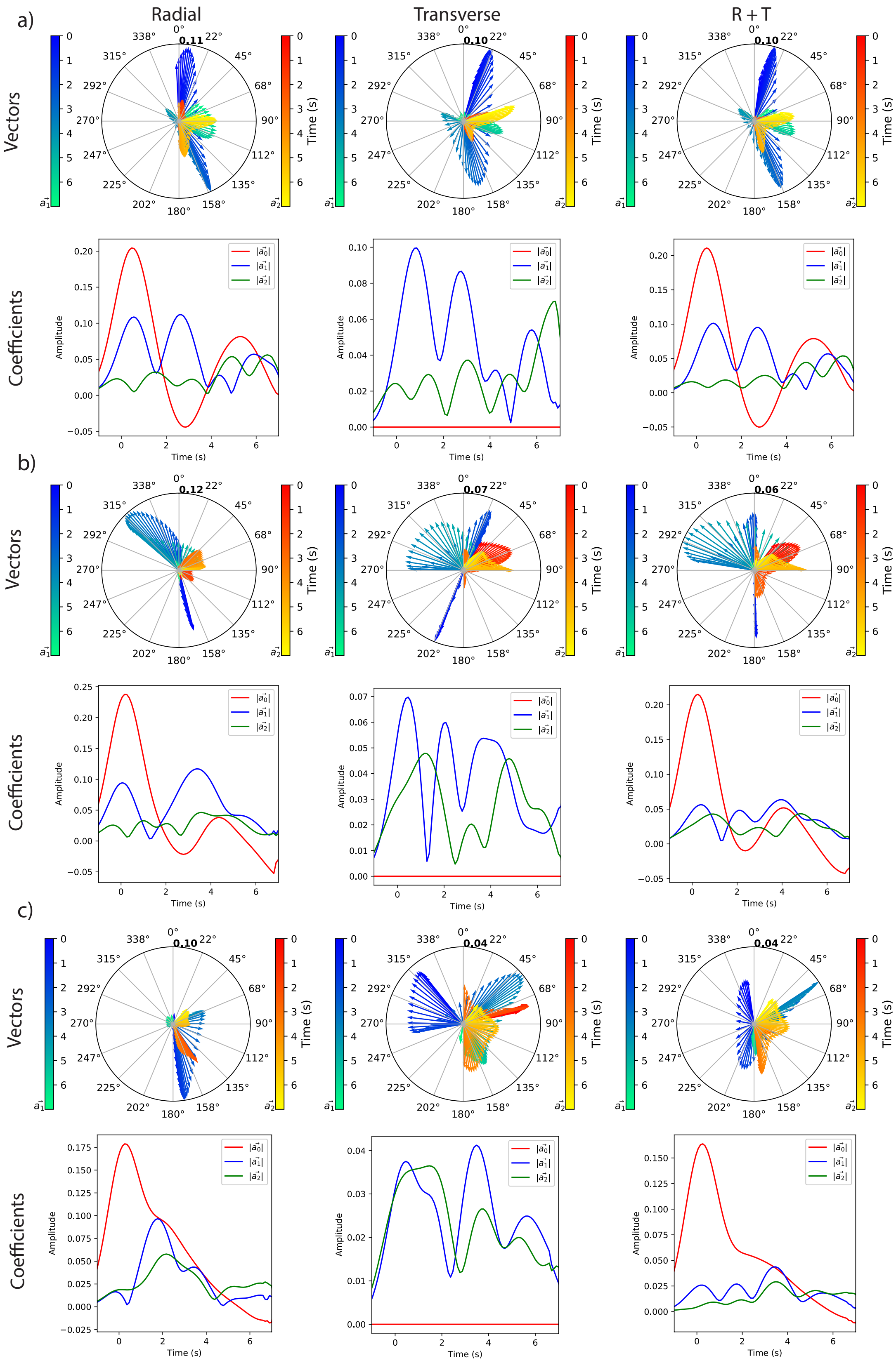

FIGURE 7.15: The same than fig. 7.14 for the stations a) GORA, b) EBER and c) EQES.

inclined or a dipping interface and an anisotropic layer are both present with similar geometry. Notice that the vectors have significant length for depths larger than the Moho in the case of the station MESA (fig. 7.14c). This vector points at a slightly different direction than the vectors at shallower depths and the lateral heterogeneity might be located in this case in the uppermost mantle.

For these stations, there exist coherence in the results obtained with radial and transverse component analyses (fig. 7.14). Using both component helps to better constrain the directions of the vectors (the third column of fig. 7.14) presenting more defined directions. Though there is coherence between the directions of the vectors, their amplitudes are slightly different depending on the approach we use, especially for the direct onset for which the radial approach gives more amplitude to the vector $\vec{a}_1$. This might be generated not only by an effect of the move-out correction which affects more the direct onset of the radial component but also for the presence of lateral variations of the velocity at very shallow depths.

Figure 7.15 displays the results of the harmonic decomposition analysis for other three stations. We select these cases as representative for stations with erratic behaviour of the vectors and no clear coherence between radial and transverse components approaches:

- Station GORA (fig. 7.15a) displays no clear alignment of the vector $\vec{a}_1$ for the consecutive peaks concentrated within the first 4 s. The second maximum of the vector located at about 3 s seems to be associated to a low velocity zone and points at the NNW direction. Probably these two vectors are recovering the lateral heterogeneity of different structures. The vector $\vec{a}_2$ exhibits the largest amplitudes for very late times and point at the predominant NNW direction. This might be attributed to anisotropy in the uppermost mantle.
- Station EBER (fig. 7.15b) shows no coherence between the radial and transverse component approaches, even though the vector $\vec{a}_1$ point at

well defined directions. The vector $\vec{a_2}$ exhibits an aleatory behaviour.

- The EQES station (fig. 7.15c) displays very erratic patterns of the vectors and no coherence between components is observed. The maximum amplitude of the radial approach is much larger than the transverse approach which makes us to think that other kind of lateral heterogeneity just affecting the radial component is present.

In order to analysis the spatial distribution of the harmonic decomposition coefficients, in figures 7.16 and 7.17, we plot on the map the vectors $\vec{a_1}$ (right panels) and $\vec{a_2}$ (left panels) of all the stations along the time:a) for the first 6s (Fig. 7.16a and 7.17a),b) for the first 3.5 s containing crustal information mainly for the station of the Alboran domain (Fig. 7.16b and 7.17b), and c) for 3.5s to 8s containing information of the lithospheric mantle for the Alboran domain station and, together, for lower crust for stations located in the External Zone (Fig. 7.16c and 7.17c). Well-defined patterns are present in the maps, that allows us to draw interesting observations.

The stations whose $\vec{a_1}$ vector have a coherent direction are mainly located nearby the coastline at longitudes between -2.5º and -1.5º (ACBG, MESA, ASCB, ALHA, MOLI, GEOD, MORA, MAZA, VELZ, VALD). In Fig. 7.17b) they present the largest amplitudes and display, except CUEV station, a NNW general trend. As expected for the case of a dipping interface, the maximum lengths of the vectors along the time coincide with the direct and Ps converted arrivals and are antiparallel. The interface dips in the direction of the converted phase, blue color in the fig. 7.17a. The direct arrival is concentrated within the first second and the Ps converted arrival within the 2.5-3.5 s time window. As we see in the figures of the appendix A, for these stations there is coherence between the radial and transverse vectors so lateral heterogeneity might not be attributed to lateral variations of the velocity structure.

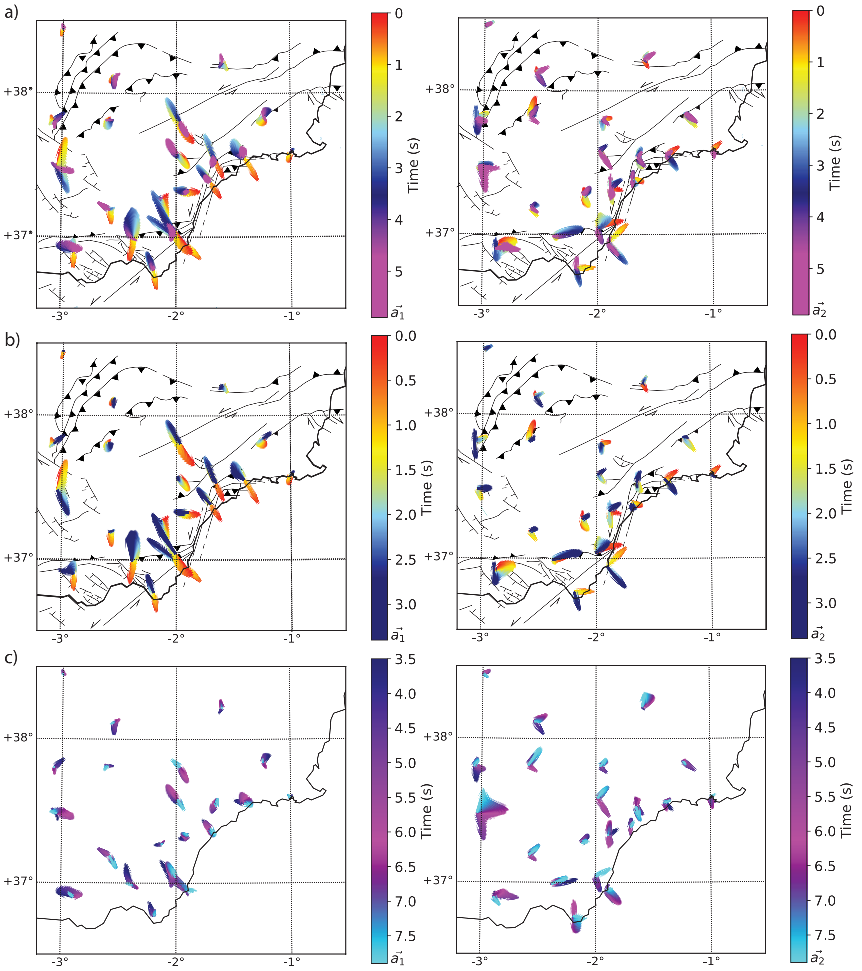

FIGURE 7.16: $\vec{a}_1$ and b) $\vec{a}_2$ vectors' map obtained with the harmonic decomposition analysis using both radial and transverse components for different time windows: (a) crustal and subcrustal delay times (0-6 s), (b) crustal delay times (0-3.5 s) and (c) subcrustal delay times (3.5-8 s). The length of the arrow is proportional to the amplitude of the vectors, being $\vec{a}_2$ the double length than $\vec{a}_1$.

.

FIGURE 7.17: same than Fig. 7.16

but translating arrival times to depth using a 1D velocity model explained in section 3.2

For the station located in the Alboran domain and nearby the main faults of the EBSZ, the time and dip direction marked by the $\vec{a_1}$ vectors is in agreement with the depth at which the Moho is located by other seismic study along the seismic network and its observed gradient, respectively (Fig. 7.11B, Pedrera et al., 2010; Mancilla et al., 2015a). An important observation is that these dip directions are perpendicular to the strike direction of the nearby fault (see CUEV and GEOD stations). This support the idea that the EBSZ fauls affect the entire crust (Julià, 2005). The pink colour in vector $\vec{a_1}$ corresponds to structures placed beneath the Moho discontinuity. Though the vector $\vec{a_1}$ located at these depths depict some direction coherence with the rest, their length is smaller.

The $\vec{a_1}$ vector of the stations located at the longitude of -3° (EBER, GORA) do not display a unique orientation. They twist toward the S and seldom N, describing a fan-like pattern. The coherence between the direct and converted arrival is not as clear as for the other stations. Furthermore, the results obtained from the radial and transverse components approaches do not exhibit a complete coherence, which makes us to think that the lateral heterogeneity might have other causes as lateral variations of the velocity that only affect to the radial component. The vector $\vec{a_1}$ of the stations located in the North and Northeast (EQES, EHUE, SESP, XIII, EMUR, and CART) do not point at privilege directions and are relatively shorter, suggesting weaker dipping and/or anisotropy.

Two patterns of the $\vec{a_2}$ vectors are observed at crustal depths (marked by Green square and red circles in Fig. 7.18). These two patters present orthogonal geometry and different depth extensions. One of them is observed in stations close to the coast (Green square Fig. 7.18) presenting larger amplitudes than the other pattern observed in stations further away in the interior (red circles in 7.18). The largest $\vec{a_2}$ vectors correspond to the stations MESA, ACBG, ASCB, and EBER, reaching the maximum amplitudes for times contained within the time windows of 0-1 s and 2-4 s covering most of the crust. They point at orthogonal directions, as expected for phases converted at the upper and lower interfaces of an anisotropic layer, marking the fast and slow axis. The axis of the observed anisotropy coincides with the direction of the $\vec{a}_1$ vector, suggesting either that the symmetric axis of the anisotropic layer is tilted or that the geometry of both lateral heterogeneities dipping and anisotropy are related.

The second pattern presents similar amplitudes in all the stations (red circles in Fig. 7.18a) and has orthogonal directions to the above observed pattern (green square in Fig. 7.18a). The location of anisotropy layer is restricted to the middle to lower crust between 10km to 30km depth.

The mechanisms of the seismic anisotropy in the crust can be divided into two main categories (e.g. Boness and Zoback, 2006): structural anisotropy and stress-induced (see Fig. 7.18b). **Structural anisotropy** occurs when macroscopic features such as fault-zone fabric polarize the S-waves with a fast direction in the plane of the feature similar to the first observed pattern in station close or on to the main faults of the EBSZ (green squares (Fig. 7.18a). The **Stress-induced shear anisotropy** is the result of regional σ_1 or SH_{max} causing microcracks to open and/or preexisting macroscopic fractures to close, generating a fast direction parallel to σ_1. This is similar to the second pattern observed in stations away from the coast (red circles in Fig 7.18a). The spatial and in depth distribution of both pattern suggest a stress-induced anisotropy in the area modify locally by the main faults of the EBSZ which produce a structural anisotropy. This structural anisotry seem to be spread along the crust supporting that these fault control the crustal deformation.

In Fig. 7.17, we separate the vectors $\vec{a}_1$ and $\vec{a}_2$ into two different time windows. The time windows corresponding to the crust a) (0-4 s) and to the uppermost mantle b) (4-8 s). For deeper structures, the length of the vector $\vec{a}_1$ decreases considerably exhibiting quite erratic patterns. However, the vector $\vec{a}_2$ shows large values with a two consecutive lobes pattern whose vectors point at orthogonal directions. These vectors correspond to stations located in a region

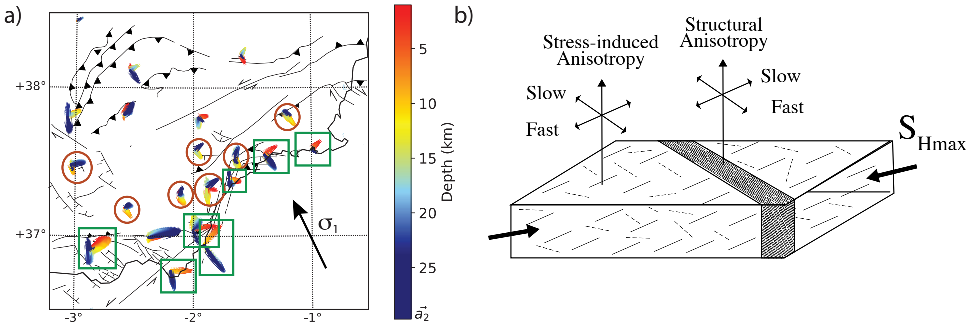

FIGURE 7.18: a)$\vec{a_2}$ vectors in the first 30 km of the crust. Green squares and red circles mark two different patterns observed. The arrow labels by σ_1 is direction of the regional compress stress retrieved by regional moment tensor inversion studies (Stich et al., 2006). b) Sketch of the anisotropy mechanism in the crust modified from Boness and Zoback, 2006

where a double Moho is present (SESP, EHUE, EQES and GORA, Mancilla et al., 2015a). This homogeneous anisotropy orientation might be then regarded to an anisotropic body/layer trapped between these two discontinuities. Similar results have been obtained in the northern Apennines by Bianchi et al., 2010.

The good regional coverage and fairly dense stations spacing allow for interpolating single station measurements into a continuous map of some observable for the entire study. Figure 7.19 shows the A_i factors, for $i = 0, 1, 2$, the misfit between harmonic decomposition and real traces for radial and transverse components and the number of RFs used in each station of the network. The A_0 factor contains the homogeneous isotropic content of the RFs, lower values imply that more lateral heterogeneity is present beneath the station. Areas with more lateral heterogeneity are located nearby the coastline between longitudes -3^{o} and -2^{o} (note that the color scale in 7.19a is inverted). The station EQES has high values for the radial and transverse misfits, suggesting that most of the lateral heterogeneity can not be recovered with our analysis and might be associated to other sources. The highest values of the factor A_1 are localized in the stations MESA and ASCB. The anisotropic factor A_2 is restricted nearby these stations too.

7.3 Conclusions

In this chapter, we present a technique for the study of lateral heterogeneity employing RFs and apply it to a real teleseismic dataset in a region geologically diverse and structurally complex. The technique exploits periodical amplitude variation with backazimuth of RFs affected by lateral heterogeneity and decompose this signal into backazimuth harmonics. It permits to separate the isotropic information from the energy due to anisotropic and/or dipping subsurface structures, becoming a useful tool for the understanding of subsurface geometries, mainly in the crust. The method successfully use both radial and transverse components which gives better constraints on the seismic structure than radial-only RFs analysis. The inclusion of the transverse component not only double the amount of dataset compared to conventional approaches, but also helps to determine if the lateral heterogeneity is due to dipping interfaces and/or anisotropic layers as the transverse component is mainly sensitive to these sources of lateral heterogeneity.

The harmonic decomposition method implemented is linear and allows to build a time dependent vector representation of the terms in the expansion, simplifying notably the interpretation. The alignment of the vectors $\vec{a}_1$ and $\vec{a}_2$ and the time delays at which they are concentrated help to remove some ambiguities inherent to the kind of lateral heterogeneity we are studying.

We illustrate the method through a synthetic study investigating three basic scenarios; a dipping interface, a flat anisotropic layer and an inclined anisotropic layer. Furthermore, we evaluate the goodness of the moveout correction on radial and transverse components and conclude that the transverse component is less sensitive to the slowness variation of RFs. This, combined to the fact that transverse RFs are mainly affected by the lateral heterogeneity due to anisotropic layers and dipping interfaces, permit through comparative radial- and transverse-only harmonic decomposition approaches determine with less ambiguity the source of the lateral heterogeneity.

We apply the harmonic decomposition method using a comparative radial and transverse component study to real RFs located in the southeastern region of the Iberian Peninsula. We obtain a continuous representation of the lateral heterogeneity with depth along the crust and the uppermost mantle, determining the orientation of anisotropy and dipping interfaces. Our study shows that crustal and uppermost mantle anisotropic characteristics might differ in their orientation. Stations located nearby the coastline and faults exhibit the presence of considerable lateral heterogeneity at crustal depths. The vector $\vec{a}_1$ is oriented predominately in a NNW direction, in agreement with previous results which report a gently dipping Moho following in this direction (Fig. 7.11B). The vector $\vec{a}_2$ seems to be geometrically related to the fault system present in the region and related to the vector $\vec{a}_1$ at crustal depths. At deeper depths, below the Moho, the vector $\vec{a}_2$ reaches the largest lengths for the stations located above a region with double Moho. This anisotropy might be related with an anisotropic structure trapped between the two Moho discontinuities.

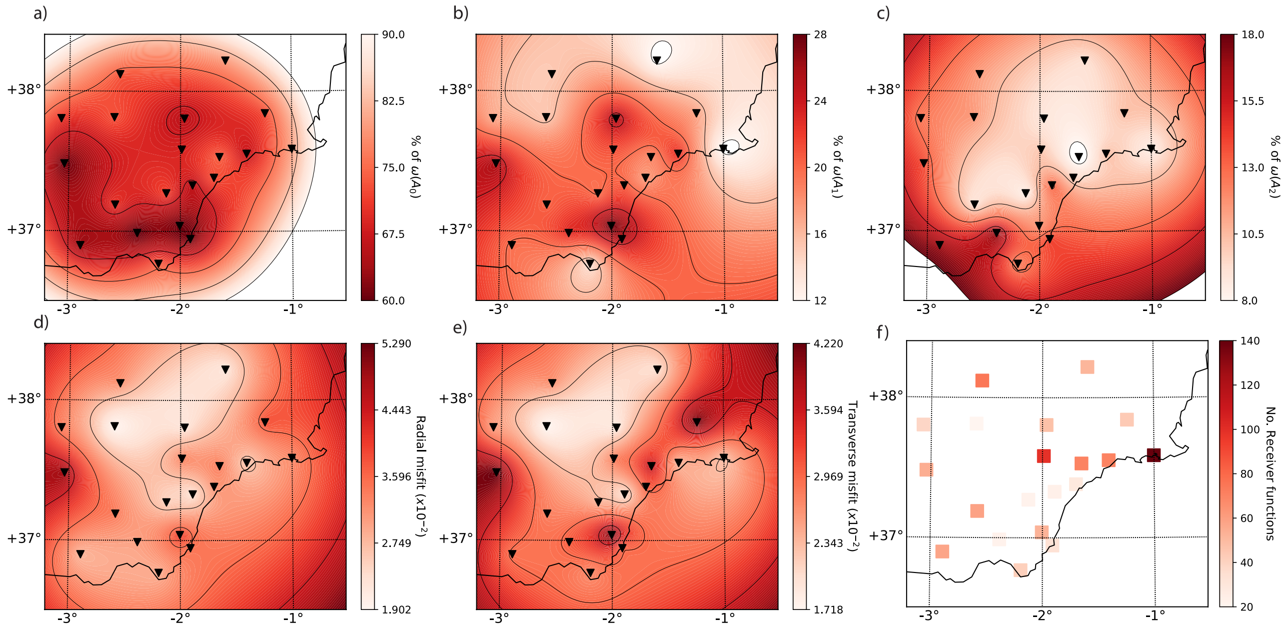

FIGURE 7.19: a), b) and c) map with weights corresponding to the factors (A_i) for i = 0,1 and 2 respectively, within the expansion. d) and e) depict the radial and transverse misfit respectively. f) Map with the stations' names.

Chapter 8

Joint Inversion of RFs and surface wave dispersion curves in Eastern Betics

The construction of crustal and uppermost mantle velocity models over extended regions is crucial to an understanding of continental tectonics and the thermal and compositional structure of the lithosphere. The 3-D model can be used not only to improve regional seismic event location but also as a starting model for other types of seismic investigations as CCP stacking and body tomography.

Velocity models are obtained in geophysics through inversion methods. An inverse problem in science is the process of computing from a set of observations the causal factors that produced them. The objective therefore is to find the best model parameters m such that (at least approximately) $d = G(m)$, where G is an operator describing the explicit relationship, the governing equations, between the observed data d and the model parameters m. We solve the inverse problem using either mathematical techniques that invert the matrix G to directly convert the measurements into our model parameters, or by trial-and-error techniques that solve the forward problem repeatedly and look for the best solution. Inverse problems often have no unique, exact, or "correct" solutions. Because the data are generally somewhat inconsistent due to errors, and our models simplify complex reality. Similarly, a range of parameters can describe the data equally well for a given model.

Many RF inversion studies have been carried out since the 1980s (e.g., Owens, Zandt, and Taylor, 1984; Mangino, Zandt, and Ammon, 1993; Julià, Vila, and Macià, 1998). Since RFs are primarily sensitive to vertical shear-wave velocity contrasts and vertical travel times (Vinnik, 1977; Langston, 1979), interpretation of such data may posses an apparent depth-velocity trade-off (Ammon, Randall, and Zandt, 1990). The simultaneous joint inversion of multiple geophysical datasets takes advantage of the complementary sensitivity to different parameters of the model that each data type has to avoid significant non-uniqueness problems and bridge resolution gaps associated with each individual dataset. Surface-wave dispersion measurements are an appropriate complementary measurement of RFs because they constrain the absolute S-wave velocity information being sensitive to vertical shear-wave velocity averages (e.g., Levshin and Ritzwoller, 1995; Shapiro et al., 2005). As a consequence, the combination of RFs and surface wave dispersion curves was a natural direction for research to determine structure near to Earth's surface, being the linear joint inversion methods particularly popular (e.g., Du and Foulger, 1999; Julià et al., 2000; Julià, Ammon, and Herrmann, 2003; Endrun et al., 2004).

Conventional approaches of RFs inversion methods assume conditions of low anisotropic and/or dipping boundaries. They invert stacked receiver functions from different backazimuth to obtain a single-velocity model, which represents the laterally homogeneous velocity structure under the receiver (e.g., Julià, Ammon, and Herrmann, 2003; Julià, 2007; Luz, Julià, and Nascimento, 2015). However in the presence of considerable lateral heterogeneity associated to dipping interfaces and/or anisotropy the inversion becomes unstable. One approach to this problem is trying to remove the effects that lateral heterogeneities cause on RFs and thus construct an independent of backazimuth receiver function, which is only sensitive to a horizontally layered isotropic effective medium. The latest strategy of obtaining an only flat-layered isotropic model sensitive to RFs is used the harmonic decomposition (HD) analysis to obtain the isotropic harmonic (a_0 coefficient) and afterwards use it in the joint inversion process that has been recently applied by (Shen, Ritzwoller, and Schulte-Pelkum, 2013).

In this chapter, we will combine the linearized joint inversion method of RFs and surface waves dispersion curves implemented by Julià et al., 2000 with the HD method explained in chapter 7.1.2 and demonstrate its relevance in scenarios with important presence of lateral heterogeneity. Furthermore, methodologies based on the HD analysis are more effective for incomplete and non-uniform azimuthal coverage than traditional ones. As a disadvantage, moveout corrections are necessary forcing not to include the multiples of the RFs. Theses multiples of RFs are quite relevant in the inversion because contain Moho reverberations such as PpPs or PsPs phases used to determine v_p/V_s ratio (Zhu and Kanamori, 2000).

8.1 Methodology

8.1.1 Linearized Joint Inversion Method

In inverse problems we cannot directly invert the observation matrix, needing to use methods from optimization. To do so, we define an objective function. This objective function is a functional that measures how close the predicted data from the recovered model fits the observed data. The standard objective function is usually of the form:

$$\phi = ||d - Gm||^2{}_2 \tag{8.1}$$

which represents the L-2 norm of the misfit between the observed data and the predicted data from the model. Computing the gradient of the objective function we achieve its goal, minimize the difference between the predicted and observed data.

We use the iterative linearized damped least-squares scheme implemented by Julià, Ammon, and Herrmann, 2003 which starting from an initial model minimizes a weighted combination of the normalized root-mean-square (RMS) of the difference between observations (y, z) and predictions (Y, Z) for each dataset; RFs and surface wave dispersion curves. The inversion procedure relies on data derivatives with respect to model parameters, which were approximated numerically through first-order differences.

$$E_{y|z} = \frac{p}{N_y} \sum_{i=1}^{N_y} (y_i - \sum_{j=1}^{M} Y_{ij} x_j)/\sigma_{y_i} + \frac{1-p}{N_z} \sum_{i=1}^{N_z} (z_i - \sum_{j=1}^{M} Z_{ij} x_j)/\sigma_{z_i} \tag{8.2}$$

In order to equalize the relative weight of each dataset during the inversion, the normalization of the RMS differences involves division by the number of

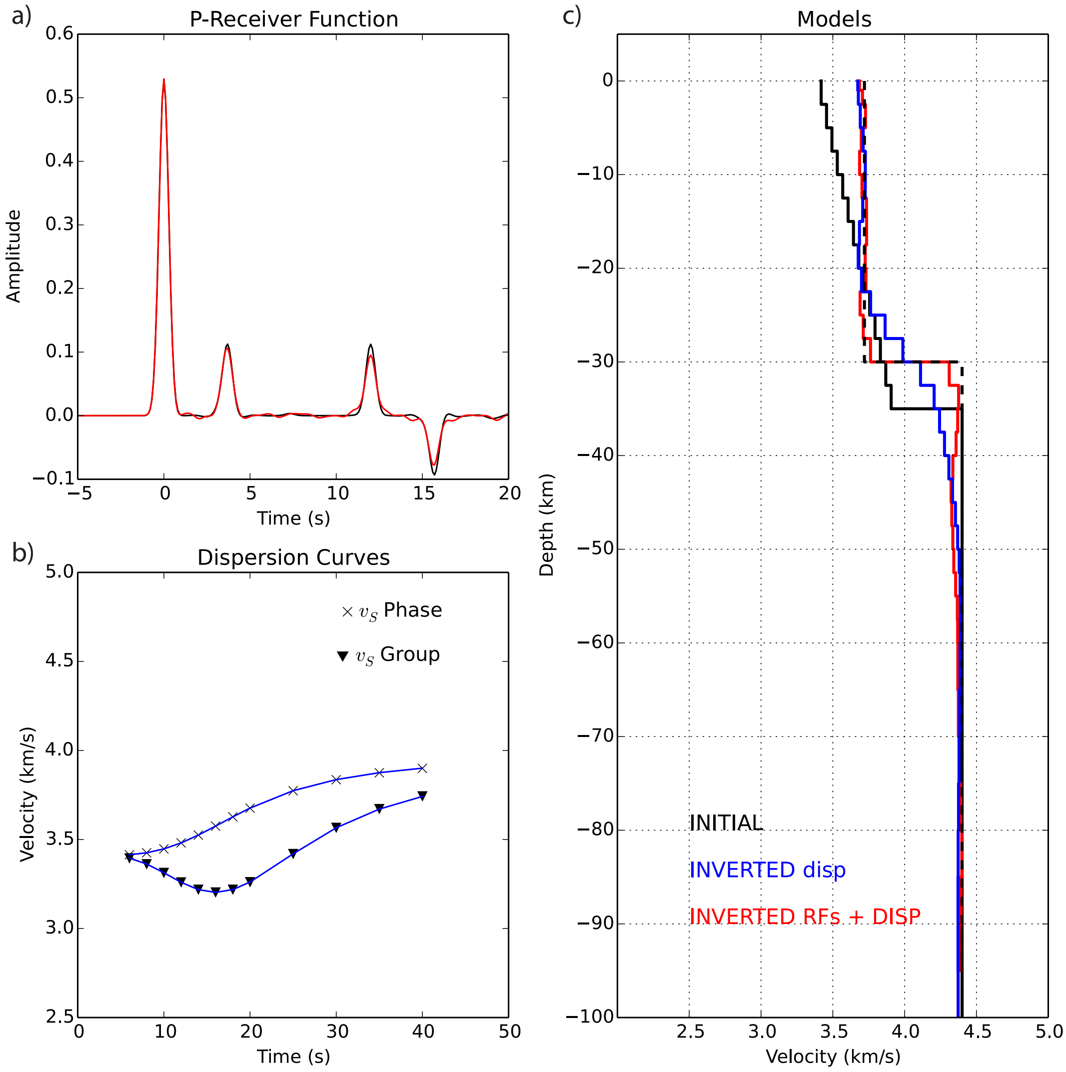

FIGURE 8.1: Synthetic experiment illustrating the goodness of the joint inversion method of PRFs and surface waves dispersion curves. Inverting only Rayleigh surface waves (phase and group velocities) dispersion curves permits to determine the averaged S-wave velocity (blue lines in b) and c)). When we include PRFs in the joint inversion, Moho depth and velocity contrast are constrained (red lines in a) and c)). Continuous and discontinuous black lines in c) depict the initial and real model, respectively.

data points (N_y,N_z) and the variance (σ_{y_i},σ_{z_i}). Two a priori parameters p and s control the influence of each dataset and the smoothness during the inversion procedure, respectively. The influence factor p controls the trade-off between fitting the RFs and the dispersion curves, and the smoothness parameter s regulates the trade-off between fitting the data and model smoothness.

The joint inversion produces earth models where details constrained by RFs are superimposed on a back-ground velocity model constrained by the dispersion measurements. We illustrate in fig. 8.1 with a synthetic experiment the convenience of using jointly both datasets. Surface waves dispersion curves constrain the absolute S wave velocity information while RFs restrict the location and jump in shear velocity. The delay time and amplitude of the Ps converted phase improves the accuracy of estimates of depth and v_{SV} contrast across the discontinuity, respectively. Furthermore, due largely to a reduction of the trade-off between Moho depth and lower crustal velocity, better determination of mantle structure below the Moho discontinuity is accomplished as well.

8.1.2 Harmonic Decomposition Analysis: Backazimuth independent receiver function

Joint inversion methods are based on the assumption that the medium under the recording station is approximately 1D. We ascertain this condition by checking out small transverse amplitudes. Traditionally, to invert the velocity model beneath a stations RFs are grouped within bins according to similar values of ray parameter and backazimuth. Binning around ray parameter is necessary to ensure that the Ps conversions are enhanced during the point-to-point averaging process because the timing of the P-to-S conversions in RFs changes with slowness. To examine the presence of lateral variations in crustal structure around the station we gather into the backazimuth. The velocity model obtained is a representative, laterally homogeneous average of

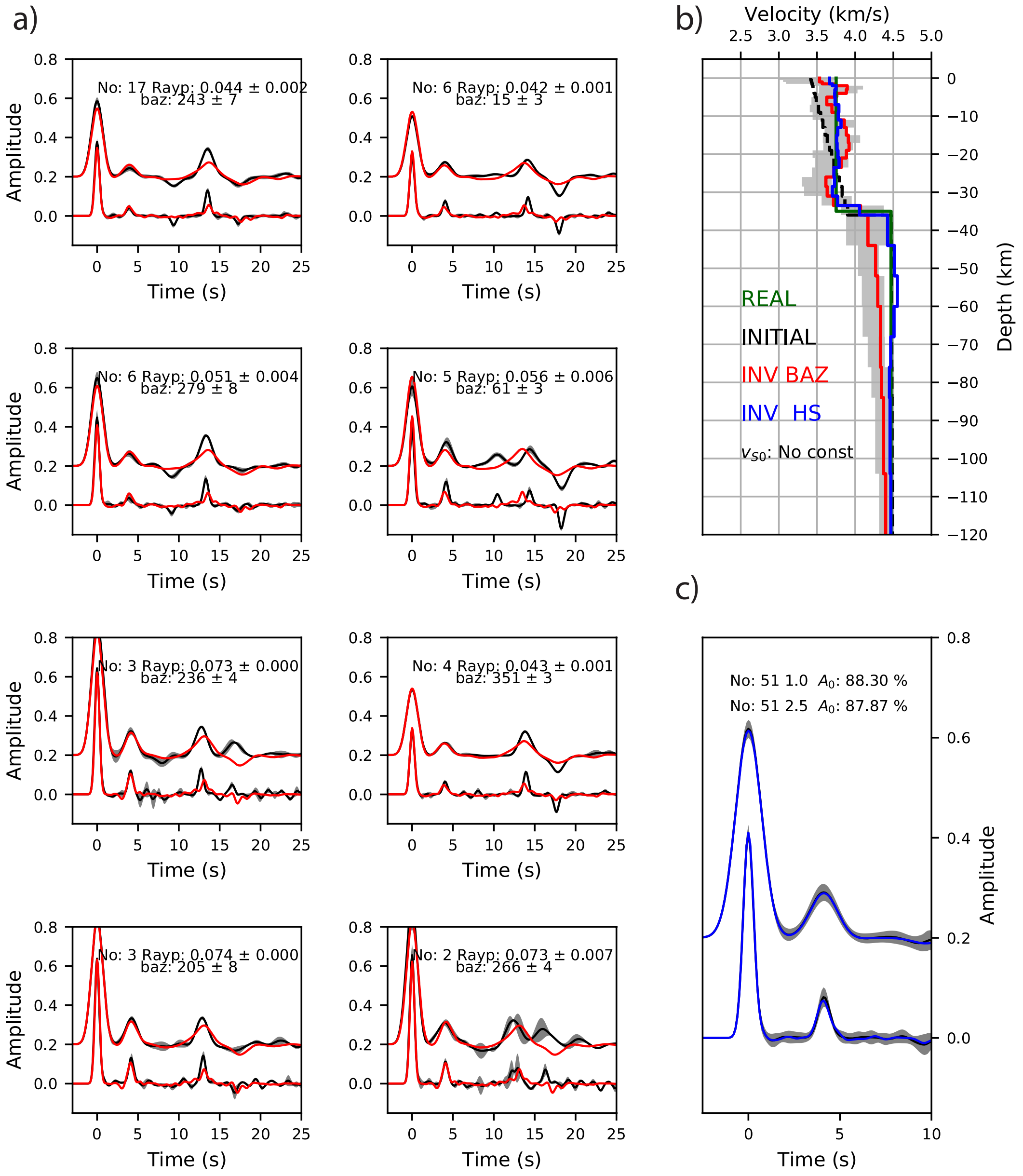

FIGURE 8.2: Inversion synthetic experiment in a media with a 35 km depth Moho dipping 10° (strike angle 0° relative to North) in which we compare the approaches of a) backazimuth grouped RFs and c) backazimuth independent RF obtained from the HD analysis. The inverted models obtained with each approach are displayed in c); red and blue lines for the BAZ and HD approaches, respectively. Initial and true models are displayed in black discontinuous and green lines.

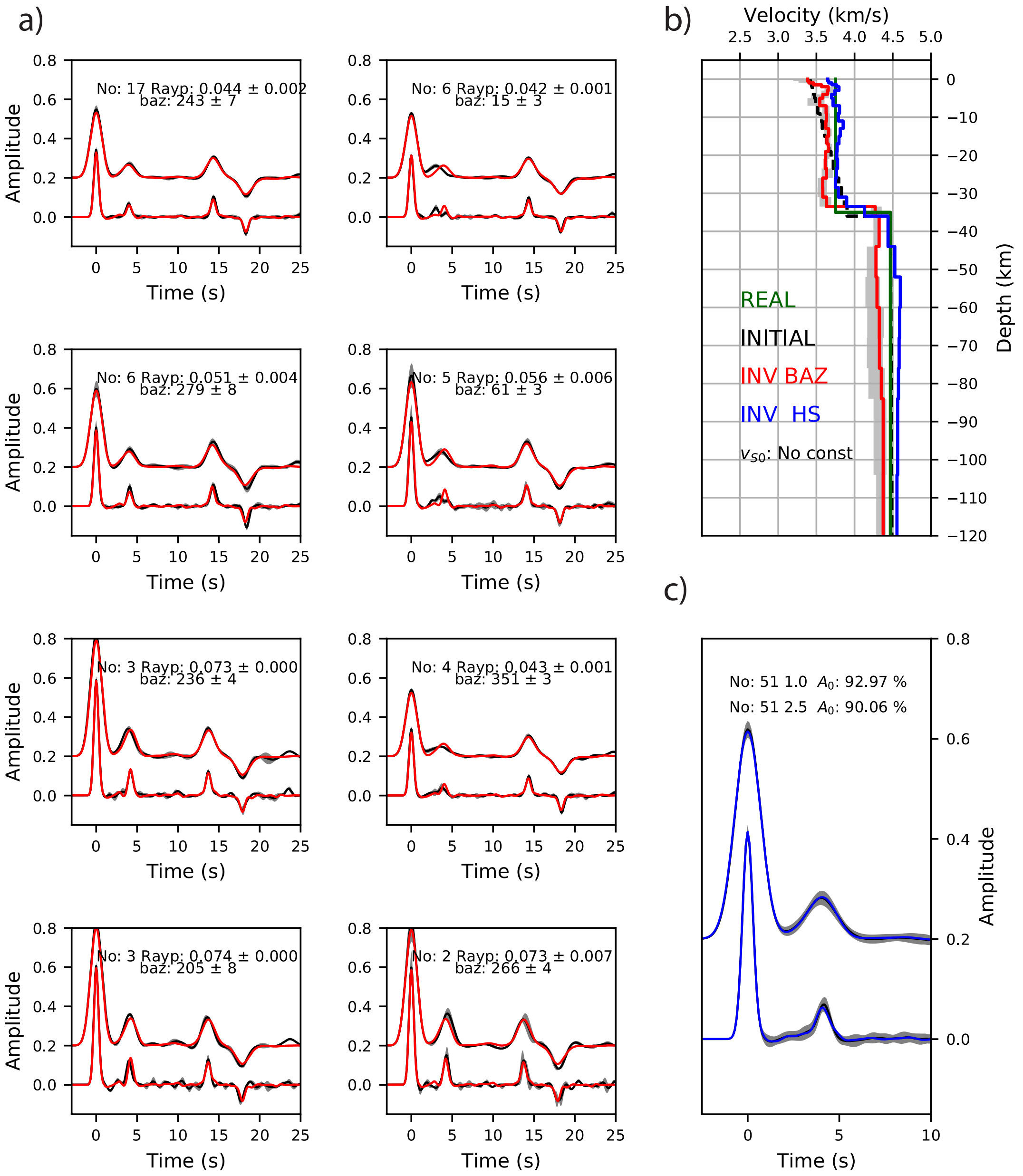

FIGURE 8.3: The same than 8.2 in a media with a 10 km width and 6 % in P- and S-waves anisotropic layer whose fast axis present a plunge of 10°.

the velocity structure under the station. In the presence of dipping and/or

anisotropic structures radial and transverse receiver function waveforms exhibit azimuthal periodicity (see chapter 7.1.2). Signals generated by this lateral heterogeneity are large to dominate RF appearance and inversion methods fail to obtain a reliable velocity model. The goal of the HD method is to remove this azimuthally periodic effect of RFs and recover an independent of the backazimuth trace which contains only information regarding the flat-layered isotropic structure of the medium.

Synthetic inversions are presented here to illuminate the capabilities of the HD analysis already described in chapter 7.1.2 to effectively obtain the 1D S wave velocity model under the station. For the inversion we use the linearized inversion procedure described in section 8.1.1. We use only the RFs dataset in order not to affect the results with the influence of the dispersion curves. As the initial model we use a modified for the Iberian Peninsula PREM model consisting in a 35 km thick crust with a gradational increase of P and S-wave velocities. The model was parameterized as a stack of layers with uniform S-wave velocity covering 210 km in depth. The layer thicknesses increased throughout the stack to reflect the decrease in resolution of seismic waves with depth, being 1.0 km thick down to 5 km depth, 2.5 km thick between 5 and 60 km depth, 5.0 km thick between 60 and 80 km depth and 10 km thick below 80 km depth. The inversion code permits us to control the strength in velocity jumps between adjacent layers through the smoothness parameter. We maintain this parameter with a very low value within the first 60 km depth to allow velocity variations of the inverted model and therefore be able to constrain accurately the Moho velocity contrast. Below 60 km depth the smoothness parameters increases to high values to avoid significant oscillations of the inverted model.

In order to emulate a realistic scenario we consider 56 Gaussian noise-added receiver functions with an azimuthal and slowness distribution similar to the teleseismic events distribution recorded in the study region (section 3.1). We calculate the synthetic seismograms using RAYSUM [Frederiksen and Bostock, 2000] and build the RFs using the time-iterative deconvolution method of Ligorria and Ammon, 1999. RFs are obtained at two overlapping frequency bands $f_c \leq 1.2Hz$ and $f_c \leq 0.5Hz$, using Gaussian filters of widths $a = 2.5$ and $a = 1.0$, respectively. Inversion of RFs with overlapping frequency contents helps discriminate sharp discontinuities from gradational transitions.

We compare inversions performed with the BAZ and HD approaches. The **BAZ approach** inverts for all the RFs grouped within bins of maximum variation in ray parameter of 0.01 s/km and 10° in backazimuth; (2) the **HD approach** inverts only for the backazimuth independent receiver function obtained with the HD technique (a_0 coefficients). In this case, the receiver function waveform is discarded after 10 s because the moveout correction is appropriate for direct Ps conversions but not for reverberations. Moveout correction is made both in time and amplitude, using as the reference value the averaged slowness of the distribution (see section 3.2.1).

On the basis of the 35 km depth 1D velocity model, we deal with two basic lateral heterogeneity scenarios; (1) a dipping Moho interface and (2) azimuthal anisotropic crustal layer:

1. The **dipping Moho** scenario is made of an interface dipping 10°. Figure 8.2 shows the results of the inversions using both approaches. The true (black) and inverted (red) RFs grouped by backazimuth and ray parameter for the high (up) and low (down) frequency bands are shown in a). The backazimuth independent receiver function (black line) obtained from the HD method and the corresponding inverted trace (blue line) are shown in b). c) Shows the starting, true, BAZ and HD inverted models in discontinuous black, green, red and blue lines, respectively.

   For the BAZ approach, a inversion is performed jointly for all the RFs grouped in bins (fig. 8.2a). The corresponding averaged and standard deviations backazimuth and slowness values for each bin are shown on top of each panel. The grey corridor around the true receiver function is made with the standard deviation of the RFs bin distribution. In order to obtain confidence bounds for each layer in the velocity-depth profile, we invert separately for each bin of RFs and compute the standard deviation of the S-wave velocity values available from each inversion model (gray corridor in c). This estimation of uncertainties might not be statistically rigorous, but satisfactorily conveys the range of variation in crustal velocity due to azimuthal variation in the earth structure around the station.

On the basis of the radial harmonic function that, defined in section 7.1.2 as

$$H(\theta,t) = a_0(t) + a_{1x}sin(\theta) + a_{1y}cos(\theta) + a_{2x}sin(2\theta) + a_{2y}sin(2\theta) \tag{8.3}$$

we estimate the uncertainty $s(t)$ of the backazimuth independent receiver function $a_0(t)$ by employing the root mean square difference over azimuth between the observed receiver functions and the radial harmonic function

$$s(t) = \left\{ N^{-1} \sum_{i=1}^{N} [R_i(\theta_i,t) - H(\theta_i,t)]^2 \right\}^{1/2} \tag{8.4}$$

This uncertainty of the backazimuth independent harmonic coefficient of the RFs is shown as a grey corridor in fig. 8.2b).

As we observe in figure 8.2c) the BAZ inverted model underestimates the Moho velocity jump and exhibits more fluctuations. The HD inverted model accurately constrain in depth and velocity contrast the discontinuity. Although in the BAZ approach we can use the total length of the RFs, due to significant variations of the RFs in amplitude and delay time along the backazimuth caused by the dipping interface, inverted and true traces do not match at some backazimuth bins, especially for multiples phases. The HD inverted and true RFs have an excellent fitness along the first 10 s of the waveform and the inverted and true models match accurately.

2. The **anisotropy scenario** consists of a 10 km width anisotropic layer with 6 % in P- and S-waves hexagonal anisotropy whose fast axis present a plunge of 10° (Fig. 8.3). In this case the Moho velocity jump is correctly captured by both approaches thought the BAZ inverted model displays an offset with respect to the true model. Since the multiples are not employed in the HD inversion approach, the inverted model do not reconstruct precisely the depth of the Moho discontinuity.

Previous results might highly depend on slowness and backazimuth distributions of the incident traces and the geometry of the lateral heterogeneity. Note that at certain backazimuth directions RFs might not be perturbed by the lateral heterogeneity, if the inversion is preferentially made up of RFs coming from these directions, the BAZ approach must be able to recover the true model.

8.2 Case Studies

We apply the joint inversion of RFs and phase and group dispersion curves to real data comparing both HD and BAZ approaches described in the previous section. Quality control included automatic rejection of RFs that did not reproduce at least 80 % of the radial waveforms after being convolved back with the vertical component and visual identification and removal of outliers. Rayleigh wave phase and group velocity maps for periods between 6 and 40 s were taken from the ambient noise tomography of Silveira, Afonso Dias, and Villaseñor, 2013. In that study, 12 months of continuous seismic recordings were collected from about 90 permanent broad-band stations with an averaged interstation distance of about 50 km in the Iberian Peninsula and Northern Morocco allowing to obtain lateral variations of the velocities as a function of period in cells of $0.5^o \times 0.5^o$. Phase and group velocity curves were interpolated to each station location of fig. 8.9.

8.2.1 Eastern Betics Zone

We employ the dataset collected by the stations distributed in the Eastern Betics zone and used in the last chapter to illustrate the HD analysis. We choose this area to test the method because a broad range of lateral heterogeneity scenarios is present as we have seen in chapter 7.1.2.

The starting model used is already described in section 8.1.2 but in these inversions we locate the Moho at 38 km. Values for P-wave velocity and density, which are required to solve the forward problem, were obtained from an assumed V_p/V_s ratio and empirical velocity-density relationships, respectively. The joint inversion allows to account for the partial sensitivity of dispersion velocities to deep structure by fixing a depth above it the models is not constrained by RFs. For the HD approach we use generally a depth of 70 km because the traces are 8 s long. Since we include the multiples in the BAZ binning approach this depth can be set to deeper values such as 180 km. The joint inversion results for individual stations are shown in appendix B. Intermediate influence and smoothness factors around 0.5 better match the data and the model simplicity.

A common feature observed in most of the joint inversions is that the inverted model obtained with the HD approach exhibits a more fluctuating behaviour. While the HD joint inversion is based on only one RF, the BAZ approach takes into account several groups of RFs binned in different azimuth ranges making the inverted model only sensitive to the primary order variation of the RFs. According to the results obtained in the last chapter we can distinguish three main lateral heterogeneity scenarios; (1) no significant presence of lateral heterogeneity, (2) prominent dipping and/or shallow anisotropy situated nearby the coastline, (3) anisotropy predominantly concentrated below the Moho in the region of the STEP fault and (4) lateral heterogeneity that might not be regarded to dipping and/or anisotropy.

1. Low lateral heterogeneity: Based on Fig. 7.16, this region might correspond to the stations with the shortest HD vectors (CART, EMUR, XIII, HR50). Since we have high values of the factor A_0, above 70 %, which represents the relative weight of the flat-layered anisotropic structure, very similar results are obtained using both approaches. As a representative example we shows the station HR50 (8.4), which exhibits the lowest values of lateral heterogeneity (weight of the A_0 term in the expansion about an 80 %). There exists an excellent fitting between inverted and real RFs for a) the BAZ binning and b) the HD approaches. c) Dispersion curves are equally well fitted using both schemes. The only difference we can find between approaches is that the HD inverted model exhibits slightly larger velocity changes along the depth. The stations CART, EMUR and XIII (see appendix B) recover percentages of the A_0 factor around a 70 %. Though similar results are obtained with both approaches, generally the Moho jump is better constrained with the HD scheme.

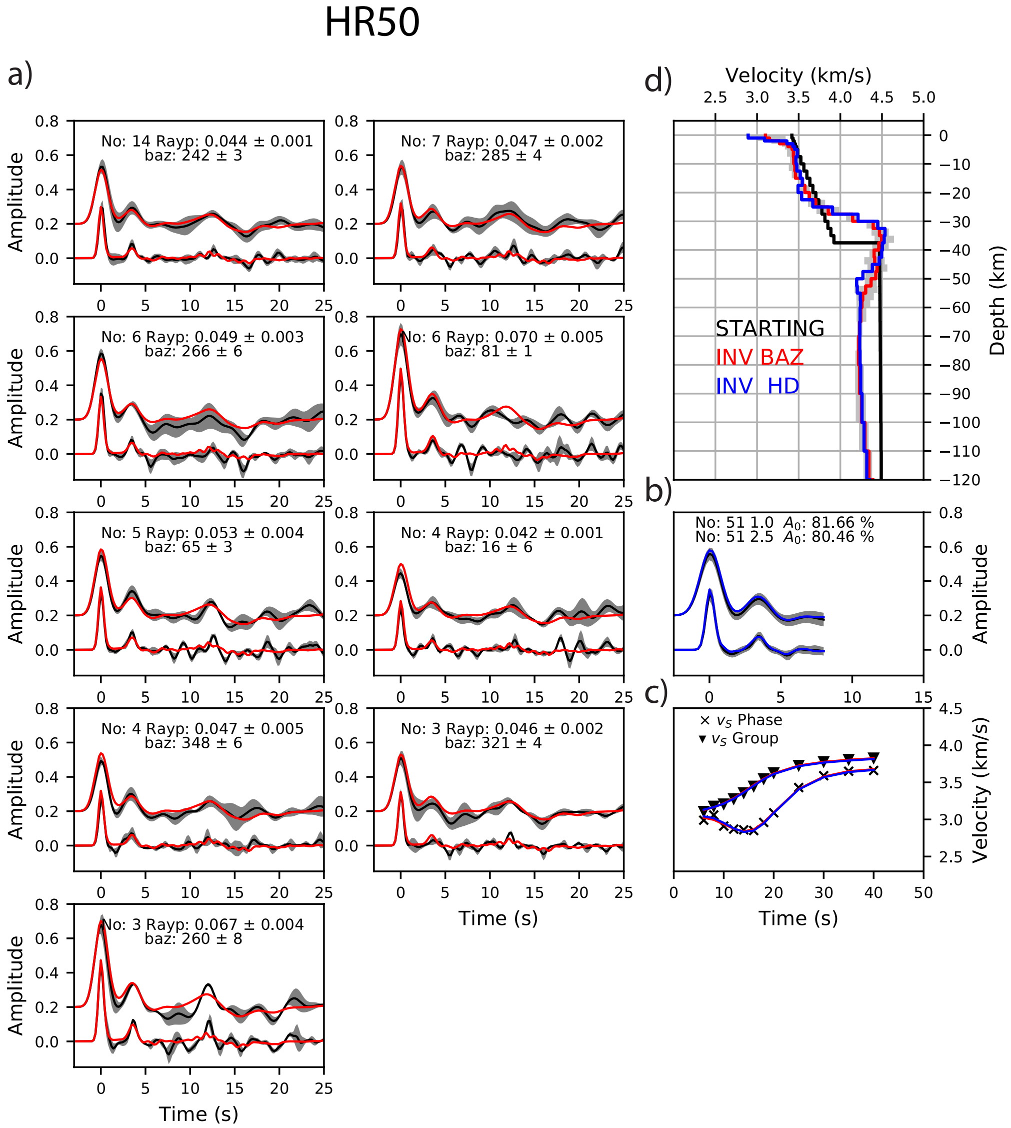

FIGURE 8.4: Joint inversion for station HR50 using a) BAZ and c) HD approaches. a) In the BAZ approach, RFs are sorted out by azimuth and slowness, each panel depicts the averaged receiver function (red curve) with its maximum variance (gray corridor). No. of RFs of each bin and averaged values of backazimuth and slowness are shown on top of the panel. b) The azimuthally independent HD $A_0(t)$ term (blue curve) with the uncertainty range (grey corridor), which is the root mean square of the residual remaining after the harmonic expansion (see section 8.1.2). The no. of RFs used in the HD and the percentage of the A_0 term in the expansion are shown on top of the panel. c) Inverted dispersion curves obtained with BAZ and HD approaches (red and blue curves, respectively). Real values for the phase and group Rayleigh waves are shown with triangles and X-shaped symbols, respectively. d) Initial, black line, and inverted models, red and blue lines for the BAZ and HD schemes, respectively.

2. Shallow lateral heterogeneity: Stations along the coast line (ACBG, MESA, ASCB, CUEV, GEOD, MORA and MAZA) depict high lateral heterogeneity at shallow depth (above the Moho discontinuity) as we have already pointed out in Fig. 7.16. Percentages of the A_0 factor in the harmonic expansion are below 70 %. We choose the MAZA station (Fig. 8.5) to show the main common and representative features of these inversions. Inverted and real RFs do not fit properly when we use the BAZ scheme. We are quite far from the isotropic flat-layered model assumption and the amplitudes of direct and converted phases are significantly affected. Note that a better fitting between real and inverted RFs is found for those backazimuth directions which are perpendicular to the dipping orientation (NNW from fig. 7.16). Traces coming from these directions are less affected by the dipping structures as we have already illustrated in section 7.1.1.

   In contrast, a good fitting exists between real and inverted dataset using the HD scheme. Only at very short times (8 s) the inverted group dispersion curve does not match exactly the real data, probably due to more sensitivity of the inversion to the RFs at these shallow depths. The HD inverted model is able to recover the Moho discontinuity with a larger jump than the BAZ model.

3. Subcrustal anisotropy: We find a set of stations that exhibit larger amplitudes of the vector $\vec{a}_2$ presumably associated to deep lower-crustal and/or subcrustal anisotropy (EQES, EHUE, SESP, VELZ and VALD). The percentages of the A_0 factor are above a 60 %. This region delimits the transition zone between the Iberian Massif and the Alboran domains in the STEP fault and is characterized by the presence of a double Moho. Again, the BAZ approach is not able to model the complexity of the RFs dataset and the double Moho is generally recovered as a smoothed increase in the velocity probably more based on the dispersion curve measurements (Fig. 8.6). However, the HD approach can discern the 2 Moho discontinuities, separating them into two velocity jumps located at 25 and 45 km depth.

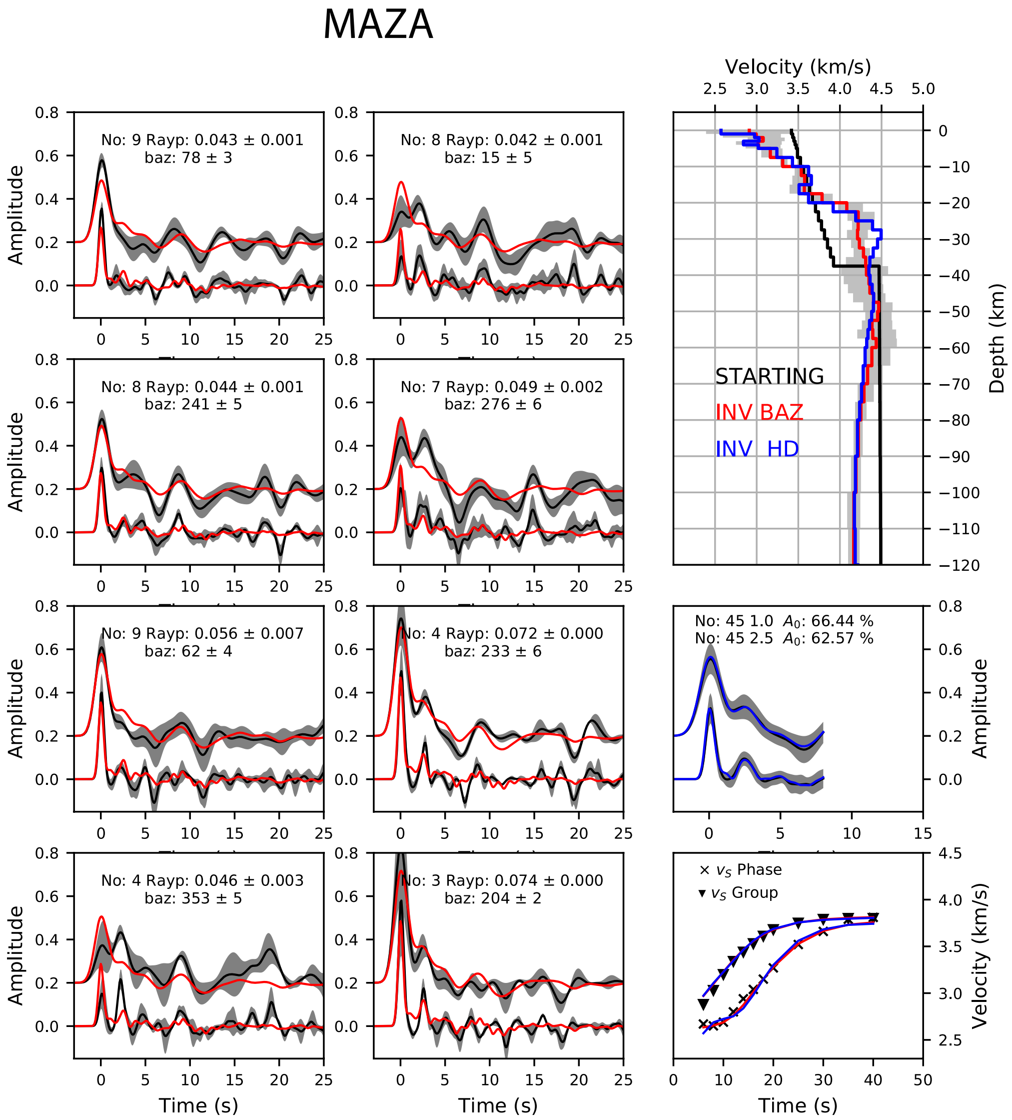

FIGURE 8.5: The same than Fig. 8.4 for MAZA station.

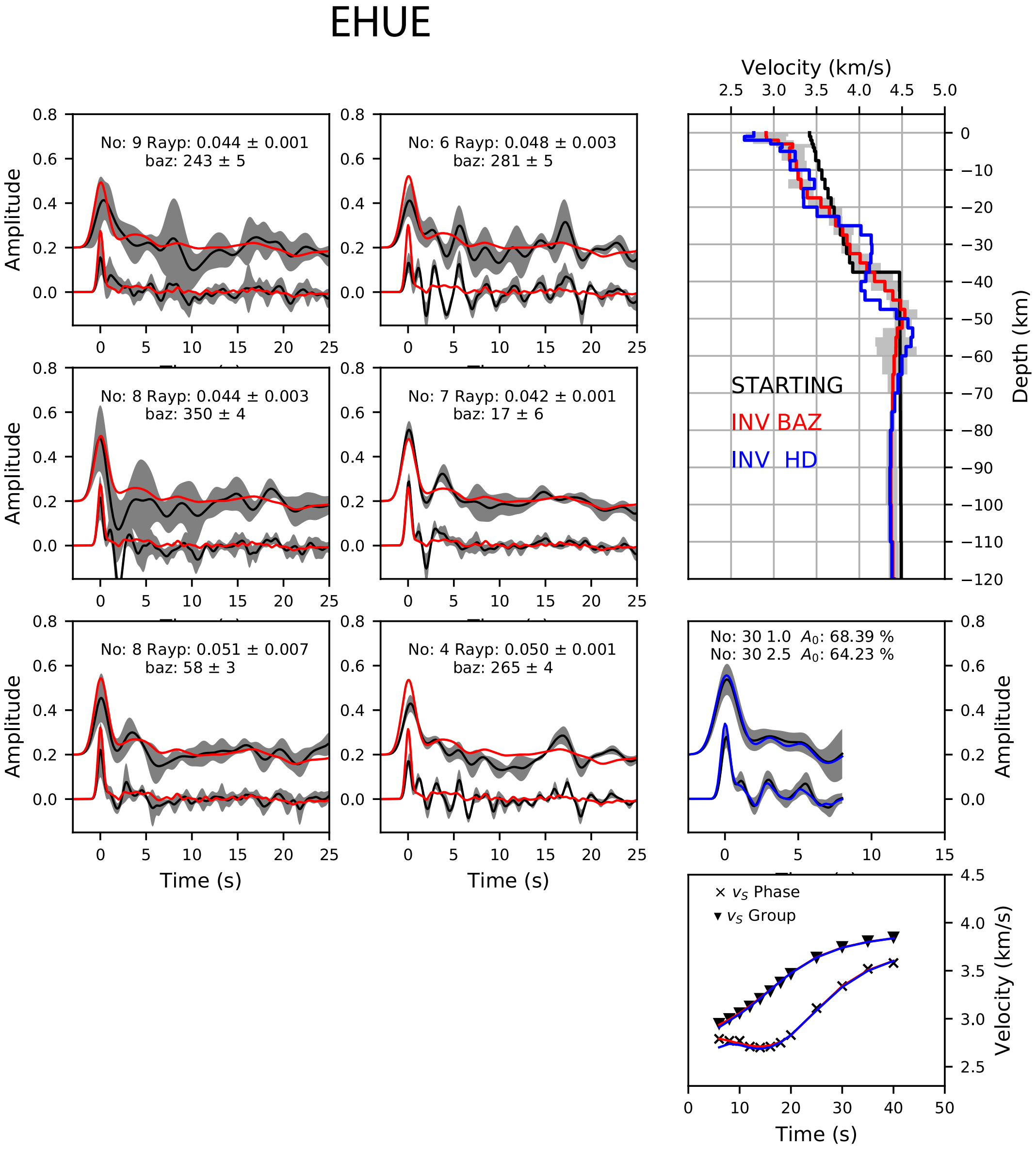

FIGURE 8.6: The same than Fig. 8.4 for EHUE station.

4. No clear origin of lateral heterogeneity: Finally, we have some stations whose lateral heterogeneity might not be attributed to dipping and/or anisotropy effects because there is not clear coherence between radial and transverse components vectors (ALHA, GORA, EBER). Very low values of percentages of the A_0 factor are found for these stations (below 60 %). Similar results for the inversions are obtained using both approaches, though discontinuities seem to be better constrained with the BAZ approach.

Similarly to fig. 7.16 in chapter 7.1.2, fig. 8.8 depicts the HD vectors $\vec{a}_1$ and $\vec{a}_2$ for depths corresponding to a) the first 50 km, b) crustal depths (0-30 km) and c) uppermost mantle depths (35-70 km). The vectors have been converted from time to depth dependence using the inverted models obtained with the HD joint inversion scheme.

The vectors reach the greatest lengths at crustal depths a) for stations located nearby the coastline at longitudes between -2.5 and -1.5. The maximum lengths corresponds to the direct and Moho conversion phases being the direction predominately NNW. At larger depths b) the amplitude of the vector $\vec{a}_1$ decreases considerably exhibiting more erratic patterns. The vector $\vec{a}_2$ shows comparable lengths to those amplitudes obtained at crustal depths. For some stations a characteristic 2-consecutive vectors pointing at orthogonal directions is present. These vectors correspond to stations located inland (VELZ, SESP, EHUE, EQES and GORA) in a region where presumably a double Moho exists. This homogeneous anisotropy orientation might be then regarded to an anisotropic body trapped between these two discontinuities. Similar results have been obtained in the northern Apennines by Bianchi et al., 2010.

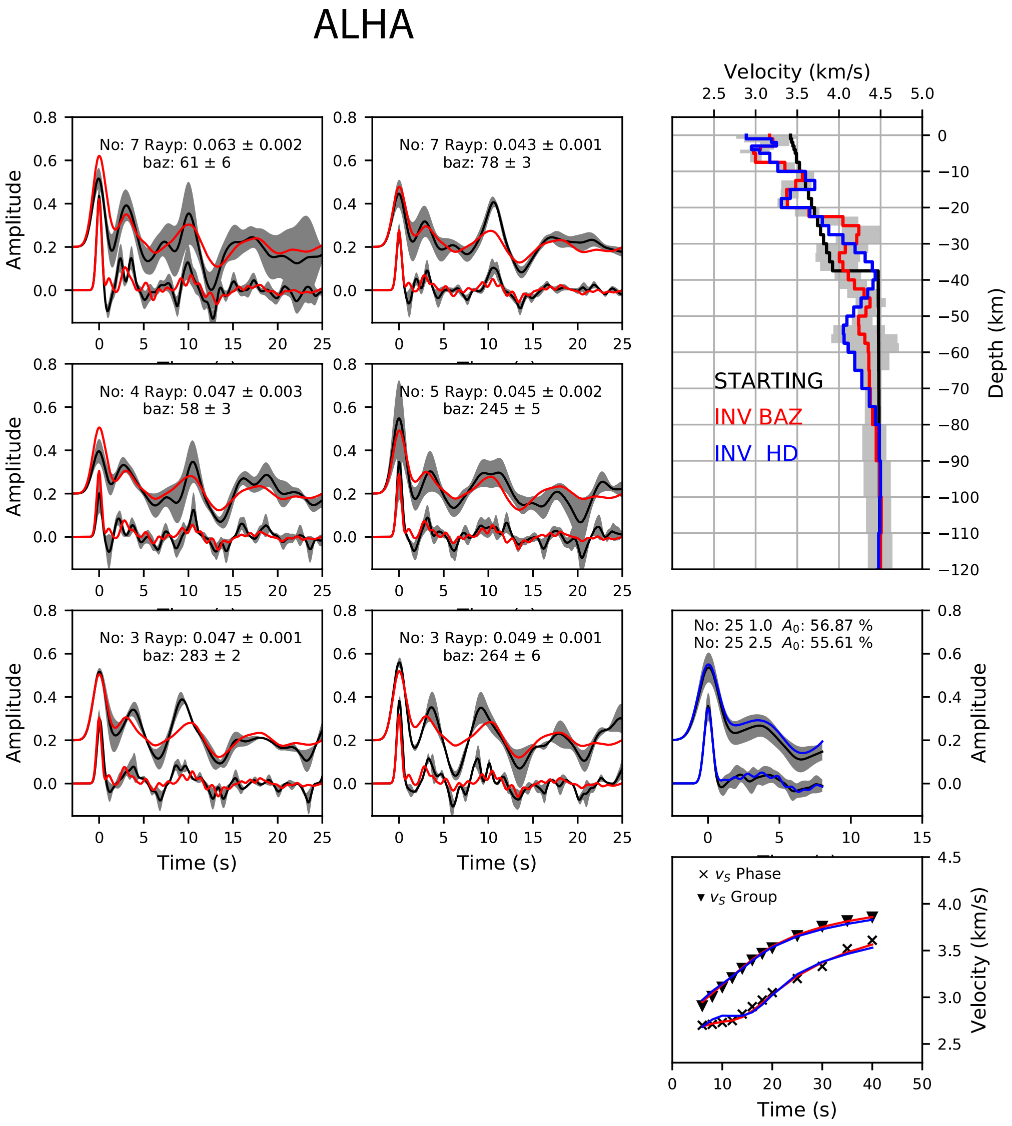

FIGURE 8.7: The same than Fig. 8.4 for EHUE station.

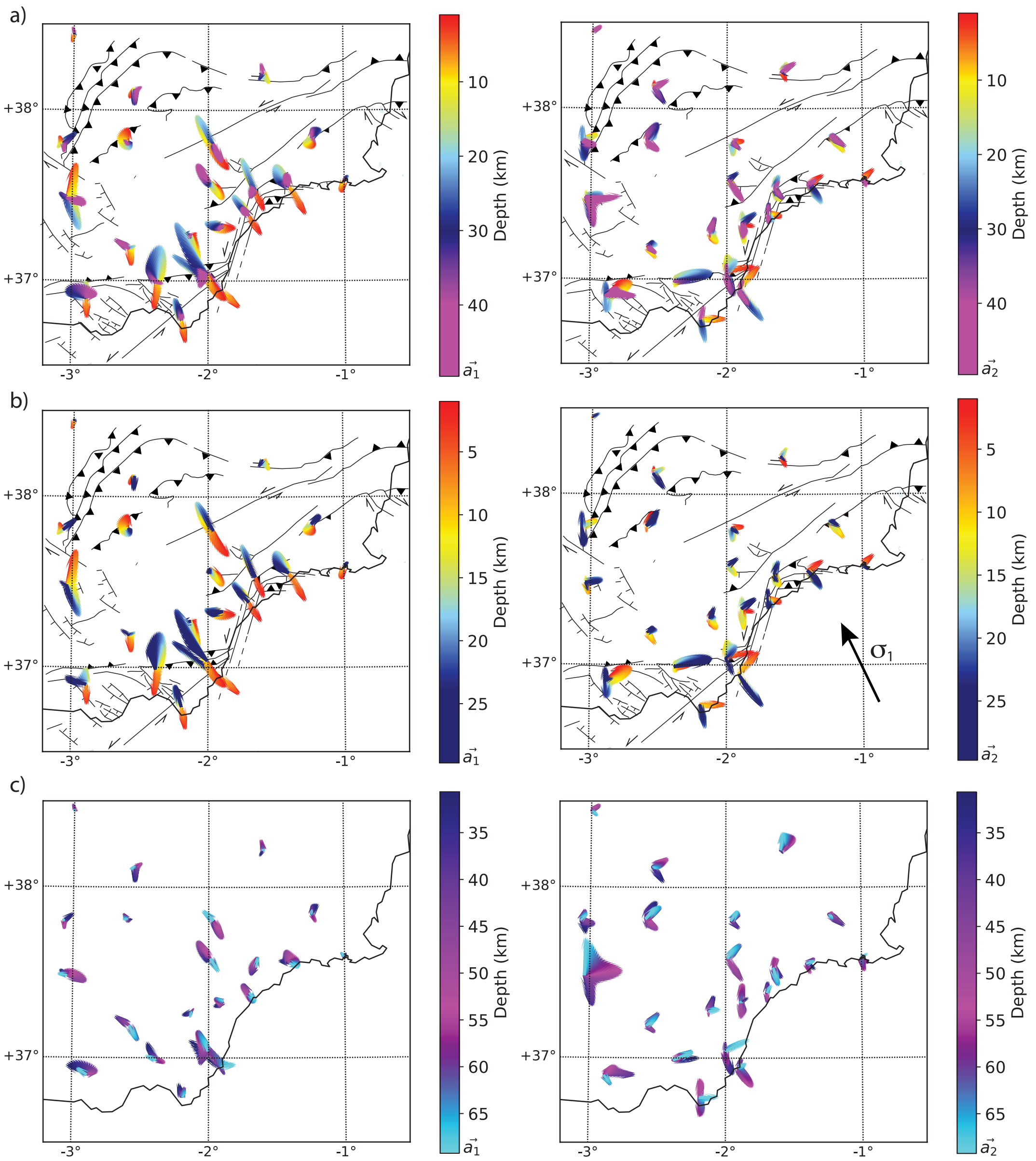

FIGURE 8.8: $\vec{a_1}$ and b) $\vec{a_2}$ vectors' maps in depth obtained with the HD analysis for a) the first 50 km, b) crustal depths (0-30 km) and c) uppermost mantle depths (35-70 km). Vectors $\vec{a_i}$ have been converted from time to depth using the joint inverted models. The length of the arrow is proportional to the amplitude of the vectors, being vectors $\vec{a_2}$ the double length than vectors $\vec{a_1}$.

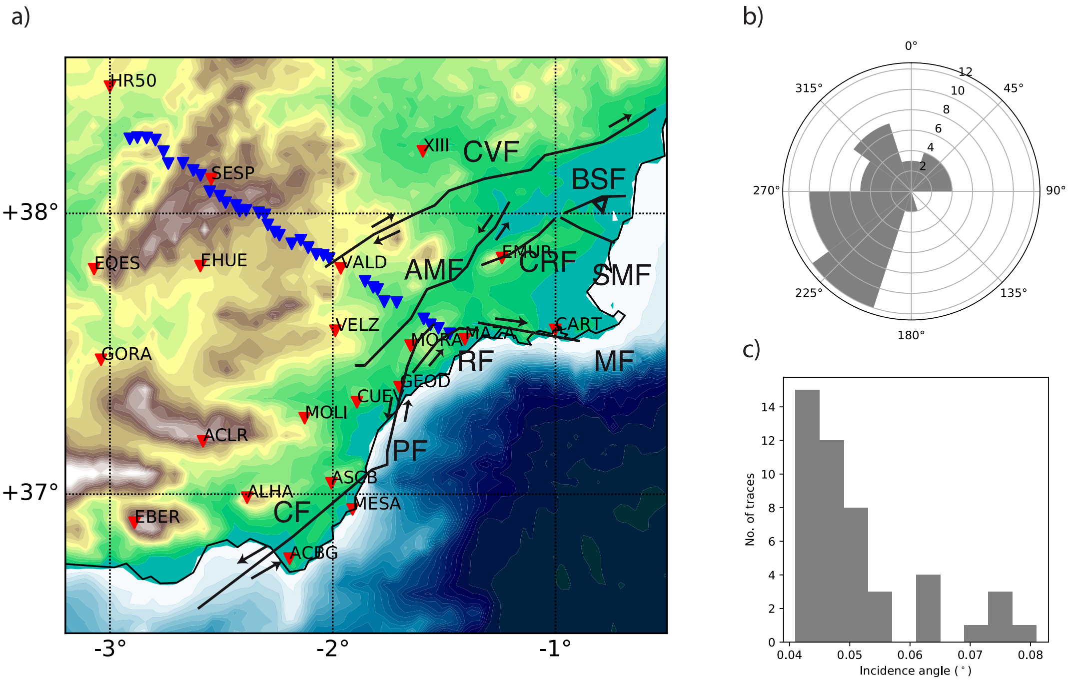

FIGURE 8.9: a) Map of the investigated area displaying the main structural features and the seismic stations (blue and red triangles for Transcorbe and permanent stations, respectively). Acronyms stand for Socovos Fault (SCF), Crevillente Fault (CVF), Alhama de Murcia Fault (AMF), Palomares Fault (PF), Carboneras Fault (CF) and Alpujarra Fault (APF). (b) Back-azimuth and (c) ray parameter distribution extracted from a representative station.

8.2.2 High-resolution Transcorbe profile

Finally, in this section we apply the joint inversion method to the high dense Transcorbe profile using both, the HD and the BAZ approaches. Figure 8.9 shows a) the seismic stations and main structural features. b) and c) display the ray parameter and back azimuth distributions for a representative station, respectively.

Thanks to the high resolution in seismic stations we can interpolate along the profile the inverted models. Figure 8.10 displays the S-wave velocity-depth cross-section employing a) BAZ and b) HD approaches. Three level lines mark the S-wave velocities of 3.2, 3.5 and 4.1 km/s to emphasize velocity variations within the profile. The deeper level line, corresponding to a 4.1 km/s S-wave velocity might be identified as the Moho discontinuity. We attach c) the CCP stacking cross-section to compare with the geometry of the crustal interfaces. Interpretative lines have been added. The topography along the profile is displayed on top of the figure. For discussion, we have divided the cross-section into 4 main zones according to the strength and geometry of the lateral heterogeneity recovered with the HD method, as we will see later.

The velocity profile obtained with the HD approach exhibits more lateral velocity variations of both, intracrustal and Moho interfaces, at all depths. As we have previously pointed out the HD joint inversion approach is based on only one receiver function, being the inverted model more sensitive to the variations of the trace. This discrepancy between approaches is more significant for the Moho discontinuity, being the HD approach able to capture the primary Moho topography already obtained with the CCP stacking. The main Moho discontinuity feature retrieved by the HD approach, and not recovered by the BAZ approach, is the prominent Moho offset located below TR19 (zone Z3 in fig. 8.10). Though the position does not fit exactly with the CCP image, in this case displaced a bit to the southeast, the Moho jump agrees in depths and length offset. The Moho discontinuity observed in the HD profile reaches a maximum depth of approx. 42 km below the stations TR22-TR18. Whereas the Moho interface that we discern with the BAZ approach remains at shallower depths of approx. 35 km in this segment. A crucial feature captured more clearly with the HD approach is the low velocity zone located in zone Z2 (marked as LV in fig. 8.10) and observed in the CCP image as well. In those zones where presumably the lateral heterogeneity is very low, as the Iberian massif (Z4 in fig. 8.10), both approaches give similar results. Though the zones closer to the coast (Z1 and Z2) reveal prominent presence of lateral heterogeneity (already reported in the previous chapter), there are no crucial differences between the S-wave velocity cross-sections obtained with both approaches.

Fig. 8.11 shows the a) HD S-wave velocity profile, b) and c) the modulo of the vectors $|\vec{a}_i|$ for $i = 1, 2$ normalized by the maximum value of each one. We mark the same zones already differentiated in figure 8.10. Lines indicating the Moho discontinuity and important crustal structures have been added. To follow the direction of the vectors along the profile we show them in fig. 8.12. Again, we differentiate a) all, b) crustal and c) subcrustal depths.

We broadly realize how the largest values of both vectors $\vec{a}_i$ concentrate in the Southeast sector of the profile (zones Z1, Z2 and Z3 in fig. 8.11 and 8.12). Zone 4 conforms the External Zone and its transition to the Iberian Massif, a stable area where no appreciable dipping and/or anisotropy exist. The drastic change in the presence of lateral heterogeneity, especially for the vector $\vec{a}_1$, coincides with the location of the STEP fault (boundary between zones Z3 and Z4). Whereas the largest values of the vector $\vec{a}_1$ are concentrated at crustal depths in the zones Z1, Z2 and Z3 (fig. 8.11b)), the vector $\vec{a}_2$ is distributed along several depths exhibiting repeatedly two-consecutive lobes patterns (fig. 8.11c)). Since different behaviours of the vectors, mainly $\vec{a}_1$, are observed in the southeast sector of the profile, we distinguish the three regions Z1, Z2 and Z3 (fig. 8.11 and 8.12). To illustrate these variations we select representative cases from each sector and show in concretely their vectors and coefficients (fig. 8.13).

In the zone Z1 the vector $\vec{a_1}$ has the two-lobes pattern pointing in opposite directions for the direct (0 delay time) and Moho converted phases. This characteristic pattern must be attributed to a NW dipping of the Moho discontinuity since, in addition the deeper pulse correlates with the depth of the crust-mantle boundary (about 20 km). To see these attributes in more detail we select from this sector the station TR02 (fig. 8.13a)). High values of the vector $\vec{a_2}$ are concentrated at a very shallow depth which is indicative of fault strain related anisotropy. Note that the vectors $\vec{a_1}$ and $\vec{a_2}$ seem to be aligned for the stations closer to the SE end of the zone Z1 (MAZA and TR02, while conforming we move towards the NW direction of the vector $\vec{a_2}$ takes a different orientation. This distinctive behaviour which regards the strain pattern with the proximity of the gauge fault has been already reported in the previous chapter.

In the section Z2 we distinguish two peaks in the vector $\vec{a_1}$ located at 10 and 30 km in depth (fig. 8.11). Now the orientation of the vector rotate towards a more NNW direction. An intracrustal interface associated to a low velocity zone seems to be involved in this geometry as we can distinguish in the CCP stacking image of fig. 8.10c). In this sector Z2 the modulo of the vector $\vec{a_2}$ exhibits large values at different depths, depicting the two consecutive lobe pattern from 40 to 80 km (fig. 8.11b). Its geometry at these depths correlates with the obtained from the vector $\vec{a_1}$ as we can see in the general trend (fig. 8.12a) and at the station selected from this sector Z2 (fig. 8.13b).

In the sector Z3 the modulo of the vector $\vec{a_1}$ displays peaks associated to the direct and converted phases. Except for VALD station, the deeper conversion is located at 25 km (fig. 8.11a), which might be associated to dipping of an intracrustal structure. Furthermore, at crustal depths this is the sector where the vector $\vec{a_1}$ reaches the largest lengths (fig. 8.12b) pointing again at a more NNW

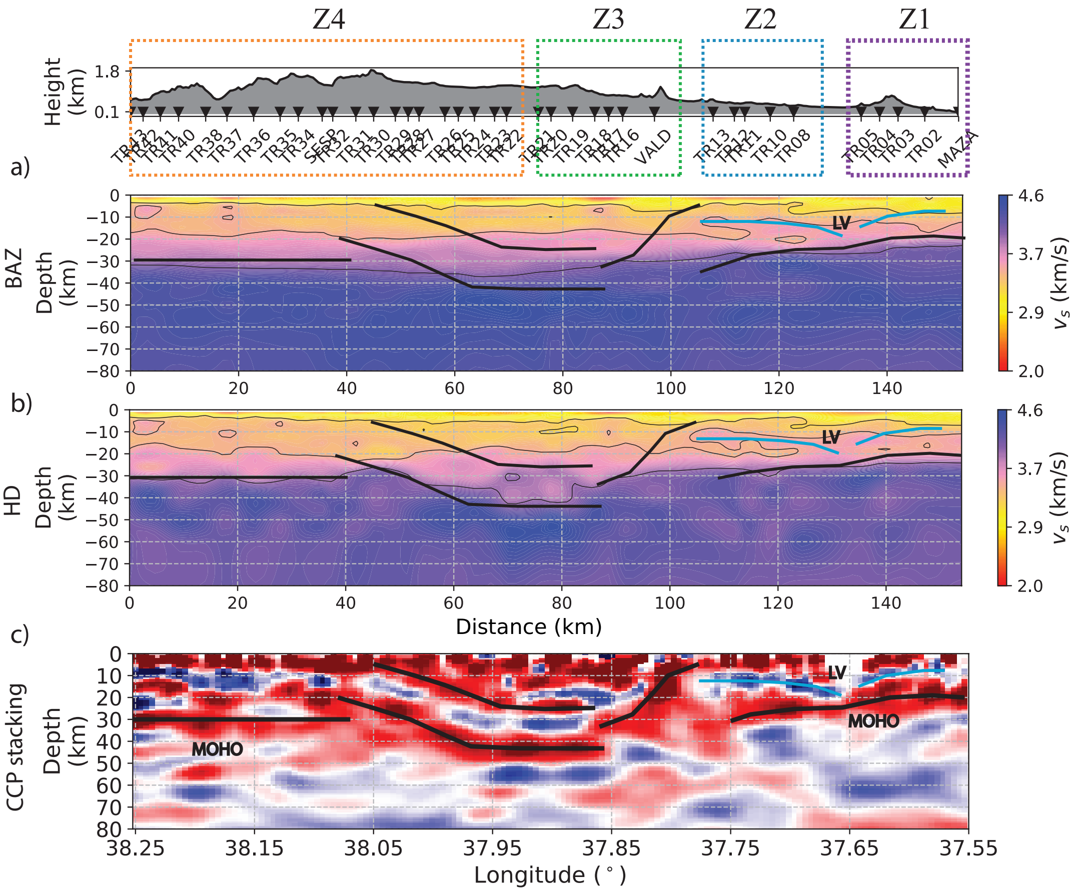

FIGURE 8.10: S-wave velocity interpolated cross sections obtained with a) BAZ and b) HD (bottom) approaches. The beginning of the profile starts at the most northern located station. Level lines mark velocities of 3.2, 3.5 and 4.1 km/s. c) CCP stacking migration using the L component of RFs.

direction. This might be caused by the STEP fault which makes this section the most deformed zone of the cross-section. Lower values of the vector $\vec{a_1}$ also appear at the Moho discontinuity depth not exhibiting a clear trend except for some stations as MAZA and TR20 (fig. 8.12c). The vector $\vec{a_2}$ has the largest lengths of the profile in this zone Z3 at subcrustal depths. Its tend seems to be in coherence with the zones Z1 and Z2.

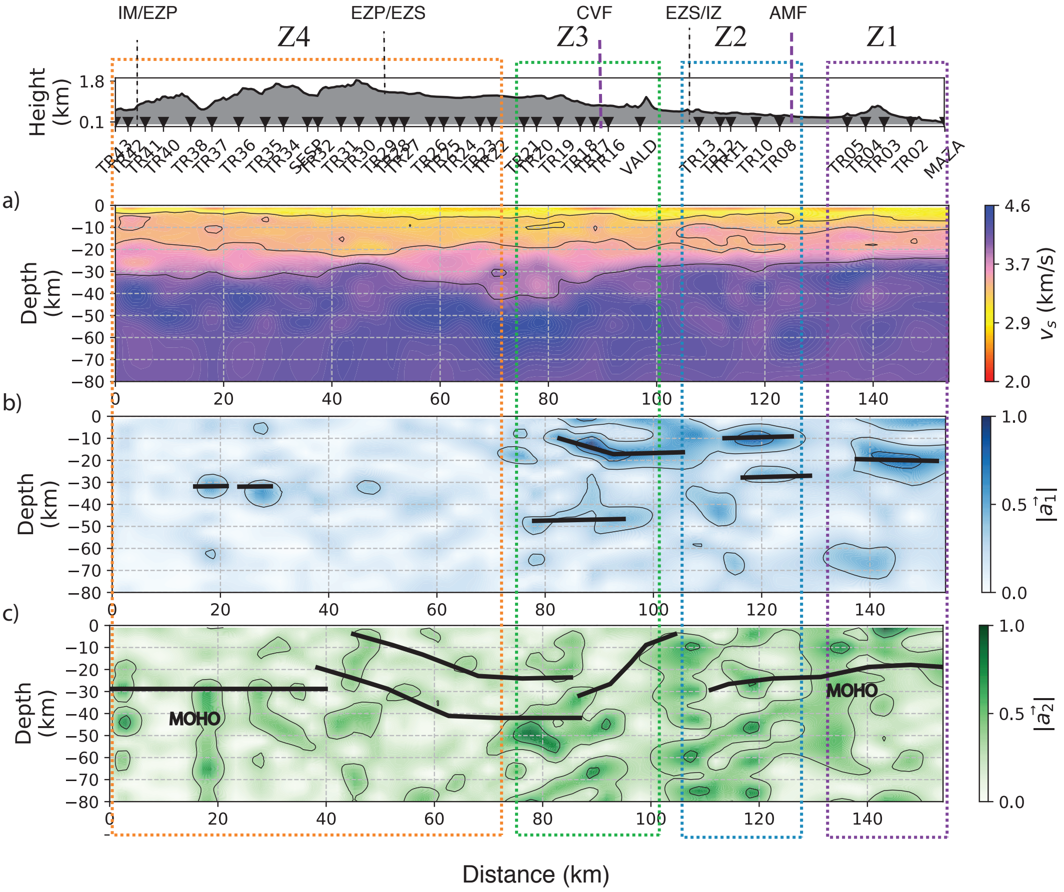

FIGURE 8.11: a) S-wave velocity interpolated profile obtained with the joint inversion method and the HD approach as indicated in Fig. 8.10. b) and c) display the length of the vectors $|\vec{a}_i|$ for $i = 1, 2$, respectively. Each slice is normalized by the maximum value of the cross-section.

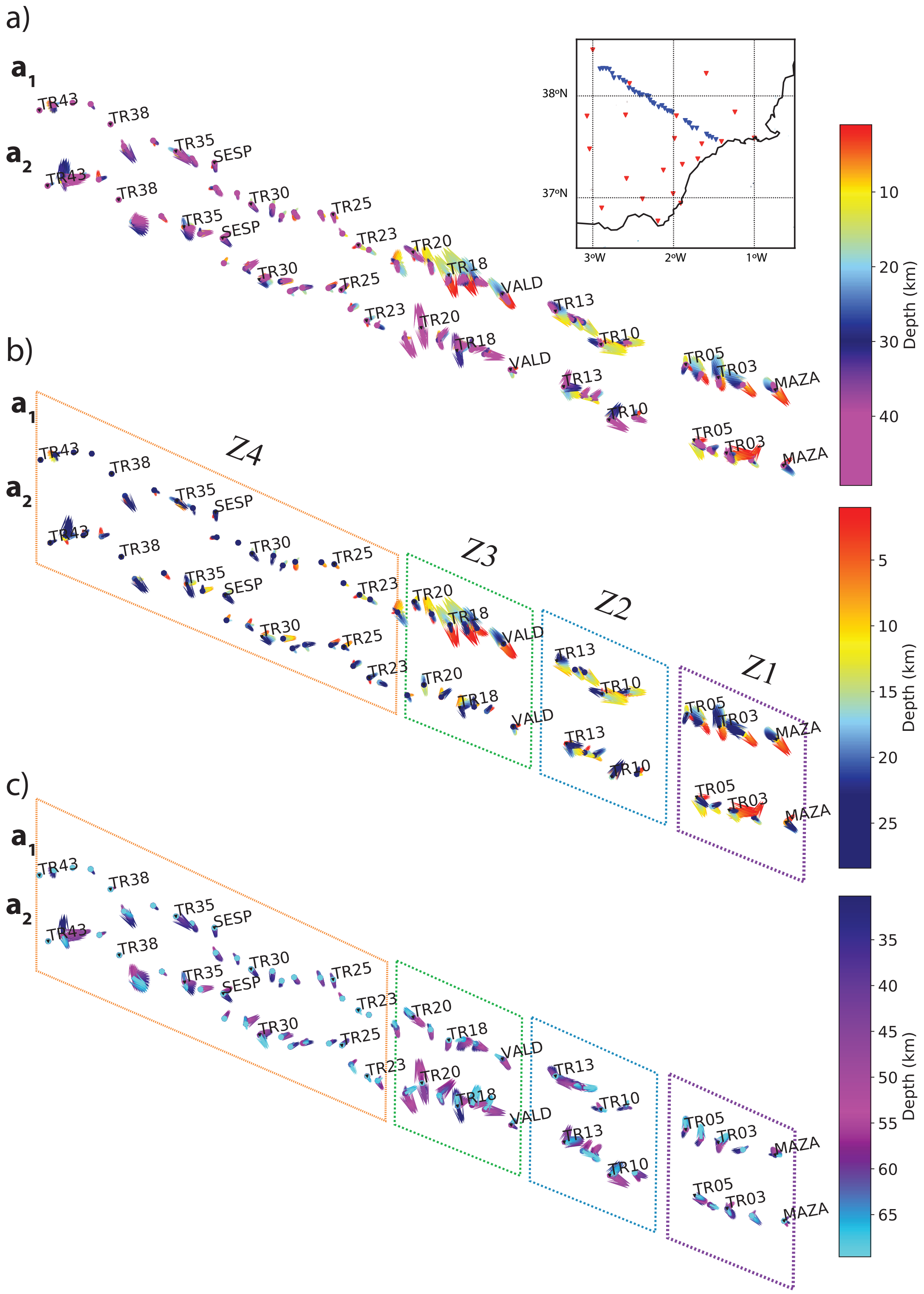

FIGURE 8.12: $\vec{a}_1$ and b) $\vec{a}_2$ vectors' map in depth obtained with the HD analysis for shallow depths a) corresponding to the crust (0-30 km) and b) to the uppermost mantle (30-80 km). Vectors $\vec{a}_i$ have been converted from time to depth using the velocity models obtained with the joint inversion. The length of the arrow is proportional to the amplitude of the vectors and the length of $\vec{a}_2$ is 1.5 factor greater than $\vec{a}_1$ to be visualized.

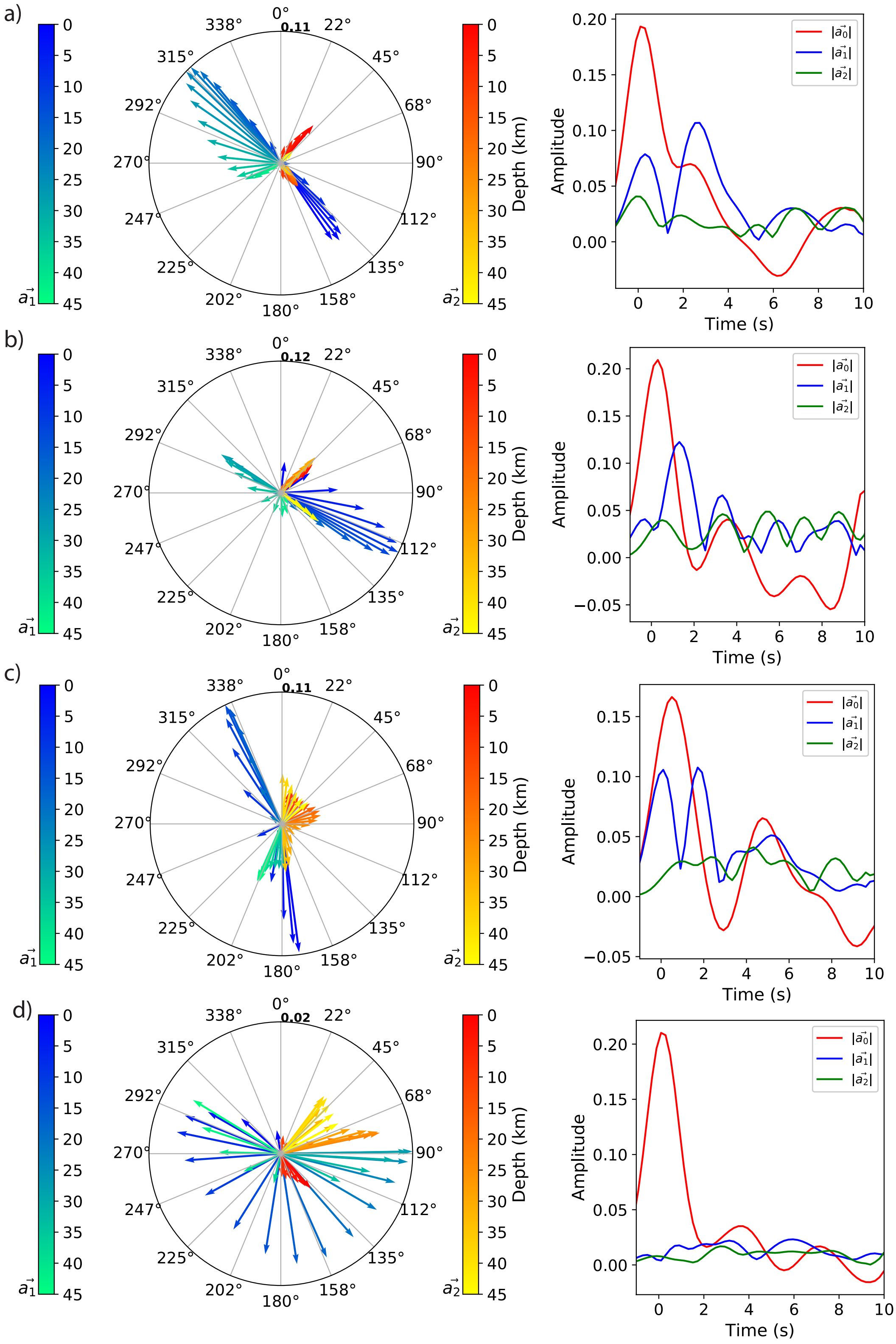

FIGURE 8.13: Direction (left) and norm of the vectors $a_n(t)$, $n = 0, 1, 2$, in depth and along the time, respectively for the stations a) TR02, b) TR10, c) TR18 and d) TR43. The vectors are normalized by the maximum amplitude of both and indicated on top of each vectors' image.

8.3 Conclusions

We demonstrate the effectiveness of the harmonic decomposition analysis to isolate the signal in RFs only sensitive to the flat-layered isotropic structure of the medium. This analysis permits to obtain an independent of the back-azimuth RF that can be used to invert the 1D S-wave velocity-depth profile. This approach is a clear advantage in presence of significant lateral heterogeneity associated to dipping and/or anisotropic layers compared to conventional schemes where RFs grouped in backazimuth ranges are inverted. We theoretically prove this performing synthetic inversion experiments with different lateral heterogeneity scenarios.

Real joint inversions of RFs and surface wave dispersion measurements comparing both approaches are as well made in the Eastern Betics zone where different types of lateral heterogeneity are present. The harmonic decomposition approach is able to capture accurately intracrustal and crust-mantle discontinuities. Compared to the BAZ approach, the HD one especially succeeds in regions where the lower crustal structure is considerably deformed, as happens along the STEP fault where a double Moho jumps is recovered.

The goodness of the HD scheme is also proved with the high-resolution Transcorbe transect. The 1D shear-wave velocity cross-section along the profile obtained with the HD approach retrieves the main crustal and upper-mantle features revealed with the CCP stacking migration; Moho offset and low velocity zone. Furthermore, the combined use of the inversion and the HD method permits the projection in depth of the lateral heterogeneity geometry. This analysis distinguishes several zones along the profile in coherence with the previous results: (1) the Alboran domain located in the SE section nearby the coastline and mainly characterized by a dipping NNW Moho discontinuity, (2) the transition zone between the Alboran domain and the Iberian Massif coinciding with the STEP fault and marked by the presence of significant dipping and/or anisotropy at crustal and subcrustal depths and (3) a stable region without considerable lateral heterogeneity.

Chapter 9

Conclusion

The main conclusions that we draw from this thesis are:

1. The analysis of a large amount of SRFs has revealed the topography of the seismic LAB discontinuity beneath the plate boundary zone between Iberia and northern Africa. The most relevant feature found is the a 200 km wide corridor with a lithospheric thickness of 120 km that we interpret as the remains of a Middle-to-Late Jurassic age lithosphere. This corridor permits to connect the Alboran slab located under the Alboran Sea and the Atlantic oceanic crust below the Gulf of Cadiz.

2. By migration high-resolution PRFs profiles we obtain the first direct images (not inverted) of the crustal and lithospheric architecture of the Betic orogen. From the interpretation of the CCP images we observe as the underthrusted Iberian lithosphere terminates sharply in both profiles following at the surface the External-Internal Zone limit. This sharp and prominent lithospheric step ($\sim$15 km) observed in both profiles is interpreted as a near-vertical STEP fault that propagates to the surface as a positive flower fault structure. This STEP fault accommodated the differences in the subduction rollback velocity along the strike, at the northern edge of the Western Mediterranean system, when the the thinned Iberian continental lithosphere started subducting under the Alboran domain. We have not observed a crustal root under the highest altitude of both profiles, especially under Sierra Nevada mountain at the Hire profile, suggesting that the high topography is produced by a combination of the uplift produced by the positive flower structure and the push up of

the asthenosphere after the lithospheric removal of the underthrusting Iberia along the STEP fault. Our results also present how the lithospheric tearing associated with a STEP propagation in a large scale subduction rollback framework can drive to high oblique continental collision which can be accommodated through crustal scale decollements and be a first order mechanism related with the built of fold and thrust belts of the peripheral External Betic Range.

3. We apply the Reverse Time Migration (RTM) methodology, which is able to exploit the complete complexity of the wavefield, to the teleseismic converted phases recorded in the high-density Hire seismic profile to create a high-resolution image of the crustal structure. RTM produces clearer images of the crustal structure and better resolution of lateral changes than CCP stacking. The main observations include a sequence of abrupt Moho offsets, one of them associated with a STEP fault, and variations in Moho dip. We propose that the principal Moho topography features conform a deformed block of 60 km length formed by continental/transitional Iberian crust which concentrates most of the deformation due to the collision. We suggest that the changes in the topography of the Moho discontinuity, and the geometry of the STEP fault in Central Betics is driven by inherited weaknesses in the Iberian paleomargin.

4. We implement a technique for the study of lateral heterogeneity employing RFs and apply it to a real teleseismic dataset in a region geologically diverse and structurally complex. The technique permits to separate the isotropic information from the energy due to anisotropic and/or dipping subsurface structures, becoming a useful tool for the understanding of subsurface geometries. The method successfully use both radial and transverse components which gives better constraints on the subsurface seismic structure than radial-only RFs analysis. The inclusion of the transverse component helps to determine if the lateral heterogeneity is due to dipping interfaces and/or anisotropic layers as the transverse component is mainly sensitive to these sources of lateral heterogeneity.

The harmonic decomposition method implemented is linear and allows to build a time dependent vector representation of the terms in the expansion, simplifying notably the interpretation. The alignment of the vectors $\vec{a}_1$ and $\vec{a}_2$ and the time delays at which they are concentrated help to remove some ambiguities inherent to the kind of lateral heterogeneity we are studying.

Through a synthetic study we illustrate the method. We investigate three basic scenarios; a dipping interface, a flat anisotropic layer and an inclined anisotropic layer. Furthermore, we evaluate the goodness of the moveout correction on radial and transverse components and conclude that the transverse component is less sensitive to the slowness variation of RFs. This, combined to the fact that transverse RFs are mainly affected by the lateral heterogeneity due to anisotropic layers and dipping interfaces, permit through comparative radial- and transverse-only harmonic decomposition approaches determine with less ambiguity the source of the lateral heterogeneity.

We apply the harmonic decomposition method using a comparative radial and transverse component study to real RFs located in the southeastern region of the Iberian Peninsula. We obtain a continuous representation of the lateral heterogeneity with depth along the crust and the uppermost mantle, determining the orientation of anisotropy and dipping interfaces. Our study shows that crustal and uppermost mantle anisotropic characteristics might differ in their orientation. Stations located nearby the coastline and faults exhibit the presence of considerable lateral heterogeneity at crustal depths. The vector $\vec{a}_1$ is oriented predominately in a NNW direction, in agreement with previous results which report a gently dipping Moho following in this direction (Fig. 7.11B). The vector $\vec{a}_2$ seems to be geometrically related to the fault system present in the region and related to the vector $\vec{a}_1$ at crustal depths. At deeper depths, below the Moho, the vector $\vec{a}_2$ reaches the largest lengths for the stations located above a region with double Moho. This anisotropy might be related with an anisotropic structure trapped between the two Moho discontinuities.

5. We demonstrate the effectiveness of the harmonic decomposition analysis to isolate the signal in RFs only sensitive to the flat-layered isotropic structure of the medium. This analysis permits to obtain an independent of the backazimuth RF that can be used to invert the 1D S-wave velocity-depth profile. This approach is a clear advantage in presence of significant lateral heterogeneity associated to dipping and/or anisotropic layers compared to conventional schemes where RFs grouped in backazimuth ranges are inverted (BAZ approach). We theoretically prove this performing synthetic inversion experiments with different lateral heterogeneity scenarios.

   Real joint inversions of RFs and surface wave dispersion measurements comparing both approaches are as well made in the Eastern Betics zone where different types of lateral heterogeneity are present. The harmonic decomposition approach is able to capture accurately intracrustal and crust-mantle discontinuities. Compared to the BAZ approach, the HD one especially succeeds in regions where the lower crustal structure is considerably deformed, as happens along the STEP fault where a double Moho jumps is recovered.

   The goodness of the HD scheme is also proved with the high-resolution Transcorbe transect. The 1D shear-wave velocity cross-section along the profile obtained with the HD approach retrieves the main crustal and upper-mantle features revealed with the CCP stacking migration; Moho offset and low velocity zone. Furthermore, the combined use of the inversion and the HD method permits the projection in depth of the lateral heterogeneity geometry. This analysis distinguishes several zones along the profile in coherence with the previous results: (1) the Alboran domain located in the SE section nearby the coastline and mainly characterized by a dipping NNW Moho discontinuity, (2) the transition zone between the Alboran domain and the Iberian Massif coinciding with the STEP fault and marked by the presence of significant dipping and/or anisotropy at crustal and subcrustal depths and (3) the stable Iberian massif region without considerable lateral heterogeneity.

Appendix A

Harmonic Decomposition Figures

Figures of this appendix show the vectors (top row for each station) and their norm (bottom row) along the time obtained with the Harmonic Decomposition method treated in chapter 7. We apply the method using only the radial component (1st column), only the transverse component (2nd column) and both of them (3rd column). This comparison between radial and transverse components helps us to elucidate if the backazimuthal variations of the amplitude can be associated to lateral heterogeneity due to dipping interfaces and/or anisotropic layer. The stations are shown according to alphabetic order. The vectors $\vec{a}_1$ and $\vec{a}_2$ are normalized by the maximum amplitude of both of them along the time. This maximum amplitude is indicated on top of every polar image.

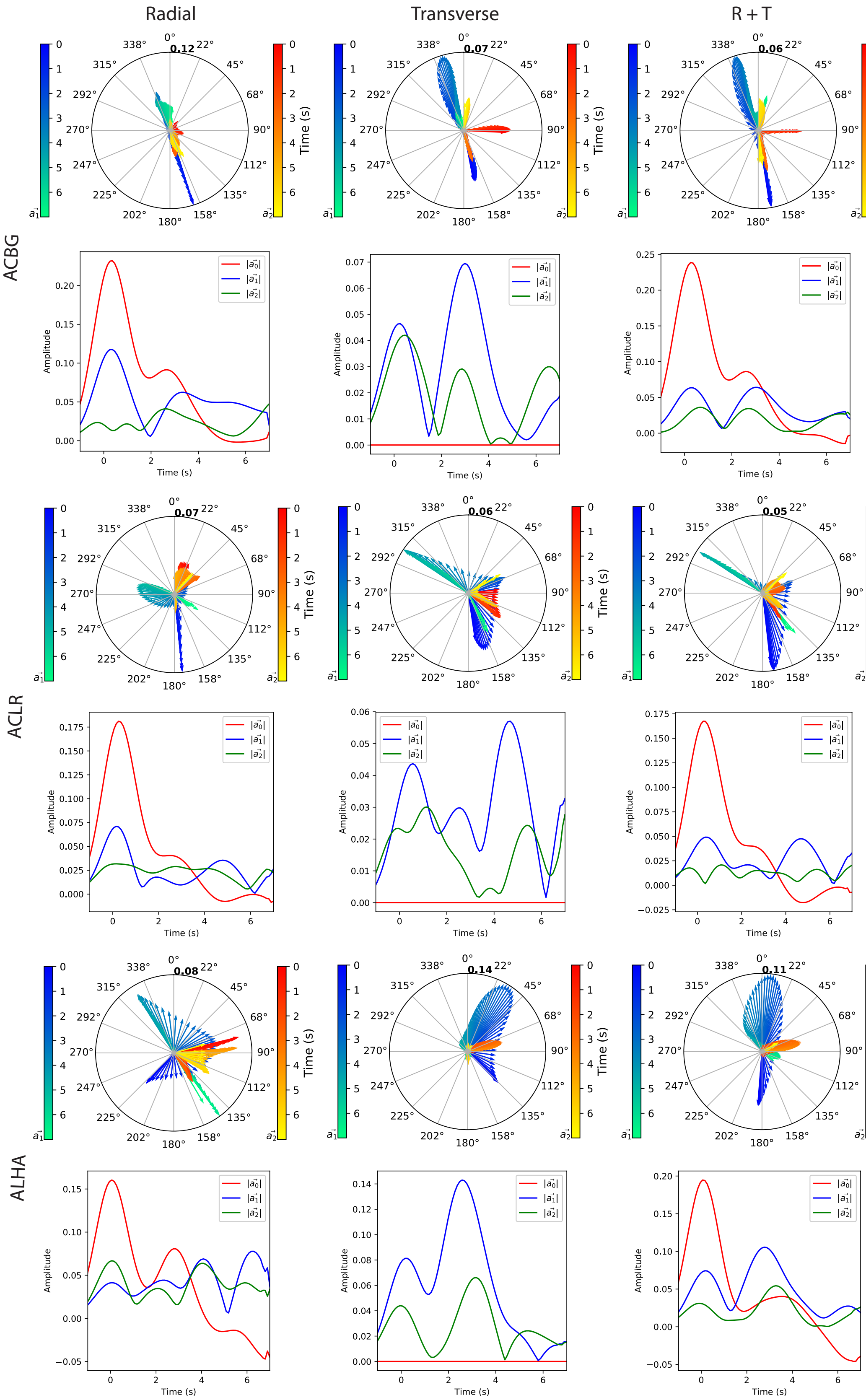
Radial
Transverse
R + T
ACBG
ACLR
ALHA
0°
22°
45°
68°
90°
112°
135°
158°
180°
202°
225°
247°
270°
292°
315°
338°
0.12
0.07
0.06
0.07
0.06
0.05
0.08
0.14
0.11
Time (s)
$\vec{a_1}$
$\vec{a_2}$
Amplitude
$|\vec{a_0}|$
$|\vec{a_1}|$
$|\vec{a_2}|$

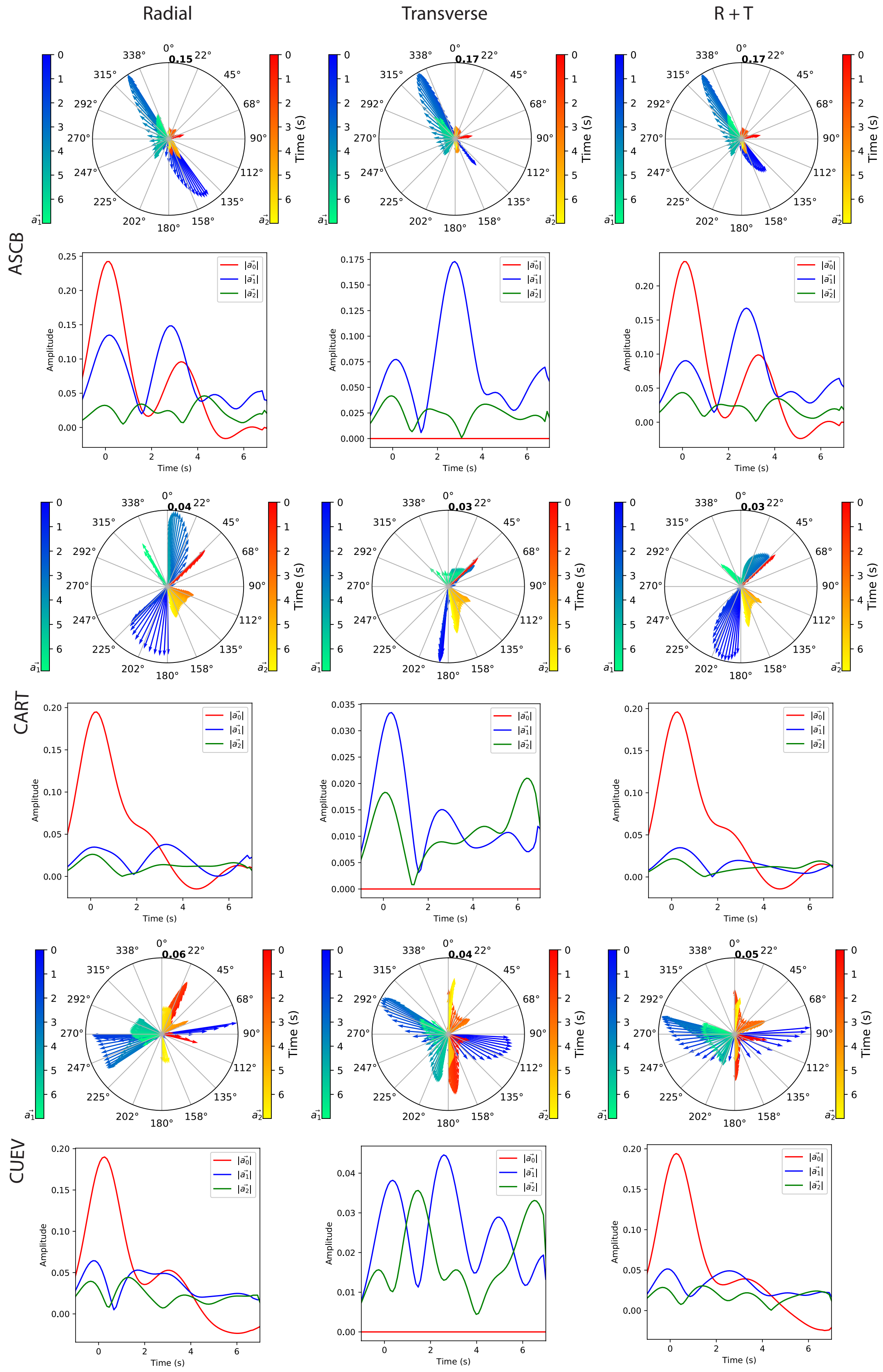
Radial
Transverse
R + T
ASCB
CART
CUEV
0°
22°
45°
68°
90°
112°
135°
158°
180°
202°
225°
247°
270°
292°
315°
338°
0.15
0.17
0.04
0.03
0.06
0.05
Time (s)
$\vec{a_1}$
$\vec{a_2}$
Amplitude
$|\vec{a_0}|$
$|\vec{a_1}|$
$|\vec{a_2}|$
Time (s)

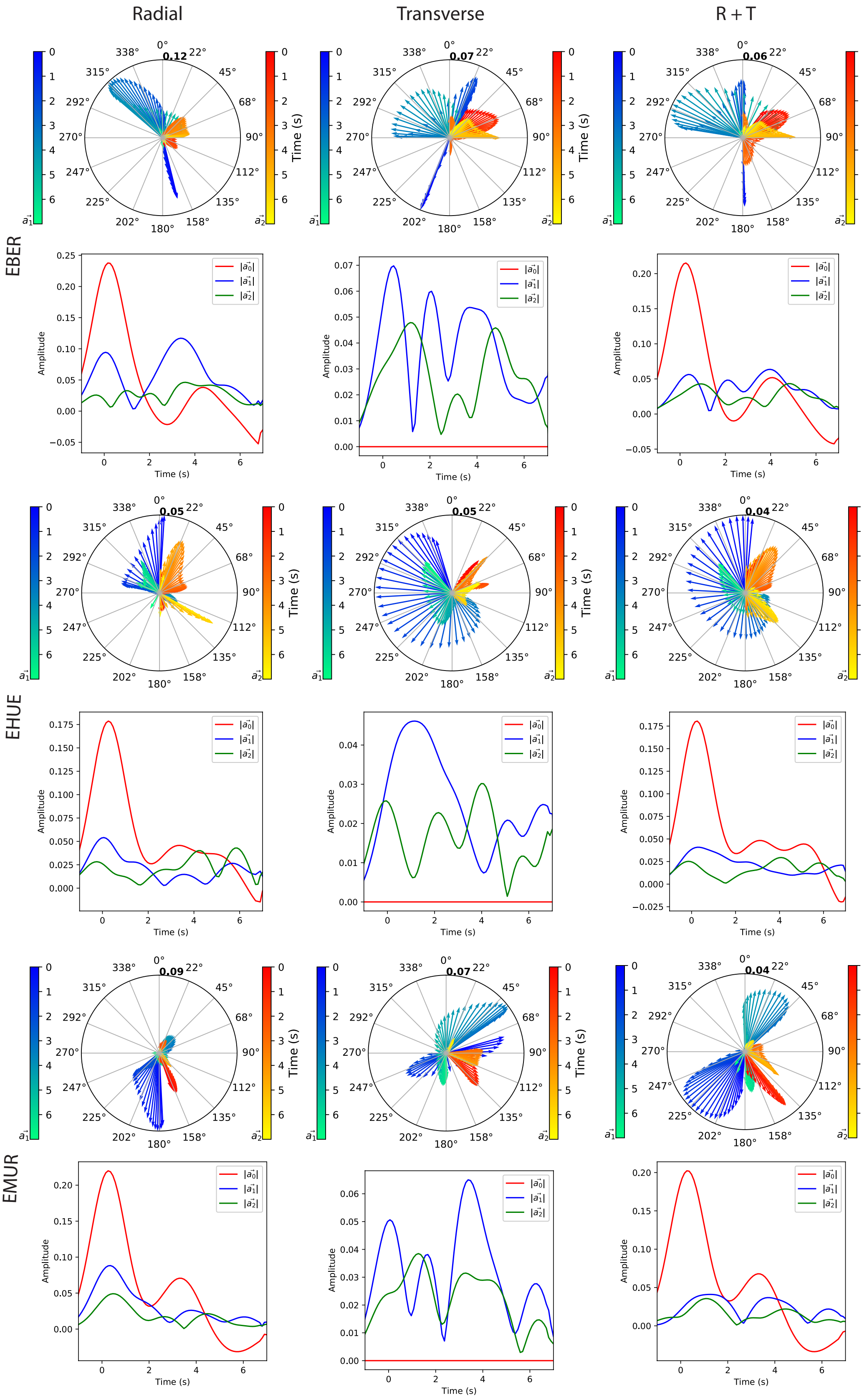
Radial
Transverse
R + T
EBER
EHUE
EMUR
0.12
0.07
0.06
0.05
0.05
0.04
0.09
0.07
0.04
0°
22°
45°
68°
90°
112°
135°
158°
180°
202°
225°
247°
270°
292°
315°
338°
Time (s)
$\vec{a_1}$
$\vec{a_2}$
Amplitude
$|\vec{a_0}|$
$|\vec{a_1}|$
$|\vec{a_2}|$

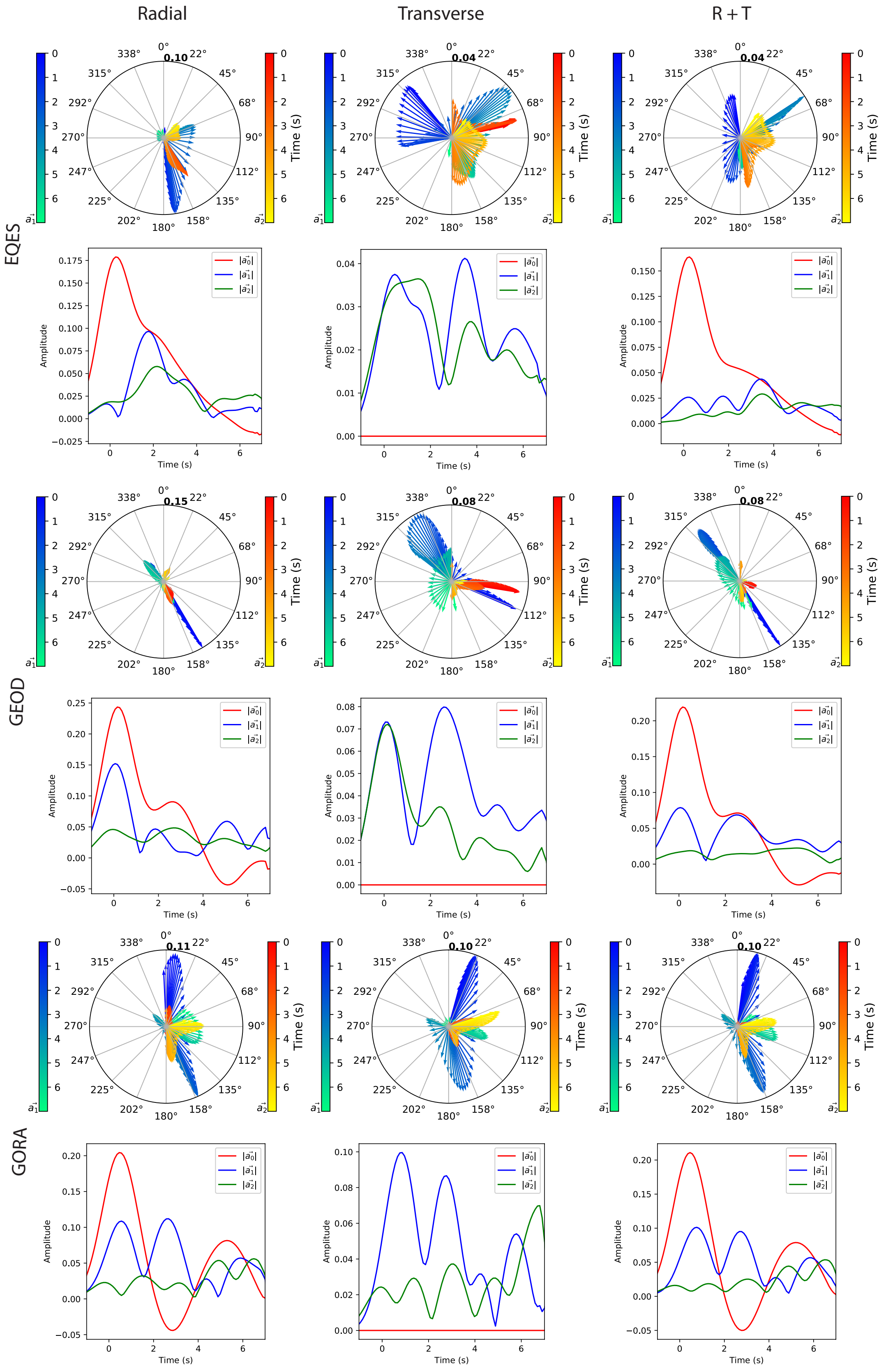
Radial
Transverse
R + T
EQES
GEOD
GORA
0°
22°
45°
68°
90°
112°
135°
158°
180°
202°
225°
247°
270°
292°
315°
338°
0.10
0.04
0.15
0.08
0.11
0.10
$\vec{a_1}$
$\vec{a_2}$
Time (s)
0
1
2
3
4
5
6
$|\vec{a_0}|$
$|\vec{a_1}|$
$|\vec{a_2}|$
Amplitude
Time (s)

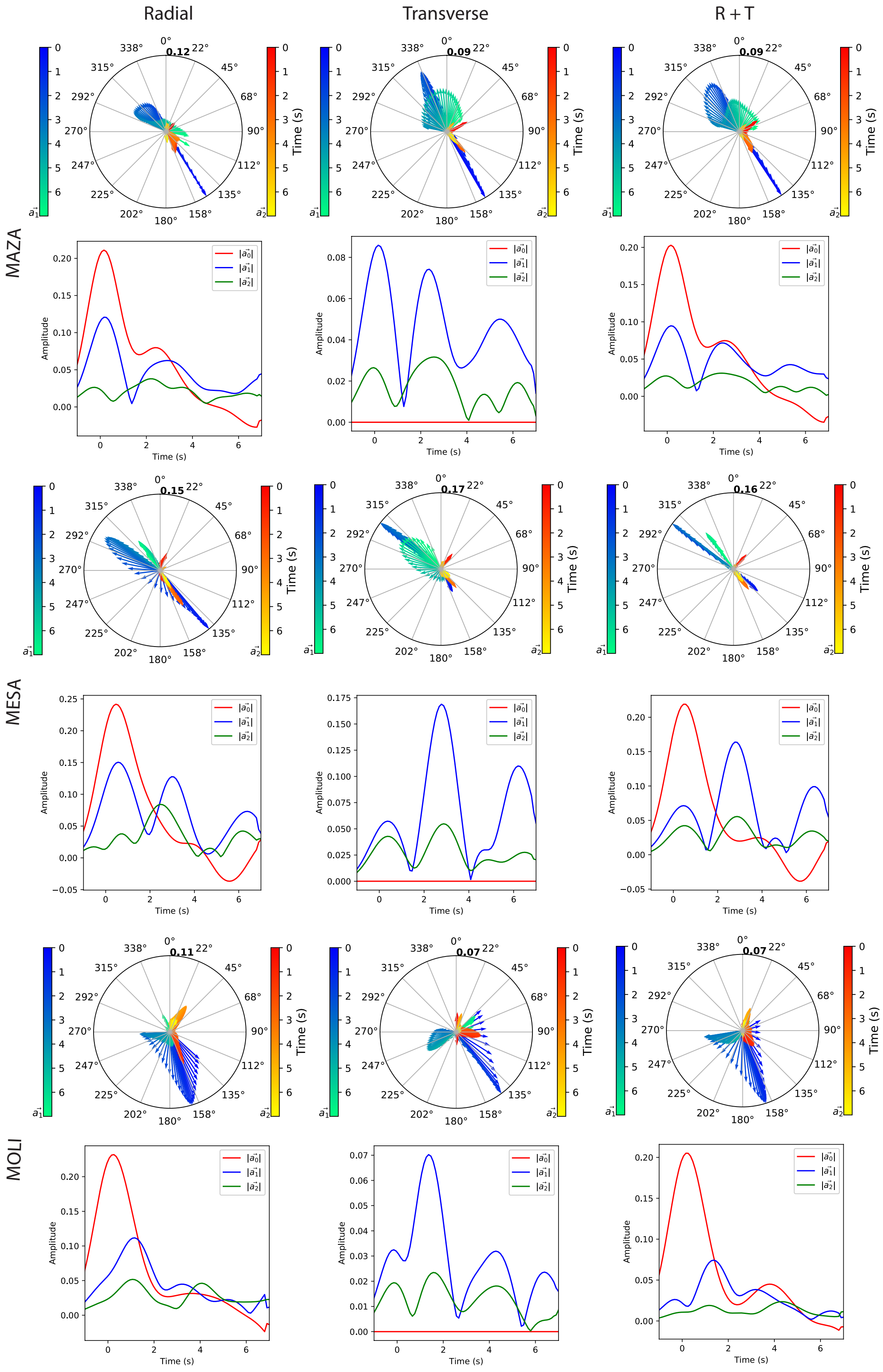
Radial
Transverse
R + T
MAZA
MESA
MOLI
0.12
0.09
0.09
0.15
0.17
0.16
0.11
0.07
0.07
0°
22°
45°
68°
90°
112°
135°
158°
180°
202°
225°
247°
270°
292°
315°
338°
$\vec{a_1}$
$\vec{a_2}$
Time (s)
0
1
2
3
4
5
6
Amplitude
$|\vec{a_0}|$
$|\vec{a_1}|$
$|\vec{a_2}|$
Time (s)

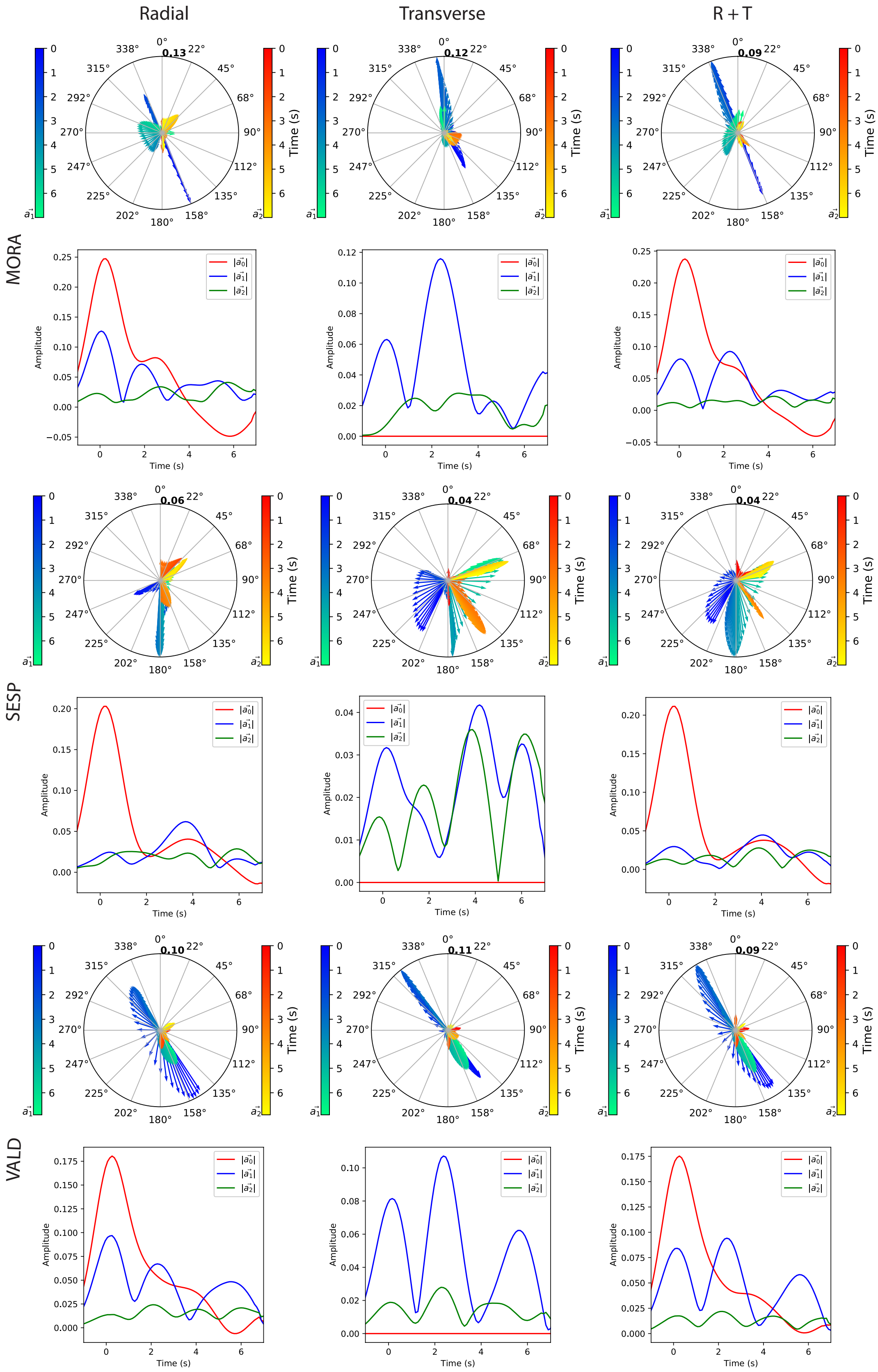
Radial
Transverse
R + T
MORA
SESP
VALD
0°
22°
45°
68°
90°
112°
135°
158°
180°
202°
225°
247°
270°
292°
315°
338°
0.13
0.12
0.09
0.06
0.04
0.04
0.10
0.11
0.09
$\vec{a_1}$
$\vec{a_2}$
Time (s)
0
1
2
3
4
5
6
Amplitude
$|\vec{a_0}|$
$|\vec{a_1}|$
$|\vec{a_2}|$

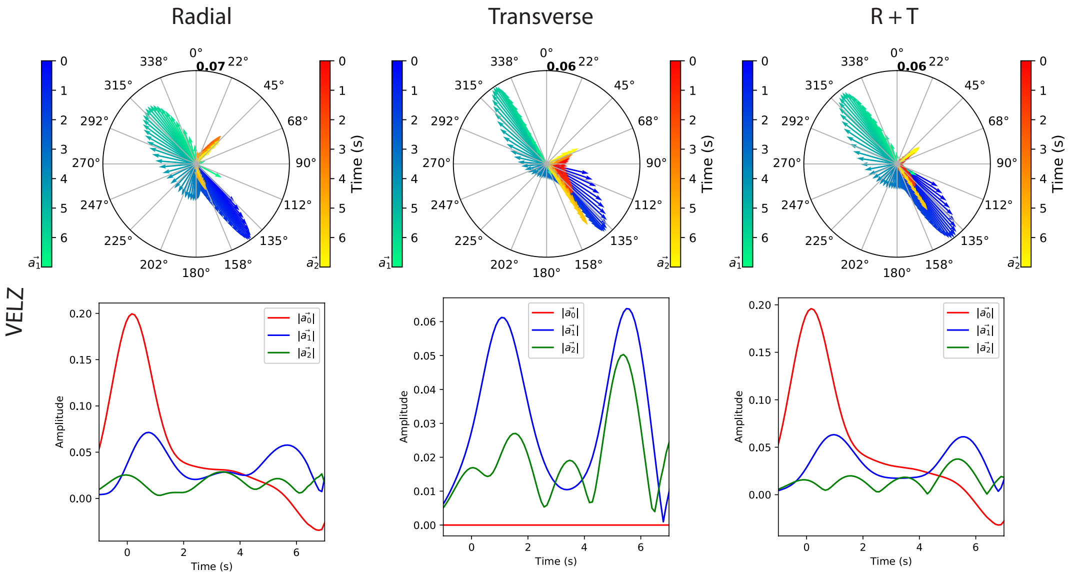
Radial
Transverse
R + T
VELZ
0.07
0.06
0.06
0°
22°
45°
68°
90°
112°
135°
158°
180°
202°
225°
247°
270°
292°
315°
338°
Time (s)
$\vec{a_1}$
$\vec{a_2}$
Amplitude
Time (s)
$|\vec{a_0}|$
$|\vec{a_1}|$
$|\vec{a_2}|$

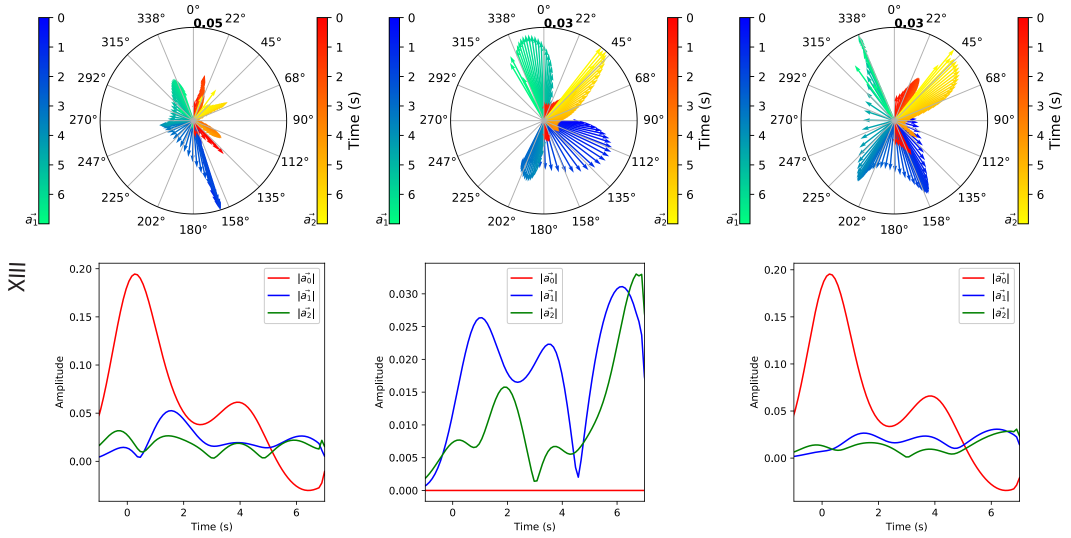
XIII
0.05
0.03
0.03
0°
22°
45°
68°
90°
112°
135°
158°
180°
202°
225°
247°
270°
292°
315°
338°
Time (s)
$\vec{a_1}$
$\vec{a_2}$
Amplitude
Time (s)
$|\vec{a_0}|$
$|\vec{a_1}|$
$|\vec{a_2}|$

Appendix B

Joint Inversion Figures

Joint inversions of RFs and phase and group dispersion curves to real data comparing both HD and BAZ approaches described in section 8.1.2.

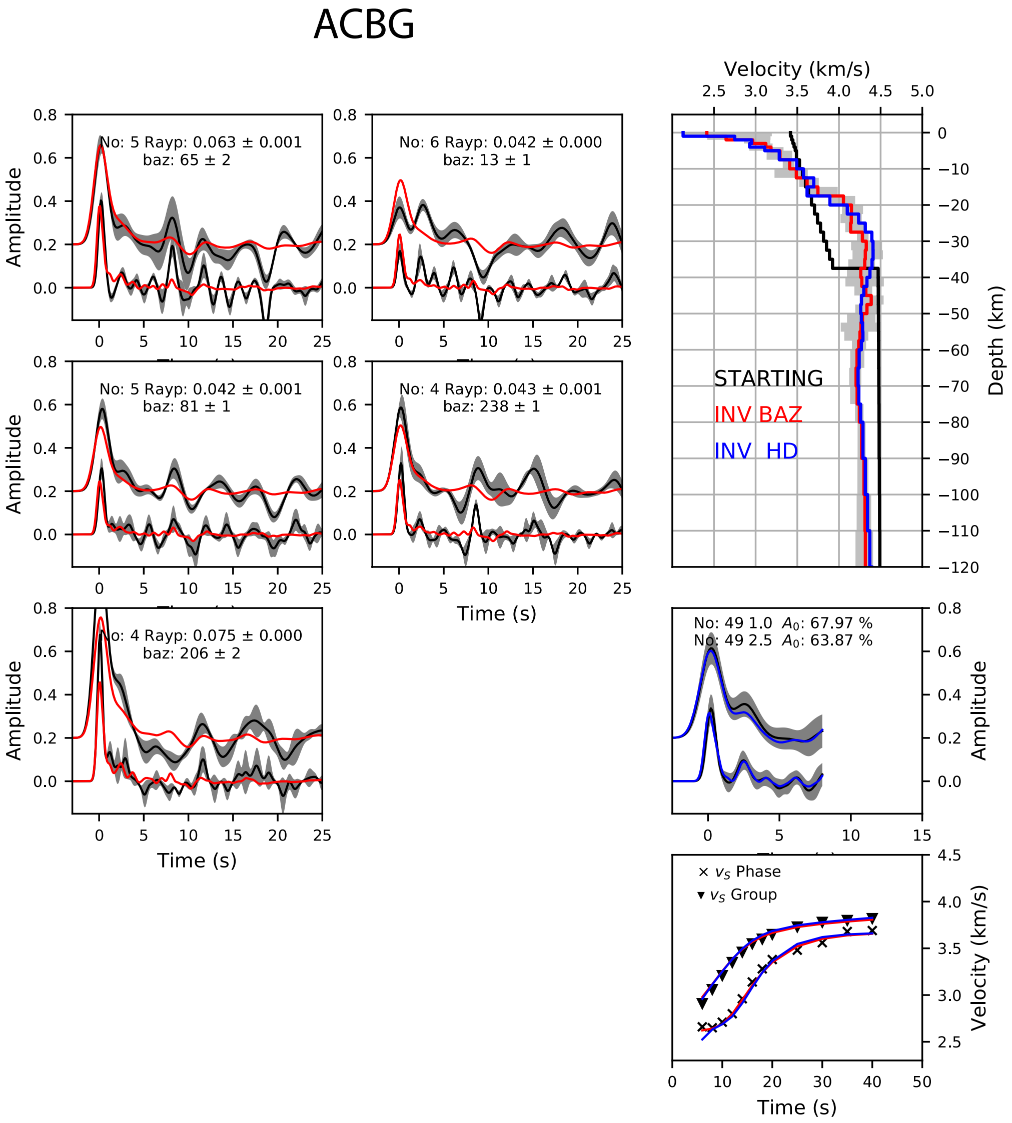
ACBG
No: 5 Rayp: 0.063 ± 0.001
baz: 65 ± 2
No: 6 Rayp: 0.042 ± 0.000
baz: 13 ± 1
No: 5 Rayp: 0.042 ± 0.001
baz: 81 ± 1
No: 4 Rayp: 0.043 ± 0.001
baz: 238 ± 1
No: 4 Rayp: 0.075 ± 0.000
baz: 206 ± 2
Amplitude
Time (s)
Velocity (km/s)
Depth (km)
STARTING
INV BAZ
INV HD
No: 49 1.0 A_0: 67.97 %
No: 49 2.5 A_0: 63.87 %
× v_S Phase
▾ v_S Group
Velocity (km/s)

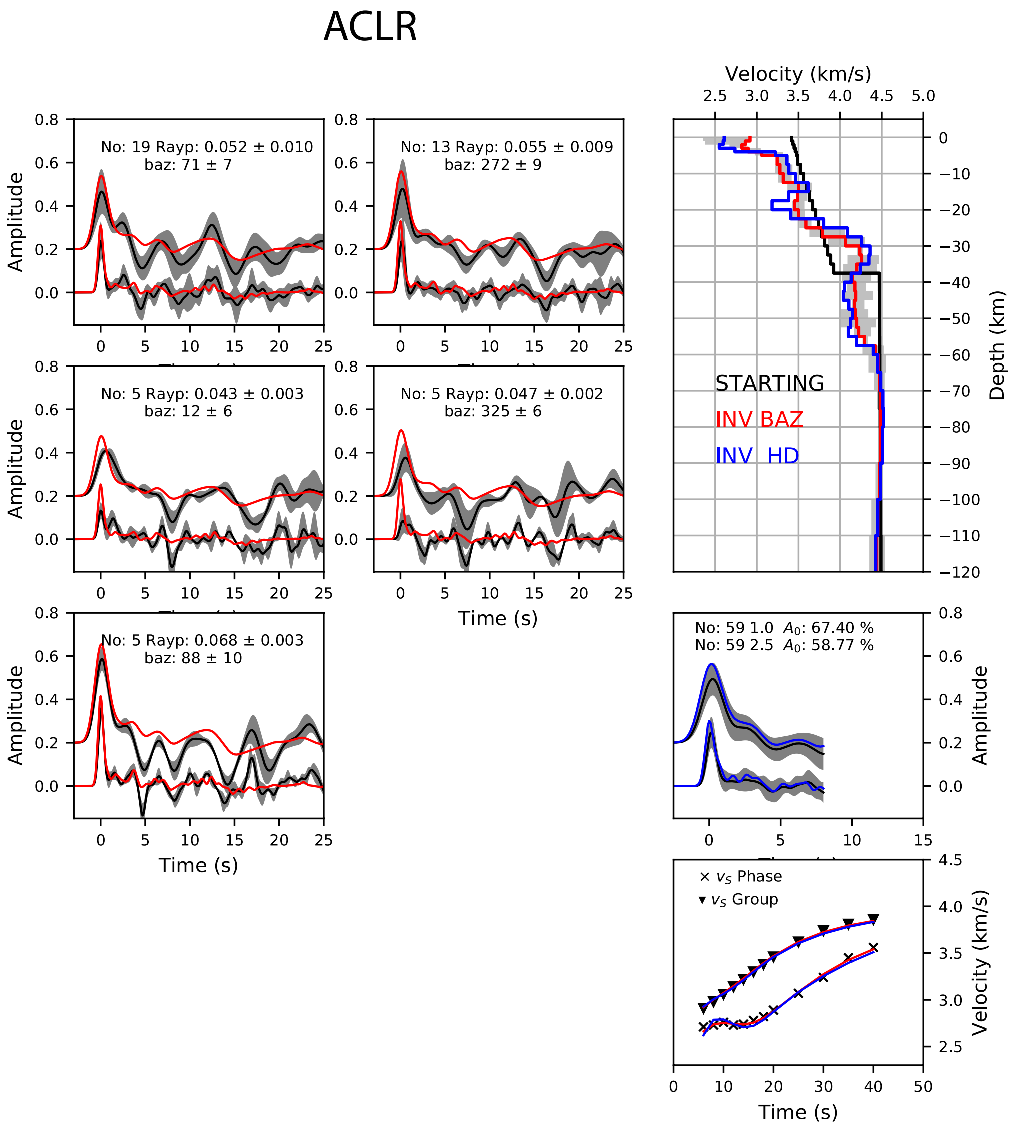
ACLR
No: 19 Rayp: 0.052 ± 0.010
baz: 71 ± 7
No: 13 Rayp: 0.055 ± 0.009
baz: 272 ± 9
No: 5 Rayp: 0.043 ± 0.003
baz: 12 ± 6
No: 5 Rayp: 0.047 ± 0.002
baz: 325 ± 6
No: 5 Rayp: 0.068 ± 0.003
baz: 88 ± 10
Amplitude
Time (s)
0.8
0.6
0.4
0.2
0.0
0
5
10
15
20
25
Velocity (km/s)
2.5
3.0
3.5
4.0
4.5
5.0
Depth (km)
0
−10
−20
−30
−40
−50
−60
−70
−80
−90
−100
−110
−120
STARTING
INV BAZ
INV HD
No: 59 1.0 A_0: 67.40 %
No: 59 2.5 A_0: 58.77 %
× v_S Phase
▾ v_S Group
Velocity (km/s)
4.5
4.0
3.5
3.0
2.5
0
10
20
30
40
50

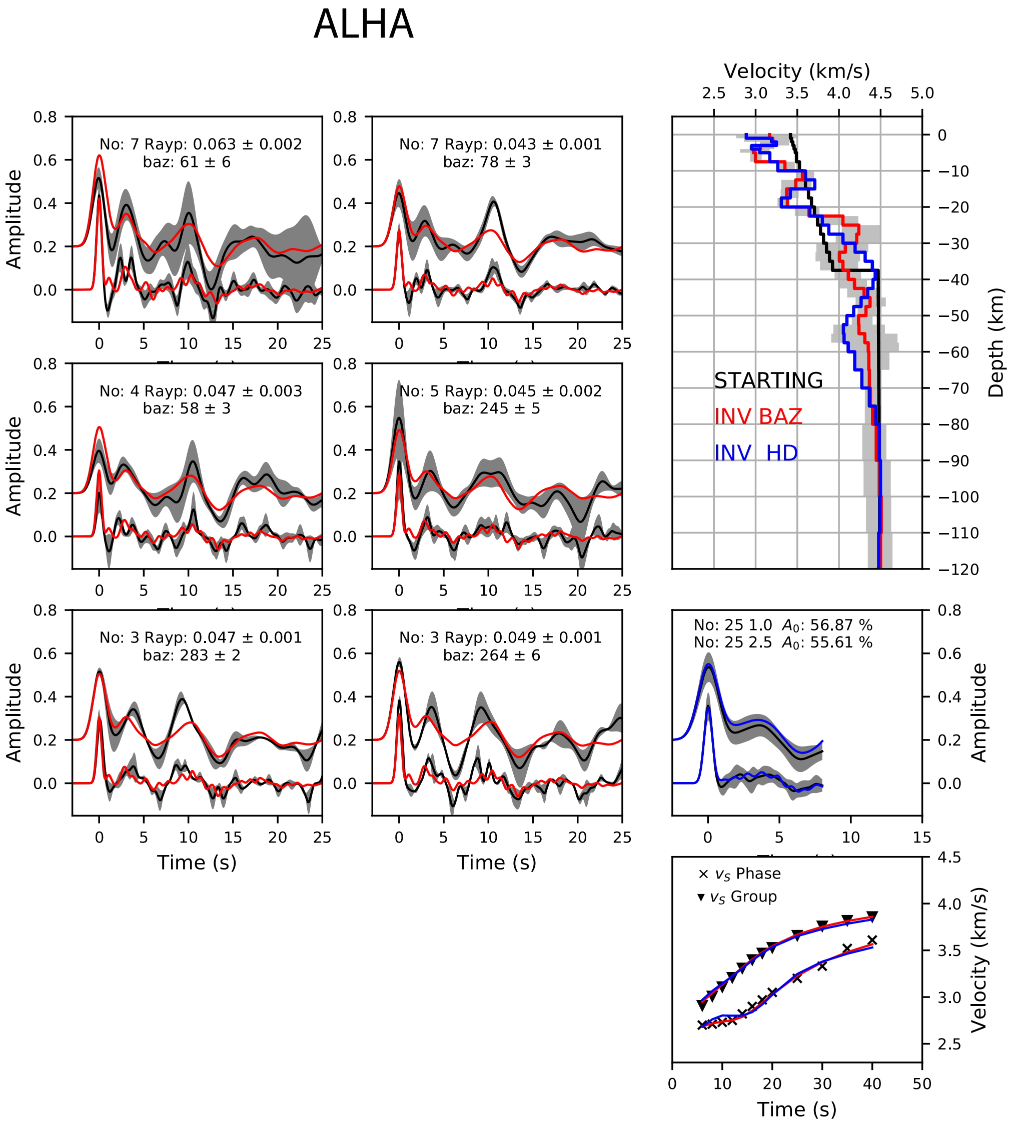
ALHA
No: 7 Rayp: 0.063 ± 0.002
baz: 61 ± 6
No: 7 Rayp: 0.043 ± 0.001
baz: 78 ± 3
No: 4 Rayp: 0.047 ± 0.003
baz: 58 ± 3
No: 5 Rayp: 0.045 ± 0.002
baz: 245 ± 5
No: 3 Rayp: 0.047 ± 0.001
baz: 283 ± 2
No: 3 Rayp: 0.049 ± 0.001
baz: 264 ± 6
Amplitude
Time (s)
Velocity (km/s)
Depth (km)
STARTING
INV BAZ
INV HD
No: 25 1.0 A_0: 56.87 %
No: 25 2.5 A_0: 55.61 %
× v_S Phase
▾ v_S Group
Velocity (km/s)
Time (s)

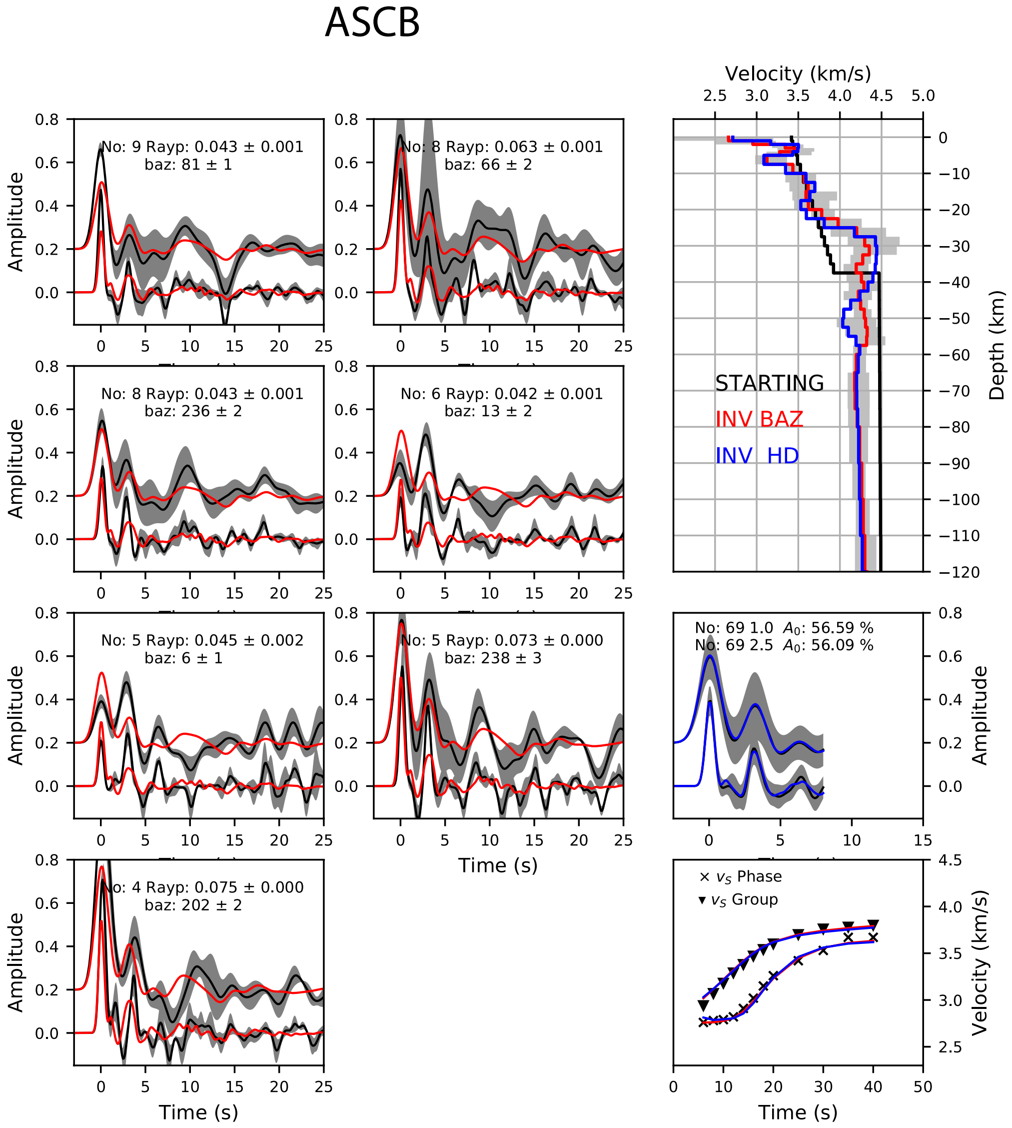
ASCB
No: 9 Rayp: 0.043 ± 0.001
baz: 81 ± 1
No: 8 Rayp: 0.063 ± 0.001
baz: 66 ± 2
No: 8 Rayp: 0.043 ± 0.001
baz: 236 ± 2
No: 6 Rayp: 0.042 ± 0.001
baz: 13 ± 2
No: 5 Rayp: 0.045 ± 0.002
baz: 6 ± 1
No: 5 Rayp: 0.073 ± 0.000
baz: 238 ± 3
No: 4 Rayp: 0.075 ± 0.000
baz: 202 ± 2
Amplitude
Time (s)
Velocity (km/s)
Depth (km)
STARTING
INV BAZ
INV HD
No: 69 1.0 A_0: 56.59 %
No: 69 2.5 A_0: 56.09 %
× v_S Phase
▾ v_S Group
Velocity (km/s)
Time (s)

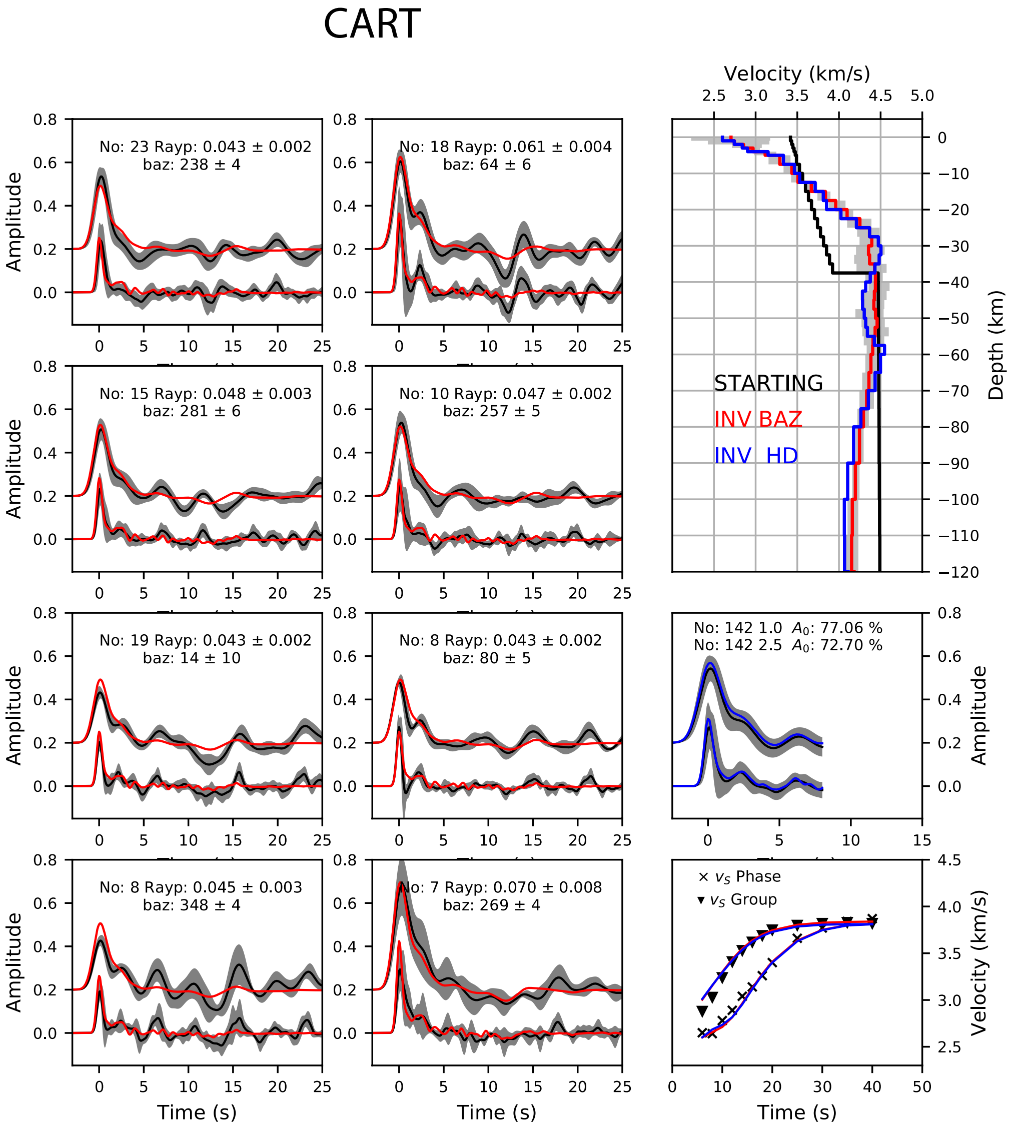
CART
No: 23 Rayp: 0.043 ± 0.002
baz: 238 ± 4
No: 18 Rayp: 0.061 ± 0.004
baz: 64 ± 6
No: 15 Rayp: 0.048 ± 0.003
baz: 281 ± 6
No: 10 Rayp: 0.047 ± 0.002
baz: 257 ± 5
No: 19 Rayp: 0.043 ± 0.002
baz: 14 ± 10
No: 8 Rayp: 0.043 ± 0.002
baz: 80 ± 5
No: 8 Rayp: 0.045 ± 0.003
baz: 348 ± 4
No: 7 Rayp: 0.070 ± 0.008
baz: 269 ± 4
Amplitude
Time (s)
Velocity (km/s)
Depth (km)
STARTING
INV BAZ
INV HD
No: 142 1.0 A_0: 77.06 %
No: 142 2.5 A_0: 72.70 %
× v_S Phase
▾ v_S Group
0.0
0.2
0.4
0.6
0.8
0
5
10
15
20
25
2.5
3.0
3.5
4.0
4.5
5.0
0
−10
−20
−30
−40
−50
−60
−70
−80
−90
−100
−110
−120
30
40
50

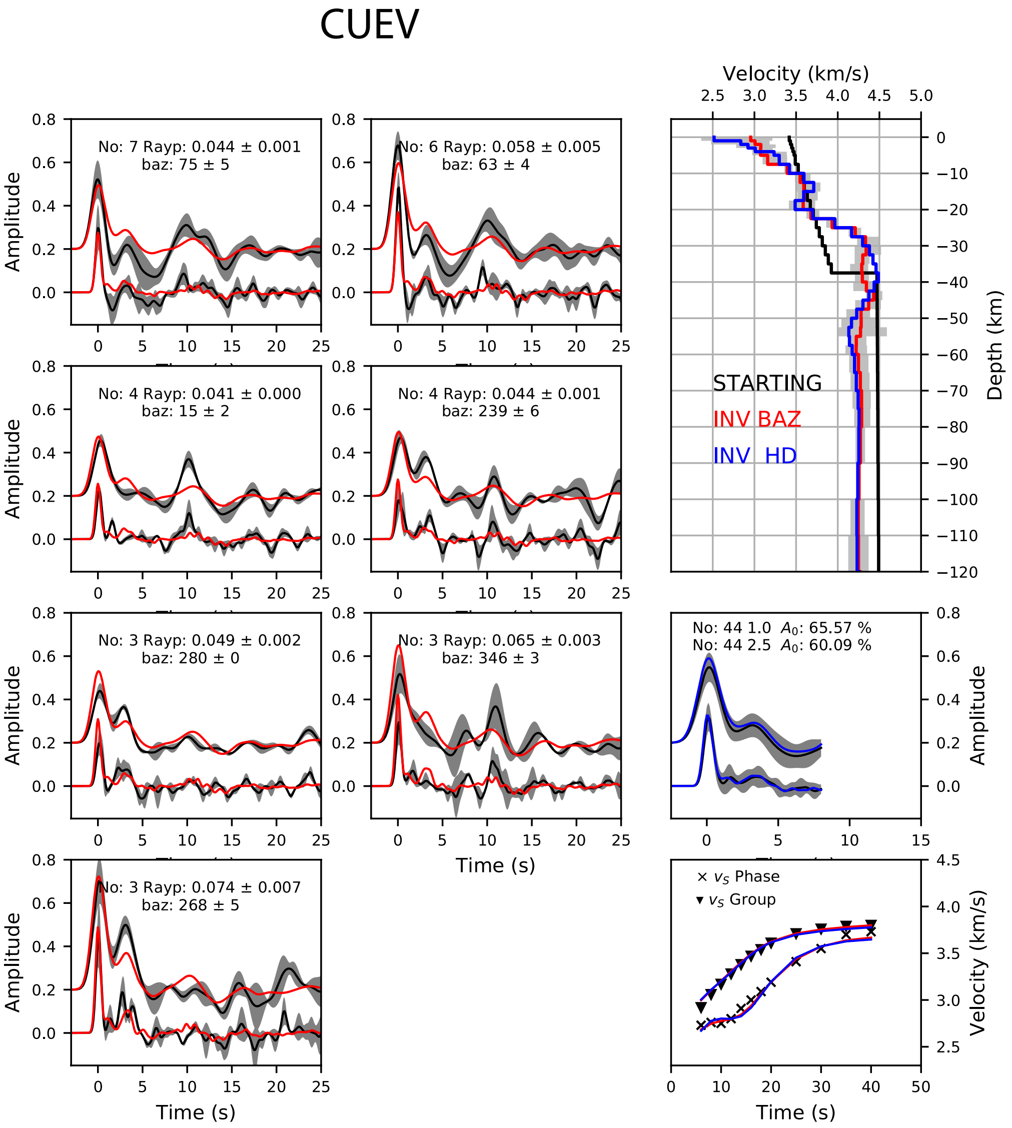
CUEV
No: 7 Rayp: 0.044 ± 0.001
baz: 75 ± 5
No: 6 Rayp: 0.058 ± 0.005
baz: 63 ± 4
No: 4 Rayp: 0.041 ± 0.000
baz: 15 ± 2
No: 4 Rayp: 0.044 ± 0.001
baz: 239 ± 6
No: 3 Rayp: 0.049 ± 0.002
baz: 280 ± 0
No: 3 Rayp: 0.065 ± 0.003
baz: 346 ± 3
No: 3 Rayp: 0.074 ± 0.007
baz: 268 ± 5
Amplitude
Time (s)
Velocity (km/s)
Depth (km)
STARTING
INV BAZ
INV HD
No: 44 1.0 A_0: 65.57 %
No: 44 2.5 A_0: 60.09 %
× v_S Phase
▾ v_S Group
Velocity (km/s)
Time (s)

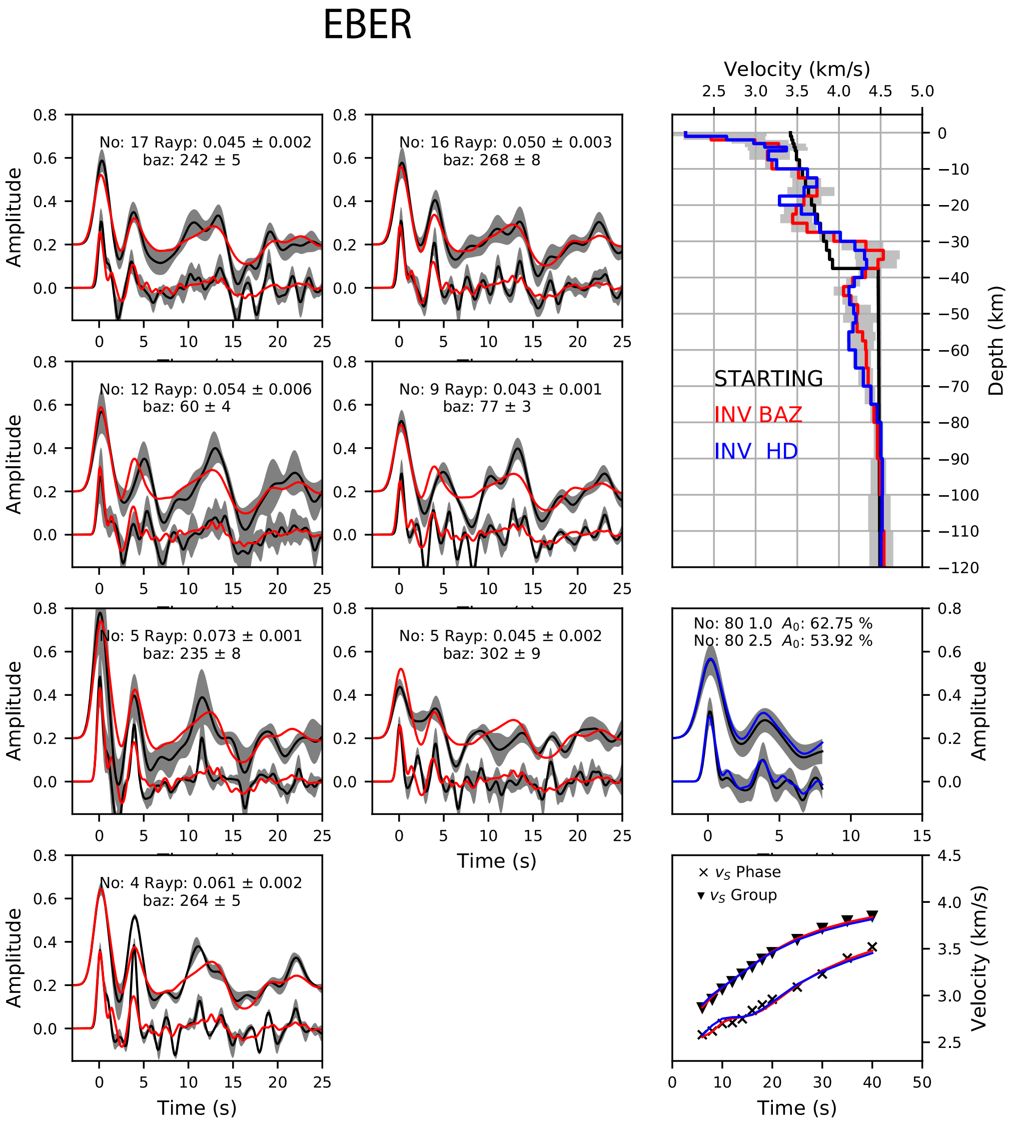
EBER
No: 17 Rayp: 0.045 ± 0.002
baz: 242 ± 5
No: 16 Rayp: 0.050 ± 0.003
baz: 268 ± 8
No: 12 Rayp: 0.054 ± 0.006
baz: 60 ± 4
No: 9 Rayp: 0.043 ± 0.001
baz: 77 ± 3
No: 5 Rayp: 0.073 ± 0.001
baz: 235 ± 8
No: 5 Rayp: 0.045 ± 0.002
baz: 302 ± 9
No: 4 Rayp: 0.061 ± 0.002
baz: 264 ± 5
Amplitude
Time (s)
Velocity (km/s)
Depth (km)
STARTING
INV BAZ
INV HD
No: 80 1.0 A_0: 62.75 %
No: 80 2.5 A_0: 53.92 %
× v_S Phase
▾ v_S Group
Velocity (km/s)
Time (s)

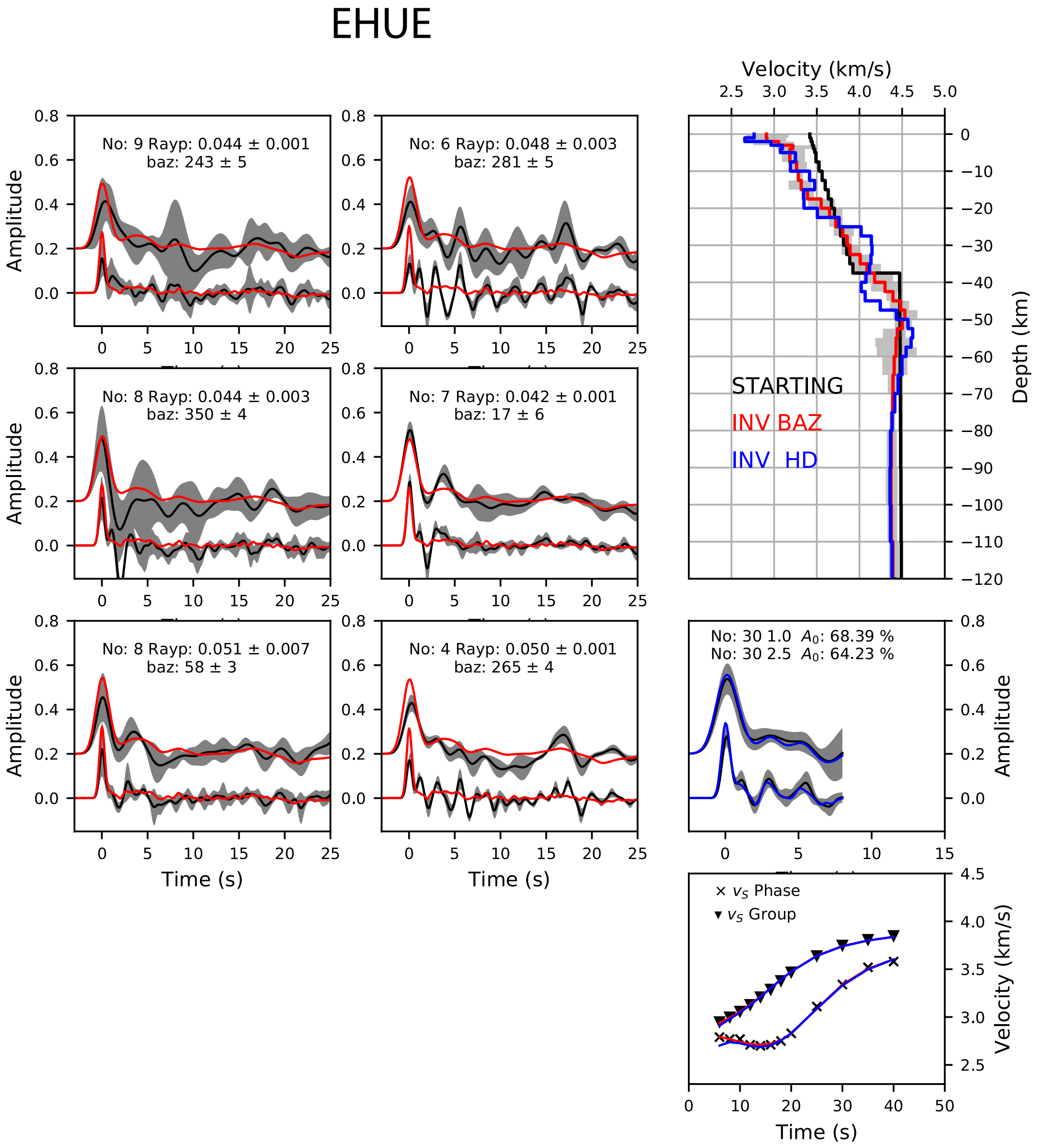
EHUE
No: 9 Rayp: 0.044 ± 0.001
baz: 243 ± 5
No: 6 Rayp: 0.048 ± 0.003
baz: 281 ± 5
No: 8 Rayp: 0.044 ± 0.003
baz: 350 ± 4
No: 7 Rayp: 0.042 ± 0.001
baz: 17 ± 6
No: 8 Rayp: 0.051 ± 0.007
baz: 58 ± 3
No: 4 Rayp: 0.050 ± 0.001
baz: 265 ± 4
Amplitude
Time (s)
Velocity (km/s)
Depth (km)
STARTING
INV BAZ
INV HD
No: 30 1.0 A_0: 68.39 %
No: 30 2.5 A_0: 64.23 %
× v_S Phase
▾ v_S Group
Velocity (km/s)
Time (s)

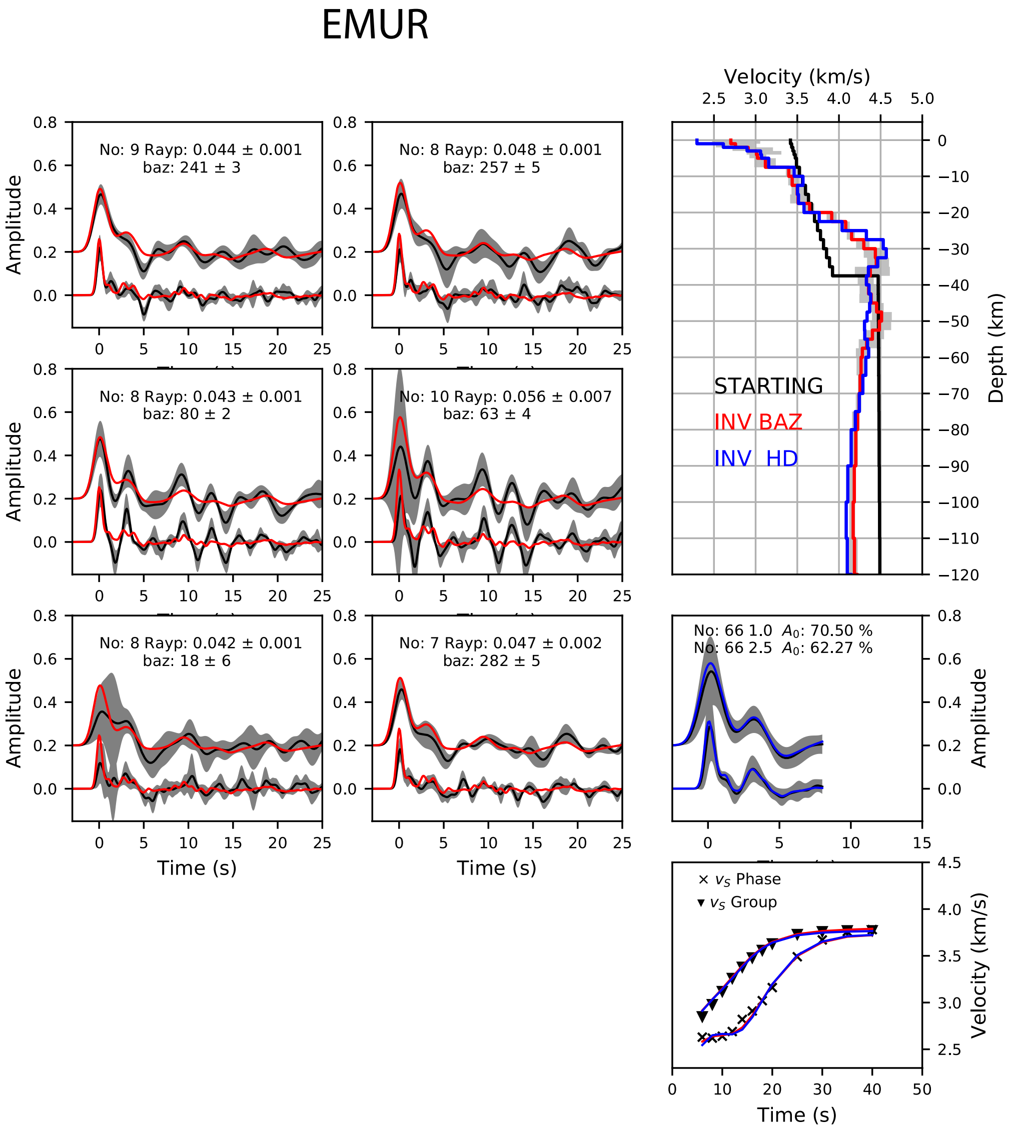
EMUR
No: 9 Rayp: 0.044 ± 0.001
baz: 241 ± 3
No: 8 Rayp: 0.048 ± 0.001
baz: 257 ± 5
No: 8 Rayp: 0.043 ± 0.001
baz: 80 ± 2
No: 10 Rayp: 0.056 ± 0.007
baz: 63 ± 4
No: 8 Rayp: 0.042 ± 0.001
baz: 18 ± 6
No: 7 Rayp: 0.047 ± 0.002
baz: 282 ± 5
Amplitude
Time (s)
Velocity (km/s)
Depth (km)
STARTING
INV BAZ
INV HD
No: 66 1.0 A_0: 70.50 %
No: 66 2.5 A_0: 62.27 %
× v_S Phase
▾ v_S Group
Velocity (km/s)
Time (s)

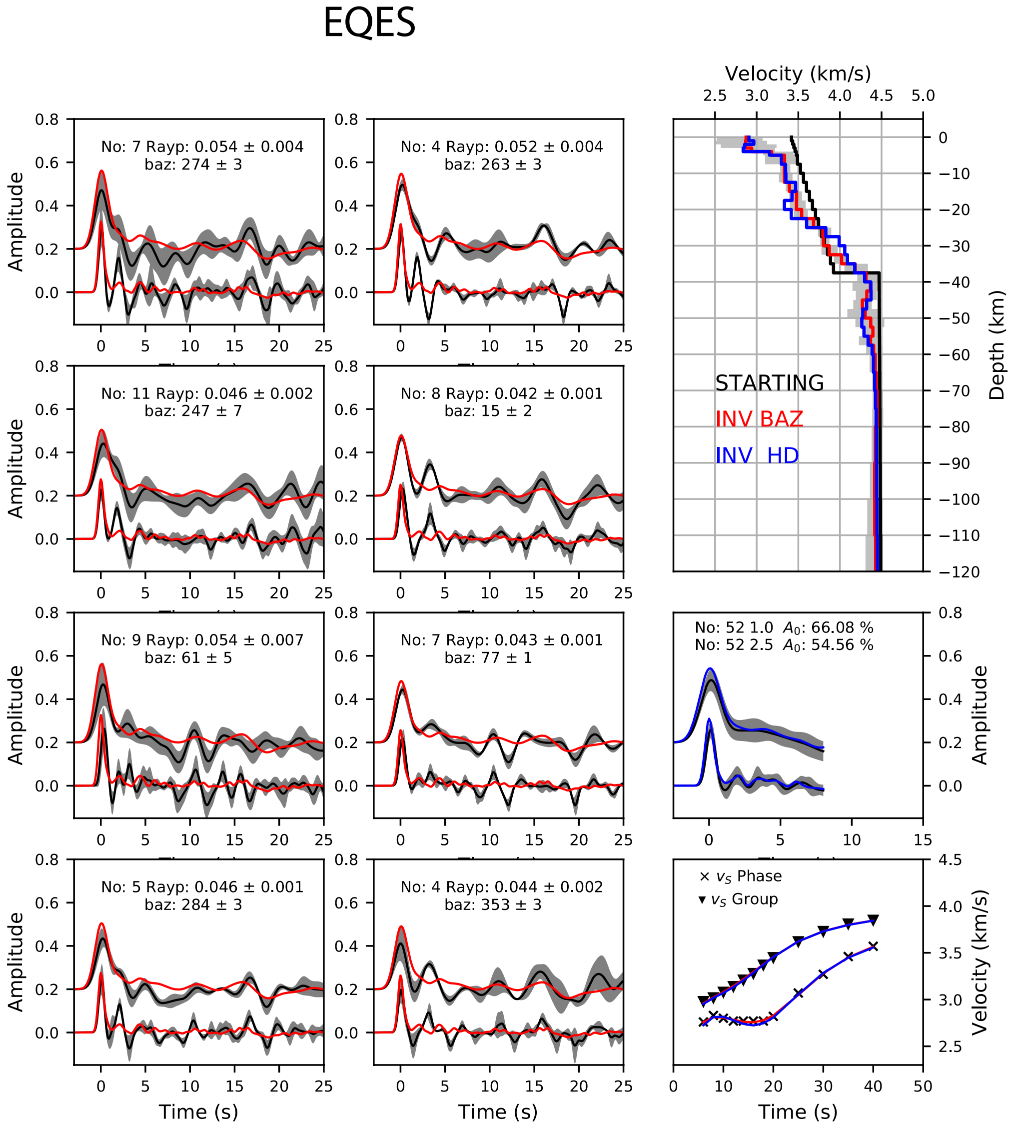
EQES
No: 7 Rayp: 0.054 ± 0.004
baz: 274 ± 3
No: 4 Rayp: 0.052 ± 0.004
baz: 263 ± 3
No: 11 Rayp: 0.046 ± 0.002
baz: 247 ± 7
No: 8 Rayp: 0.042 ± 0.001
baz: 15 ± 2
No: 9 Rayp: 0.054 ± 0.007
baz: 61 ± 5
No: 7 Rayp: 0.043 ± 0.001
baz: 77 ± 1
No: 5 Rayp: 0.046 ± 0.001
baz: 284 ± 3
No: 4 Rayp: 0.044 ± 0.002
baz: 353 ± 3
Amplitude
Time (s)
Velocity (km/s)
Depth (km)
STARTING
INV BAZ
INV HD
No: 52 1.0 A_0: 66.08 %
No: 52 2.5 A_0: 54.56 %
× v_S Phase
▾ v_S Group
Velocity (km/s)
0.8
0.6
0.4
0.2
0.0
0
5
10
15
20
25
2.5
3.0
3.5
4.0
4.5
5.0
−10
−20
−30
−40
−50
−60
−70
−80
−90
−100
−110
−120
30
40
50

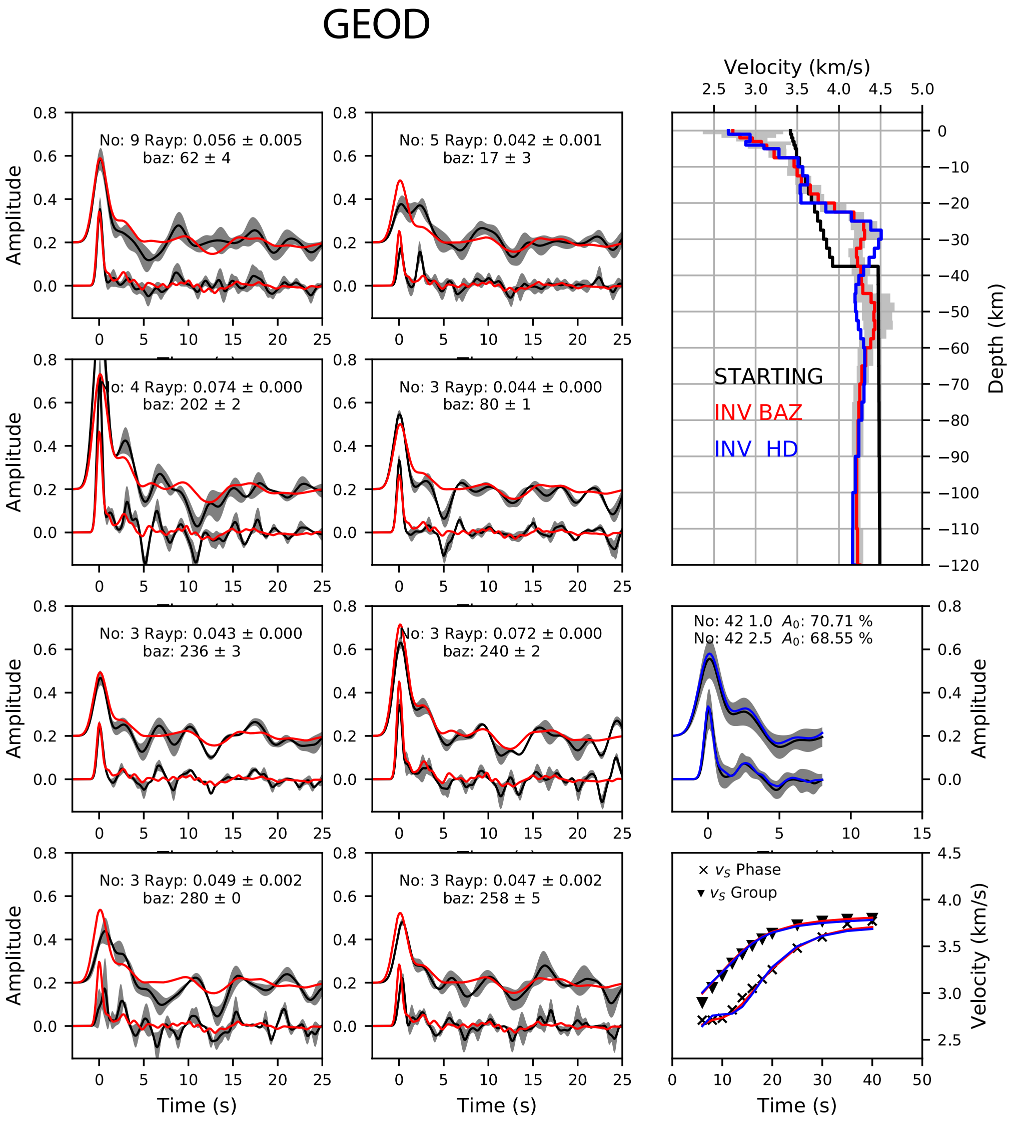
GEOD
No: 9 Rayp: 0.056 ± 0.005
baz: 62 ± 4
No: 5 Rayp: 0.042 ± 0.001
baz: 17 ± 3
No: 4 Rayp: 0.074 ± 0.000
baz: 202 ± 2
No: 3 Rayp: 0.044 ± 0.000
baz: 80 ± 1
No: 3 Rayp: 0.043 ± 0.000
baz: 236 ± 3
No: 3 Rayp: 0.072 ± 0.000
baz: 240 ± 2
No: 3 Rayp: 0.049 ± 0.002
baz: 280 ± 0
No: 3 Rayp: 0.047 ± 0.002
baz: 258 ± 5
Amplitude
Time (s)
Velocity (km/s)
Depth (km)
STARTING
INV BAZ
INV HD
No: 42 1.0 A_0: 70.71 %
No: 42 2.5 A_0: 68.55 %
× v_S Phase
▾ v_S Group
Velocity (km/s)
0.8
0.6
0.4
0.2
0.0
0
5
10
15
20
25
2.5
3.0
3.5
4.0
4.5
5.0
0
−10
−20
−30
−40
−50
−60
−70
−80
−90
−100
−110
−120
30
40
50

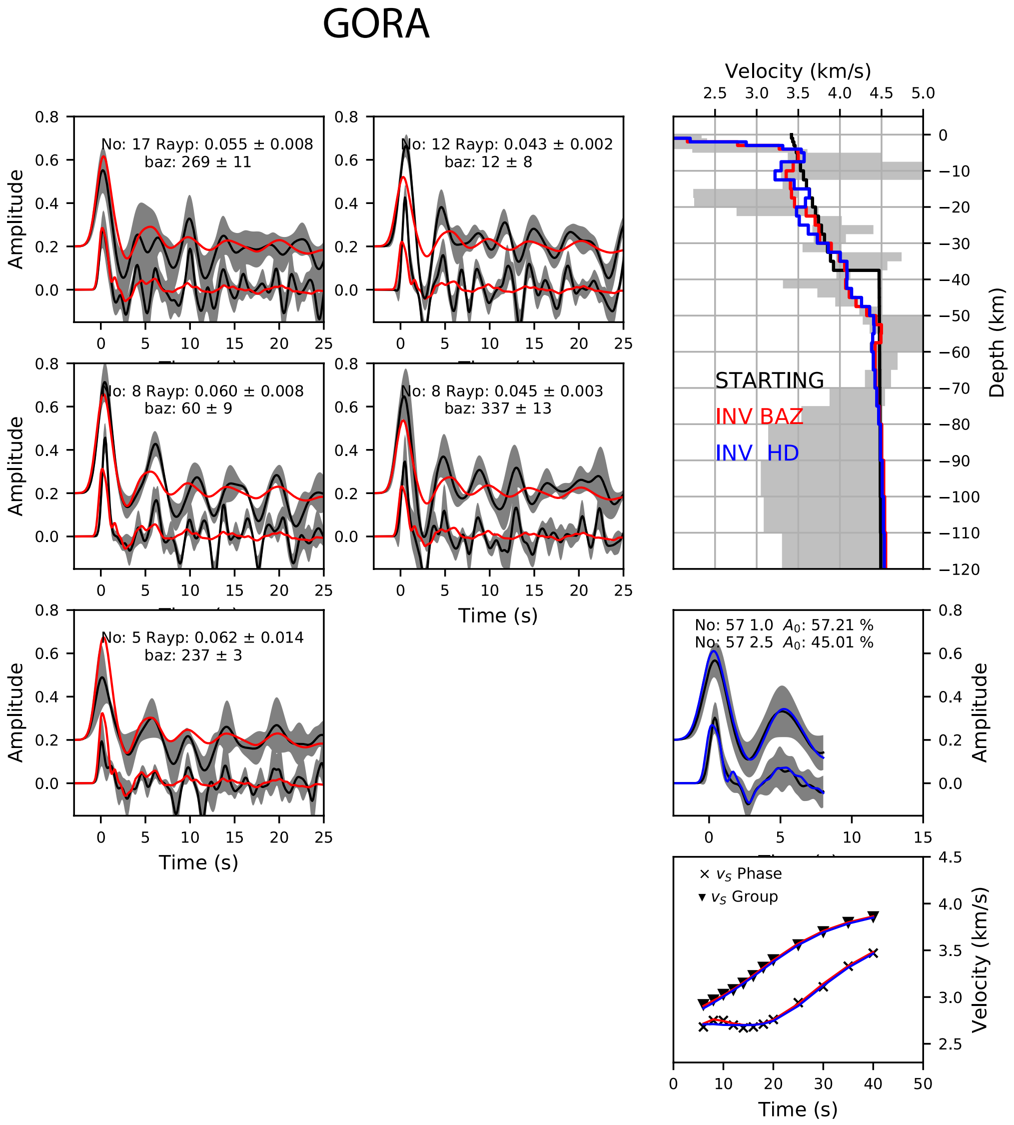
GORA
No: 17 Rayp: 0.055 ± 0.008
baz: 269 ± 11
No: 12 Rayp: 0.043 ± 0.002
baz: 12 ± 8
No: 8 Rayp: 0.060 ± 0.008
baz: 60 ± 9
No: 8 Rayp: 0.045 ± 0.003
baz: 337 ± 13
No: 5 Rayp: 0.062 ± 0.014
baz: 237 ± 3
Amplitude
Time (s)
0.8
0.6
0.4
0.2
0.0
0
5
10
15
20
25
Velocity (km/s)
2.5
3.0
3.5
4.0
4.5
5.0
Depth (km)
0
−10
−20
−30
−40
−50
−60
−70
−80
−90
−100
−110
−120
STARTING
INV BAZ
INV HD
No: 57 1.0 A_0: 57.21 %
No: 57 2.5 A_0: 45.01 %
× v_S Phase
▾ v_S Group
Velocity (km/s)
4.5
4.0
3.5
3.0
2.5
30
40
50

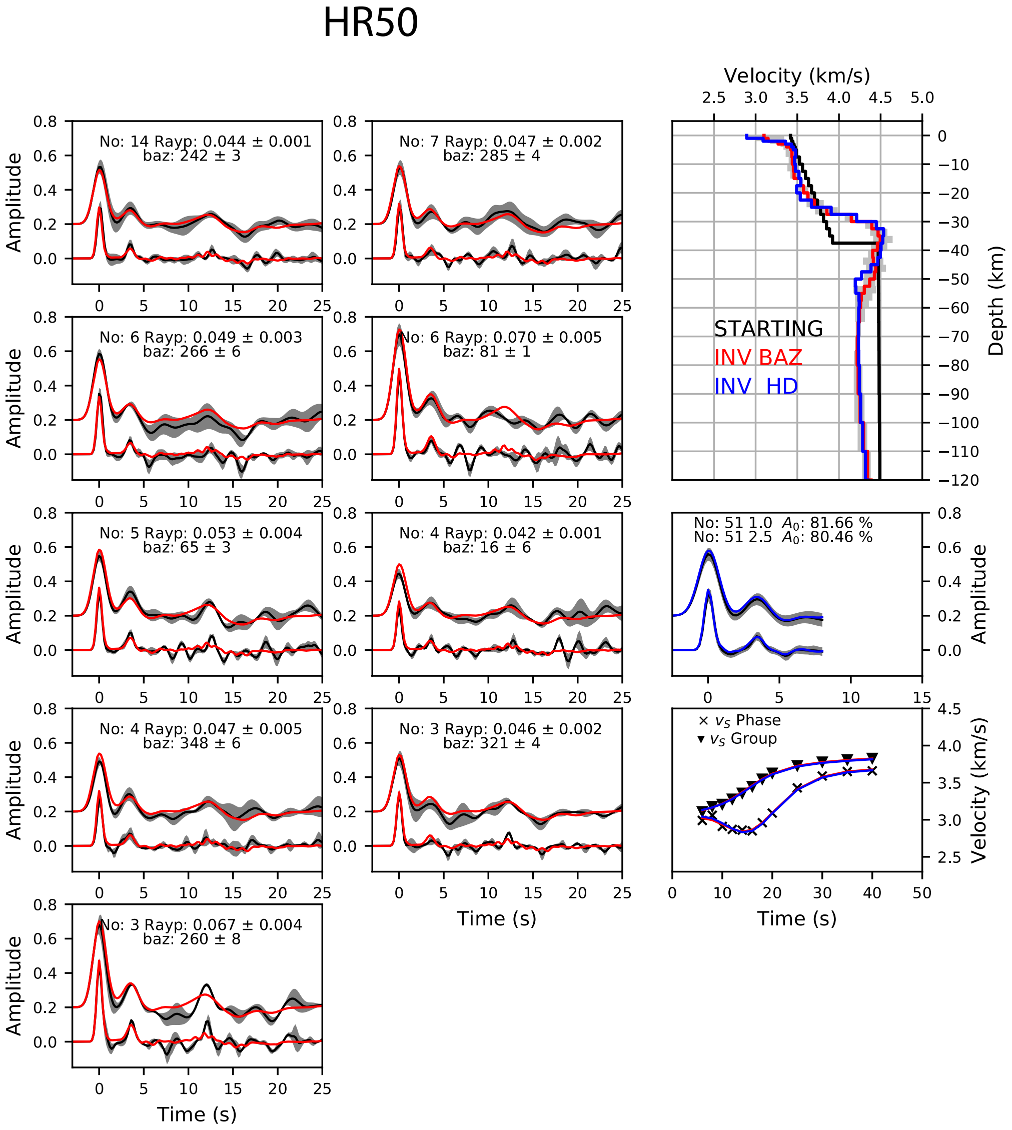
HR50
No: 14 Rayp: 0.044 ± 0.001
baz: 242 ± 3
No: 7 Rayp: 0.047 ± 0.002
baz: 285 ± 4
No: 6 Rayp: 0.049 ± 0.003
baz: 266 ± 6
No: 6 Rayp: 0.070 ± 0.005
baz: 81 ± 1
No: 5 Rayp: 0.053 ± 0.004
baz: 65 ± 3
No: 4 Rayp: 0.042 ± 0.001
baz: 16 ± 6
No: 4 Rayp: 0.047 ± 0.005
baz: 348 ± 6
No: 3 Rayp: 0.046 ± 0.002
baz: 321 ± 4
No: 3 Rayp: 0.067 ± 0.004
baz: 260 ± 8
Amplitude
Time (s)
0.8
0.6
0.4
0.2
0.0
0
5
10
15
20
25
Velocity (km/s)
2.5
3.0
3.5
4.0
4.5
5.0
Depth (km)
0
−10
−20
−30
−40
−50
−60
−70
−80
−90
−100
−110
−120
STARTING
INV BAZ
INV HD
No: 51 1.0 A_0: 81.66 %
No: 51 2.5 A_0: 80.46 %
× v_S Phase
▾ v_S Group
Velocity (km/s)
4.5
4.0
3.5
3.0
2.5
0
10
20
30
40
50

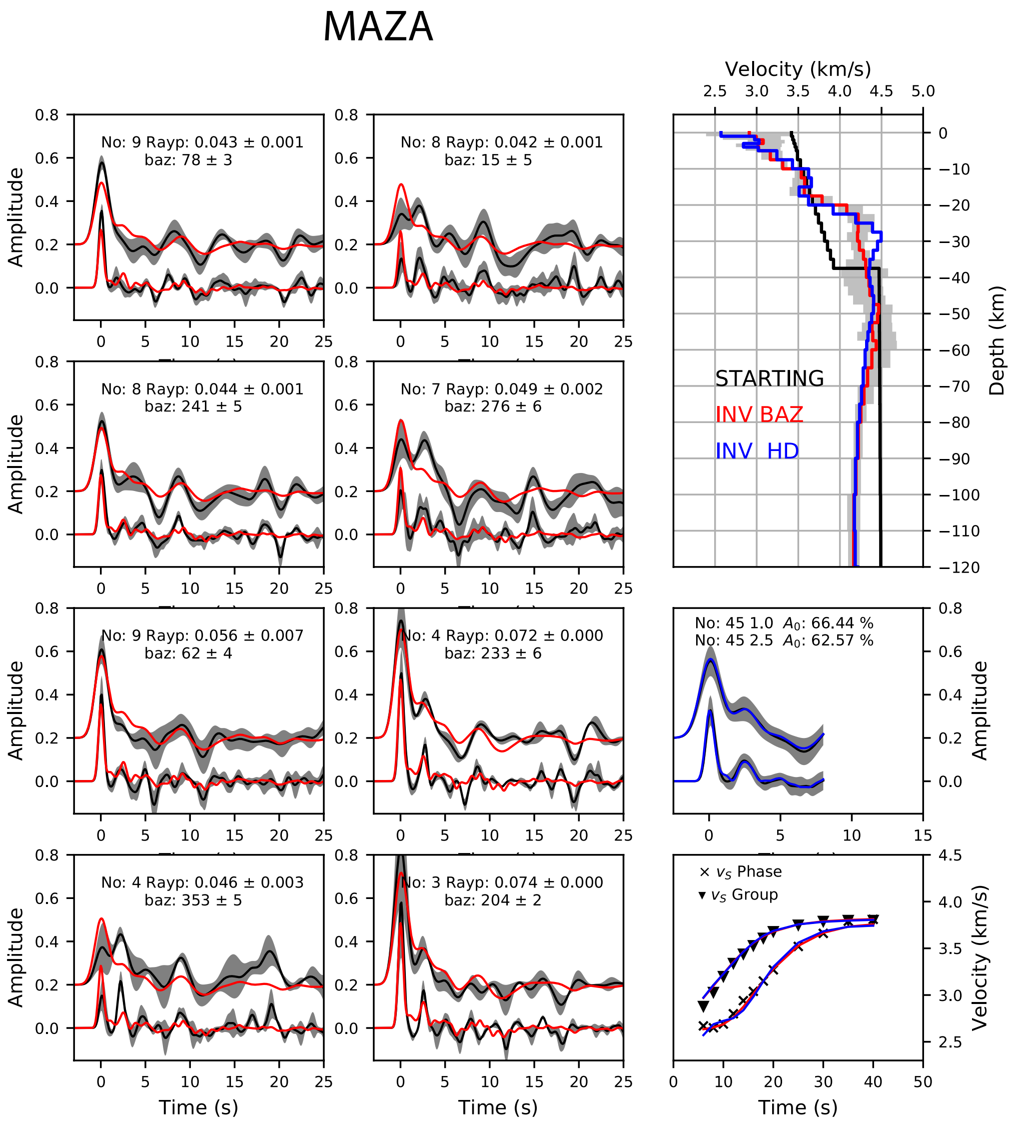
MAZA
No: 9 Rayp: 0.043 ± 0.001
baz: 78 ± 3
No: 8 Rayp: 0.042 ± 0.001
baz: 15 ± 5
No: 8 Rayp: 0.044 ± 0.001
baz: 241 ± 5
No: 7 Rayp: 0.049 ± 0.002
baz: 276 ± 6
No: 9 Rayp: 0.056 ± 0.007
baz: 62 ± 4
No: 4 Rayp: 0.072 ± 0.000
baz: 233 ± 6
No: 4 Rayp: 0.046 ± 0.003
baz: 353 ± 5
No: 3 Rayp: 0.074 ± 0.000
baz: 204 ± 2
Amplitude
Time (s)
Velocity (km/s)
Depth (km)
STARTING
INV BAZ
INV HD
No: 45 1.0 A_0: 66.44 %
No: 45 2.5 A_0: 62.57 %
× v_S Phase
▾ v_S Group
Velocity (km/s)
Time (s)

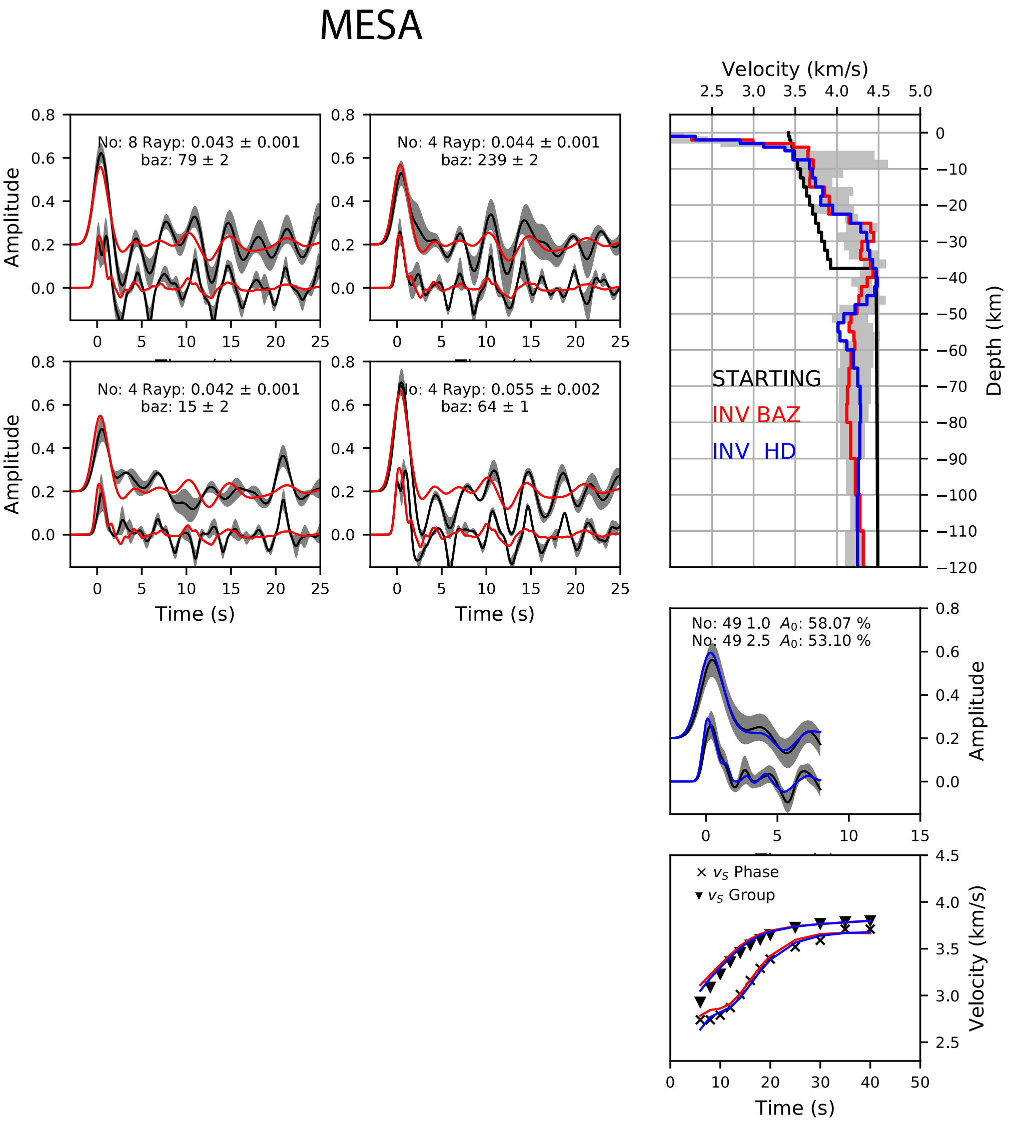

MESA

No: 8 Rayp: 0.043 ± 0.001
baz: 79 ± 2
No: 4 Rayp: 0.044 ± 0.001
baz: 239 ± 2
No: 4 Rayp: 0.042 ± 0.001
baz: 15 ± 2
No: 4 Rayp: 0.055 ± 0.002
baz: 64 ± 1
Amplitude
Time (s)
Velocity (km/s)
Depth (km)
STARTING
INV BAZ
INV HD
No: 49 1.0 A_0: 58.07 %
No: 49 2.5 A_0: 53.10 %
× v_S Phase
▾ v_S Group
Velocity (km/s)
Time (s)

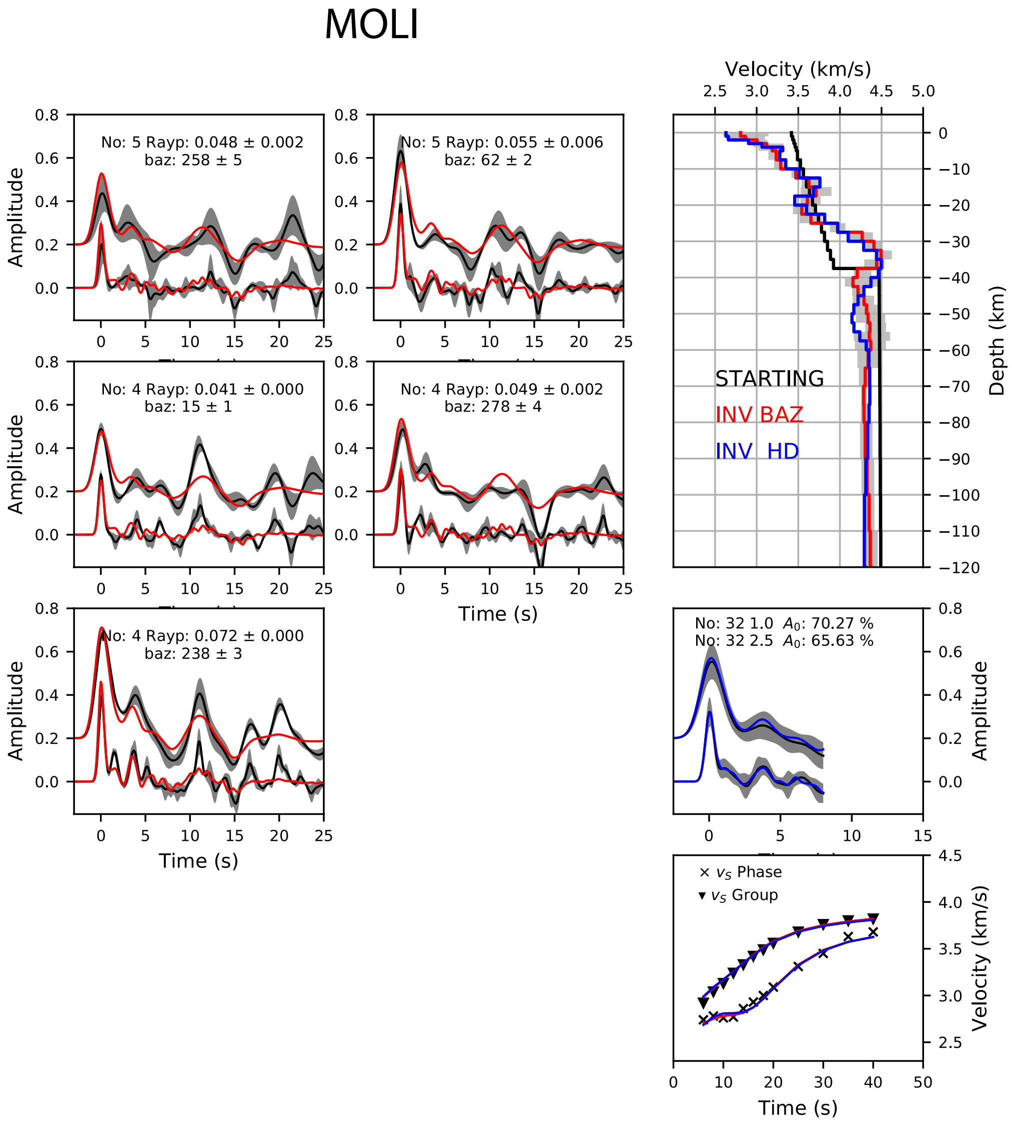
MOLI
No: 5 Rayp: 0.048 ± 0.002
baz: 258 ± 5
No: 5 Rayp: 0.055 ± 0.006
baz: 62 ± 2
No: 4 Rayp: 0.041 ± 0.000
baz: 15 ± 1
No: 4 Rayp: 0.049 ± 0.002
baz: 278 ± 4
No: 4 Rayp: 0.072 ± 0.000
baz: 238 ± 3
Amplitude
Time (s)
Velocity (km/s)
Depth (km)
STARTING
INV BAZ
INV HD
No: 32 1.0 A_0: 70.27 %
No: 32 2.5 A_0: 65.63 %
× v_S Phase
▾ v_S Group
Velocity (km/s)
Time (s)

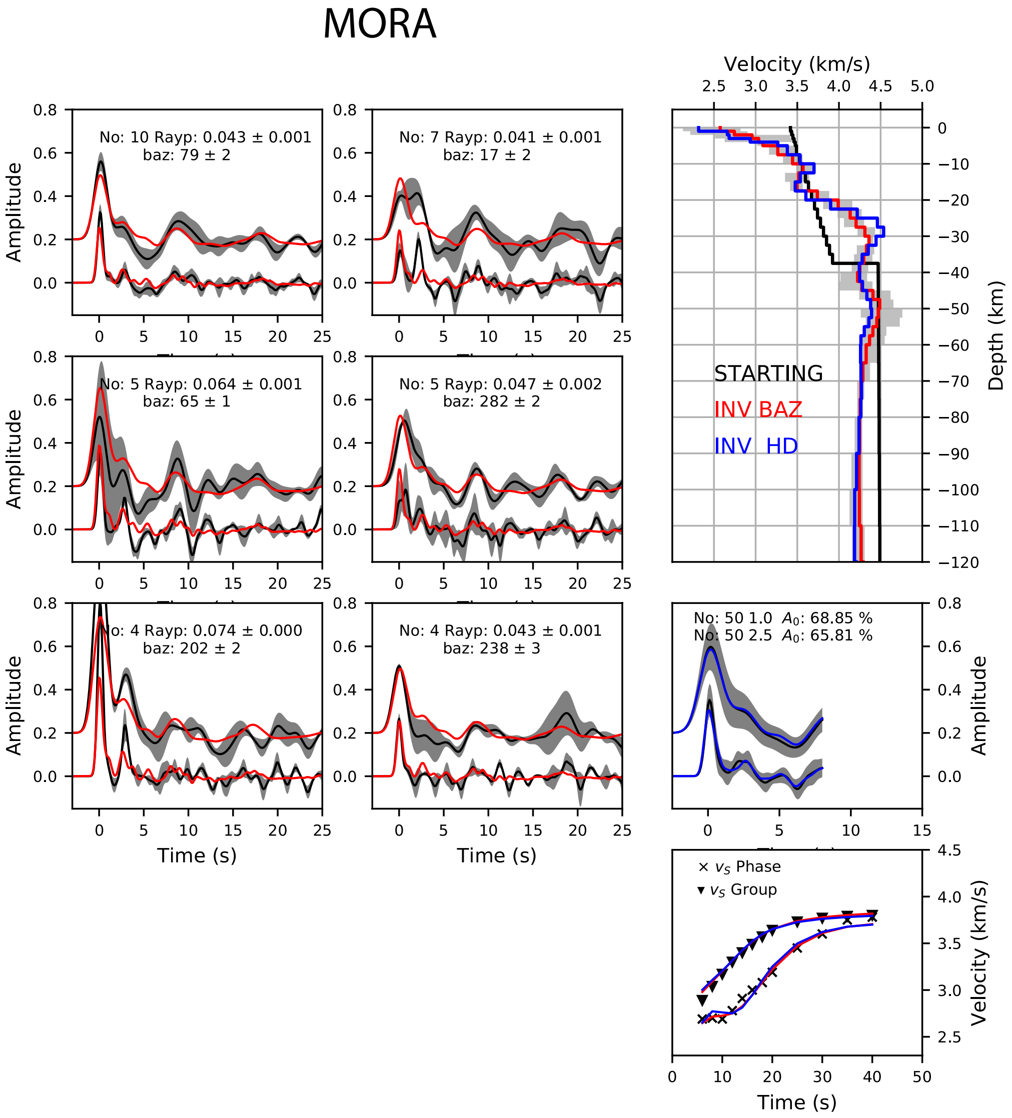
MORA
No: 10 Rayp: 0.043 ± 0.001
baz: 79 ± 2
No: 7 Rayp: 0.041 ± 0.001
baz: 17 ± 2
No: 5 Rayp: 0.064 ± 0.001
baz: 65 ± 1
No: 5 Rayp: 0.047 ± 0.002
baz: 282 ± 2
No: 4 Rayp: 0.074 ± 0.000
baz: 202 ± 2
No: 4 Rayp: 0.043 ± 0.001
baz: 238 ± 3
Amplitude
Time (s)
Velocity (km/s)
Depth (km)
STARTING
INV BAZ
INV HD
No: 50 1.0 A_0: 68.85 %
No: 50 2.5 A_0: 65.81 %
× v_S Phase
▾ v_S Group
Velocity (km/s)
Time (s)

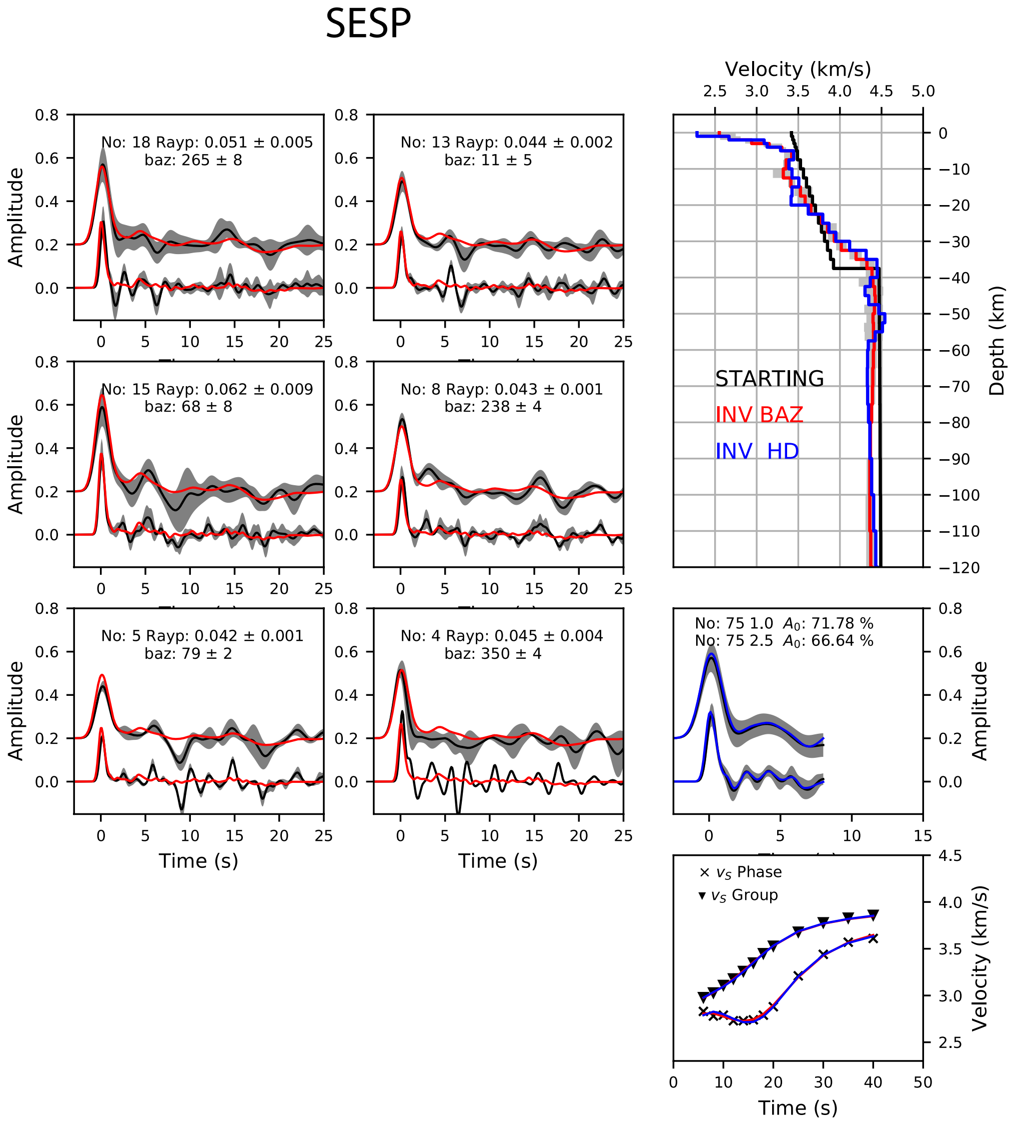
SESP
No: 18 Rayp: 0.051 ± 0.005
baz: 265 ± 8
No: 13 Rayp: 0.044 ± 0.002
baz: 11 ± 5
No: 15 Rayp: 0.062 ± 0.009
baz: 68 ± 8
No: 8 Rayp: 0.043 ± 0.001
baz: 238 ± 4
No: 5 Rayp: 0.042 ± 0.001
baz: 79 ± 2
No: 4 Rayp: 0.045 ± 0.004
baz: 350 ± 4
Amplitude
Time (s)
Velocity (km/s)
Depth (km)
STARTING
INV BAZ
INV HD
No: 75 1.0 A_0: 71.78 %
No: 75 2.5 A_0: 66.64 %
× v_S Phase
▾ v_S Group
Velocity (km/s)
Time (s)

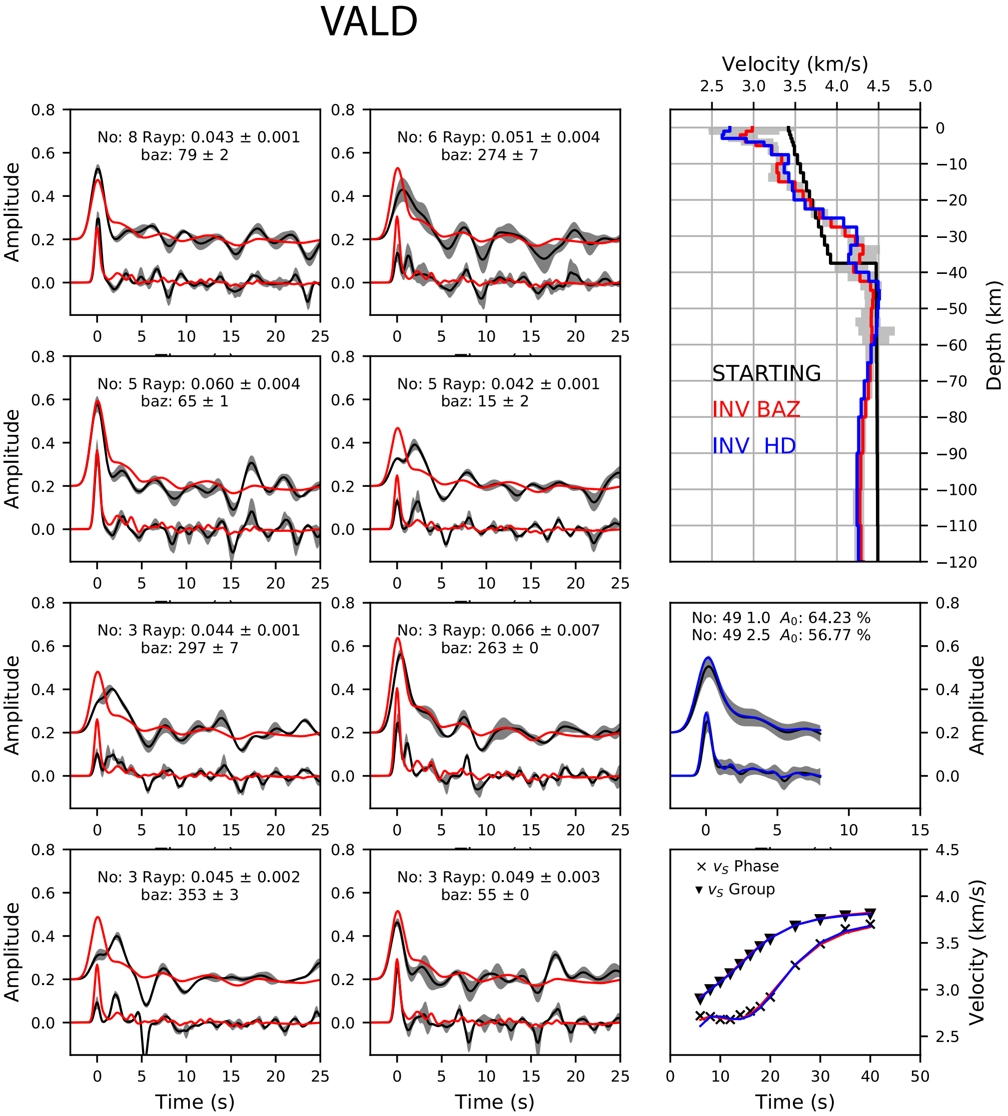
VALD
No: 8 Rayp: 0.043 ± 0.001
baz: 79 ± 2
No: 6 Rayp: 0.051 ± 0.004
baz: 274 ± 7
No: 5 Rayp: 0.060 ± 0.004
baz: 65 ± 1
No: 5 Rayp: 0.042 ± 0.001
baz: 15 ± 2
No: 3 Rayp: 0.044 ± 0.001
baz: 297 ± 7
No: 3 Rayp: 0.066 ± 0.007
baz: 263 ± 0
No: 3 Rayp: 0.045 ± 0.002
baz: 353 ± 3
No: 3 Rayp: 0.049 ± 0.003
baz: 55 ± 0
Amplitude
Time (s)
Velocity (km/s)
Depth (km)
STARTING
INV BAZ
INV HD
No: 49 1.0 A_0: 64.23 %
No: 49 2.5 A_0: 56.77 %
× v_S Phase
▾ v_S Group
Velocity (km/s)
Time (s)

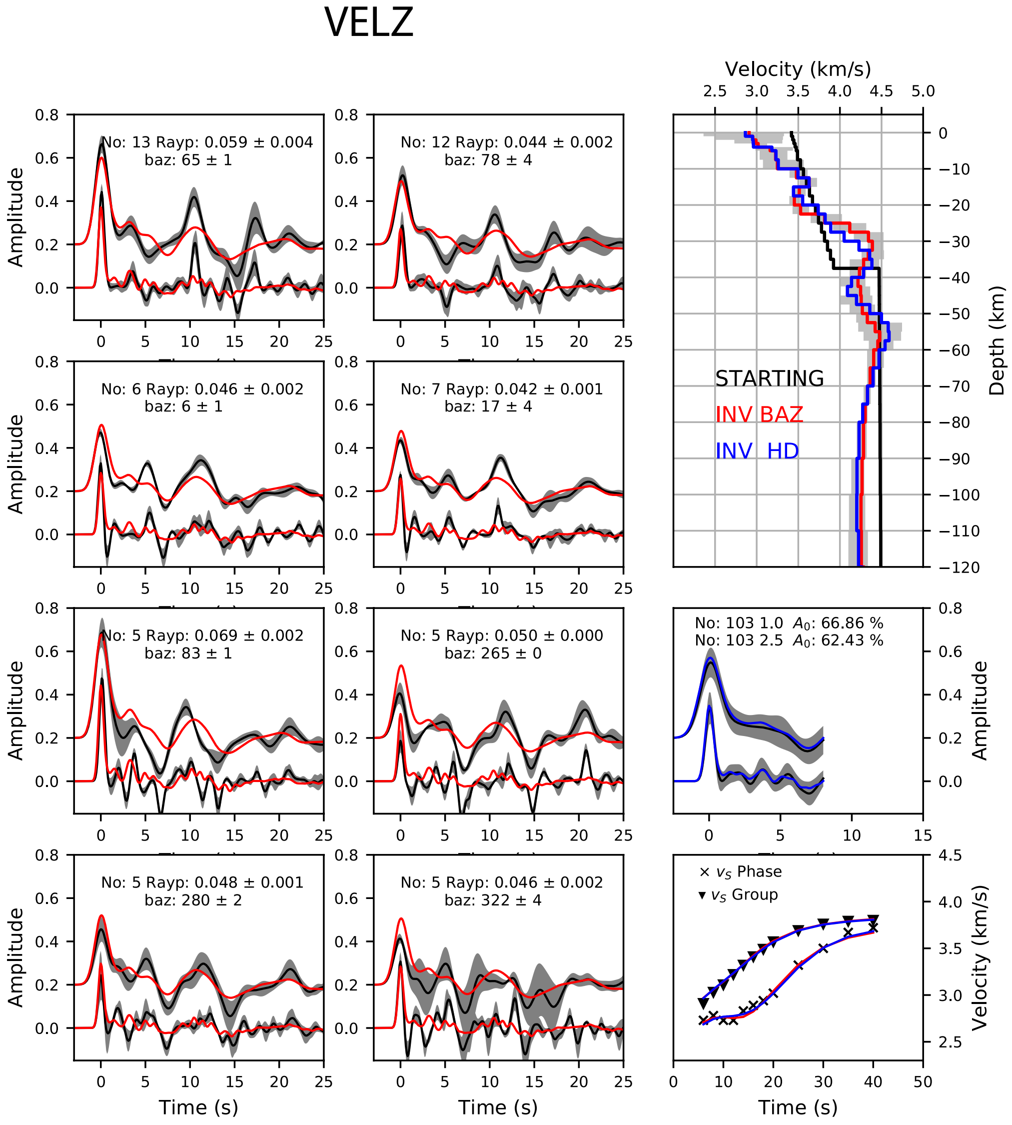
VELZ
No: 13 Rayp: 0.059 ± 0.004
baz: 65 ± 1
No: 12 Rayp: 0.044 ± 0.002
baz: 78 ± 4
No: 6 Rayp: 0.046 ± 0.002
baz: 6 ± 1
No: 7 Rayp: 0.042 ± 0.001
baz: 17 ± 4
No: 5 Rayp: 0.069 ± 0.002
baz: 83 ± 1
No: 5 Rayp: 0.050 ± 0.000
baz: 265 ± 0
No: 5 Rayp: 0.048 ± 0.001
baz: 280 ± 2
No: 5 Rayp: 0.046 ± 0.002
baz: 322 ± 4
Amplitude
Time (s)
Velocity (km/s)
Depth (km)
STARTING
INV BAZ
INV HD
No: 103 1.0 A_0: 66.86 %
No: 103 2.5 A_0: 62.43 %
× v_S Phase
▾ v_S Group
0.8
0.6
0.4
0.2
0.0
0
5
10
15
20
25
2.5
3.0
3.5
4.0
4.5
5.0
−10
−20
−30
−40
−50
−60
−70
−80
−90
−100
−110
−120
30
40
50

XIII

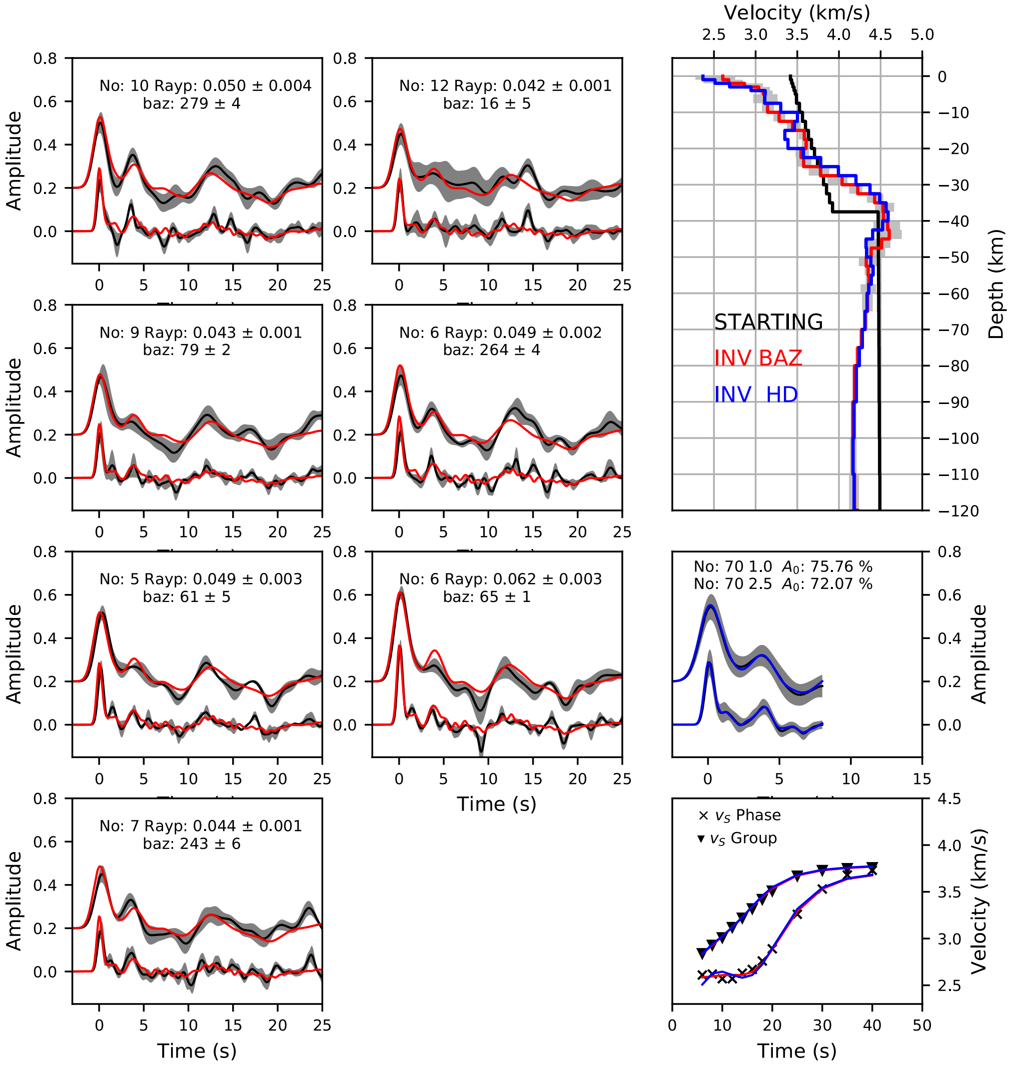
No: 10 Rayp: 0.050 ± 0.004
baz: 279 ± 4
No: 12 Rayp: 0.042 ± 0.001
baz: 16 ± 5
No: 9 Rayp: 0.043 ± 0.001
baz: 79 ± 2
No: 6 Rayp: 0.049 ± 0.002
baz: 264 ± 4
No: 5 Rayp: 0.049 ± 0.003
baz: 61 ± 5
No: 6 Rayp: 0.062 ± 0.003
baz: 65 ± 1
No: 7 Rayp: 0.044 ± 0.001
baz: 243 ± 6
Amplitude
Time (s)
Velocity (km/s)
Depth (km)
STARTING
INV BAZ
INV HD
No: 70 1.0 A_0: 75.76 %
No: 70 2.5 A_0: 72.07 %
× v_S Phase
▾ v_S Group
Velocity (km/s)
Time (s)

Bibliography

Abers, Geoffrey A (1998). “Array measurements of phases used in receiver-function calculations: Importance of scattering”. In: *Bulletin of the Seismological Society of America* 88.1, pp. 313–318. ISSN: 0037-1106. URL: `http://dx.doi.org/`.

Abma, Ray, Clyde Kelley, and John Kaldy (2007). “Sources and treatments of migration-introduced artifacts and noise”. In: pp. 2349–2353. ISSN: 10523812. DOI: `10.1190/1.2792955`. URL: `http://dx.doi.org/10.1190/1.2792955`.

Abt, David L. et al. (2010). “North American lithospheric discontinuity structure imaged by <i>Ps</i> and <i>Sp</i> receiver functions”. In: *Journal of Geophysical Research* 115.B9, B09301. ISSN: 0148-0227. DOI: `10.1029/2009JB006914`. URL: `http://doi.wiley.com/10.1029/2009JB006914`.

Ammon, B Y Charles J (1991). “The isolation of receiver effects from teleseismic P waveforms”. In: 81.6, pp. 2504–2510.

Ammon, Charles J., George E. Randall, and George Zandt (1990). “On the nonuniqueness of receiver function inversions”. In: *Journal of Geophysical Research* 95.B10, p. 15303. ISSN: 0148-0227. DOI: `10.1029/JB095iB10p15303`. URL: `http://doi.wiley.com/10.1029/JB095iB10p15303`.

Ammon, Charles J and George Zandt (1993). “Receiver structure beneath the southern Mojave Block, California”. In: *Bulletin of the Seismological Society of America* 83.3, pp. 737–755. ISSN: 0037-1106. URL: `http://dx.doi.org/`.

Anderson, Don L. (1995). “Lithosphere, asthenosphere, and perisphere”. In: *Reviews of Geophysics* 33.1, p. 125. ISSN: 8755-1209. DOI: `10.1029/94RG02785`. URL: `http://doi.wiley.com/10.1029/94RG02785`.

Artemieva, Irina. (2011). *The Lithosphere : an Interdisciplinary Approach*. Cambridge University Press, p. 796. ISBN: 9780521843966.

Audebert, François et al. (1997). “Imaging complex geologic structure with single-arrival Kirchhoff prestack depth migration”. In: 62.5, pp. 1533–1543.

URL: http://sepwww.stanford.edu/sep/biondo/PDF/Journals/Geophysics/GPY01533.pdf.

Ayala, Concepción et al. (2016). "Updated Bouguer anomalies of the Iberian Peninsula: a new perspective to interpret the regional geology". In: *Journal of Maps* 12.5, pp. 1089–1092. ISSN: 1744-5647. DOI: 10.1080/17445647.2015.1126538. URL: https://www.tandfonline.com/doi/full/10.1080/17445647.2015.1126538.

Azañón, J. M. et al. (2004). "Small-scale faulting, topographic steps and seismic ruptures in the Alhambra(Granada, southeast Spain". In: *Journal of Quaternary Science* 19.3, pp. 219–227. ISSN: 0267-8179. DOI: 10.1002/jqs.838. URL: http://doi.wiley.com/10.1002/jqs.838.

Azañón, J.M. et al. (2015). "Relief and drainage evolution during the exhumation of the Sierra Nevada (SE Spain): Is denudation keeping pace with uplift?" In: *Tectonophysics* 663, pp. 19–32. ISSN: 0040-1951. DOI: 10.1016/J.TECTO.2015.06.015. URL: https://www.sciencedirect.com/science/article/pii/S0040195115003108.

Azañón, Jose Miguel, Ana Crespo-Blanco, and Victor Garcia-Dueñas (1997). "Continental collision, crustal thinning and nappe forming during the pre-Miocene evolution of the Alpujarride Complex (Alboran Domain, Betics)". In: *Journal of Structural Geology* 19.8, pp. 1055–1071. ISSN: 0191-8141. DOI: 10.1016/S0191-8141(97)00031-X. URL: https://www.sciencedirect.com/science/article/pii/S019181419700031X.

Badji, Rabia et al. (2015). "Geophysical evidence for a transform margin offshore Western Algeria: a witness of a subduction-transform edge propagator?" In: *Geophysical Journal International* 200.2, pp. 1029–1045. ISSN: 1365-246X. DOI: 10.1093/gji/ggu454. URL: http://academic.oup.com/gji/article/200/2/1029/614422/Geophysical-evidence-for-a-transform-margin.

Baes, Marzieh, Rob Govers, and Rinus Wortel (2011). "Subduction initiation along the inherited weakness zone at the edge of a slab: Insights from numerical models". In: *Geophysical Journal International* 184.3, pp. 991–1008. ISSN: 0956540X. DOI: 10.1111/j.1365-246X.2010.04896.x. URL: https:

//academic.oup.com/gji/article-lookup/doi/10.1111/j.1365-246X.2010.04896.x.

Balanya, J C and V Garcia-Duenas (1987). “Structural trends of the Alboran Domain on both sides of the Straits of Gibraltar. Les directions structurales dans le Domaine d’Alboran de part et d’autre du Detroit de Gibraltar”. In: *Comptes Rendus - Academie des Sciences, Serie II* 304, pp. 929–932.

Balanyá, J. C. et al. (2007). “Structural trend line pattern and strain partitioning around the Gibraltar Arc accretionary wedge: Insights as to the mode of orogenic arc building”. In: *Tectonics* 26.2, n/a–n/a. ISSN: 02787407. DOI: 10.1029/2005TC001932. URL: http://doi.wiley.com/10.1029/2005TC001932.

Banda, E. et al. (1983). “Crustal structure beneath Spain from deep seismic sounding experiments”. In: *Physics of the Earth and Planetary Interiors* 31.4, pp. 277–280. ISSN: 0031-9201. DOI: 10.1016/0031-9201(83)90087-0. URL: https://www.sciencedirect.com/science/article/pii/0031920183900870.

Banda, E. et al. (1993). “Lateral variation of the crust in the Iberian peninsula: New evidence from the Betic Cordillera”. In: *Tectonophysics* 221.1, pp. 53–66. ISSN: 0040-1951. DOI: 10.1016/0040-1951(93)90027-H. URL: https://www.sciencedirect.com/science/article/pii/004019519390027H.

Banks, Chris J. and John Warburton (1991). “Mid-crustal detachment in the Betic system of southeast Spain”. In: *Tectonophysics* 191.3-4, pp. 275–289. ISSN: 00401951. DOI: 10.1016/0040-1951(91)90062-W. URL: http://linkinghub.elsevier.com/retrieve/pii/004019519190062W.

Bartolome, R. et al. (2012). “Evidence for active strike-slip faulting along the Eurasia-Africa convergence zone: Implications for seismic hazard in the southwest Iberian margin”. In: *Geology* 40.6, pp. 495–498. ISSN: 0091-7613. DOI: 10.1130/G33107.1. URL: https://pubs.geoscienceworld.org/geology/article/40/6/495-498/130873.

Benzaggagh, Mohamed et al. (2014). “Oceanic units in the core of the External Rif (Morocco): Intramargin hiatus or South-Tethyan remnants?” In: *Journal of Geodynamics* 77, pp. 4–21. ISSN: 0264-3707. DOI: 10.1016/J.JOG.2013.10.003. URL: https://www.sciencedirect.com/science/article/pii/S026437071300149X.

Berg, Ewout van den and Michael P. Friedlander (2008). "Probing the Pareto Frontier for Basis Pursuit Solutions". In: *SIAM Journal on Scientific Computing*. ISSN: 1064-8275. DOI: 10.1137/080714488. arXiv: arXiv:1109.2345v1.

Bezada, M.J. and E.D. Humphreys (2012). "Contrasting rupture processes during the April 11, 2010 deep-focus earthquake beneath Granada, Spain". In: *Earth and Planetary Science Letters* 353-354, pp. 38–46. ISSN: 0012821X. DOI: 10.1016/j.epsl.2012.08.001. URL: https://linkinghub.elsevier.com/retrieve/pii/S0012821X12004281.

Bezada, M.J. et al. (2013). "Evidence for slab rollback in westernmost Mediterranean from improved upper mantle imaging". In: *Earth and Planetary Science Letters* 368, pp. 51–60. ISSN: 0012821X. DOI: 10.1016/j.epsl.2013.02.024. URL: http://linkinghub.elsevier.com/retrieve/pii/S0012821X13000915.

Bianchi, I, G Bokelmann, and K Shiomi (2015). "Journal of Geophysical Research : Solid Earth Crustal anisotropy across northern Japan". In: DOI: 10.1002/2014JB011681.Received.

Bianchi, I. et al. (2010). "Mapping seismic anisotropy using harmonic decomposition of receiver functions: An application to Northern Apennines, Italy". In: *Journal of Geophysical Research* 115.B12, pp. 1–14. ISSN: 0148-0227. DOI: 10.1029/2009JB007061.

Bianchi, Irene et al. (2016). "Crustal structure and deformation across a mature slab tear zone: the case of southern Tyrrhenian subduction (Italy)". In: *Geophysical Research Letters* 43.24, pp. 12,380–12,388. ISSN: 00948276. DOI: 10.1002/2016GL070978. URL: http://doi.wiley.com/10.1002/2016GL070978.

Bijwaard, Harmen and Wim Spakman (2000). "Non-linear global <i>P</i> -wave tomography by iterated linearized inversion". In: *Geophysical Journal International* 141.1, pp. 71–82. ISSN: 0956540X. DOI: 10.1046/j.1365-246X.2000.00053.x. URL: https://academic.oup.com/gji/article-lookup/doi/10.1046/j.1365-246X.2000.00053.x.

Blanco, Maria Jose and Wim Spakman (1993). "The P-wave velocity structure of the mantle below the Iberian Peninsula: evidence for subducted lithosphere below southern Spain". In: *Tectonophysics* 221.1, pp. 13–34. ISSN: 00401951. DOI: 10.1016/0040-1951(93)90025-F.

Bokelmann, Getz et al. (2011). "Testing oceanic subduction and convective removal models for the Gibraltar arc: Seismological constraints from dispersion and anisotropy". In: *Tectonophysics* 502.1-2, pp. 28–37. ISSN: 00401951. DOI: `10.1016/j.tecto.2010.08.004`. URL: `http://linkinghub.elsevier.com/retrieve/pii/S004019511000329X`.

Boness, Naomi L. and Mark D. Zoback (2006). "Mapping stress and structurally controlled crustal shear velocity anisotropy in California". In: *Geology* 34.10, pp. 825–828. ISSN: 00917613. DOI: `10.1130/G22309.1`.

Booth-Rea, G. et al. (2007). "Crustal types and tertiary tectonic evolution of the Alborán sea, western Mediterranean". In: *Geochemistry, Geophysics, Geosystems* 8.10, pp. 1–25. ISSN: 15252027. DOI: `10.1029/2007GC001639`.

Booth-Rea, Guillermo et al. (2003). "A 'core-complex-like structure' formed by superimposed extension, folding and high-angle normal faulting. The Santi Petri dome (western Betics, Spain)". In: *Comptes Rendus Geoscience* 335.2, pp. 265–274. ISSN: 1631-0713. DOI: `10.1016/S1631-0713(03)00026-9`. URL: `https://www.sciencedirect.com/science/article/pii/S1631071303000269`.

Bostock, M. G. (1998). "Mantle stratigraphy and evolution of the Slave province". In: *Journal of Geophysical Research: Solid Earth* 103.B9, pp. 21183–21200. ISSN: 01480227. DOI: `10.1029/98JB01069`. URL: `http://doi.wiley.com/10.1029/98JB01069`.

Brytik, Valeriy, Maarten V. De Hoop, and Robert D. van der Hilst (2012). "Elastic-Wave inverse scattering based on reverse time migration With active and passive source reflection data". In: *Inverse Problems and Applications: Inside Out II* 60, p. 411. URL: `https://books.google.com/books?hl=en{\&}lr={\&}id=Lbv84eqj6iMC{\&}oi=fnd{\&}pg=PA411{\&}dq=Elastic-wave+inverse+scattering+based+on+reverse+time+migration+with+active+and+pas-+sive+source+reflection+data,+in+Inside+Out:+Inverse+Problems{\&}ots=8u1nRCfTzb{\&}sig=RWmYuzKfr6g3Ki`.

Buforn, E., C. Sanz de Galdeano, and A. Udías (1995). "Seismotectonics of the Ibero-Maghrebian region". In: *Tectonophysics* 248.3-4, pp. 247–261. ISSN: 0040-1951. DOI: `10.1016/0040-1951(94)00276-F`. URL: `https://www.sciencedirect.com/science/article/pii/004019519400276F`.

Buforn, E., A. Udías, and R. Madariaga (1991). "Intermediate and deep earthquakes in Spain". In: *Pure and Applied Geophysics PAGEOPH* 136.4, pp. 375–393. ISSN: 0033-4553. DOI: `10.1007/BF00878576`. URL: `http://link.springer.com/10.1007/BF00878576`.

Buforn, E. et al. (2004). "Seismic Sources on the Iberia-African Plate Boundary and their Tectonic Implications". In: *Pure and Applied Geophysics* 161.3, pp. 623–646. ISSN: 0033-4553. DOI: `10.1007/s00024-003-2466-1`. URL: `http://link.springer.com/10.1007/s00024-003-2466-1`.

Buforn, E. et al. (2011). "The 2010 Granada, Spain, Deep Earthquake". In: *Bulletin of the Seismological Society of America* 101.5, pp. 2418–2430. ISSN: 0037-1106. DOI: `10.1785/0120110022`. URL: `https://pubs.geoscienceworld.org/bssa/article/101/5/2418-2430/326585`.

Buland, Ray and C H Chapman (1983). "The computation of seismic travel times". In: *Bulletin of the Seismological Society of America* 73.5, pp. 1271–1302. ISSN: 0037-1106. URL: `http://dx.doi.org/`.

Buontempo, L. et al. (2008). "Seismic anisotropy beneath southern Iberia from SKS splitting". In: *Earth and Planetary Science Letters* 273.3-4, pp. 237–250. ISSN: 0012-821X. DOI: `10.1016/J.EPSL.2008.06.024`. URL: `https://www.sciencedirect.com/science/article/pii/S0012821X08003944`.

Buontempo, Luisa and Andreas Wuestefeld (2013). "Complex fault structure interactions of crustal shear zones revealed by seismic anisotropy: an example in the eastern betic cordillera (Spain)". In: *Terra Nova* 25.1, pp. 57–64. ISSN: 09544879. DOI: `10.1111/ter.12005`. URL: `http://doi.wiley.com/10.1111/ter.12005`.

Calvert, A. and Gerardo Alguacil (2000). "Geodynamic evolution of the lithosphere and upper mantle beneath the Alboran region of the western Mediterranean: Constraints from travel time tomography". In: 105.

Candès, Emmanuel et al. (2006). "Fast Discrete Curvelet Transforms". In: *Multiscale Modeling & Simulation* 5.3, pp. 861–899. ISSN: 1540-3459. DOI: `10.1137/05064182X`. URL: `http://epubs.siam.org/doi/10.1137/05064182X`.

Cassidy, J.F. (1992). "Numerical experiments in broadband receiver function analysis". In: *Bulletin of the Seismological Society of America* 82.3, pp. 1453–1474.

Chalouan, Ahmed and André Michard (1990). "The Ghomarides Nappes, Rif Coastal Range, Morocco: A Variscan chip in the Alpine Belt". In: *Tectonics* 9.6, pp. 1565–1583. ISSN: 02787407. DOI: `10.1029/TC009i006p01565`. URL: `http://doi.wiley.com/10.1029/TC009i006p01565`.

Chen, Ling, Lianxing Wen, and Tianyu Zheng (2005). "A wave equation migration method for receiver function imaging: 2. Application to the Japan subduction zone". In: *Journal of Geophysical Research: Solid Earth* 110.B11. ISSN: 01480227. DOI: `10.1029/2005JB003666`. URL: `http://doi.wiley.com/10.1029/2005JB003666`.

Chertova, M. V. et al. (2014). "Underpinning tectonic reconstructions of the western Mediterranean region with dynamic slab evolution from 3-D numerical modeling". In: *Journal of Geophysical Research: Solid Earth* 119.7, pp. 5876–5902. ISSN: 21699313. DOI: `10.1002/2014JB011150`. URL: `http://doi.wiley.com/10.1002/2014JB011150`.

Clark, S. A. et al. (2008). "Characterizing the Caribbean–South American plate boundary at 64°W using wide-angle seismic data". In: *Journal of Geophysical Research* 113.B7, B07401. ISSN: 0148-0227. DOI: `10.1029/2007JB005329`. URL: `http://doi.wiley.com/10.1029/2007JB005329`.

Comas, M.C. et al. (1999). "The origin and tectonic history of the Alboran Basin: insights from Leg 161 results". In: *Proceedings of the Ocean Drilling Program, 161 Scientific Results*. Ocean Drilling Program. DOI: `10.2973/odp.proc.sr.161.262.1999`. URL: `http://www-odp.tamu.edu/publications/161{\_}SR/chap{\_}44/chap{\_}44.htm`.

Conrad, Clinton P. and Carolina Lithgow-Bertelloni (2006). "Influence of continental roots and asthenosphere on plate-mantle coupling". In: *Geophysical Research Letters* 33.5, p. L05312. ISSN: 0094-8276. DOI: `10.1029/2005GL025621`. URL: `http://doi.wiley.com/10.1029/2005GL025621`.

Crotwell, H Philip, Thomas J Owens, and Jeroen Ritsema (1999). "The TauP Toolkit: Flexible Seismic Travel-time and Ray-path Utilities". In: *Seismological Research Letters* 70.2, pp. 154–160. ISSN: 0895-0695. URL: `http://dx.doi.org/10.1785/gssrl.70.2.154`.

De Galdeano, C. Sanz, J. Rodriguez-Fernandez, and A. C. Lopez-Garrido (1985). "A strike-slip fault corridor within the Alpujarra Mountains (Betic Cordilleras, Spain)”. In: *Geologische Rundschau* 74.3, pp. 641–655. ISSN: 0016-7835. DOI: `10.1007/BF01821218`. URL: `http://link.springer.com/10.1007/BF01821218`.

De Larouzière, F.D. et al. (1988). “The Betic segment of the lithospheric Trans-Alboran shear zone during the Late Miocene”. In: *Tectonophysics* 152.1-2, pp. 41–52. ISSN: 0040-1951. DOI: `10.1016/0040-1951(88)90028-5`. URL: `https://www.sciencedirect.com/science/article/pii/0040195188900285`.

De Smet, M.E.M. (1984). “Wrenching in the external zone of the Betic Cordilleras, southern Spain”. In: *Tectonophysics* 107.1-2, pp. 57–79. ISSN: 0040-1951. DOI: `10.1016/0040-1951(84)90028-3`. URL: `https://www.sciencedirect.com/science/article/pii/0040195184900283`.

Díaz, J. and J. Gallart (2009). “Crustal structure beneath the Iberian Peninsula and surrounding waters: A new compilation of deep seismic sounding results”. In: *Physics of the Earth and Planetary Interiors* 173.1-2, pp. 181–190. ISSN: 00319201. DOI: `10.1016/j.pepi.2008.11.008`. URL: `http://linkinghub.elsevier.com/retrieve/pii/S0031920108003531`.

Diaz, J. et al. (2010). “Mantle dynamics beneath the Gibraltar Arc (western Mediterranean) from shear-wave splitting measurements on a dense seismic array”. In: *Geophysical Research Letters* 37.18, n/a–n/a. ISSN: 00948276. DOI: `10.1029/2010GL044201`. URL: `http://doi.wiley.com/10.1029/2010GL044201`.

Do Couto, Damien et al. (2016). “Tectonic and stratigraphic evolution of the Western Alboran Sea Basin in the last 25 Myrs”. In: *Tectonophysics* 677-678, pp. 280–311. ISSN: 0040-1951. DOI: `10.1016/J.TECTO.2016.03.020`. URL: `https://www.sciencedirect.com/science/article/pii/S0040195116300142`.

Docherty, Craig and Enric Banda (1995). “Evidence for the eastward migration of the Alboran Sea based on regional subsidence analysis: A case for basin formation by delamination of the subcrustal lithosphere?” In: *Tectonics* 14.4, pp. 804–818. ISSN: 02787407. DOI: `10.1029/95TC00501`. URL: `http://doi.wiley.com/10.1029/95TC00501`.

Douma, Huub and Maarten V. de Hoop (2007). “Leading-order seismic imaging using curvelets”. In: *Geophysics* 72.6, S231. ISSN: 00168033. DOI: `10.1190/1.2785047`.

Du, Z. J. and G. R. Foulger (1999). "The crustal structure beneath the northwest fjords, Iceland, from receiver functions and surface waves". In: *Geophysical Journal International* 139.2, pp. 419–432. ISSN: 0956-540X. DOI: 10.1046/j.1365-246x.1999.00945.x. URL: https://academic.oup.com/gji/article-lookup/doi/10.1046/j.1365-246x.1999.00945.x.

Dueker, Kenneth G. and Anne F. Sheehan (1997). "Mantle discontinuity structure from midpoint stacks of converted P to S waves across the Yellowstone hotspot track". In: *Journal of Geophysical Research: Solid Earth* 102.B4, pp. 8313–8327. ISSN: 01480227. DOI: 10.1029/96JB03857. URL: http://doi.wiley.com/10.1029/96JB03857.

Duggen, S. et al. (2005). "Post-Collisional Transition from Subduction- to Intraplate-type Magmatism in the Westernmost Mediterranean: Evidence for Continental-Edge Delamination of Subcontinental Lithosphere". In: *Journal of Petrology* 46.6, pp. 1155–1201. ISSN: 1460-2415. DOI: 10.1093/petrology/egi013. URL: http://academic.oup.com/petrology/article/46/6/1155/1485435/PostCollisional-Transition-from-Subduction-to.

Duggen, Svend et al. (2004). "Magmatic evolution of the Alboran region: The role of subduction in forming the western Mediterranean and causing the Messinian Salinity Crisis". In: *Earth and Planetary Science Letters* 218.1-2, pp. 91–108. ISSN: 0012-821X. DOI: 10.1016/S0012-821X(03)00632-0. URL: https://www.sciencedirect.com/science/article/pii/S0012821X03006320.

Dündar, Süleyman et al. (2011). "Receiver function images of the base of the lithosphere in the Alboran Sea region". In: *Geophysical Journal International* 187.2, pp. 1019–1026. ISSN: 0956540X. DOI: 10.1111/j.1365-246X.2011.05216.x. URL: http://gji.oxfordjournals.org/cgi/doi/10.1111/j.1365-246X.2011.05216.x.

Duretz, T. et al. (2012). "Thermomechanical modeling of slab eduction". In: *Journal of Geophysical Research: Solid Earth* 117.B8, n/a–n/a. ISSN: 01480227. DOI: 10.1029/2012JB009137. URL: http://doi.wiley.com/10.1029/2012JB009137.

Echeverria, Anna et al. (2013). "Crustal deformation in eastern Betics from CuaTeNeo GPS network". In: *Tectonophysics* 608, pp. 600–612. ISSN: 0040-1951.

DOI: 10.1016/J.TECTO.2013.08.020. URL: https://www.sciencedirect.com/science/article/pii/S0040195113005118?via{\%}3Dihub.

Eckhardt, C. and W. Rabbel (2011). "P-receiver functions of anisotropic continental crust: a hierarchic catalogue of crustal models and azimuthal waveform patterns". In: *Geophysical Journal International* 187.1, pp. 439–479. ISSN: 0956540X. DOI: 10.1111/j.1365-246X.2011.05159.x. URL: http://gji.oxfordjournals.org/cgi/doi/10.1111/j.1365-246X.2011.05159.x.

Endrun, B. et al. (2004). "Lithospheric structure in the area of Crete constrained by receiver functions and dispersion analysis of Rayleigh phase velocities". In: *Geophysical Journal International* 158.2, pp. 592–608. ISSN: 0956540X. DOI: 10.1111/j.1365-246X.2004.02332.x. URL: https://academic.oup.com/gji/article-lookup/doi/10.1111/j.1365-246X.2004.02332.x.

Faccenna, Claudio et al. (2001). "History of subduction and back-arc extension in the Central Mediterranean". In: *Geophysical Journal International* 145.3, pp. 809–820. ISSN: 0956540X. DOI: 10.1046/j.0956-540x.2001.01435.x. URL: https://academic.oup.com/gji/article-lookup/doi/10.1046/j.0956-540x.2001.01435.x.

Faccenna, Claudio et al. (2004). "Lateral slab deformation and the origin of the western Mediterranean arcs". In: *Tectonics* 23.1, n/a–n/a. ISSN: 02787407. DOI: 10.1029/2002TC001488. URL: http://doi.wiley.com/10.1029/2002TC001488.

Faccenna, Claudio et al. (2014). "Mantle dynamics in the Mediterranean". In: *Reviews of Geophysics* 52.3, pp. 283–332. ISSN: 87551209. DOI: 10.1002/2013RG000444. URL: http://doi.wiley.com/10.1002/2013RG000444.

Farra, V et al. (1991). "Inversion of teleseismic S particle motion for azimuthal anisotropy in the upper mantle: a feasibility study". In: *Geophys. J. lnt* 106, pp. 421–431. URL: http://seismo.berkeley.edu/{~}barbara/REPRINTS/Farra1991.pdf.

Farra, Véronique and L.P. Vinnik (2000). "Upper mantle strati cation by P and S receiver functions ¨ ronique Farra and Lev Vinnik *". In: *Physics*.

Flinch, Joan F., Albert W. Bally, and Shengu Wu (1996). "Emplacement of a passive-margin evaporitic allochthon in the Betic Cordillera of Spain". In: *Geology* 24.1, p. 67. ISSN: 0091-7613. DOI: 10.1130/0091-7613(1996)024<0067:

EOAPME>2.3.CO;2. URL: https://pubs.geoscienceworld.org/geology/article/24/1/67-70/206452.

Frassetto, A. et al. (2010). "Improved imaging with phase-weighted common conversion point stacks of receiver functions". In: *Geophysical Journal International*, no–no. ISSN: 0956540X. DOI: 10.1111/j.1365-246X.2010.04617.x. URL: http://gji.oxfordjournals.org/cgi/doi/10.1111/j.1365-246X.2010.04617.x.

Frederiksen, a. W. and M. G. Bostock (2000). "Modelling teleseismic waves in dipping anisotropic structures". In: *Geophysical Journal International* 141.2, pp. 401–412. ISSN: 0956-540X. DOI: 10.1046/j.1365-246x.2000.00090.x. URL: http://doi.wiley.com/10.1046/j.1365-246x.2000.00090.x.

Frizon de Lamotte, Dominique et al. (2011). "The southernmost margin of the Tethys realm during the Mesozoic and Cenozoic: Initial geometry and timing of the inversion processes". In: *Tectonics* 30.3, n/a–n/a. ISSN: 02787407. DOI: 10.1029/2010TC002691. URL: http://doi.wiley.com/10.1029/2010TC002691.

Fukao, Yoshio (1973). "Thrust faulting at a lithospheric plate boundary the Portugal earthquake of 1969". In: *Earth and Planetary Science Letters* 18.2, pp. 205–216. ISSN: 0012-821X. DOI: 10.1016/0012-821X(73)90058-7. URL: https://www.sciencedirect.com/science/article/pii/0012821X73900587.

Fullea, J. et al. (2007). "A rapid method to map the crustal and lithospheric thickness using elevation, geoid anomaly and thermal analysis. Application to the Gibraltar Arc System, Atlas Mountains and adjacent zones". In: *Tectonophysics* 430.1-4, pp. 97–117. ISSN: 00401951. DOI: 10.1016/j.tecto.2006.11.003. URL: http://linkinghub.elsevier.com/retrieve/pii/S004019510600535X.

Fullea, J. et al. (2010). "The structure and evolution of the lithosphere–asthenosphere boundary beneath the Atlantic–Mediterranean Transition Region". In: *Lithos* 120.1-2, pp. 74–95. ISSN: 0024-4937. DOI: 10.1016/J.LITHOS.2010.03.003. URL: https://www.sciencedirect.com/science/article/pii/S0024493710000782.

Galdeano, C. SANZ and J. A. Vera (1992). "Stratigraphic record and palaeogeographical context of the Neogene basins in the Betic Cordillera, Spain".

In: *Basin Research* 4.1, pp. 21–36. ISSN: 0950091X. DOI: `10.1111/j.1365-2117.1992.tb00040.x`. URL: `http://doi.wiley.com/10.1111/j.1365-2117.1992.tb00040.x`.

Gallais, Flora, David Graindorge, and Marc André Gutscher (2014). "Propagation of a lithospheric tear fault (STEP) through the western boundary of the Calabrian accretionary wedge offshore eastern Sicily (Southern Italy)". In: *Tectonophysics* 610, pp. 200–203. ISSN: 00401951. DOI: `10.1016/j.tecto.2013.10.012`. URL: `http://dx.doi.org/10.1016/j.tecto.2012.12.026`.

Garcia-Castellanos, D. and A. Villaseñor (2011). "Messinian salinity crisis regulated by competing tectonics and erosion at the Gibraltar arc". In: *Nature* 480.7377, pp. 359–363. ISSN: 0028-0836. DOI: `10.1038/nature10651`. URL: `http://www.nature.com/articles/nature10651`.

Garcia-Castellanos, Daniel (2002). "Interplay between lithospheric flexure and river transport in foreland basins". In: *Basin Research* 14.2, pp. 89–104. ISSN: 0950-091X. DOI: `10.1046/j.1365-2117.2002.00174.x`. URL: `http://doi.wiley.com/10.1046/j.1365-2117.2002.00174.x`.

García-Dueñas, V., J. C. Balanyá, and J. M. Martínez-Martínez (1992). "Miocene extensional detachments in the outcropping basement of the northern Alboran Basin (Betics) and their tectonic implications". In: *Geo-Marine Letters* 12.2-3, pp. 88–95. ISSN: 0276-0460. DOI: `10.1007/BF02084917`. URL: `http://link.springer.com/10.1007/BF02084917`.

García-Hernández, M. et al. (1980). "Mesozoic palaeogeographic evolution of the External Zones of the Betic Cordillera". In: *Geologie en Mijnbouw* 59.2, pp. 155–168. ISSN: 0016-7746. DOI: `-`. URL: `http://digital.csic.es/handle/10261/29167`.

Gilbert, Hersh J. et al. (2003). "Receiver functions in the western United States, with implications for upper mantle structure and dynamics". In: *Journal of Geophysical Research: Solid Earth* 108.B5, pp. 1–19. ISSN: 01480227. DOI: `10.1029/2001JB001194`. URL: `http://doi.wiley.com/10.1029/2001JB001194`.

Girardin, Nicole and Véronique Farra (1998). "Azimuthal anisotropy in the upper mantle from observations of P-to-S converted phases: application to southeast Australia". In: *Geophysical Journal International* 133.3, pp. 615–629. ISSN: 0956540X. DOI: `10.1046/j.1365-246X.1998.00525.x`.

Govers, R. and M. J R Wortel (2005). "Lithosphere tearing at STEP faults: Response to edges of subduction zones". In: *Earth and Planetary Science Letters*. ISSN: 0012821X. DOI: `10.1016/j.epsl.2005.03.022`.

Gràcia, Eulàlia et al. (2003). "Crustal architecture and tectonic evolution of the Gulf of Cadiz (SW Iberian margin) at the convergence of the Eurasian and African plates". In: *Tectonics* 22.4, n/a–n/a. ISSN: 02787407. DOI: `10.1029/2001TC901045`. URL: `http://doi.wiley.com/10.1029/2001TC901045`.

Grose, Christopher J. and Juan Carlos Afonso (2013). "Comprehensive plate models for the thermal evolution of oceanic lithosphere". In: *Geochemistry, Geophysics, Geosystems* 14.9, pp. 3751–3778. ISSN: 15252027. DOI: `10.1002/ggge.20232`. URL: `http://doi.wiley.com/10.1002/ggge.20232`.

Gung, Yuancheng, Mark Panning, and Barbara Romanowicz (2003). "Global anisotropy and the thickness of continents". In: *Nature* 422.6933, pp. 707–711. ISSN: 0028-0836. DOI: `10.1038/nature01559`. URL: `http://www.nature.com/articles/nature01559`.

Gutierrez-Alonso, G. et al. (2011). "Lithospheric delamination in the core of Pangea: Sm-Nd insights from the Iberian mantle". In: *Geology* 39.2, pp. 155–158. ISSN: 0091-7613. DOI: `10.1130/G31468.1`. URL: `https://pubs.geoscienceworld.org/geology/article/39/2/155-158/130509`.

Gutscher, M (2002). "Evidence for active subduction beneath Gibraltar". In: DOI: `10.1130/0091-7613(2002)030<1071`.

Gutscher, M.-A. (2004). "What Caused the Great Lisbon Earthquake?" In: *Science* 305.5688, pp. 1247–1248. ISSN: 0036-8075. DOI: `10.1126/science.1101351`. URL: `http://www.sciencemag.org/cgi/doi/10.1126/science.1101351`.

Gutscher, M.-A. et al. (2012). "The Gibraltar subduction: A decade of new geophysical data". In: *Tectonophysics* 574-575, pp. 72–91. ISSN: 00401951. DOI: `10.1016/j.tecto.2012.08.038`. URL: `http://linkinghub.elsevier.com/retrieve/pii/S0040195112005276`.

Gutscher, Marc-André et al. (2017). "Active tectonics of the Calabrian subduction revealed by new multi-beam bathymetric data and high-resolution seismic profiles in the Ionian Sea (Central Mediterranean)". In: *Earth and Planetary Science Letters* 461, pp. 61–72. ISSN: 0012821X. DOI: `10.1016/j.`

epsl.2016.12.020. URL: https://linkinghub.elsevier.com/retrieve/pii/S0012821X16307336.

Heit, B. et al. (2007). "An S receiver function analysis of the lithospheric structure in South America". In: *Geophysical Research Letters* 34.14, p. L14307. ISSN: 0094-8276. DOI: 10.1029/2007GL030317. URL: http://doi.wiley.com/10.1029/2007GL030317.

Heit, Benjamin et al. (2017). "Tearing of the mantle lithosphere along the intermediate-depth seismicity zone beneath the Gibraltar Arc - The onset of lithospheric delamination". In: *Geophysical Research Letters* January. ISSN: 00948276. DOI: 10.1002/2017GL073358. URL: http://doi.wiley.com/10.1002/2017GL073358.

Heit, B., Yuan, X., Mancilla, F. (2010). *High resolution seismological profiling across Sierra Nevada (HIRE)*. DOI: https://doi.org/10.14470/4P7565788335.

Hoop, Maarten V. de, Robert D. van der Hilst, and Peng Shen (2006). "Wave-equation reflection tomography: annihilators and sensitivity kernels". In: *Geophysical Journal International* 167.3, pp. 1332–1352. ISSN: 0956540X. DOI: 10.1111/j.1365-246X.2006.03132.x. URL: https://academic.oup.com/gji/article-lookup/doi/10.1111/j.1365-246X.2006.03132.x.

Houseman, Gregory A. and Peter Molnar (1997). "Gravitational (Rayleigh-Taylor) instability of a layer with non-linear viscosity and convective thinning of continental lithosphere". In: *Geophysical Journal International* 128.1, pp. 125–150. ISSN: 0956540X. DOI: 10.1111/j.1365-246X.1997.tb04075.x. URL: https://academic.oup.com/gji/article-lookup/doi/10.1111/j.1365-246X.1997.tb04075.x.

Iribarren, L. et al. (2007a). "The structure of the Atlantic–Mediterranean transition zone from the Alboran Sea to the Horseshoe Abyssal Plain (Iberia–Africa plate boundary)". In: *Marine Geology* 243.1-4, pp. 97–119. ISSN: 0025-3227. DOI: 10.1016/J.MARGEO.2007.05.011. URL: https://www.sciencedirect.com/science/article/pii/S0025322707001466.

— (2007b). "The structure of the Atlantic–Mediterranean transition zone from the Alboran Sea to the Horseshoe Abyssal Plain (Iberia–Africa plate boundary)". In: *Marine Geology* 243.1-4, pp. 97–119. ISSN: 0025-3227. DOI: 10.1016/J.MARGEO.2007.05.011. URL: https://www.sciencedirect.com/science/article/pii/S0025322707001466.

Jabaloy-Sánchez, A., E.M. Fernández-Fernández, and F. González-Lodeiro (2007). "A cross section of the eastern Betic Cordillera (SE Spain) according field data and a seismic reflection profile". In: *Tectonophysics* 433.1-4, pp. 97–126. ISSN: 00401951. DOI: `10.1016/j.tecto.2006.11.004`. URL: `http://linkinghub.elsevier.com/retrieve/pii/S0040195106005348`.

Jaupart, C and J.C Mareschal (1999). "The thermal structure and thickness of continental roots". In: *Lithos* 48.1-4, pp. 93–114. ISSN: 0024-4937. DOI: `10.1016/S0024-4937(99)00023-7`. URL: `https://www.sciencedirect.com/science/article/pii/S0024493799000237`.

Jolivet, L. et al. (2008). "Subduction, convergence and the mode of backarc extension in the Mediterranean region". In: *Bulletin de la Societe Geologique de France* 179.6, pp. 525–550. ISSN: 0037-9409. DOI: `10.2113/gssgfbull.179.6.525`. URL: `http://bsgf.geoscienceworld.org/cgi/doi/10.2113/gssgfbull.179.6.525`.

Jolivet, Laurent and Claudio Faccenna (2000). "Mediterranean extension and the Africa-Eurasia collision". In: *Tectonics* 19.6, pp. 1095–1106. ISSN: 02787407. DOI: `10.1029/2000TC900018`. URL: `http://doi.wiley.com/10.1029/2000TC900018`.

Jolliffe, I T (2004). "Principal component analysis (second edition)". In: *Principal component analysis (second edition)*.

Jones, Craig H. and Robert A. Phinney (1998). "Seismic structure of the lithosphere from teleseismic converted arrivals observed at small arrays in the southern Sierra Nevada and vicinity, California". In: *Journal of Geophysical Research: Solid Earth* 103.B5, pp. 10065–10090. ISSN: 01480227. DOI: `10.1029/97JB03540`. URL: `http://doi.wiley.com/10.1029/97JB03540`.

Julià, J. (2005). "Seismic signature of intracrustal magmatic intrusions in the Eastern Betics (Internal Zone), SE Iberia". In: *Geophysical Research Letters* 32.16, p. L16304. ISSN: 0094-8276. DOI: `10.1029/2005GL023274`. URL: `http://doi.wiley.com/10.1029/2005GL023274`.

Julià, Jordi (2007). "Constraining velocity and density contrasts across the crust – mantle boundary with receiver function amplitudes Jordi Juli ′". In: pp. 286–301. DOI: `10.1111/j.1365-2966.2007.3502.x`.

Julià, Jordi, Charles J. Ammon, and Robert B. Herrmann (2003). "Lithospheric structure of the Arabian Shield from the joint inversion of receiver functions and surface-wave group velocities". In: *Tectonophysics* 371.1-4, pp. 1–21. ISSN: 00401951. DOI: `10.1016/S0040-1951(03)00196-3`.

Julià, Jordi, Josep Vila, and Ramon Macià (1998). "The receiver structure beneath the Ebro basin, Iberian Peninsula". In: *Bulletin of the Seismological Society of America* 88.6, pp. 1538–1547. ISSN: 0037-1106. URL: `https://dx.doi.org/`.

Julià, Jordi et al. (2000). "Joint inversion of receiver function and surface wave dispersion observations". In: *Geophysical Journal International* 143.1, pp. 99–112. ISSN: 0956540X. DOI: `10.1046/j.1365-246x.2000.00217.x`. URL: `http://doi.wiley.com/10.1046/j.1365-246x.2000.00217.x`.

Kanasewich, E. R. (1983). *Time sequence analysis in geophysics*. 3rd. Edmonton, Alberta: The University of Alberta Press.

Kearey, Philip., Keith A. Klepeis, and Frederick J. Vine (2009). *Global Tectonics*. Wiley, p. 711. ISBN: 9781118688083. URL: `https://books.google.es/books?hl=en{\&}lr={\&}id=JBF8UGc{\_}M-sC{\&}oi=fnd{\&}pg=PT48{\&}ots=b9C7M61Ntm{\&}sig=QQFqvLg4YHJW1FWcMBMA4HwsFJY{\&}redir{\_}esc=y{\#}v=onepage{\&}q{\&}f=false`.

Keith, Colum M. and Stuart Crampin (1977). "Seismic body waves in anisotropic media: propagation through a layer". In: *Geophysical Journal International* 49.1, pp. 209–223. ISSN: 0956-540X. DOI: `10.1111/j.1365-246X.1977.tb03709.x`. URL: `https://academic.oup.com/gji/article-lookup/doi/10.1111/j.1365-246X.1977.tb03709.x`.

Kennett, B. L. N. (1991). "The Removal of Free Surface Interactions From Three-Component Seismograms". In: *Geophysical Journal International* 104.1, pp. 153–154. ISSN: 0956540X. DOI: `10.1111/j.1365-246X.1991.tb02501.x`. URL: `http://gji.oxfordjournals.org/cgi/doi/10.1111/j.1365-246X.1991.tb02501.x`.

Kind, R. et al. (2015). "Thickness of the lithosphere beneath Turkey and surroundings from S-receiver functions". In: *Solid Earth*. ISSN: 18699529. DOI: `10.5194/se-6-971-2015`.

Kind, Rainer, Xiaohui Yuan, and Prakash Kumar (2012). “Seismic receiver functions and the lithosphere–asthenosphere boundary”. In: *Tectonophysics* 536-537, pp. 25–43. ISSN: 00401951. DOI: `10.1016/j.tecto.2012.03.005`. URL: `http://linkinghub.elsevier.com/retrieve/pii/S0040195112001333`.

Kosarev, G. (1999). “Seismic Evidence for a Detached Indian Lithospheric Mantle Beneath Tibet”. In: *Science* 283.5406, pp. 1306–1309. ISSN: 00368075. DOI: `10.1126/science.283.5406.1306`.

Koulali, a. et al. (2011). “New GPS constraints on active deformation along the Africa–Iberia plate boundary”. In: *Earth and Planetary Science Letters* 308.1-2, pp. 211–217. ISSN: 0012821X. DOI: `10.1016/j.epsl.2011.05.048`. URL: `http://linkinghub.elsevier.com/retrieve/pii/S0012821X11003414`.

Kumar, P. et al. (2005a). “The lithosphere-asthenosphere boundary in the Tien Shan-Karakoram region from S receiver functions: Evidence for continental subduction”. In: *Geophysical Research Letters* 32.7, n/a–n/a. ISSN: 00948276. DOI: `10.1029/2004GL022291`. URL: `http://doi.wiley.com/10.1029/2004GL022291`.

Kumar, P. et al. (2005b). “The lithosphere–asthenosphere boundary in the North-West Atlantic region”. In: *Earth and Planetary Science Letters* 236.1-2, pp. 249–257. ISSN: 0012-821X. DOI: `10.1016/J.EPSL.2005.05.029`. URL: `https://www.sciencedirect.com/science/article/pii/S0012821X05003523`.

Kumar, P. et al. (2012). “The lithosphere-asthenosphere boundary observed with USArray receiver functions”. In: *Solid Earth* 3.1, pp. 149–159. ISSN: 18699510. DOI: `10.5194/se-3-149-2012`.

Kumar, Prakash et al. (2006). “Imaging the colliding Indian and Asian lithospheric plates beneath Tibet”. In: *Journal of Geophysical Research: Solid Earth* 111.6, pp. 1–11. ISSN: 21699356. DOI: `10.1029/2005JB003930`.

Langston, CA (1979). “Structure under Mount Rainier, Washington, inferred from teleseismic body waves”. In: *Journal of Geophysical Research: Solid Earth (...* 84.9, pp. 4749–4762. URL: `http://onlinelibrary.wiley.com/doi/10.1029/JB084iB09p04749/full`.

Langston, Charles A. (1989). “Scattering of teleseismic body waves under Pasadena, California”. In: *Journal of Geophysical Research* 94.B2, p. 1935. ISSN: 0148-0227.

DOI: 10.1029/JB094iB02p01935. URL: http://doi.wiley.com/10.1029/JB094iB02p01935.

Last, Robert J. et al. (1997). "Crustal structure of the East African Plateau from receiver functions and Rayleigh wave phase velocities". In: *Journal of Geophysical Research: Solid Earth* 102.B11, pp. 24469–24483. ISSN: 01480227. DOI: 10.1029/97JB02156. URL: http://doi.wiley.com/10.1029/97JB02156.

Levander, A et al. (2014). "Subduction-driven recycling of continental margin lithosphere". In: *Nature* 515. DOI: 10.1038/nature13878.

Levin, Vadim and Jeffrey Park (1997). "P-SH conversions in a flat-layered medium with anisotropy of arbitrary orientation". In: pp. 253–266.

Levshin, Anatoli L. and Michael H. Ritzwoller (1995). "Characteristics of surface waves generated by events on and near the Chinese nuclear test site". In: *Geophysical Journal International* 123.1, pp. 131–148. ISSN: 0956540X. DOI: 10.1111/j.1365-246X.1995.tb06666.x. URL: https://academic.oup.com/gji/article-lookup/doi/10.1111/j.1365-246X.1995.tb06666.x.

Li, Xueqing, Xiaohui Yuan, and Rainer Kind (2007). "The lithosphere-asthenosphere boundary beneath the western United States". In: *Geophysical Journal International* 170.2, pp. 700–710. ISSN: 0956540X. DOI: 10.1111/j.1365-246X.2007.03428.x. URL: https://academic.oup.com/gji/article-lookup/doi/10.1111/j.1365-246X.2007.03428.x.

Ligorria, Pablo and Charles J Ammon (1999). "Iterative Deconvolution and Receiver-Function Estimation". In: October, pp. 1395–1400.

Liu, Zhen and Jeffrey Park (2017). "Seismic receiver function interpretation: Ps splitting or anisotropic underplating?" In: *Geophysical Journal International* 208.3, pp. 1332–1341. ISSN: 1365246X. DOI: 10.1093/gji/ggw455.

Lonergan, Lidia and Nicky White (1997). "Origin of the Betic-Rif mountain belt". In: 16.3, pp. 504–522.

Luz, Rosana M N, Jordi Julià, and Aderson F Nascimento (2015). "Journal of Geophysical Research : Solid Earth Crustal structure of the eastern Borborema Province , NE Brazil , from the joint inversion of receiver functions and surface wave dispersion : Implications for plateau uplift". In: pp. 3848–3869. DOI: 10.1002/2015JB011872.Received.

Magni, V. et al. (2017). “Continental underplating after slab break-off”. In: *Earth and Planetary Science Letters* 474, pp. 59–67. ISSN: 0012-821X. DOI: `10.1016/J.EPSL.2017.06.017`. URL: `https://www.sciencedirect.com/science/article/pii/S0012821X17303278`.

Mancilla, F.L. et al. (2015a). “Crustal thickness and images of the lithospheric discontinuities in the Gibraltar arc and surrounding areas”. In: *Geophysical Journal International* 105.3-4, pp. 2969–2980. ISSN: 1365-246X. DOI: `10.1093/gji/ggv390`. URL: `https://academic.oup.com/gji/article/203/3/1804/2594794/Crustal-thickness-and-images-of-the-lithospheric`.

Mancilla, Flor De Lis, Jordi Diaz, and Scientific Team (2015). “High resolution Moho topography map beneath Iberia and Northern Morocco from RF analysis”. In: *Tectonophysics* 15, p. 7628. ISSN: 00401951. DOI: `10.1016/j.tecto.2015.06.017`. URL: `http://dx.doi.org/10.1016/j.tecto.2015.06.017`.

Mancilla, Flor De Lis et al. (2012). “Crustal thickness variations in northern Morocco”. In: *Journal of Geophysical Research* 117.B2, B02312. ISSN: 0148-0227. DOI: `10.1029/2011JB008608`. URL: `http://doi.wiley.com/10.1029/2011JB008608`.

Mancilla, Flor De Lis et al. (2013). “Delamination in the Betic Range: Deep structure, seismicity, and GPS motion”. In: *Geology* 41.3, pp. 307–310. ISSN: 00917613. DOI: `10.1130/G33733.1`.

Mancilla, Flor de Lis et al. (2015b). “Slab rupture and delamination under the Betics and Rif constrained from receiver functions”. In: *Tectonophysics*. ISSN: 00401951. DOI: `10.1016/j.tecto.2015.06.028`. URL: `http://linkinghub.elsevier.com/retrieve/pii/S0040195115003595`.

Mancilla, Flor de Lis et al. (2018). “A STEP fault in Central Betics, associated with lateral lithospheric tearing at the northern edge of the Gibraltar arc subduction system”. In: *Earth and Planetary Science Letters* 486, pp. 32–40. ISSN: 0012821X. DOI: `10.1016/j.epsl.2018.01.008`. URL: `http://linkinghub.elsevier.com/retrieve/pii/S0012821X18300189`.

Mangino, Stephen G, George Zandt, and Charles J Ammon (1993). "The receiver structure beneath Mina, Nevada". In: *Bulletin of the Seismological Society of America* 83.2, pp. 542–560. ISSN: 0037-1106. URL: https://dx.doi.org/.

Martín, R. et al. (2015). "Moment tensor solutions for the Iberian-Maghreb region during the IberArray deployment (2009–2013)". In: *Tectonophysics* 663, pp. 261–274. ISSN: 00401951. DOI: 10.1016/j.tecto.2015.08.012. URL: https://linkinghub.elsevier.com/retrieve/pii/S0040195115004394.

Martínez-García, P. et al. (2013). "Strike-slip tectonics and basin inversion in the Western Mediterranean: the Post-Messinian evolution of the Alboran Sea". In: *Basin Research* 25.4, pp. 361–387. ISSN: 0950091X. DOI: 10.1111/bre.12005. URL: http://doi.wiley.com/10.1111/bre.12005.

Martínez-Martínez, J. M. and J. M. Azañón (1997). "Mode of extensional tectonics in the southeastern Betics (SE Spain): Implications for the tectonic evolution of the peri-Alborán orogenic system". In: *Tectonics* 16.2, pp. 205–225. ISSN: 02787407. DOI: 10.1029/97TC00157. URL: http://doi.wiley.com/10.1029/97TC00157.

Martínez-Martínez, J. M., J. I. Soto, and J. C. Balanyá (2002). "Orthogonal folding of extensional detachments: Structure and origin of the Sierra Nevada elongated dome (Betics, SE Spain)". In: *Tectonics* 21.3, pp. 3–1–3–20. ISSN: 02787407. DOI: 10.1029/2001TC001283. URL: http://doi.wiley.com/10.1029/2001TC001283.

Martínez-Martínez, José Miguel et al. (2006). "Active transfer fault zone linking a segmented extensional system (Betics, southern Spain): Insight into heterogeneous extension driven by edge delamination". In: *Tectonophysics* 422.1-4, pp. 159–173. ISSN: 0040-1951. DOI: 10.1016/J.TECTO.2006.06.001. URL: https://www.sciencedirect.com/science/article/pii/S0040195106003143?via{\%}3Dihub.

Masana, E. et al. (2004). "The Alhama de Murcia fault (SE Spain), a seismogenic fault in a diffuse plate boundary: Seismotectonic implications for the Ibero-Magrebian region". In: *Journal of Geophysical Research: Solid Earth* 109.B1. ISSN: 01480227. DOI: 10.1029/2002JB002359. URL: http://doi.wiley.com/10.1029/2002JB002359.

Maupin, V. and J. Park (2007). “Theory and Observations - Wave Propagation in Anisotropic Media”. In: *Treatise on Geophysics* 1, pp. 289–321. DOI: `10.1016/B978-044452748-6.00007-9`.

Meijninger, B. M. L. and R. L. M. Vissers (2006). “Miocene extensional basin development in the Betic Cordillera, SE Spain revealed through analysis of the Alhama de Murcia and Crevillente Faults”. In: *Basin Research* 18.4, pp. 547–571. ISSN: 0950091X. DOI: `10.1111/j.1365-2117.2006.00308.x`. URL: `http://doi.wiley.com/10.1111/j.1365-2117.2006.00308.x`.

Michard, André et al. (1983). “The inner Rif metamorphic nappes, Sebtids, Morocco, a piece of a Pennic type, Alpine pile of nappes, including the upper mantle. Les nappes cristallophylliennes du Rif (Sebtides, Maroc), temoins d’un edifice alpin de type pennique incluant le manteau supe”. In: *Comptes Rendus des Seances-Academie des Sciences, Serie II* 296, pp. 1337–1340.

Michard, André et al. (2002). “How does the Alpine belt end between Spain and Morocco ?” In: *Bulletin de la Societe Geologique de France* 173.1, pp. 3–15. ISSN: 0037-9409. DOI: `10.2113/173.1.3`. URL: `https://pubs.geoscienceworld.org/bsgf/article/173/1/3-15/88295`.

Miller, Meghan S. et al. (2015). “Imaging Canary Island hotspot material beneath the lithosphere of Morocco and southern Spain”. In: *Earth and Planetary Science Letters* 431, pp. 186–194. ISSN: 0012821X. DOI: `10.1016/j.epsl.2015.09.026`. URL: `http://linkinghub.elsevier.com/retrieve/pii/S0012821X15005932`.

Molnar, Peter and Tanya Atwater (1978). “Interarc spreading and Cordilleran tectonics as alternates related to the age of subducted oceanic lithosphere”. In: *Earth and Planetary Science Letters* 41.3, pp. 330–340. ISSN: 0012-821X. DOI: `10.1016/0012-821X(78)90187-5`. URL: `https://www.sciencedirect.com/science/article/pii/0012821X78901875`.

Morales, J. et al. (1990). “Basement structure of the Granada basin, Betic Cordilleras, southern Spain”. In: *Tectonophysics* 177.4, pp. 337–348. ISSN: 0040-1951. DOI: `10.1016/0040-1951(90)90394-N`. URL: `https://www.sciencedirect.com/science/article/pii/004019519090394N`.

Morales, José et al. (1997). “The depth of the earthquake activity in the Central Betics (Southern Spain)”. In: *Geophysical Research Letters* 24.24, pp. 3289–

3292. ISSN: 00948276. DOI: 10.1029/97GL03306. URL: http://doi.wiley.com/10.1029/97GL03306.

Morel, Jean Luc and Mustapha Meghraoui (1996). "Goringe-Alboran-Tell tectonic zone: A transpression system along the Africa-Eurasia plate boundary". In: *Geology* 24.8, p. 755. ISSN: 0091-7613. DOI: 10.1130/0091-7613(1996)024<0755:GATTZA>2.3.CO;2. URL: https://pubs.geoscienceworld.org/geology/article/24/8/755-758/190580.

Nagaya, Mamoru et al. (2008). "Receiver functions of seismic waves in layered anisotropic media: Application to the estimate of seismic anisotropy". In: *Bulletin of the Seismological Society of America* 98.6, pp. 2990–3006. ISSN: 00371106. DOI: 10.1785/0120080130.

Naghizadeh, Mostafa and Mauricio D Sacchi (2010). "Beyond alias hierarchical scale curvelet interpolation of regularly and irregularly sampled seismic data". In: 75.6.

Negredo, Ana M. et al. (2002). "Neotectonic modeling of the Ibero-Maghrebian region". In: *Journal of Geophysical Research: Solid Earth* 107.B11, ETG 10–1–ETG 10–15. ISSN: 01480227. DOI: 10.1029/2001JB000743. URL: http://doi.wiley.com/10.1029/2001JB000743.

Nieto, L. M. and J. Rey (2004). "Magnitude of lateral displacement on the Crevillente Fault Zone(Betic Cordillera, SE Spain): stratigraphical and sedimentological considerations". In: *Geological Journal* 39.1, pp. 95–110. ISSN: 0072-1050. DOI: 10.1002/gj.946. URL: http://doi.wiley.com/10.1002/gj.946.

Nijholt, Nicolai and Rob Govers (2015). "The role of passive margins on the evolution of Subduction-Transform Edge Propagators (STEPs)". In: *Journal of Geophysical Research: Solid Earth* 120.10, pp. 7203–7230. ISSN: 21699313. DOI: 10.1002/2015JB012202. URL: http://doi.wiley.com/10.1002/2015JB012202.

Nocquet, J.-M. and E. Calais (2003). "Crustal velocity field of western Europe from permanent GPS array solutions, 1996-2001". In: *Geophysical Journal International* 154.1, pp. 72–88. ISSN: 0956540X. DOI: 10.1046/j.1365-246X.2003.01935.x. URL: https://academic.oup.com/gji/article-lookup/doi/10.1046/j.1365-246X.2003.01935.x.

Olugboji, Tolulope Morayo et al. (2016). “Crustal anisotropy beneath Pacific Ocean-Islands from harmonic decomposition of receiver functions”. In: *Geochemistry, Geophysics, Geosystems*, pp. 810–832. DOI: `10.1002/2015GC006166.Received`.

Oreshin, Serge et al. (2002). “Lithosphere and asthenosphere of the Tien Shan imaged by S receiver functions”. In: *Geophysical Research Letters* 29.8, pp. 32–1–32–4. ISSN: 00948276. DOI: `10.1029/2001GL014441`. URL: `http://doi.wiley.com/10.1029/2001GL014441`.

Owens, Thomas J., George Zandt, and Steven R. Taylor (1984). “Seismic evidence for an ancient rift beneath the Cumberland Plateau, Tennessee: A detailed analysis of broadband teleseismic <i>P</i> waveforms”. In: *Journal of Geophysical Research: Solid Earth* 89.B9, pp. 7783–7795. ISSN: 01480227. DOI: `10.1029/JB089iB09p07783`. URL: `http://doi.wiley.com/10.1029/JB089iB09p07783`.

Özalaybey, Serdar et al. (1997). “Shear-wave velocity structure in the northern Basin and Range province from the combined analysis of receiver functions and surface waves”. In: *Bulletin of the Seismological Society of America* 87.1, pp. 183–199. ISSN: 0037-1106. URL: `http://dx.doi.org/`.

Özbakır, Ali D. et al. (2013). “The Pliny–Strabo trench region: A large shear zone resulting from slab tearing”. In: *Earth and Planetary Science Letters* 375, pp. 188–195. ISSN: 0012-821X. DOI: `10.1016/J.EPSL.2013.05.025`. URL: `https://www.sciencedirect.com/science/article/pii/S0012821X13002707`.

Palomeras, I. et al. (2009). “Nature of the lithosphere across the Variscan orogen of SW Iberia: Dense wide-angle seismic reflection data”. In: *Journal of Geophysical Research* 114.B2, B02302. ISSN: 0148-0227. DOI: `10.1029/2007JB005050`. URL: `http://doi.wiley.com/10.1029/2007JB005050`.

Palomeras, I. et al. (2014). “Finite-frequency Rayleigh wave tomography of the western Mediterranean: Mapping its lithospheric structure”. In: *Geochemistry, Geophysics, Geosystems* 15.1, pp. 140–160. ISSN: 15252027. DOI: `10.1002/2013GC004861`. URL: `http://doi.wiley.com/10.1002/2013GC004861`.

Palomeras, I. et al. (2017). “Lithospheric structure of Iberia and Morocco using finite-frequency Rayleigh wave tomography from earthquakes and seismic ambient noise". In: *Geochemistry, Geophysics, Geosystems*. ISSN: 15252027. DOI: 10.1002/2016GC006657. URL: http://doi.wiley.com/10.1002/2016GC006657.

Park, R. G. (1988). *Geological Structures and Moving Plates*. Springer Netherlands, p. 337. ISBN: 9789401716857. URL: https://books.google.es/books?hl=en{\&}lr={\&}id=KyUHCAAAQBAJ{\&}oi=fnd{\&}pg=PT15{\&}ots=TWAm9rCFYQ{\&}sig=ZRnzHyNqOUzFh9jmk20RNLTASCs{\&}redir{_}esc=y{\#}v=onepage{\&}q{\&}f=false.

Pasyanos, Michael E. (2010). "Lithospheric thickness modeled from long-period surface wave dispersion". In: *Tectonophysics* 481.1-4, pp. 38–50. ISSN: 0040-1951. DOI: 10.1016/J.TECTO.2009.02.023. URL: https://www.sciencedirect.com/science/article/pii/S0040195109000997.

Pasyanos, Michael E. et al. (2007). "Seismic structure of Kuwait". In: *Geophysical Journal International* 170.1, pp. 299–312. ISSN: 0956540X. DOI: 10.1111/j.1365-246X.2007.03398.x. URL: https://academic.oup.com/gji/article-lookup/doi/10.1111/j.1365-246X.2007.03398.x.

Pearce, F. D. et al. (2012). "Seismic investigation of the transition from continental to oceanic subduction along the western Hellenic Subduction Zone". In: *Journal of Geophysical Research* 117.B7, B07306. ISSN: 0148-0227. DOI: 10.1029/2011JB009023. URL: http://doi.wiley.com/10.1029/2011JB009023.

Pedrera, Antonio et al. (2010). "Crustal-scale transcurrent fault development in a weak-layered crust from an integrated geophysical research: Carboneras Fault Zone, eastern Betic Cordillera, Spain". In: *Geochemistry, Geophysics, Geosystems* 11.12. ISSN: 15252027. DOI: 10.1029/2010GC003274.

Pérez-Peña, José Vicente et al. (2010). "Active tectonics in the Sierra Nevada (Betic Cordillera, SE Spain): Insights from geomorphic indexes and drainage pattern analysis". In: *Geomorphology* 119.1-2, pp. 74–87. ISSN: 0169-555X. DOI: 10.1016/J.GEOMORPH.2010.02.020. URL: https://www.sciencedirect.com/science/article/pii/S0169555X10001042.

Pérez-Valera, Luis Alfonso et al. (2013). "Age distribution of lamproites along the Socovos Fault (southern Spain) and lithospheric scale tearing". In: *Lithos* 180-181, pp. 252–263. ISSN: 0024-4937. DOI: 10.1016/J.LITHOS.2013.08.016. URL: https://www.sciencedirect.com/science/article/pii/S002449371300279X.

Piana Agostinetti, Nicola (2015). "The structure of the Moho in the Northern Apennines: Evidence for an incipient slab tear fault?" In: *Tectonophysics* 655, pp. 88–96. ISSN: 0040-1951. DOI: `10.1016/J.TECTO.2015.05.013`. URL: `https://www.sciencedirect.com/science/article/pii/S0040195115002802`.

Piana Agostinetti, Nicola, Jeffrey Park, and Francesco Pio Lucente (2008). "Mantle wedge anisotropy in Southern Tyrrhenian Subduction Zone (Italy), from receiver function analysis". In: *Tectonophysics* 462.1-4, pp. 35–48. ISSN: 00401951. DOI: `10.1016/j.tecto.2008.03.020`. URL: `http://dx.doi.org/10.1016/j.tecto.2008.03.020`.

Piromallo, Claudia and Andrea Morelli (2003). "<i>P</i> wave tomography of the mantle under the Alpine-Mediterranean area". In: *Journal of Geophysical Research: Solid Earth* 108.B2. ISSN: 01480227. DOI: `10.1029/2002JB001757`. URL: `http://doi.wiley.com/10.1029/2002JB001757`.

Platt, J. and G. Houseman (2003). "Evidence for active subduction beneath Gibraltar: Comment and Reply: COMMENT". In: *Geology* 31.1, e22–e22. ISSN: 0091-7613. DOI: `10.1130/0091-7613-31.1.e22`. URL: `http://geology.gsapubs.org/cgi/doi/10.1130/0091-7613-31.1.e22`.

Platt, J. P. and R.L.M. Vissers (1989). "Extensional collapse of thickened continental lithosphere: A working hypothesis for the Alboran Sea and Gibraltar arc". In: *Geology* 17.6, p. 540. ISSN: 0091-7613. DOI: `10.1130/0091-7613(1989)017<0540:ECOTCL>2.3.CO;2`. URL: `https://pubs.geoscienceworld.org/geology/article/17/6/540-543/204912`.

Platt, John P. et al. (2006). "Early Miocene continental subduction and rapid exhumation in the western Mediterranean". In: *Geology* 34.11, p. 981. ISSN: 0091-7613. DOI: `10.1130/G22801A.1`. URL: `https://pubs.geoscienceworld.org/geology/article/34/11/981-984/129464`.

Platt, John P. et al. (2013). "The Betic-Rif Arc and Its Orogenic Hinterland: A Review". en. In: *Annual Review of Earth and Planetary Sciences* 41.1, pp. 313–357. ISSN: 0084-6597. DOI: `10.1146/annurev-earth-050212-123951`. URL: `http://www.annualreviews.org/doi/full/10.1146/annurev-earth-050212-123951`.

Platt, J.P. (2007). "From orogenic hinterlands to Mediterranean-style back-arc basins: a comparative analysis". In: *Journal of the Geological Society* 164.2, pp. 297–311. ISSN: 0016-7649. DOI: 10.1144/0016-76492006-093. URL: http://jgs.lyellcollection.org/lookup/doi/10.1144/0016-76492006-093.

Platt, J.P. et al. (1983). "The structure and tectonic evolution of the Aguilón fold-nappe, Sierra Alhamilla, Betic Cordilleras, SE Spain". In: *Journal of Structural Geology* 5.5, pp. 519–538. ISSN: 0191-8141. DOI: 10.1016/0191-8141(83)90057-3. URL: https://www.sciencedirect.com/science/article/pii/0191814183900573.

Poujol, A. et al. (2014). "Active tectonics of the Northern Rif (Morocco) from geomorphic and geochronological data". In: *Journal of Geodynamics* 77, pp. 70–88. ISSN: 0264-3707. DOI: 10.1016/J.JOG.2014.01.004. URL: https://www.sciencedirect.com/science/article/pii/S0264370714000143.

Rehault, Jean-Pierre, Gilbert Boillot, and Alain Mauffret (1984). "The Western Mediterranean Basin geological evolution". In: *Marine Geology* 55.3-4, pp. 447–477. ISSN: 0025-3227. DOI: 10.1016/0025-3227(84)90081-1. URL: https://www.sciencedirect.com/science/article/pii/0025322784900811.

Revenaugh, J. (1995). "A Scattered-Wave Image of Subduction Beneath the Transverse Ranges". In: *Science* 268.5219, pp. 1888–1892. ISSN: 0036-8075. DOI: 10.1126/science.268.5219.1888. URL: http://www.ncbi.nlm.nih.gov/pubmed/17797531http://www.sciencemag.org/cgi/doi/10.1126/science.268.5219.1888.

Rondenay, Stéphane (2009). "Upper mantle imaging with array recordings of converted and scattered teleseismic waves". In: *Surveys in Geophysics* 30.4-5, pp. 377–405. ISSN: 01693298. DOI: 10.1007/s10712-009-9071-5.

Rosenbaum, Gideon, Gordon Lister, and Cecile Duboz (2002). "Reconstruction of the tectonic evolution of the Western Mediterranean since the Oligocene". In: *Journal of the Virtual Explorer* 8, pp. 107–130. DOI: 10.3809/jvirtex.2002.00053.

Royden, Leigh H. (1993). "The tectonic expression slab pull at continental convergent boundaries". In: *Tectonics* 12.2, pp. 303–325. ISSN: 02787407. DOI: 10.1029/92TC02248. URL: http://doi.wiley.com/10.1029/92TC02248.

Rychert, Catherine A., Karen M. Fischer, and Stéphane Rondenay (2005). "A sharp lithosphere–asthenosphere boundary imaged beneath eastern North

America". In: *Nature* 436.7050, pp. 542–545. ISSN: 0028-0836. DOI: 10.1038/nature03904. URL: http://www.nature.com/articles/nature03904.

Rychert, Catherine A., Nicholas Harmon, and Cynthia Ebinger (2014). "Receiver function imaging of lithospheric structure and the onset of melting beneath the Galápagos Archipelago". In: *Earth and Planetary Science Letters* 388, pp. 156–165. ISSN: 0012-821X. DOI: 10.1016/J.EPSL.2013.11.027. URL: https://www.sciencedirect.com/science/article/pii/S0012821X13006614.

Rychert, Catherine A. and Nick Harmon (2018). "Predictions and Observations for the Oceanic Lithosphere From <i>S</i> -to- <i>P</i> Receiver Functions and <i>SS</i> Precursors". In: *Geophysical Research Letters* 45.11, pp. 5398–5406. ISSN: 00948276. DOI: 10.1029/2018GL077675. URL: http://doi.wiley.com/10.1029/2018GL077675.

Rychert, Catherine A., Stéphane Rondenay, and Karen M. Fischer (2007). "<i>P</i> -to- <i>S</i> and <i>S</i> -to- <i>P</i> imaging of a sharp lithosphere-asthenosphere boundary beneath eastern North America". In: *Journal of Geophysical Research* 112.B8, B08314. ISSN: 0148-0227. DOI: 10.1029/2006JB004619. URL: http://doi.wiley.com/10.1029/2006JB004619.

Rychert, Catherine A. and Peter M. Shearer (2009). "A Global View of the Lithosphere-Asthenosphere Boundary". In: *Science* 324.5926, pp. 495–498. ISSN: 0036-8075. DOI: 10.1126/SCIENCE.1169754. URL: http://science.sciencemag.org/content/324/5926/495.

Sallarès, Valentí et al. (2011). "Seismic evidence for the presence of Jurassic oceanic crust in the central Gulf of Cadiz (SW Iberian margin)". In: DOI: 10.1016/j.epsl.2011.09.003. URL: http://ac.els-cdn.com/S0012821X11005140/1-s2.0-S0012821X11005140-main.pdf?{_}tid=64fb8560-4f6d-11e7-9587-00000aacb35f{\&}acdnat=1497271872{_}d85ac3e77fc2e73772cf977c661b42c0.

Sanz de Galdeano, C. et al. (2007). "Anomalías gravimétricas de la cuenca de Guadix-Baza (Cordillera Bética, España)". In: *Bol. Geol. Min.* 118 (4), pp. 763–774. ISSN: 0366-0176. URL: http://digital.csic.es/handle/10261/29422.

Sanz de Galdeano, Carlos and Carlos (2008). “The Cadiz-Alicante Fault: an important discontinuity in the Betic Cordillera”. In: ISSN: 0214-2708. URL: `http://hdl.handle.net/10261/29430`.

Sartori, R. et al. (1994). “Eastern segment of the Azores-Gibraltar line (central-eastern Atlantic) : An oceanic plate boundary with diffuse compressional deformation”. In: *Geology* 22.6, p. 555. ISSN: 0091-7613. DOI: `10.1130/0091-7613(1994)022<0555:ESOTAG>2.3.CO;2`. URL: `https://pubs.geoscienceworld.org/geology/article/22/6/555-558/206121`.

Savage, Martha Kane (1998). “Lower crustal anisotropy or dipping boundaries? Effects on receiver functions and a case study in New Zealand”. In: *Journal of Geophysical Research* 103.B7, p. 15069. ISSN: 0148-0227. DOI: `10.1029/98JB00795`. URL: `http://doi.wiley.com/10.1029/98JB00795`.

Scarfì, L. et al. (2018). “Slab narrowing in the Central Mediterranean: the Calabro-Ionian subduction zone as imaged by high resolution seismic tomography”. In: *Scientific Reports* 8.1, p. 5178. ISSN: 2045-2322. DOI: `10.1038/s41598-018-23543-8`. URL: `http://www.nature.com/articles/s41598-018-23543-8`.

Schimmel, Martin and Hanneke Paulssen (1997). “Noise reduction and detection of weak, coherent signals through phase-weighted stacks”. In: *Geophysical Journal International* 130.2, pp. 497–505. ISSN: 0956540X. DOI: `10.1111/j.1365-246X.1997.tb05664.x`. URL: `http://doi.wiley.com/10.1111/j.1365-246X.1997.tb05664.x`.

Schneider, Felix Michael (2014). “Imaging an Intra-continental Subduction in Central Asia with Teleseismic Receiver Functions”. In:

Schulte-Pelkum, V. and Y. Ben-Zion (2012). “Apparent Vertical Moho Offsets under Continental Strike-Slip Faults from Lithology Contrasts in the Seismogenic Crust”. In: *Bulletin of the Seismological Society of America* 102.6, pp. 2757–2763. ISSN: 0037-1106. DOI: `10.1785/0120120139`. URL: `https://pubs.geoscienceworld.org/bssa/article/102/6/2757-2763/331605`.

Schulte-Pelkum, Vera et al. (2005). “Imaging the Indian subcontinent beneath the Himalaya.” In: *Nature* 435.7046, pp. 1222–1225. ISSN: 0028-0836. DOI: `10.1038/nature03678`.

Seber, Dogan et al. (1996). "Geophysical evidence for lithospheric delamination beneath the Alboran Sea and Rif–Betic mountains". In: *Nature* 379.6568, pp. 785–790. ISSN: 0028-0836. DOI: `10.1038/379785a0`. URL: `http://www.nature.com/articles/379785a0`.

Serpelloni, E. et al. (2007). "Kinematics of the Western Africa-Eurasia plate boundary from focal mechanisms and GPS data". In: *Geophysical Journal International* 169.3, pp. 1180–1200. ISSN: 0956540X. DOI: `10.1111/j.1365-246X.2007.03367.x`. URL: `https://academic.oup.com/gji/article-lookup/doi/10.1111/j.1365-246X.2007.03367.x`.

Serrano, Inma et al. (2005). "Seismic anisotropy and velocity structure beneath the southern half of the Iberian Peninsula". In: *Physics of the Earth and Planetary Interiors* 150.4, pp. 317–330. ISSN: 00319201. DOI: `10.1016/j.pepi.2004.12.003`.

Shang, Xuefeng (2014). "Inverse scattering : theory and application to the imaging of the Earth's seismic discontinuities". In:

Shang, Xuefeng, Maarten V. De Hoop, and Robert D. Van Der Hilst (2012). "Beyond receiver functions: Passive source reverse time migration and inverse scattering of converted waves". In: *Geophysical Research Letters* 39.15. ISSN: 00948276. DOI: `10.1029/2012GL052289`.

Shang, Xuefeng, Maarten V. de Hoop, and Robert D. van der Hilst (2017). "Common conversion point stacking of receiver functions versus passive-source reverse time migration and wavefield regularization". In: *Geophysical Journal International* 209.2, pp. 923–934. ISSN: 0956-540X. DOI: `10.1093/gji/ggx069`. URL: `https://academic.oup.com/gji/article-lookup/doi/10.1093/gji/ggx069`.

Shapiro, Nikolai M et al. (2005). "High-resolution surface-wave tomography from ambient seismic noise." In: *Science (New York, N.Y.)* 307.5715, pp. 1615–8. ISSN: 1095-9203. DOI: `10.1126/science.1108339`. URL: `http://www.ncbi.nlm.nih.gov/pubmed/15761151`.

Sheehan, Anne F. et al. (2000). "Seismic migration processing of <i>P-SV</i> converted phases for mantle discontinuity structure beneath the Snake River Plain, western United States". In: *Journal of Geophysical Research: Solid Earth*

105.B8, pp. 19055–19065. ISSN: 01480227. DOI: 10.1029/2000JB900112. URL: http://doi.wiley.com/10.1029/2000JB900112.

Shen, Weisen, Michael H. Ritzwoller, and Vera Schulte-Pelkum (2013). "A 3-D model of the crust and uppermost mantle beneath the Central and Western US by joint inversion of receiver functions and surface wave dispersion". In: *Journal of Geophysical Research: Solid Earth* 118.1, pp. 262–276. ISSN: 21699356. DOI: 10.1029/2012JB009602.

Silveira, Graça, Nuno Afonso Dias, and Antonio Villaseñor (2013). "Seismic imaging of the western Iberian crust using ambient noise: Boundaries and internal structure of the Iberian Massif". In: *Tectonophysics* 589, pp. 186–194. ISSN: 00401951. DOI: 10.1016/j.tecto.2012.12.025. URL: http://www.scopus.com/inward/record.url?eid=2-s2.0-84875378283{\&}partnerID=tZOtx3y1.

Spakman, Wim, M J R Wortel, and Rinus Wortel (2004). "Tomographic View on Western Mediterranean Geodynamics Chapter 2 A Tomographic View on Western Mediterranean Geodynamics". In: pp. 31–52.

Spakman, Wim et al. (2018). "Puzzling features of western Mediterranean tectonics explained by slab dragging". In: *Nature Geoscience* February. ISSN: 1752-0894. DOI: 10.1038/s41561-018-0066-z. URL: http://www.nature.com/articles/s41561-018-0066-z.

Stampfli, G.M and G.D Borel (2002). "A plate tectonic model for the Paleozoic and Mesozoic constrained by dynamic plate boundaries and restored synthetic oceanic isochrons". In: *Earth and Planetary Science Letters* 196.1-2, pp. 17–33. ISSN: 0012-821X. DOI: 10.1016/S0012-821X(01)00588-X. URL: https://www.sciencedirect.com/science/article/pii/S0012821X0100588X.

Stein, Carol A. and Seth Stein (1992). "A model for the global variation in oceanic depth and heat flow with lithospheric age". In: *Nature* 359.6391, pp. 123–129. ISSN: 0028-0836. DOI: 10.1038/359123a0. URL: http://www.nature.com/articles/359123a0.

Stich, D, Ammon C.J., and Morales J. (2003). "Moment tensor solutions for small and moderate earthquakes in the Ibero-Maghreb region". In: *Journal of Geophysical Research* 108.

Stich, D et al. (2009). "Imaging lateral heterogeneity in the northern Apennines from time reversal of reflected surface waves". In: *Geophys. J. Int.* 177, pp. 543–554.

Stich, Daniel, Flor de Lis Mancilla, and Jose Morales (2005). "Crust-mantle coupling in the Gulf of Cadiz (SW-Iberia)". In: *Geophysical Research Letters* 32.13, p. L13306. ISSN: 0094-8276. DOI: 10.1029/2005GL023098. URL: http://doi.wiley.com/10.1029/2005GL023098.

Stich, Daniel, Rosa Martín, and Jose Morales (2010). "Moment tensor inversion for Iberia–Maghreb earthquakes 2005–2008". In: *Tectonophysics* 483.3-4, pp. 390–398. ISSN: 00401951. DOI: 10.1016/j.tecto.2009.11.006. URL: https://linkinghub.elsevier.com/retrieve/pii/S0040195109006258.

Stich, Daniel et al. (2006). "Kinematics of the Iberia–Maghreb plate contact from seismic moment tensors and GPS observations". In: *Tectonophysics* 426.3-4, pp. 295–317. ISSN: 00401951. DOI: 10.1016/j.tecto.2006.08.004. URL: http://linkinghub.elsevier.com/retrieve/pii/S0040195106003969.

Stich, Daniel et al. (2007). "Source analysis of the February 12th 2007, M w 6.0 Horseshoe earthquake: Implications for the 1755 Lisbon earthquake". In: *Geophysical Research Letters* 34.12, p. L12308. ISSN: 0094-8276. DOI: 10.1029/2007GL030012. URL: http://doi.wiley.com/10.1029/2007GL030012.

Thurner, Sally et al. (2014). "Ongoing lithospheric removal in the western Mediterranean: Evidence from Ps receiver functions and thermobarometry of Neogene basalts (PICASSO project)". In: *Geochemistry, Geophysics, Geosystems* 15.4, pp. 1113–1127. ISSN: 15252027. DOI: 10.1002/2013GC005124.

Torne, M and M Fernhndez (2000). "Lithospheric Structure Beneath the Alboran Basin : Results from 3D Gravity Modeling and Tectonic Relevance". In: 105, pp. 3209–3228.

Tromp, Jeroen, Carl Tape, and Qinya Liu (2005). "Seismic tomography, adjoint methods, time reversal and banana-doughnut kernels". In: *Geophysical Journal International* 160.1, pp. 195–216. ISSN: 0956540X. DOI: 10.1111/j.1365-246X.2004.02453.x.

Turner, S. P. et al. (1999). "Magmatism Associated with Orogenic Collapse of the Betic-Alboran Domain, SE Spain". In: *Journal of Petrology* 40.6, pp. 1011–1036. ISSN: 0022-3530. DOI: 10.1093/petroj/40.6.1011. URL: https:

//academic.oup.com/petrology/article-lookup/doi/10.1093/petroj/40.6.1011.

Van Hinsbergen, Douwe J J, Reinoud L M Vissers, and Wim Spakman (2014). "Origin and consequences of western Mediterranean subduction, rollback, and slab segmentation". In: *Tectonics* 33.4, pp. 393–419.

VanDecar, J C and R S Crosson (1990). "Determination of teleseismic relative phase arrival times using multi-channel cross-correlation and least squares". In: *Bulletin of the Seismological Society of America* 80.1, pp. 150–169. ISSN: 0037-1106. URL: http://dx.doi.org/.

Vergés, Jaume and Manel Fernàndez (2012). "Tethys–Atlantic interaction along the Iberia–Africa plate boundary: The Betic–Rif orogenic system". In: *Tectonophysics* 579, pp. 144–172. ISSN: 00401951. DOI: 10.1016/j.tecto.2012.08.032. URL: http://linkinghub.elsevier.com/retrieve/pii/S0040195112005215.

Villaseñor, Antonio et al. (2015). "Subduction and volcanism in the Iberia–North Africa collision zone from tomographic images of the upper mantle". In: *Tectonophysics* 663, pp. 238–249. ISSN: 00401951. DOI: 10.1016/j.tecto.2015.08.042.

Vinnik, L., E. Kurnik, and V. Farra (2005). "Lehmann discontinuity beneath North America: No role for seismic anisotropy". In: *Geophysical Research Letters* 32.9. URL: http://www.ipgp.fr/fr/lehmann-discontinuity-beneath-north-america-no-role-for-seismic-anisotropy.

Vinnik, L. P., V. Farra, and R. Kind (2004). "Deep structure of the Afro-Arabian hotspot by S receiver functions". In: *Geophysical Research Letters* 31.11, n/a–n/a. ISSN: 00948276. DOI: 10.1029/2004GL019574. URL: http://doi.wiley.com/10.1029/2004GL019574.

Vinnik, L.P. (1977). "Detection of waves converted from p to sv in the mantle*1 l.p." In: 15.October 1976, pp. 39–45.

Virieux, Jean (1986). "P-SV wave propagation in heterogeneous media: Velocity-stress finite-difference method". In: *Geophyisics* 51.Ii, pp. 1933–1942.

Vissers, R. L. M. and B. M. L. Meijninger (2011). "The 11 May 2011 earthquake at Lorca (SE Spain) viewed in a structural-tectonic context". In: *Solid Earth* 2.2, pp. 199–204. ISSN: 1869-9529. DOI: 10.5194/se-2-199-2011. URL: https://www.solid-earth.net/2/199/2011/.

Vissers, R. L. M., J. P. Platt, and D. van der Wal (1995). “Late orogenic extension of the Betic Cordillera and the Alboran Domain: A lithospheric view”. In: *Tectonics* 14.4, pp. 786–803. ISSN: 02787407. DOI: `10.1029/95TC00086`. URL: `http://doi.wiley.com/10.1029/95TC00086`.

Walker, K. T. et al. (2005). “Shear-wave splitting around the Eifel hotspot: evidence for a mantle upwelling”. In: *Geophysical Journal International* 163.3, pp. 962–980. ISSN: 0956540X. DOI: `10.1111/j.1365-246X.2005.02636.x`. URL: `https://academic.oup.com/gji/article-lookup/doi/10.1111/j.1365-246X.2005.02636.x`.

Yu, Chunquan, Yingcai Zheng, and Xuefeng Shang (2017). “Crazyseismic: A MATLAB GUI[U+2010]Based Software Package for Passive Seismic Data Preprocessing”. In: *Seismological Research Letters* 88.2A, pp. 410–415. ISSN: 0895-0695. DOI: `10.1785/0220160207`. URL: `http://srl.geoscienceworld.org/lookup/doi/10.1785/0220160207`.

Yuan, X. et al. (2000). “Subduction and collision processes in the Central Andes constrained by converted seismic phases”. In: *Nature* 408.6815, pp. 958–961. ISSN: 0028-0836. DOI: `10.1038/35050073`. URL: `http://www.nature.com/articles/35050073`.

Yuan, Xiaohui et al. (1997). “Lithospheric and upper mantle structure of southern Tibet from a seismological passive source experiment”. In: *Journal of Geophysical Research: Solid Earth* 102.B12, pp. 27491–27500. ISSN: 01480227. DOI: `10.1029/97JB02379`. URL: `http://doi.wiley.com/10.1029/97JB02379`.

Yuan, Xiaohui et al. (2006). “The S receiver functions: synthetics and data example”. In: *Geophysical Journal International* 165.2, pp. 555–564. ISSN: 0956540X. DOI: `10.1111/j.1365-246X.2006.02885.x`. URL: `http://gji.oxfordjournals.org/cgi/doi/10.1111/j.1365-246X.2006.02885.x`.

Zeck, H.P. (1996). “Betic-Rif orogeny: subduction of Mesozoic Tethys lithosphere under eastward drifting Iberia, slab detachment shortly before 22 Ma, and subsequent uplift and extensional tectonics”. In: *Tectonophysics* 254.1-2, pp. 1–16. ISSN: 0040-1951. DOI: `10.1016/0040-1951(95)00206-5`. URL: `https://www.sciencedirect.com/science/article/pii/0040195195002065`.

Zhai, Yongbo and A. Levander (2011). “Receiver function imaging in strongly laterally heterogeneous crust: Synthetic modeling of BOLIVAR data”. In:

Earthquake Science 24.1, pp. 45–54. ISSN: 1674-4519. DOI: 10.1007/s11589-011-0768-4. URL: http://link.springer.com/10.1007/s11589-011-0768-4.

Zhu, Lupei and Hiroo Kanamori (2000). "Moho depth variation in southern California from teleseismic receiver functions". In: *Journal of Geophysical Research* 105.B2, p. 2969. ISSN: 0148-0227. DOI: 10.1029/1999JB900322. URL: http://doi.wiley.com/10.1029/1999JB900322.

Zitellini, N. et al. (2009). "The quest for the Africa–Eurasia plate boundary west of the Strait of Gibraltar". In: *Earth and Planetary Science Letters* 280.1-4, pp. 13–50. ISSN: 0012-821X. DOI: 10.1016/J.EPSL.2008.12.005. URL: https://www.sciencedirect.com/science/article/pii/S0012821X0800753X.